Aeraulic transfer mechanisms through openings on enclosures in maintenance and dismantling sites : evaluation of aerosol aerodynamic behavior contribution to backflow phenomenon

Zeinab Rida

THÈSE

En vue de l'obtention du

DOCTORAT DE L'UNIVERSITÉ DE TOULOUSE

Délivré par :

Institut National Polytechnique de Toulouse (Toulouse INP)

Discipline ou spécialité :

Dynamique des fluides

Présentée et soutenue par :

Mme ZEINAB RIDA

le lundi 31 janvier 2022

Titre :

Aeraulic transfer mechanisms through openings on enclosures in maintenance and dismantling sites: Evaluation of aerosol aerodynamic behavior contribution to backflow phenomenon

---

Ecole doctorale :

Mécanique, Energétique, Génie civil, Procédés (MEGeP)

Unité de recherche :

Institut de Mécanique des Fluides de Toulouse (IMFT)

Directeur(s) de Thèse :

M. ERIC CLIMENT

Rapporteurs :

MME ANNE TANIERE, UNIVERSITE LORRAINE

MME EVELYNE GEHIN, UNIVERSITE PARIS EST CRETEIL

Membre(s) du jury :

M. OLIVIER VAUQUELIN, AIX-MARSEILLE UNIVERSITE, Président

M. ERIC CLIMENT, TOULOUSE INP, Membre

M. LUC LAFANECHÈRE, EDF LYON, Invité(e)

MME CORINNE PREVOST, IRSN, Membre

M. THOMAS GELAIN, IRSN, Membre

Acknowledgements

My PhD thesis was done at the 'Institut de Radioprotection et de Sûreté Nucléaire' (IRSN, site CEA-Saclay), in collaboration with 'Institut de Mécanique des Fluides de Toulouse' (IMFT) and EDF. Due to covid restrictions, a part of my work was done online from home.

I would like first to thank Professor Eric CLIMENT, university professor at the University of Toulouse and the director of IMFT. I had the pleasure to collaborate with you, first as my master internship supervisor and then as my PhD thesis director. Your advice and scientific observations contributed greatly to the outcome of this work. I really appreciate your human qualities and your professionalism.

I would like also to thank my PhD supervisors Corinne PREVOST and Thomas GELAIN. Thank you, Corinne, for the intense experimental support and the long fruitful discussions that we had. I appreciate your friendly attitude and the 'expressions françaises' that you taught me! Thank you, Thomas, for your kindness and for supporting me massively in the numerical part of this work. The 'licences numériques' will be no longer saturated!

I also want to thank Luc LAFANECHERE, Audrey AMPHOUX and, Marjorie JACQUELIN from EDF for their special assistance. Our collaboration showed the industrial interest of this research work.

In the context of my work at IRSN, I want to thank Laurent BOUILLOUX, head of the 'Service de Confinement et de l'Aérodispersion des polluants' (SCA), for welcoming me into his teams. I would like also to thank his adjoint Laurent RICCIARDI and wishing him good luck in the next 'pronostics'. I would like also to thank Jérôme RICHARD, Head of 'Laboratoire d'Etudes et de Modélisation en Aérodispersion et Confinement' (LEMAC), for allowing me to carry out this research work in excellent conditions despite the covid restrictions.

I want to express my acknowledgments to Nadia LIATIMI and Florent DANY for their technical support on the experimental part of this work. I am grateful to the trainee Lou-Ane Le BERRE that gave me a major experimental support during our work. I would also like to thank the PhD student Delphine COSTA for the sweet moments that we had and wishing her good luck in her PhD defense. I would also like to thank my colleagues at LEMAC for their good humor.

Finally, I am very grateful to my family for supporting me during these three years. Accomplishing this work was not possible without you. A special thanks to Mostafa for his encouragement during the redaction of this report. Thank you for always being there for me.

Mécanismes de transfert aéraulique au travers d'ouvertures d'enceintes de confinement : évaluation de la contribution du comportement aérodynamique des aérosols au phénomène de rétrodiffusion

Le contexte de ma thèse concerne la sûreté des enceintes ventilées mises en œuvre sur les chantiers de maintenance et de démantèlement de sites nucléaires. Il s'agit de caractériser l'efficacité du confinement dynamique des enceintes de type « sas » en étudiant le phénomène de rétrodiffusion d'un polluant gazeux ou particulaire. Ce phénomène de rétrodiffusion peut se produire à travers des ouvertures nominales ou accidentelles sur ces dispositifs de confinement suite à une perturbation aéraulique se produisant à l'intérieur ou à l'extérieur de l'enceinte. Nos travaux s'inscrivent dans la continuité de ceux de S. Kaissoun[1] qui a étudié expérimentalement et numériquement le phénomène de la rétrodiffusion locale d'un polluant gazeux au niveau d'une ouverture rectangulaire d'une maquette expérimentale à échelle réduite. Dans le cadre de ma thèse, nous avons ajouté une enveloppe externe autour de la maquette expérimentale afin de caractériser la quantité globale des polluants rétrodiffusés. Les principaux objectifs de ma thèse sont les suivants. D'une part, on veut caractériser expérimentalement la rétrodiffusion à l'aide de techniques laser de visualisation (Schlieren, PIV) et mesurer les quantités locales et globales de polluants gazeux et particulaires pour un aérosol de diamètre aérodynamique 5 µm émis au travers d'une ouverture en utilisant les techniques de traçage dédiées. D'autre part, on veut valider la capacité des modèles hybrides CFD de turbulence (DES-SST) à retranscrire la rétrodiffusion des polluants gazeux et particulaires. Les résultats expérimentaux et numériques finalement obtenus permettent de dresser les deux conclusions suivantes. Les comportements aérauliques du gaz et de l'aérosol de 5 µm sont similaires à proximité de l'ouverture pour nos conditions aérauliques. La capacité du modèle hybride DES-SST à reproduire le phénomène de rétrodiffusion est validée qualitativement et quantitativement. Des études expérimentales et numériques du phénomène de rétrodiffusion ont finalement été réalisées sur un sas à échelle réelle présentant des parois souples en vinyle, à la fois pour un polluant gazeux et un polluant particulaire. Les résultats quantitatifs préliminaires obtenus expérimentalement sont en bon accord avec des simulations numériques pour le sas à échelle réelle.

Mots clés : rétrodiffusion, aérosol, gaz, confinement dynamique, jet de perturbation, écoulements aux ouvertures, modèles hybrides

Aeraulic transfer mechanisms through openings on enclosures in maintenance and dismantling sites: Evaluation of aerosol aerodynamic behavior contribution to backflow phenomenon

The context of my thesis concerns the safety of ventilated enclosures implemented on maintenance and dismantling sites of nuclear sites. It aims to characterize the efficiency of dynamic containment of ventilated airlocks by studying the backflow of gaseous and particulate pollutants. Backflow phenomenon can occur through nominal or accidental openings on ventilated enclosures under the effect of an internal or external aeraulic disturbance. Our works are the continuation of S. Kaissoun[1] works who studied the phenomenon of local backflow of a gaseous pollutant at a rectangular opening on a small-size enclosure. As part of my thesis, we added an external envelope around the experimental enclosure in order to characterize the overall quantity of pollutants coming from the backflow. The main objectives of my thesis are as follow. On one hand, we aim to characterize the backflow phenomenon experimentally using laser visualization techniques (Schlieren, PIV) and to measure the local and global quantities of gaseous and 5 µm particulate pollutants emitted through an opening using dedicated tracing techniques. On the other hand, we aim to validate the capacity of hybrid CFD turbulence models (SST-DES) to qualitatively and quantitatively transcribe the unsteady backflow phenomena of gaseous and particulate pollutants. The experimental and numerical results obtained allow us to draw the following two conclusions. First, the aeraulic behavior of gas and 5 µm aerosol is similar near the opening for our aeraulic conditions. Secondly, the capacity of SST-DES hybrid model to reproduce the backflow phenomenon is qualitatively and quantitatively validated. Experimental and numerical studies of the backflow phenomenon were finally carried out on a full-size airlock with flexible vinyl walls. Preliminary works show that quantitative results obtained experimentally matches those obtained from numerical simulations.

Keywords: backflow phenomenon, aerosol, gas, dynamic containment, perturbation jet, flow at openings, hybrid models

[1]Kaissoun, S. (2018). Mécanismes de transfert aéraulique au travers d'ouvertures : application à l'efficacité du confinement dynamique d'enceintes de chantier.

TABLE OF CONTENTS

INTRODUCTION 19

1 Bibliography 22

1.1. Containment in nuclear systems and backflow phenomenon 22

1.1.1 Containment in nuclear systems 22

1.1.1.1 Containment systems 22

1.1.1.2 Airlocks with flexible walls 24

1.1.1.3 Dynamic containment criteria 25

1.1.2 Backflow phenomenon 28

1.1.2.1 Phenomena related to the backflow 29

1.1.2.2 Coefficients related to the backflow 30

1.1.2.3 Tracing techniques 31

1.1.2.4 Various works on pollutant backflow phenomenon described in the literature 31

1.2. Mixing of gases and particles in a gas flow 39

1.2.1 Mixing of gas in turbulent flow 39

1.2.2 Particle-laden flows 40

1.2.2.1 Characterization of the aerosol 41

1.2.2.2 Classification of two-phase turbulent flows 41

1.2.2.2.1 Based on their volume fraction 41

1.2.2.2.2 Based on their Stokes number 42

1.2.2.3 Works on particle-laden flows 44

1.3. Numerical simulations for turbulence 47

1.3.1 Turbulence modelling: 47

1.3.1.1 Unsteady Reynolds-averaged Navier–Stokes (URANS) modelling 48

1.3.1.2 LES modelling 49

1.3.1.3 Hybrid models 49

1.3.1.4 Direct numerical simulation (DNS) method 52

1.3.2 Particle-laden turbulent flows approaches 52

1.3.2.1 Dusty gas approach 53

1.3.2.2 Equilibrium Eulerian approach 53

1.3.2.3 Eulerian approach 53

1.3.2.4 Lagrangian point-particle approach 56
1.3.2.5 Fully resolved approach 56
2 Experimental study of backflow air leakage through an opening from a depressurized enclosure ... 58
3. Experiments 73
3.1 Local backflow 78
3.1.1 Visualization of the backflow 78
3.1.1.1 Materials and methods 78
3.1.1.2 Counter-current internal disturbing jet 78
3.1.1.2.1 Rigid frontal wall 78
3.1.1.2.2 Flexible frontal wall 82
3.1.1.3 Parietal internal disturbing jet 84
3.1.2 Quantification of the backflow phenomenon 87
3.1.2.1 Material and methods (scheme procedure for gas and aerosol) 87
3.1.2.1.1 Aerosol devices 88
3.1.2.1.2 Scheme procedure for gas and aerosol 92
3.1.2.2 Results for internal counter-current disturbing jet of the gaseous/particulate pollutants and rigid/flexible frontal wall 95
3.1.2.2.1 Results of gaseous pollutant with the rigid frontal wall 95
3.1.2.2.2 Results of particulate pollutant with the rigid frontal wall 97
3.1.2.2.3 Comparison of results for gaseous/particulate pollutants within the enclosure of rigid/flexible frontal wall 99
3.1.2.3 Results for internal parietal disturbing jet of the gaseous/particulate pollutants and rigid/flexible frontal wall 101
3.1.2.4 Comparison of the local backflow between the frontal and parietal disturbances for the gaseous and particulate pollutants 102
3.2 Global quantification of the backflow phenomenon 104
3.2.1 Description of the envelope 104
3.2.2 Evaluation of the impact of envelope on the flow near the opening 105
Velocities profiles 107
3.2.3 Characterization of the air exchange rate and particles deposition measurement inside the envelope 109
3.2.3.1 Characterization of the air exchange rate in the envelope and its homogeneity 110
3.2.3.2 Estimation of the particle deposition inside the envelope 111
3.2.3.3 Experimental estimation of the gaseous and particulate decay curves within the envelope 112

3.2.4 Quantification of the global backflow phenomenon 114
3.2.4.1 Description of the operating procedure to collect backflow pollutants 114
3.2.4.2 Results of the global quantification for the internal counter-current free jet 117
3.2.4.2.1 Results for gaseous/particulate pollutants corresponding to three inlet velocities 117
3.2.4.2.2 Comparison of results for gaseous/particulate pollutants within the enclosure of rigid/flexible frontal wall 120
3.2.4.3 Results of global backflow coefficients for internal parietal free jet 121
3.2.4.3.1 Comparison of results for gaseous/particulate pollutants within the enclosure of rigid/flexible frontal wall 121
3.2.5 Comparison of local and global backflow coefficients 122
3.3 Synthesis of experimental results 123
4 Numerical simulations validation 128
4.1 Local backflow 129
4.1.1 Visualization of the backflow phenomenon 131
4.1.1.1 Preliminary works using a passive tracer 131
4.1.1.1.1 Boundary conditions and simulation characteristics of the transient model 131
4.1.1.1.2 Initial conditions related to steady state conditions 132
4.1.1.1.3 Transient results using SST-DES hybrid model (passive scalar fields) 133
4.1.1.1.4 Comparison between experimental and numerical visualization fields 136
4.1.1.2 Visualizations using two-phase flow matching our experimental procedure 137
4.1.1.2.1 Boundary conditions and simulation characteristics of the unsteady regime 137
4.1.1.2.2 Initial conditions related to steady state conditions 138
4.1.1.2.3 Helium and aerosol transient simulations 139
4.1.2 Quantification of the local backflow using two-phase flow simulations 143
4.1.2.1 Procedure 143
4.1.2.2 Backflow coefficients for gaseous and particulate release due to counter-current internal disturbing jet 144
4.1.2.2.1 Comparison of experimental and numerical quantitative results corresponding to counter-current internal disturbing jet 146
4.1.2.3 Gaseous and particulate backflow coefficients of the parietal internal disturbing jet . 148
4.1.2.3.1 Comparison of experimental and numerical quantitative results corresponding to parietal internal disturbing jet 149
4.1.3 Impact of the aerodynamic diameter 150
4.2 Global quantification 153

4.2.1 Impact of the envelope on the flow near the opening 155
4.2.1.1 Boundary conditions 156
4.2.1.2 Simulation characteristics (RANS) 156
4.2.2 Estimate of the gaseous and particulate decay evolutions within the envelope and particle deposition within the envelope 159
4.2.2.1 Injection phase – equilibrium regime 160
4.2.2.1.1 Boundary conditions 160
4.2.2.1.2 Simulation characteristics (RANS) 160
4.2.2.2 Decay phase - transient regime 163
4.2.2.2.1 Boundary conditions 163
4.2.2.2.2 Simulation characteristics of the unsteady regime 163
4.2.3 Global quantification of the backflow 166
4.2.3.1 Boundary conditions 166
4.2.3.2 Simulation characteristics of the unsteady regime 167
4.2.3.3 Initial conditions related to steady state 167
4.2.3.4 Visualization of backflow in the envelope 168
4.2.3.4.1 Results for helium 168
4.2.3.4.2 Visualization results of helium and 5 µm aerosols 171
4.2.3.5 Quantitative results for the backflow phenomenon 172
4.2.3.5.1 Determination of the global and mass backflow coefficients 172
4.2.3.5.2 Comparison of experimental and numerical backflow coefficients 174
5 Application to a full-size airlock 179
5.1 Experimental study 179
5.1.1 Experimental procedure 180
5.1.2 Backflow coefficients results for the full-size airlock 184
5.2 Numerical simulations 185
5.2.1 Numerical procedure 186
5.2.1.1 Description of the geometry and characteristics of the mesh 186
5.2.1.2 Boundary conditions 187
5.2.1.3 Simulation characteristics of the unsteady regime model 188
5.2.1.4 Steady state for the initial conditions 189
5.2.2 Numerical results on the backflow 189
5.2.2.1 Visualization 189

5.2.2.2 Quantitative results 191
5.2.3 Comparison between the experimental and numerical backflow coefficients 192
Conclusions & Perspectives 194
Appendix 1. Laser visualizations 199
Appendix 2. Determination of the uncertainties 208
Appendix 3. Simulation sensitivity of the backflow coefficient K (%) 211
Appendix 4. Feasibility study of the Background Oriented Schlieren (BOS) technique 216
References 228

LIST OF FIGURES

Figure 1-1 Schemes of a static containment system (left) and a dynamic containment system (right) 23
Figure 1-2 Schematic diagram of the composition of the different containment levels (ISO-16647, 2018). 24
Figure 1-3 Airlock with flexible walls (left) and dismantling operations inside an intervention airlock (right) 24
Figure 1-4 Mechanical strength tests on flexible airlock with negative pressure (from left to right): -10 Pa, -40 Pa, -100 Pa (Ducos, 2016) 25
Figure 1-5 System for controlling low negative pressure in flexible airlocks: SMARTDOG 27
Figure 1-6 Scheme of the backflow during a dynamic containment 28
Figure 1-7 Flow configurations near an orifice 30
Figure 1-8 Backflow downstream an obstacle 30
Figure 1-9 Photos taken from vertically above the experimental isolation room (left-hand side) and the corridor (right-side hand). (a) The door is closed. (b) The door is opened and the dye starts to escape. (c) Transport of the dye into the adjacent room. (Tanga, et al., 2005) 32
Figure 1-10 False color images showing time sequence of a door exchange flow in the plane view. (1) – (2) correspond to when the door is opening, and (3) corresponds to when the door is closed. (Eames, 2009) 33
Figure 1-11 Smoke visualization (anteroom side-view) of the single hinged door and manikin passage induced airflow patterns. The time in the parenthesis denotes the time elapsed since the door started opening (Kalliomaki, 2016). 34
Figure 1-12 (Left): Air supply system to laboratory in a fume cupboard (Durst & Pereira, 1991), (Right): General view of a ventilated gloves box (Cruz, 2011) 34
Figure 1-13 Flow visualization (left) and LES numerical simulation for vortex formation (right) near the operator arm (Cruz, 2011) 36
Figure 1-14 Horizontal PIV field at the right side of the fume cupboard (Prévost, 2000) 36
Figure 1-15 Intervention airlock with a calibrated opening of 100 m (Ducos, 2016) 36
Figure 1-16 Laser visualizations of the vertical plane outside the enclosure under the influence of an external parietal disturbance, showing the tracer backflow near the opening (Kaissoun, 2018) 37
Figure 1-17 Vertical profiles of the gaseous tracer flow for different turbulence models: U-RANS and LES (S. Kaissoun) and hybrid models SAS-SST and DES (M. Tsongo Kighoma, 2018) at t = 9 s ……38
Figure 1-18 Contours of passive scalar plane for the DNS of a turbulent planar jet (Da Silva, 2015)... 40
Figure 1-19 Map of interactions between particles and turbulence depending on the particles volume fraction (Elghobashi S., 1991) 42
Figure 1-20 Regime distribution depending on Stokes number 43
Figure 1-21 (left) Particle interaction with simple two-dimensional flows, (right) Cartoon of particles interacting with vortex ring (LONGMIRE 1992) 44
Figure 1-22 Single-phase (top) and particle-laden flow (middle) St_D=0.43, Re_D=23000; particle-laden flow (down) St_D=0.93, Re_D=23000 (Longmire & Eaton, 1992) 45
Figure 1-23 Basic physical mechanisms of modification of turbulent energy in gas flows with low-inertia and large particles (Varaksin, 2007) 46

Figure 1-24 Change in turbulent intensity as function of length scale ratio (Gore 1989)..... 46
Figure 1-25 (left): Sketch showing the preferential sweeping mechanism for a heavy particle interacting with local flow vertical structure (Wang & Maxey, 1993) 47
Figure 1-26 Scheme of different turbulence numerical types 48
Figure 1-27 Different approaches for turbulent particle-laden flow. Their applicability is separated in terms of timescale and length-scale ratios (Balachandar & Eaton, 2010). 52
Figure 1-28 Deposition laws on vertical walls in function of the dimensionless particle relaxation time (Nerisson, 2011) 55
Figure 1-29 Eulerian-Eulerian and Eulerian-Lagrangian treatment for a gas-particle flow in a grid (Hirche, Birkholz, & Hinrichsen, 2019) 56
Figure 3-1 Schemes showing the sampling method of the disturbing jet velocity: (a) V without the presence of the frontal wall (S. Kaissoun) and (b) V_{dist}, with the presence of the frontal wall in our case..... 73
Figure 3-2 Evolution of the velocity of the disturbing jet at 3 cm from the opening in function of velocity of the disturbing jet at the nozzle's outlet V_0 74
Figure 3-3 Gaseous backflow coefficient K (%) versus V_0/U_{ope} for the three values of the inflow velocity at the opening (0.5, 1 and 1.5 m/s) in comparison with S. KAISSOUN's results 75
Figure 3-4 Scheme of the two disturbance configurations: counter-current disturbing jet and parietal transverse disturbing jet 76
Figure 3-5 Pictures for counter-current disturbance configuration (left) and parietal disturbance configuration (right) 76
Figure 3-6 The enclosure with rigid frontal wall (left) and flexible frontal wall (right)..... 77
Figure 3-7 Laser visualization images in the vertical plane of the opening corresponding to: (a,b) an inflow velocity U_{ope} = 1 m/s and a counter-current internal turbulent jet of V_0 = 6 m/s and (c) an inflow velocity U_{ope} = 0.5 m/s and a counter-current internal turbulent jet of V_0 = 3.2 m/s 79
Figure 3-8 Laser visualizations in the median horizontal plane at the opening of the enclosure with its rigid frontal wall corresponding to U_{ope} = 1 m/s and with a counter-current internal disturbing jet of velocity near the opening V_{dist} = 0.4 m/s, 0.6 m/s, 0.9 m/s and 1.5 m/s respectively 80
Figure 3-9 Corresponding PIV fields in the median horizontal plane at the opening of the enclosure with its rigid frontal wall for U_{ope} = 1 m/s and with a counter-current internal disturbing jet of velocity near the opening V_{dist} = 0.4 m/s, 0.6 m/s, 0.9 m/s and 1.5 m/s respectively 81
Figure 3-10 Vertical laser visualization fields with vinyl flexible frontal wall of an inflow U_{ope} = 1 m/s and a counter-current disturbing jet of V_{dist} = 1.5 m/s outside the enclosure with dt = 1 ms..... 82
Figure 3-11 Vertical visualization fields passing through the opening inside the enclosure with its flexible frontal wall for an inflow of U_{ope} = 0.5 m/s and different disturbing jets of velocity V_{dist} = 0.6 m/s, 1 m/s and 1.5 m/s..... 83
Figure 3-12 Laser visualizations outside the enclosure in the inclined vertical median plane containing the opening of the enclosure with its flexible frontal wall for an inflow of velocity U_{ope} = 0.5 m/s and a parietal disturbing jet of velocity V_{dist} = 0.8 m/s (left) and V_{dist} = 2m/s (right)..... 84
Figure 3-13 Laser visualization fields in the median horizontal plane of the opening for the enclosure with its flexible frontal wall of an inflow U_{ope} = 0.5 m/s and a parietal disturbing jet of progressive velocities V_{dist} = 0.7 m/s, 1 m/s, 1.6 m/s and 2 m/s respectively. 85

Figure 3-14 Corresponding PIV fields in the median horizontal plane of the opening with a flexible frontal wall and an inflow U_{ope} = 0.5 m/s with a parietal disturbing jet of velocities V_{dist} = 0.7 m/s, 1 m/s, 1.6 m/s and 2 m/s respectively. 86
Figure 3-15 (left): Scheme of an ultrasonic aerosol generator constituted of a nebulized base and a drying column with 1: fluorescein sodium solution, 2: vibrating ceramic, 3: droplets of diameter d_g, 4: dispersion of air flow, 5: drying air flow, 6: dried particles of diameter d_p; (right): picture of particles generator LIXEA connected to the enclosure 88
Figure 3-16 The front face of Aerodynamic Particle Sizer (APS) 89
Figure 3-17 Particles sizes distribution at the outlet of the generator. 90
Figure 3-18 Closed filter holder (left) and open filter holder (right) 91
Figure 3-19 A volumetric flowmeter connected to a piston pump 91
Figure 3-20 Fluorimeter analyzer (ESE type) 92
Figure 3-21 Diagram of the operating devices used for the backflow quantification in our enclosure 93
Figure 3-22 Experimental enclosure with the gaseous samplers around the opening in the case of a counter-current perturbation 95
Figure 3-23 Evolution of the gas backflow coefficient K (%) as a function of V_{dist}/ U_{ope} for the three values of the inflow velocity at the opening (0.5, 1 and 1.5 m/s) in the case of a counter-current internal free jet disturbance 96
Figure 3-24 Left: diagram of the positions of the filter samplers around the opening in the case of a counter-current perturbation (front and side views) – Right: 5 filter samplers located around the opening of the enclosure 97
Figure 3-25 Evolution of the backflow coefficient K (%) versus V_{dist}/Uope for the particulate pollutant of 5 µm, for the three values of the inflow velocity at the opening (0.5, 1 and 1.5 m/s) in the case of a counter-current internal free jet disturbance 98
Figure 3-26 Left: diagram of the locations of the filter samplers around the opening in the case of a counter-current perturbation (front and side views) – Right: 3 filter samplers located around the opening at left, face and down positions 99
Figure 3-27 Evolution of the backflow coefficient K (%) versus V_{dist}/U_{ope} for an inflow velocity at the opening U_{ope} = 0.5 m/s in the case of a counter-current internal free jet disturbance for the gaseous and 5 µm particulate pollutants and for the enclosure with rigid frontal wall and flexible frontal wall 99
Figure 3-28 Evolution of the backflow coefficient K (%) versus V_{dist}/U_{ope} for an inflow velocity at the opening U_{ope} = 0.5 m/s in the case of an internal parietal free jet disturbance for the gaseous and 5 µm particulate pollutant and for the enclosure with rigid and flexible frontal walls respectively.. 101
Figure 3-29 Evolution of the backflow coefficient K (%) as a function of V_{dist}/U_{ope} for an inflow velocity at the opening U_{ope} = 0.5 m/s in the case of a rigid frontal wall disturbance for the gaseous and 5 µm particulate pollutants and for the internal counter-current and parietal disturbing jet ... 102
Figure 3-30 3D view of the envelope surrounding the enclosure 104
Figure 3-31 Experimental envelope surrounding the enclosure 105
Figure 3-32 Picture of devices implementation for the PIV experiments inside the envelope 106
Figure 3-33 Diagram of the PIV devices used for the vertical visualization inside the envelope 106
Figure 3-34 Time-averaged velocity fields acquired near the opening for an inflow velocity U_{ope} = 1 m/s and an air exchange rate of the envelope R =3 h^{-1}, in the vertical median plane (0,29 x 0,29) m^2 107

Figure 3-35 Velocity profiles deduced from the vertical velocity fields at 8 cm inside the enclosure corresponding toU_{ope} = 0.5 m/s and to each R experimental case 108
Figure 3-36 Velocity profiles deduced from the vertical velocity fields at 8 cm inside the enclosure corresponding to U_{ope} = 1 m/s and to each R experimental case 108
Figure 3-37 Velocity profiles deduced from the vertical velocity fields at 8 cm inside the enclosure corresponding to U_{ope} = 1.5 m/s and to each R experimental case 109
Figure 3-38 Time evolution of C/Ceq corresponding to the envelope with a closed enclosure and for a theoretical exchange rate of the envelope around 3 h^{-1}..... 110
Figure 3-39 Estimation of the deposition rate of particles inside the envelope using an aerosol particle sizer 111
Figure 3-40 Mass concentration versus aerodynamic particle diameter corresponding to the injection outlet and the envelope extraction..... 112
Figure 3-41 Time evolution of C/C_{eq} corresponding to the helium and 5 µm particles for a renewal rate of the envelope about 3 h^{-1} 113
Figure 3-42 Experimental apparatus for the global quantification of the backflow..... 115
Figure 3-43 Schematic diagram of the devices used for characterizing the global backflow coefficients in the envelope..... 116
Figure 3-44 Evolution of the global gaseous backflow coefficient K (%) versus V_{dist}/ U_{ope} for the three values of the inflow velocity at the opening (0.5, 1 and 1.5 m/s) in the case of a counter-current internal free jet disturbance..... 118
Figure 3-45 Global particulate backflow coefficient K_{env} (%) versus V_{dist}/U_{ope} for U_{ope} = 0.5 m/s, 1 m/s and 1.5 m/s in the case of a counter-current internal free jet disturbance..... 119
Figure 3-46 Corrected global particulate backflow coefficient $K_{corrected}$ (%) versus V_{dist}/U_{ope} for U_{ope} = 0.5 m/s, 1 m/s and 1.5 m/s taking into account the deposition of particles inside the envelope..... 119
Figure 3-47 Evolution of the global backflow coefficients K_{env} (%) versus V_{dist}/U_{ope} for an entrance velocity at the opening U_{ope} = 0.5 m/s in the case of a counter-current internal free jet disturbance for the gaseous and 5 µm particulate pollutant and for the enclosure with rigid and flexible frontal wall 120
Figure 3-48 Evolution of the global backflow coefficients K (%) versus V_{dist}/U_{ope} for an entrance velocity at the opening U_{ope} = 0.5 m/s in the case of an internal parietal free jet disturbance for the gaseous and 5 µm particulate pollutant and for the enclosure with rigid and flexible frontal wall... 121
Figure 3-49 Evolution of the local backflow coefficients K (%) versus V_{dist}/U_{ope} for a velocity at the opening U_{ope} = 0.5 m/s for different disturbing jet types, frontal wall types and pollutant types 123
Figure 3-50 Evolution of the global backflow coefficients K (%) versus V_{dist}/U_{ope} for a velocity at the opening U_{ope} = 0.5 m/s for different disturbing jet types, frontal wall types and pollutant types 124
Figure 3-51 Evolution of gaseous and particulate mass backflow coefficients in function of V_{dist} /U_{ope} for U_{ope} = 0.5 m/s for the case of counter-current disturbing jet for the enclosure with its rigid frontal wall 126
Figure 3-52 Evolution of the mean backflow velocity near the opening $V_{backflow}$ in function of ($V_{disturbance}$ - U_{ope}) for the counter-current disturbing jet 127
Figure 4-1 Geometry of the simulation domain..... 130
Figure 4-2 Experimental chamber meshing in the vertical plane in the case of counter-current disturbing jet 130

Figure 4-3 Horizontal plane crossing the opening showing the volumetric flowrates for the numerical simulations 132
Figure 4-4 Velocity field in the vertical (left) and horizontal (right) median planes crossing the opening for RANS simulations 133
Figure 4-5 Passive tracer fields of concentration in the vertical median plane of the opening for the SST-DES simulation for U_{ope} = 1m/s and V_0 = 10 m/s for different times 134
Figure 4-6 Passive tracer concentration fields in the horizontal median plane of the opening for the SST-DES simulation for U_{ope} = 1 m/s and V_0 = 10 m/s for different times 135
Figure 4-7 Top: laser visualization fields in the vertical median plane for an inflow of U_{ope}= 1 m/s and for three values of V_0: 3,2 m/s (a), 6 m/s (b) and 11,7 m/s (c) respectively. Bottom: numerical simulations of tracer in the vertical median plane for an inflow U_{ope} = 1 m/s and for three values of V_0 : 3 m/s (a), 6 m/s (b) and 12 m/s (c) respectively at different times 136
Figure 4-8 Boundary conditions for the numerical model of the enclosure in the case of counter-current disturbing jet 137
Figure 4-9 Helium molar fraction (left) and particles mass concentration (right) fields in the horizontal median plane of the opening for the URANS initial conditions 139
Figure 4-10 Helium molar fraction (left) and particles mass concentration (right) fields in the vertical median plane of the opening for U_{ope} = 1 m/s and V_0 = 16 m/s for the counter-current disturbing jet 140
Figure 4-11 Helium molar fraction (left) and particles mass concentration (right) fields in the horizontal median plane for U_{ope} = 1 m/s and V_0 = 16 m/s for the counter-current disturbing jet 140
Figure 4-12 Helium molar fraction (left) and particles mass concentration (right) fields in the vertical median plane of the opening corresponding to U_{ope} = 1 m/s and V_0 = 40 m/s for the case of parietal internal disturbing jet 141
Figure 4-13 Helium molar fraction (left) and particles mass concentration (right) fields in the horizontal median plane of the opening corresponding to U_{ope} = 1 m/s and V_0 = 40 m/s for the case of parietal internal disturbing jet 142
Figure 4-14 Velocity magnitude (left) and helium molar fraction (right) fields in the horizontal median plane of the opening corresponding to U_{ope} = 1 m/s and V_0 = 40 m/s for the case of parietal internal disturbing jet for t = 9s 142
Figure 4-15 Pointwise samplers near the opening to monitor the pollutants concentration 143
Figure 4-16 Evolution of the gaseous backflow coefficient K (%) as a function of V_{dist}/U_{ope} corresponding to U_{ope} = 0.5 m/s, 1 m/s and 1.5 m/s respectively obtained from SST-DES simulations in the case of counter-current internal disturbing jet 144
Figure 4-17 Evolution of the particulate backflow coefficient K (%) as a function of V_{dist}/U_{ope} corresponding to U_{ope} = 0.5 m/s, 1 m/s and 1.5 m/s respectively obtained from SST-DES simulations in the case of counter-current internal disturbing jet 145
Figure 4-18 Comparison of the gaseous and particulate pollutant backflow coefficient K (%) versus V_{dist}/U_{ope} for the inflow velocity 0.5 m/s at the opening in the case of a counter-current internal free jet disturbance obtained from the DES simulations 145
Figure 4-19 Circular samplers located near the opening for each case (5 samplers then 3 samplers) 146

Figure 4-20 Evolution of the gaseous and the particulate backflow coefficient K (%) versus V_{dist}/U_{ope} for the inflow velocity 0.5 m/s at the opening in the case of a counter-current internal jet calculated using five collectors near the opening in experimental and numerical works 147
Figure 4-21 Evolution of the gaseous and the particulate backflow coefficient K (%) versus V_{dist}/U_{ope} for the inflow velocity 0.5 m/s at the opening in the case of a counter-current internal jet calculated using three collectors near the opening in our experimental and numerical works 147
Figure 4-22 Three samplers added near the opening for the case of parietal internal jet 148
Figure 4-23 Evolution of the gaseous backflow coefficient K (%) as a function of V_{dist}/U_{ope} corresponding to U_{ope} = 0.5 m/s, 1 m/s and 1.5 m/s respectively obtained from SST-DES simulations in the case of parietal disturbing jet 148
Figure 4-24 Comparison of the gaseous and the 5 µm particulate pollutant backflow coefficients K (%) versus V_{dist}/U_{ope} for the inflow velocity 0.5 m/s at the opening in the case of a parietal internal jet disturbance obtained from the DES simulations 149
Figure 4-25 Evolution of the gaseous and the particulate backflow coefficients K (%) versus V_{dist}/U_{ope} for the inflow velocity 0.5 m/s at the opening, in the case of a parietal internal jet calculated using three samplers near the opening for our experimental and numerical studies 150
Figure 4-26 Helium molar fraction (left) and particles mass concentration (right) fields in the horizontal median plane of the opening corresponding to U_{ope} = 0.5 m/s and V_0 = 10 m/s for the case of counter-current internal disturbing jet. The aerodynamic diameter of particles is respectively 5 µm, 20 µm, 50 µm and 100 µm 151
Figure 4-27 Geometry of the simulation domain 154
Figure 4-28 3D view of the envelope meshing 155
Figure 4-29 3D view of the envelope meshing containing the enclosure 155
Figure 4-30 Horizontal median plane of the opening corresponding to an inflow velocity at the opening U_{ope} = 0.5 m/s and renewal rate within the envelope respectively: R = 0 h^{-1}, 1 h^{-1}, 5 h^{-1} and then 10 h^{-1} 157
Figure 4-31 Schemes of the location of velocity profiles near the opening in the vertical (left) and horizontal (right) planes 158
Figure 4-32 Vertical (left) and horizontal (right) velocity profiles at the opening of the enclosure for an inflow velocity of 0.5 m/s for different values of air exchange rates of the envelope 159
Figure 4-33 Geometry of the envelop surrounding the enclosure and simulation domain 160
Figure 4-34 Molar fraction of helium (up) and particles mass concentration (bottom) in the vertical planes passing respectively through the envelope inlet, the injection and the envelope outlet at equilibrium when particles injection is located at the inlet of the envelope 161
Figure 4-35 Particles deposition on the upper wall of the enclosure and at the floor of the envelope 162
Figure 4-36 Concentration of helium and aerosol at the extraction outlet of envelope during the injection phase (0 < t < 8000 s) and the decay phase (t > 8000 s) 164
Figure 4-37 Time evolution of C/C_{eq} corresponding to the helium and the 5 µm particles from experiments and numerical simulations for an exchange rate of the envelope about 3 h^{-1} 165
Figure 4-38 Helium molar fraction (left) and particle mass concentration (right) fields in the horizontal median plane of the opening for the RANS initial conditions 168
Figure 4-39 Helium molar fraction fields in the horizontal plane passing respectively through the enclosure opening for t = 208 s (top) and t = 306 s (bottom) respectively 169

Figure 4-40 Helium molar fraction fields in the vertical planes passing respectively through the envelope inlet, the enclosure opening and the envelope outlet for t = 290 s (top) and t = 299 s (bottom)respectively 170
Figure 4-41 Helium molar fraction (left) and particles mass concentration (right), respectively, fields in the horizontal plane passing through the enclosure opening for t = 318 s 171
Figure 4-42 Helium molar fraction (left) and particles mass concentration (right) fields, respectively, in the vertical planes passing through the envelope inlet, the enclosure opening and the envelope outlet for t = 314 s 171
Figure 4-43 Helium concentration in the envelope outlet for U_{ope} = 0.5 m/s and V_0 = 14 m/s 172
Figure 4-44 Helium mass flowrate in the extraction units of the enclosure at initial conditions (top) and during the generation of the disturbing jet (bottom) 173
Figure 4-45 Experimental and numerical global backflow coefficients for helium and 5 µm aerosol in function of V_{dist}/U_{ope} 175
Figure 4-46 Evolution of experimental and numerical gaseous mass backflow coefficients in function of V_{dist}/U_{ope} for U_{ope} = 0.5 m/s 175
Figure 4-47 Evolution of experimental and numerical particulate mass backflow coefficients in function of V_{dist}/U_{ope} for U_{ope} = 0.5 m/s 176
Figure 4-48 Evolution of the experimental and numerical mean backflow velocities $V_{backflow}$ near the opening in function of ($V_{disturbance}$ - U_{ope}) for the counter-current disturbing jet 176
Figure 5-1 Dimensions of the airlock located inside the external envelope (Prevost, 2020) 180
Figure 5-2 Picture of the real airlock with its flexible vinyl walls 180
Figure 5-3 Sketch of the experimental equipments corresponding to a counter-current internal disturbing jet (Prevost, 2020) 182
Figure 5-4 Experimental device inside the airlock in the case of a counter-current disturbing jet 183
Figure 5-5 Three samplers added near the opening of the airlock 184
Figure 5-6 Evolution of the gaseous and particulate backflow coefficients K (%) versus V_{dist}/U_{ope} near the opening in the case of the counter-current internal disturbing jet 184
Figure 5-7 Evolution of the gaseous and particulate backflow coefficients K (%) in function of V_{dist}/U_{ope} near the opening in the case of the parietal internal disturbing jet 185
Figure 5-8 Numerical domain for the full-size airlock 186
Figure 5-9 External 3D view of the mesh for the airlock 187
Figure 5-10 Internal 3D view of the mesh inside the airlock 187
Figure 5-11 Helium molar fraction fields in the vertical median plane of the opening at different time steps for V_{dist}/U_{ope} = 3 190
Figure 5-12 Helium molar fraction (left) and particles mass concentration (right) fields in the vertical median plane of the opening of the airlock for t = 47 s for an inflow velocity of U_{ope} = 0.5 m/s and for the case of a counter-current disturbing jet 191
Figure 5-13 Evolution of the numerical backflow coefficient K (%) versus V_{dist}/U_{ope} for helium and 5 µm diameter aerosol in the case of an inflow of U_{ope} = 0.5 m/s and a counter-current internal jet .. 191
Figure 5-14 Experimental and numerical backflow coefficients K (%) in function of V_{dist}/U_{ope} for helium and 5 µm aerosol in the case of an inflow of U_{ope}=0.5 m/s and a counter-current internal disturbing jet 192
Figure 0-1 Synthetic figure for experimental and numerical mass backflow coefficients K_m (%) for gas and 5 µm aerosol in function of V_{dist}/U_{ope} in the case of counter-current disturbing jet 197

Figure 0-2 Parity curve ($\pm$ 25 %) between the experimental and numerical backflow coefficients .. 198
Figure 0-3 Visualizations fields in the median horizontal plane of the opening of the enclosure with its rigid frontal wall and with a counter-current internal disturbing jet 200
Figure 0-4 Visualizations fields in the median vertical plane in the opening of the enclosure with its rigid frontal wall and with a counter-current internal disturbing jet 202
Figure 0-5 Visualizations fields in the median horizontal plane in the opening of the enclosure with its flexible frontal wall and with a countercurrent internal disturbing jet, outside the enclosure 203
Figure 0-6 Visualizations fields in the median horizontal plane in the opening of the enclosure with its flexible frontal wall and with a counter-current internal disturbing jet, inside the enclosure 204
Figure 0-7 Visualizations fields in the median horizontal plane in the opening of the enclosure with its flexible frontal wall and with a counter-current internal disturbing jet, inside the enclosure 205
Figure 0-8 Visualizations fields in the median horizontal plane in the opening of the enclosure with its flexible frontal wall and with a parietal internal disturbing jet, outside the enclosure 206
Figure 0-9 Visualizations fields in the median horizontal plane in the opening of the enclosure with its flexible frontal wall and with a parietal internal disturbing jet, inside the enclosure 207
Figure 0-10 Schemes of the filter samplers near the opening used for our simulations in positions 1 and 4 (side views) 211
Figure 0-11 Particles mass concentration at the five discs samplers near the opening 212
Figure 0-12 Evolution of the particulate backflow coefficient K(%) as a function of V_{dist}/U_{ope} calculated through the punctual samplers then at the 5 discs at 4 positions near the opening 212
Figure 0-13 Sampler mean concentration over the concentration of the sampler facing the opening for each sampler location for U_{ope} = 0.5 m/s and V_0 = 10 m/s 213
Figure 0-14 Circular samplers added near the opening for each case. Rrom left to right: 1 sampler, 3 samplers and 5 samplers 214
Figure 0-15 Evolution of the particulate backflow coefficient K (%) as a function of V_{dist}/U_{ope} calculated through 1 filter, 3 filters and 5 filters placed near the opening 215
Figure 0-16 Scheme of the optical setup for BOS technique (RICHARD & RAFFEL, 2001) 217
Figure 0-17 (left): Displacement vector module maps for development of a helium jet for a pressure of 2 bars (DUBOIS, 2008) – (right): Normalized density contours for the rectangular axisymmetric nozzle jet obtained by BOS measurements (TIPNIS, 2013) 219
Figure 0-18 Typical BOS image (left) and the displacement data (right) for a one z-elevation for the development of an axisymmetric hydrogen jet (KOTCHOURKO, 2013) 220
Figure 0-19 Displacement field proportional to density gradients tested by NASA on a helicopter during a flight (RICHARD & RAFFEL, 2001) 221
Figure 0-20 Preliminary tests apparatus on a jet of helium 222
Figure 0-21 Procedure of images acquisition and post processing for a pure helium circular jet of 1 cm diameter 223
Figure 0-22 Evolution of calculated density as a function of helium concentration 223
Figure 0-23 Visualization of backflow of helium from a rectangular cell 224
Figure 0-24 Implementation of BOS equipment near the opening of the enclosure 225
Figure 0-25 Visualization of the density gradients resulting near the opening in the case of an internal counter-current disturbance 225

LIST OF TABLES

Table 1-1 Indicative guide to the usual criteria values in containment configurations (ISO-16647, 2018)..... 27
Table 1-2 Synthesis table showing parameters related to S. Kaissoun's study and our study 57
Table 4-1 Boundary conditions for the DES simulations..... 132
Table 4-2 Numerical parameters for the DES modelling..... 132
Table 4-3 Initial conditions for the RANS simulation 133
Table 4-4 Boundary conditions for the DES modelling 138
Table 4-5 The simulation characteristics used for the DES simulation 138
Table 4-6 Initial conditions for the RANS simulation 139
Table 4-7 Stokes number related to each particle aerodynamic diameter 152
Table 4-8: Boundary conditions for the RANS simulations 156
Table 4-9: The simulation characteristics used for the URANS and the hybrid models 156
Table 4-10 Boundary conditions for the RANS model..... 160
Table 4-11 The simulation characteristics used for the RANS simulations..... 161
Table 4-12 Experimental and numerical deposition rates inside the envelope..... 162
Table 4-13 Boundary conditions of the decay phase 163
Table 4-14 The simulation characteristics used for the URANS modelling..... 163
Table 4-15 Experimental and numerical values of helium and aerosol exchange rates..... 165
Table 4-16: Boundary conditions for the DES model 166
Table 4-17 The simulation characteristics used for the DES modelling 167
Table 4-18 Initial conditions for the RANS simulation 167
Table 4-19 The simulation characteristics used for the RANS 168
Table 5-1 Values of the experimental V_0 and V_{dist} for the case of a counter-current disturbing jet... 181
Table 5-2 Boundary conditions for the SST-DES model 188
Table 5-3 The simulation characteristics used for the DES simulations..... 189
Table 5-4 Boundary conditions for the steady state conditions 189
Table 5-5 Simulation characteristics for the steady state conditions 189

NOMENCLATURE

Acronyms

APS	Aerodynamic Particle Sizer
CFD	Computational Fluid Dynamics
IMFT	Institut de Mécanique des Fluides de Toulouse
IRSN	Institut de Radioprotection et de Sûreté Nucléaire
DES	Detached Eddy Simulation
RANS	Reynolds Averaged Navier-Stokes
URANS	Unsteady Reynolds Averaged Navier-Stokes
LDA	Laser Doppler Anemometry
LES	Large Eddy Simulation
DES	Detached Eddy Simulation
DNS	Direct Numerical Simulation
PIV	Particle Image Velocimetry
PVC	PolyVinyl Chloride
SF_6	Sulfur hexafluoride
SAS	Scale-Adaptive Simulation
SST	Shear Stress Transport
SMARTDOG	Système de Mesure et Alarme garantissant la non-Rétrodiffusion

Latin letters

$C_{aerosol-in}$	Aerosol concentration inside the chamber	(mg/m^3)
$C_{aerosol-out}$	Aerosol concentration outside the chamber	(mg/m^3)
C_{eq}	Concentration at the equilibrium	(ppm.v)
C_{gas-in}	Gas concentration inside the chamber	(ppm.v)
$C_{gas-out}$	Gas concentration outside the chamber	(ppm.v)
C_p	Particles concentration	(kg/m^3)
C_M	Aerosol concentration at the first calculation point	(kg/m^3)

C_v	Volume concentration	(m^3/m^3)
D	Deposition rate	(%)
d_{ae}	Aerodynamic diameter	(m)
d_{ev}	Equivalent diameter in volume	(m)
d_p	Particle diameter	(m)
d_p^+	Particle dimensionless diameter	(-)
D	Duct diameter	(m)
D_B	Brownian diffusion coefficient	($m^2.s^{-1}$)
$D_{p,ij}^t$	Particle turbulent dispersion tensor components	($m^2.s^{-1}$)
D_t	Turbulent diffusivity	($m^2.s^{-1}$)
D_Φ	Molecular diffusivity of the passive scalar	($m^2.s^{-1}$)
E	Dynamic containment efficiency	(%)
F	Resonance frequency of the piezoelectric ceramic	(Hz)
g_i	Gravity acceleration in *i* direction	(m/s^2)
I_0	Intensity of incident radiation	(-)
I_p	Dimensionless integral for deposition velocity	(-)
I_t	Intensity of transmitted radiation	(-)
J	Particle deposition flux on the wall	($kg/m^2/s$)
k	Local transfer coefficient	(s/m^3)
K	Backflow coefficient	(%)
K_{env}	Global backflow coefficient	(%)
K_m	Mass backflow coefficient	(%)
l	Optical path	(m)
$L_{k-\omega}$	Turbulence length scale	(m)
m	Mass	(kg)
n	vector normal to the wall	(-)
P	Pressure	(Pa)
P_{rel}	Relative pressure	(Pa)
q	Flowrate of the tracer	(Nl/h)

$q_{backflow\text{-}out}$	Mass flowrate of the backflow	(kg/s)
$Q_{disturbance}$	Disturbance volumetric flowrate	(m^3/h)
$Q_{extraction}$	Volumetric flowrate at extraction	(m^3/h)
$Q_{injection}$	Volumetric flowrate at injection	(m^3/h)
$Q_{opening}$	Volumetric flowrate at the opening	(m^3/h)
Q	Volumetric flowrate	(m^3/h)
R	Air exchange rate	(h^{-1})
Re	Reynolds number	(-)
Sc_B	Brownian Schmidt number	(-)
S_p	Source term applied on particles	(kg/m^3/s)
Sc_t	Schmidt number	(-)
Stk	Stokes number	(-)
St_D	Strouhal number	(-)
t	time	(s)
u^*	Fluid friction velocity	(m/s)
$U(x)$	Eddy velocity scale	(m/s)
U_{ext}	Velocity at the extraction units	(m/s)
U_f	Fluid velocity	(m/s)
U_{ope}	Velocity at the opening	(m/s)
$U_{s,p}$	Particles slip velocity	(m/s)
V	Disturbance velocity at the opening (Kaissoun)	(m/s)
V_{dist}	Disturbance velocity at the opening	(m/s)
V_{aer}	Aerosol volume	(m^3)
V_0	Disturbance velocity at the nozzle	(m/s)
V_d^+	Dmensionless aerosol deposition velocity	(-)
y^+	Dimensionless distance to the wall	(-)
Y_p	Mass fraction of particles	(-)

Greek letters

α	Correction factor of turbulent viscosity	(-)
α_g	Constant specific to the generator	(-)
Δ	Local mesh spacing	(-)
$\delta(x)$	Eddy lengthscale	(m)
ε	Dissipation of turbulent kinetic energy	(m^2/s^3)
ε_s	Molar absorption coefficient of the solution	($L.mol^{-1}.m^{-1}$)
n, w	constant	(-)
κ	Von Karman's constant	(-)
k	Fluid turbulent kinetic energy	(m^2/s^2)
λ	Function of Sc_B, τ_p^+ and d_p^+	(-)
λ_0, λ_1	constant	(-)
Ω	dimensionless turbulent Stokes number	(-)
μ	Dynamic viscosity	(kg/m/s)
μ_t	Turbulent viscosity	(kg/m/s)
ρ	Density	(kg/m^3)
$\sigma_{C_{He}}$	Standard deviation of helium concentration	(ppm.v)
σ_s	Surface tension of the solution	($N.m^{-1}$)
σ_t	Turbulent Schmidt number	(-)
τ	Relaxation time	(s)
τ_f	Fluid relaxation time	(s)
τ_p	Particle relaxation time	(s)
τ_p^+	Particle dimensionless relaxation time	(-)
ν_t	Kinematic turbulent viscosity	($m^2.s^{-1}$)
$\emptyset$	Mass fraction	(-)
$\emptyset_v$	Volumetric fraction	(-)
χ	Dynamic shape factor	(-)
ω	Turbulent frequency of vorticity	(s^{-1})

INTRODUCTION

In the context of nuclear safety, maintenance and dismantling sites require the use of ventilated enclosures around contaminated areas to prevent the spread of contamination into the surrounding environment. Airlocks with flexible walls are enclosures that are set under low negative pressure drop compared to their external environment. Air enters the airlock through openings under the forcing of extraction system following the principle of dynamic containment. However, due to some operating works and aeraulic disturbances occurring inside or outside these airlocks, flow inversions could occur near nominal or accidental openings and lead to the transfer of pollutants to outside the airlock. This phenomenon is commonly referred to as "backflow". The aeraulic disturbances include aeraulic or mechanical movements, an air flow alone or loaded with particles induced by a blowing process, or an upward flow induced by a thermal plume inside or outside the airlock.

Many standards such as (ISO-17873, 2004) and (ISO-16647, 2018) recommend to maintain a fixed value of negative pressure drop within the airlock or a minimum value of velocity at the opening U_{ope} of the airlock to prevent the spread of pollutants to outside the enclosure. In the past, three values of inlet velocity at the opening were recommended: 1.5 m/s for the tritium, 1 m/s for the plutonium 238 and 0.5 m/s for any other pollutants. Additionally, these standards recommend that each scenario must be investigated in a specific way.

This study follows S. Kaissoun's PhD (Kaissoun, 2018) on safety of maintenance and dismantling sites. It is a topic of mutual interest between IRSN and EDF on the evaluation of ventilation criteria currently used to guarantee the effectiveness of dynamic containment of airlocks during operations of maintenance or dismantling. It aims to identify and reproduce the aerodynamic configurations that lead to the backflow of pollutants to outside ventilated airlocks in order to understand, predict and finally prevent them within the maintenance and dismantling sites. S. Kaissoun studied the phenomenon of local backflow of a gaseous pollutant at the level of a rectangular opening of fixed dimensions created on the wall of a small-size enclosure. She performed first an experimental approach using laser visualization and gas tracing techniques and then a numerical CFD study by comparing various turbulence models such as URANS, LES and DNS.

Our study aims to characterize the efficiency of the dynamic containment on airlocks by studying the phenomenon of backflow of gaseous tracer but also the case of particulate pollutant composed of 5 µm particles. In addition, among the configurations leading to these transfer phenomena initially tested by S. Kaissoun, we have chosen to test only two disturbance scenarios linked to the presence of internal counter-current and wall jets. We are interested in collecting experimentally the global quantity of gaseous and particulate pollutants that result from the backflow around the opening. The ventilated enclosure had successively a rigid and then flexible frontal wall. As part of my thesis, we added an external envelope around the experimental enclosure designed by S. Kaissoun, in order to characterize the overall quantity of gaseous and particulate pollutants coming from the backflow, and then to compare with the results obtained with the numerical simulation carried out with the same input data. It is then a question of testing the ability of hybrid turbulence CFD models to reproduce the backflow phenomenon of pollutants near the opening and beyond.

As a summary, the main objectives of my PhD Thesis are listed below:

• Experimentally, we want to characterize on the one hand the backflow phenomenon near the opening using laser visualization techniques (Schlieren and PIV techniques). On the other hand, we focus on the measurement of the local and global quantities of gaseous and 5 µm particulate pollutants emitted through an opening using dedicated tracing techniques;

• Numerically, we want to validate the reliability of hybrid CFD turbulence models (DES-SST) to qualitatively and quantitatively predict the unsteady backflow phenomena of gaseous and particulate pollutants near the opening and inside the envelope.

• Once we validated the turbulence model on a small-size enclosure, we aim to perform experimental and numerical studies on full-size airlock in order to validate the hybrid turbulence model on it. This will allow us further to study numerically other types of disturbance configurations on full-size airlocks or others ventilated enclosures.

We should mention that there is no use of similarity between the small-size enclosure and the full-size airlock. In our study, we mainly aimed to highlight the backflow phenomenon near the opening.

This manuscript is composed of 5 chapters.

Chapter 1 constitutes the state of art related to our study and is divided into three parts. The first part is related to ventilated systems implemented on nuclear sites and recommendations to guaranty an efficient dynamic containment. Works on backflow through enclosure of various opening dimensions are also presented. The second part describes the dispersion of gaseous and particulate pollutants in a flow and shows different kinds of gas-particles interactions. The third part presents different types of CFD turbulence modelling and computational approaches for particulate flow modelling.

Chapter 2 represents the article “Experimental study of backflow air leakage through an opening from a depressurized enclosure” that corresponds to experimental results for the backflow of a gaseous pollutant. It is based on the experimental setup and results for the local backflow near the opening of a gaseous pollutant (S. Kaissoun’s works), in addition to our contribution on the visualization part. In this chapter, we describe visualization and tracing techniques that we use further in our study to characterize the backflow under the effect of internal and external disturbing jets.

Chapter 3 is dedicated to the experimental setup for different disturbing jets and frontal wall types for the small-size enclosure and consists in two parts. The first part presents the characterization of the local backflow phenomenon near the opening. In this part, we show results obtained with laser visualizations and PIV analysis and backflow quantitative results corresponding to gaseous and 5 µm particulate pollutants. The second part consists in the global measurements of gaseous and particulate backflow using the external envelope in terms of backflow coefficient evolutions.

Chapter 4 comments on our numerical simulations using the hybrid SST-DES turbulence model for the small-size enclosure. It is also divided into two parts: the characterization of the local backflow near the opening and the global analysis of the backflow using the external envelope. Results corresponding to gaseous and 5 µm particulate pollutants, under the effect of counter-current and parietal internal jets respectively are presented in terms of visualization fields and quantitative analysis. Comparison between experimental and numerical results are also presented in this chapter.

Chapter 5 presents our experimental and numerical studies on a full-size airlock for gaseous and 5 µm particulate pollutants. Experiments are done in an airlock with flexible walls under the effect of counter-current and parietal internal jets. Numerical validation using SST-DES model for the counter-current disturbing jet case is discussed.

1 Bibliography

In this chapter, we present the state of art related to numerical and experimental studies of backflow phenomenon of gaseous and particulate pollutants near an opening during a dynamic containment. In the first part, we explain the containment systems implemented on nuclear sites during maintenance or dismantling operations and we present the airlock with flexible walls that we are interested to investigate. Then we detail the risk of backflow phenomenon encountered in nominal or accidental opening. Due to the wide range of opening dimensions and accidental configurations presented in literature, we detail first different configurations, and then we concentrate our talk on the small opening dimension that is not mentioned in the literature, and that follows S. Kaissoun works (Kaissoun, 2018). Our second part is attribute to the dispersion and mixing of gaseous and particulate pollutants in a gas flow. We specifically describe the dispersion of particulate pollutants part since this represents a new contribution to S. Kaissoun's works. We present generalities about aerosol characteristics, then we treat different regimes in particle-laden flows and works about the effect of particles on turbulence. The third part corresponds to numerical simulations theory where we present different turbulence models from URANS, to hybrid model DES, then LES and DNS and computational approaches of particle-laden flows (Dusty gas, Eulerian, Lagrangian or fully resolved approaches).

1.1. Containment in nuclear systems and backflow phenomenon

1.1.1 Containment in nuclear systems

Site containments and nuclear installations undergoing decommissioning are characterized by their temporary and evolving nature depending on operations to be carried out. Broadly, containment systems are composed of a set of physical barriers and / or auxiliary dynamic systems designed to prevent the leakage of products contained in relevant internal environment to external environment (nuclear or chemical and biochemical industry for example), or the entrance of substances from external environment to internal environment, especially in the case of the food industry, pharmaceuticals or microelectronics. In the nuclear field, the purposes of these containment systems are to ensure the protection of workers, the public and the environment against any radioactive contamination, and to guaranty the protection of equipment and locals in order to maintain the level of radiological cleanliness and avoid any dissemination of contaminants (ISO-16647, 2018).

1.1.1.1 Containment systems

The main containment types are the static containment and the dynamic containment as shown in Figure ***1-1***. Simultaneously, depending on the risk level, a stato-dynamic containment could be adapted. In most situations, dynamic containment automatically adds to the static containment of the system and therefore maintains its containment performance in case of degradation of the static barriers.

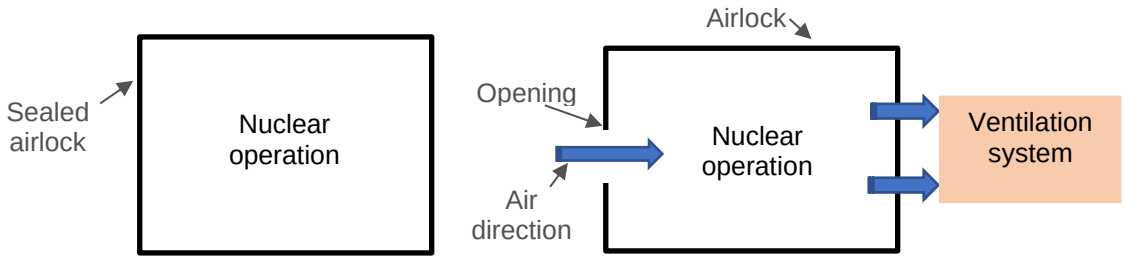

Figure 1-1 Schemes of a static containment system (left) and a dynamic containment system (right)

A static containment is a sealed containment enclosure as shown in Figure 1-1(left) and represents the most effective way to prevent the release of radioactive substances. Static containment is concerned by various types: flexible walls (vinyl, heat-shrinkable materials, etc.), semi-rigid walls (polycarbonate, etc.), building walls, walls of rooms containing radioactive substances and / or envelopes surrounding the process, etc. It can be made up of a more or less complex combination of these structures.

A scheme of dynamic containment system is shown in Figure 1-1(b). Dynamic containment usually complements static containment. It is based on the implementation of a dynamic barrier provided by an air direction, an air velocity or a level of depression through an opening between the inside and the outside of the containment. The principle is to keep the highest depression in the areas where radioactive materials are present (process equipment, glove boxes or site airlock), so that air flows are directed from the least contaminated areas to the most contaminated areas. Depressions between different areas are necessary to create the required air inlet flow in nominal or accidental openings. They are maintained through control valves, speed regulators, centrifugal fans, etc.

Dynamic containment is generally ensured by a ventilation system, which makes it possible to obtain in the confined area: a main air direction from the outside to the inside of the containment, an air velocity calibrated to openings and / or a standard temporary opening and a depression in the confinement system. The air exchange rate is the ratio between the ventilation rate of an enclosure, under normal conditions of use, and the volume of the enclosure or compartment. It is determined by conventional ventilation requirements necessary to maintain the required depressions in containment zones. Air exchange rates usually implemented in site containments range from 1 to 30 depending on radiological issues, volumes of containments and the type of tools used.

The number of containments barriers required during an operation must be determined by a risk assessment and the following factors must be considered: seriousness and probable frequency of potential accidents, quantity of radioactivity substance, radiotoxicity and potential for dispersion (gas, liquid, solid) of concerned materials. Depending on radiological issues and existing configurations, the implementation of one to three containment levels is mandatory. Usually, a double containment is put in place. Figure 1-2 summarizes the composition of different containment levels. The existing containment is a nuclear type ventilation of buildings, locals, or climatic shelters (sun, rain, wind, snow, extreme temperatures). Site containment is made up of temporary walls: flexible airlock (vinyl), semi-rigid (polycarbonate) or rigid (metallic or masonry) airlock. An additional closer containment is implemented as close as possible to the source of contamination and consists of a containment airlock or a close containment (tight sleeve, ventilated waterproof box, etc.).

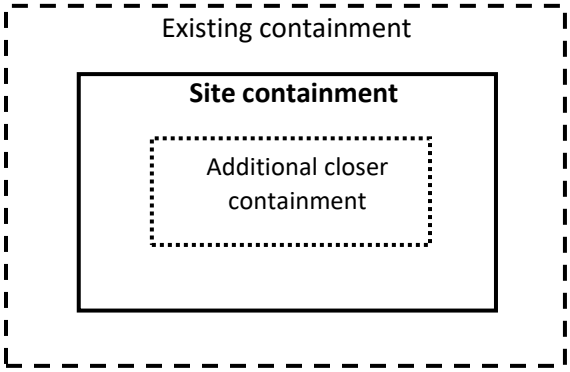

Figure 1-2 Schematic diagram of the composition of the different containment levels (ISO-16647, 2018)**.**

Site containment airlocks are also called “intervention airlocks or work airlocks”. They may exist in three types (Areva, 2012) in nuclear facilities: rigid walls, semi-rigid walls and flexible vinyl walls (Figure 1-3). Each airlock type is implemented in the site depending on the operation requirements. The airlock with metal walls is suitable for very long-term assemblies and/or when mechanical or chemical resistance is required. The airlock with interchangeable transparent rigid walls is implemented for moderate mechanical systems requirement. Is characterized by its rapid assembly and suitable for large volumes. Airlocks with flexible walls is detailed in the following and represents the basis of our study.

1.1.1.2 Airlocks with flexible walls

Our study is based on this type of vinyl airlock as shown in Figure 1-3. . The main objective of our work lies in testing the efficiency of dynamic containment through this airlock type.

Figure 1-3 Airlock with flexible walls (left) and dismantling operations inside an intervention airlock (right)

Airlocks with flexible walls are made of flexible polyethylene or PVC (vinyl) sheets fixed with adhesives on a mounting structure. They are considered as light structures and require few resources for their assembly and disassembly. Their main advantages are the very short lead times for their implementation and their reduced cost. Due to their flexibility, they are also adapted to cramped and congested places. However

their low mechanical resistance that are accentuated by the aging of the vinyl and their fragility to tears, cuts and holes are their main drawbacks.

Soft vinyl walls are the containment enclosures for which the aeraulics criteria are the least restrictive despite their frequent and fast implementation in nuclear facilities. They are frequently used in dismantling operations. However, to ensure no dispersion of pollutant outside the airlock, we should define the best criterion to follow whether the value of negative pressure P in the airlock or the value of inflow air velocity U_{ope} at openings.

Lafanechère (Lafanechère, 2009) mentioned a specific negative pressure for each type of airlock in order to limit the dispersion of pollutants outside airlocks. Flexible (vinyl) airlocks are generally used to maintain an air direction, and up to a negative pressure of around 2 daPa (up to 4 daPa under certain conditions). Semi-rigid (polycarbonate) airlocks are generally used up to a negative pressure of around 8 daPa (or even above under certain conditions). For high vacuum levels, rigid airlocks (masonry or metal) are generally used.

Ducos et al. (Ducos, 2016) performed mechanical strength tests on vinyl airlocks of dimension 30 m^3 with increased negative pressure. Results are shown in Figure 1-4. They found that of a negative pressure of about -10 Pa, a deformation of the airlock starts to appear. When they increases the negative pressure to -25 Pa, the Tarlatan (type of adhesive) peels off at the level of the ground water. For a negative pressure (up to -40 Pa), significant deformation of the airlock and localized detachments are found. For a negative pressure of -100 Pa, there was a perforation of the airlock.

Figure 1-4 Mechanical strength tests on flexible airlock with negative pressure (from left to right): -10 Pa, -40 Pa, -100 Pa (Ducos, 2016)

1.1.1.3 Dynamic containment criteria

Recommendations are presented to guarantee an efficient containment of radioactive materials in a ventilated enclosure used on dismantled or maintenance sites. In order to size and to control the efficiency of containment systems, nuclear operators have to use standards or guides of ventilation written from their own repositories. Containment performance is most often based on qualitative controls as controlling the air flow direction near openings or checking the enclosure walls deformation due the negative pressure. Additionally, operators rely on radiological monitoring outside the enclosure in order to identify the presence of dispersed substances.

The design requirements for static or stato-dynamic site containments depend on the risks of radioactive dissemination in gaseous or particulate form, generated by the sites. Criteria for negative pressure imposed in the airlock and / or velocity (in the favorite direction) measured at the openings in dynamic site containments are retained by the operators depending on the site set up. These criteria are inspired by values recommended by standards with some adaptations linked to particularities of dismantling sites.

ISO-17873, 2004

The standard (ISO-17873, 2004) mainly deals with containment of laboratories and factories scale. It associates each airlock site with a containment class which can range from C1 (very low risks) to C4 (very high risks) based on the operations planned within this containment. It recommends a minimum pressure difference of about 40 Pa between adjacent zones of different classification. When risk of containment is high, it recommends negative pressure values (compared to a reference pressure outside the building): between 80 and 100 Pa for areas with a moderate risk of contamination (class C2), between 120 and 140 Pa for areas with high risk (class C3) and between 220 and 300 Pa for areas with a very high contamination potential (class C4). The standard recalls that, in the past, minimum air velocities were recommended at the openings (0.5 m/s for all types of contaminants, except for plutonium 238 and tritium: 1 m/s and 1.5 m/s respectively). However it specifies that each case must be studied specifically.

The operator EDF sets its dynamic containment criteria of the site depending on whether the latter is in a ventilated room in low pressure (several daPa) relative to the outside or not. In the first case, a static containment or a check of the direction of the air are sufficient for sites with low radiological risk (C1, C2). For medium-risk sites (C3), a minimum velocity criterion at the level of leaks (0.5 m/s) is required; for higher risks (C4), minimum depressions ranging from 40 to 80 Pa are imposed in the airlock. In the second case (airlock on the outside or in a room that is not in low pressure), the requirements on dynamic containment are higher; sites of class C2 and C3 present significant negative pressure, between 20 and 80 Pa, and those in class C4 are in negative pressure between 60 and 100 Pa (Lafanechère, 2009).

CEA and ORANO retain minimum negative pressures of 20 to 40 Pa between (CEA, 2011) (AREVA, 2012), and velocity criteria at openings identical to those mentioned in the standard (ISO-17873, 2004). As a result, CEA has designed a patented system (SMARTDOG[1], CEA patent n ° 12.51872 of February 29, 2012) as shown in Figure 1-5 for controlling low negative pressure in flexible airlocks, which consists in monitoring the value of the flow velocity through a calibrated orifice of 10 cm in diameter connected to the airlock. The low velocity alarm is 1.1 m/s.

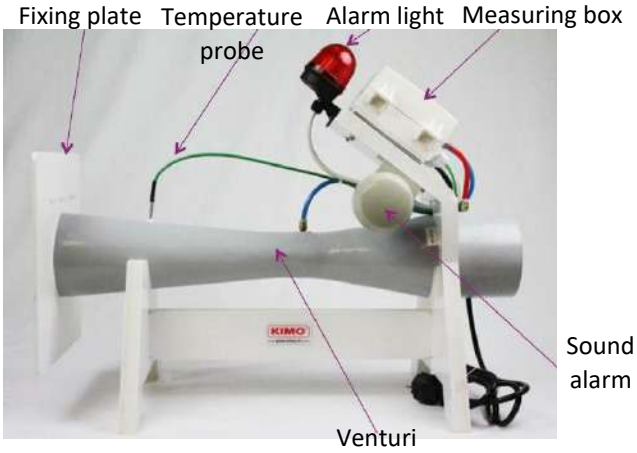

Figure 1-5 System for controlling low negative pressure in flexible airlocks: SMARTDOG

[1]Système de Mesure et Alarme garantissant la non RéTrodiffusion - Dismantling Operations Guarantee

ISO 16647, 2018

The standard (ISO-16647, 2018) is applied to maintenance and/or sanitation ventilated devices implemented on nuclear sites such as the one studied in our case. It aims to specify the applicable constraints relating to the design and operation of containment systems providing safety and protection functions in nuclear worksites and installations being dismantled, in order to protect against particulate and/or gaseous form of radioactive substances. Table ***1-1*** below gives, as an indication, the usual values of dynamic containment criteria (like air direction, air velocities, negative pressures) in various containments according to their classification and in the case where there is only one or two levels of containment implemented.

Table 1-1 Indicative guide to the usual criteria values in containment configurations (ISO-16647, 2018).

Nature of the room or area	Containment criteria if there is only one level of containment	Containment criteria if it is the second level of containment	Containment classification
Rooms free from any atmospheric contamination	Atmospheric pressure, or slight overpressure	Atmospheric pressure, or slight overpressure	Not classified
Areas with very low levels of surface or atmospheric contamination.	Static containment, or sense of air	No containment, or static containment, or sense of air	D1
Areas with moderate air contamination potential	Air velocity in line with a calibrated opening (3)	No containment, or static containment, or direction of air	D2
Areas with a high potential for atmospheric contamination	≥ 20 Pa (1)	Air velocity in line with a calibrated opening (2), (3) (and	D3

		≥ 20 Pa [(1)] for 1st containment level)	
Areas with a very high potential for atmospheric contamination.	≥ 40 Pa [(1)] (It is recommended to implement at least two levels of containment)	Air velocity in line with a calibrated opening [(2), (3)] (and ≥ 20 Pa [(1)] for 1st containment level)	D4
Areas with extreme potential for atmospheric contamination.	Criteria to be studied on a case-by-case basis	Criteria to be studied on a case-by-case basis	D4*

[(1)] Compared to the reference outside atmospheric pressure.

[(2)] Compared to the atmosphere of the existing containment.

[(3)] For example air speed > 1 m/s in a calibrated orifice of Ø 100 mm.

For the vinyl airlock consisting of flexible walls, we saw above that for a pressure of -10 Pa, the airlock structure starts to be degraded. Then for containment class ranging from D3 to D4*, this airlock type is not appropriate because the walls of the device could be torn under the effect of strong negative pressure. Instead, an airlock with semi-rigid or metallic walls is more appropriate. For classes D1 and D2, the criteria that is important to investigate is the direction and the value of the velocity at the opening U_{ope}. In our study, we follow the recommendation that for potential risk areas, each configuration should be studied on a case-by-case basis and we will be interested in studying the efficiency of fixed air velocity criteria at the opening during a dynamic containment of a flexible airlock, notably the three velocities commonly used: 0.5 m/s, 1 m/s and 1.5 m/s.

1.1.2 Backflow phenomenon

Dismantling operations are usually carried out inside low pressure enclosures using exhaust fans. Dynamic containment of hazardous material is ensured by a directional airflow through the openings. The opening may be due to the activity of operators within the airlock (related to the flapping of the doors curtain or produced by the passage of operators or equipment for example) or due to an accidental event (local tear, cut or burn at the flexible wall…) Due to operators activities, unsteady flow inversions may occur through the opening and then lead to the transfer of pollutants outside the enclosure. The transfer of contamination outside a ventilated enclosure through existing or accidental openings is commonly referred to as "backflow" phenomenon that is shown in Figure ***1-6***.

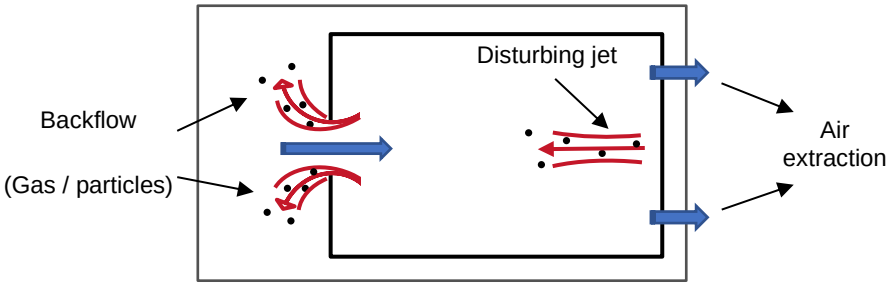

Figure 1-6 Scheme of the backflow during a dynamic containment

This phenomenon is more likely to occur in low pressure enclosures compared to their external environment, such as maintenance or dismantling airlocks implemented in nuclear facilities. The presence of an aeraulic disturbance within these depressurized enclosures could affect the dynamic containment efficiency, and results in backflow of gaseous or particulate contaminations to the external environment. By relying on the databases of accidents / incidents listed by IRSN, we can distinguish various typical disturbing scenarios existing in nuclear dismantling or maintenance operations. These scenarios contribute to the local transfer of pollutants to the outside of ventilated enclosure either due to geometrics of the enclosure or the movement of the operators and equipment into the enclosure, or even the internal or external flows related to the ventilation. Likewise, these pollutant transfers can be induced by processes generating heat flows such as an upward flow induced by a thermal plume inside the enclosure, or dispersion of contents (cutting or blowing of materials for example). Figure ***1-6*** corresponds to the case of a disturbing jet flow facing the opening as I studied it in one part of my thesis work. We are interested to identify the aerodynamics conditions leading to the pollutant leakage, to understand how the dispersion phenomenon does happen near the edges and what is the appropriate turbulence model to numerically simulate this kind of flow. We decide to concentrate our study on two types of disturbing scenarios, mainly the countercurrent internal disturbing free jet and the parietal transverse internal jet that could describe the presence of internal flows related to the ventilation or the processes of cutting or blowing materials inside the enclosure resulting in the dispersion of materials near the opening.

1.1.2.1 Phenomena related to the backflow

The backflow covers three physical phenomena of different types (Berne, 1997), (Dupoux, Laborde, & Prevost, 1997):

The diffusion phenomenon

In a flow at rest, the differences in concentration tend to accumulate under the action of microscopic phenomena (due to random agitation of gas molecules, known as molecular diffusion), or macroscopic phenomena (due to fluctuations in the flow, known as turbulent diffusion). These effects contribute in all directions and for all flows types and therefore tend to transfer the pollutants outside the enclosure. This phenomenon is taken into account in our study and is related to the mixing and diffusion of the pollutants within the flow and is accented under the effect of the disturbing jet.

The detachment phenomenon

These effects are directly related to the type of airflow in the openings. These openings appear generally with sharp edges for the passage of air. Then airflow tends to take off from the wall, inducing vortices near or downstream of the opening as shown in Figure 1-7. Thus, through these vortices, a pollutant can escape the main flow and overcome the dynamic containment. Simultaneously, a second phenomenon can occur: the passage of a flow near the opening edge generates turbulence, resulting in increased turbulent diffusion and greater backscatter. This phenomenon is highlighted in our study and is related to the thickness of the frontal wall of our enclosure that varies from 1 mm to 5 mm as we will see further.

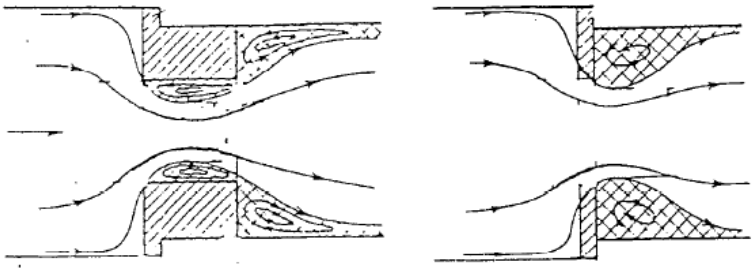

Figure 1-7 Flow configurations near an orifice

Wake phenomenon

These effects are related to the presence of an obstacle as the body of the operator in front of an opening of the containment. Depending of the flow velocity near the opening, the shape and the dimensions of the obstacle, a stable recirculation system could be create downstream the obstacle as shown in Figure 1-8, able to bring the pollutant outside the enclosure and to the operator. In our study, the presence of obstacles near the opening can be related to the presence of filter samplers near the opening. The number and position of these samplers could modify the flow.

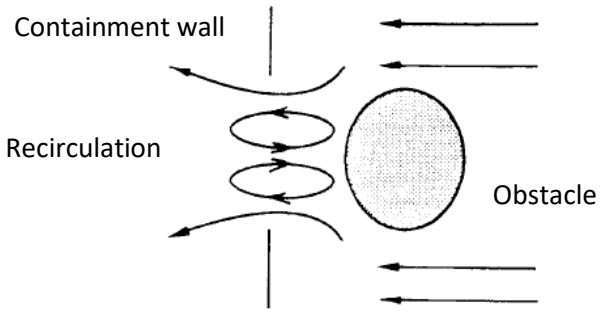

Figure 1-8 Backflow downstream an obstacle

Among the three causes of backscatter that we have identified, the last two effects involve complex phenomena that are not analytically accessible.

1.1.2.2 Coefficients related to the backflow

In order to study the containment efficiency in nuclear airlocks, we have to quantify the phenomenon of pollutant transfer outside the airlocks. Many coefficients are defined as follows (Dupoux, Laborde, & Prevost, 1997):

- The local transfer coefficient k (s/m^3) is commonly used to quantify the pollutants transfer occurring in dynamic containment. It represents the ratio between the pollutant concentration transferred to the outside of the airlock near the opening $C_{outside}$ (ppm), and the volume flowrate of the pollutant injected from a source inside the airlock q_s (l/h). k (s/m^3) $=\frac{C_{outside}\ (ppm)}{q_s\ (l/h)}$.
- The backflow coefficient K (%) as defined by S. Kaissoun. It is the ratio between the mean pollutant concentration backflowed locally at the opening outside the enclosure $\overline{C_{out}}$ (ppm), and the

pollutant concentration measured inside the enclosure $\overline{C_{in,eq}}$ (ppm) at equilibrium. This coefficient is expressed as a percentage.

$K\,(\%) = \frac{\overline{C_{out}}\,(ppm)}{\overline{C_{in,eq}}\,(ppm)} \times 100.$

We choose to use this backflow coefficient in our study in order to study the efficiency of the dynamic containment.

- The dynamic containment efficiency E (%) that is directly related to the backflow coefficient by the equation :

$E\,(\%) = 1 - K\,(\%)$

Generally, these coefficients described above related to the characterization of the backflow depend on many factors, as the enclosure dimensions, the aeraulic parameters (the inflow velocity at the opening), the nature of the pollutant (gaseous or particulate) and the obstacles presence (nature, geometry ..). We commonly use gaseous and particulate tracing techniques to identify the pollutants concentration.

1.1.2.3 Tracing techniques

Gas and particulate tracing techniques are used to identify the concentration of the real pollutants that transfer to outside the enclosure near the opening as we present further (Prevost, 2003). Gas or particulate tracing consists in marking, by means of an element (gas or aerosol) suitably chosen, the gas flows traversing the system being studied, and in measuring the evolution in space and/or in time of the resulting concentrations. In the context of the analysis of complex systems, this technique can provide two types of information:

- the measurement of the static and dynamic operating parameters of the system itself (air flow, transit time, residence time distribution, ...),

- the characterization of the interactions between the system and its environment, for monitoring the quality of the process and its safety (transfer coefficient, contamination analysis,..).

The dispersion of an element (tracer or real pollutant) in the gas flow results from a set of relatively complex phenomena such as molecular diffusion, turbulent diffusion, gravity effects, effects specific to aerosol (sedimentation, impaction), ..

1.1.2.4 Various works on pollutant backflow phenomenon described in the literature

Works on large openings of isolation rooms in hospitals

In many hospitals, negative pressure isolation rooms are used to house patients who are highly infectious, and maintains the spread of air and bacteria within the isolation room. Their efficiency is closely related to room air distribution. Airflows induced by door opening motion and healthcare workers passage can lead to a breakdown in isolation conditions and causes the dispersion of infectious air out of the isolation room across the doorway. The door dimensions in hospitals are considered as large openings (usually about 1 m × 2 m).

Droplets and particles of different sizes are released from breathing, coughing or sneezing. After release these particles and droplets undergo evaporative water loss in the air to become droplet nuclei. However, large particles (diameter >20 µm) may rapidly deposit onto wall surfaces because the force of gravity is more significant than ventilation induced effects. Smaller particles (0.1-10 µm) may be suspended for a

long time and contribute to disease transmission over great distances (Xie, Li, Chwang, Ho, & Seto, 2007). Thus fine particles and gaseous pathogens are significantly influenced by ventilation and airflow patterns.

Tanga et al. (Tanga, et al., 2005) investigated the containment efficiency of isolation rooms in hospital, where a patient admitted to a negative pressure isolation room has transferred viruses to a nurse that frequently handed equipment through the doorway, without entering the patient room. Tests applied on an experimental model demonstrated that, despite negative pressure, opening the door results in the transport on infectious air from the isolation room to outside and then the breakdown of the isolation conditions. A water tank was built with food dye to simulate infectious aerosols in an isolation room. Photos in Figure 1-9 shows how the dye escapes from the isolation room to the doorway when the door is opened. The patient's room was set at a negative pressure of approximately 3 Pa, and undergoes 8 /h total air renewal rates changes. The hinged door opened into the isolation room.

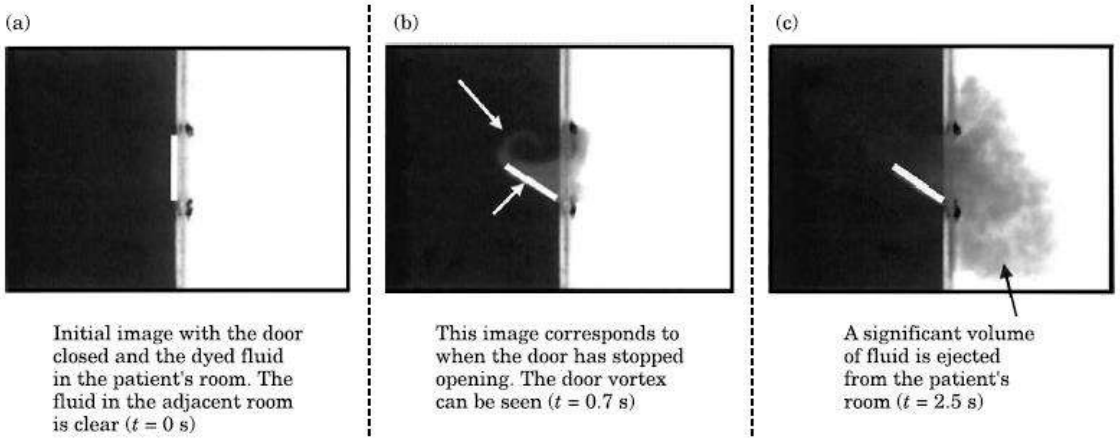

Figure 1-9 Photos taken from vertically above the experimental isolation room (left-hand side) and the corridor (right-side hand). (a) The door is closed. (b) The door is opened and the dye starts to escape. (c) Transport of the dye into the adjacent room. (Tanga, et al., 2005)

Eames et al. (Eames, Shoaib, Klettner, & Taban, 2009) analyzed experimentally and numerically the performance of a force-ventilation isolation room and the transport of particles to outside the room caused by the movement of people and doors opening/closing. They investigated experimentally the particulate contaminant (< 20 µm) exchange generated by a door opening/closing in an isolation room. These small particles move passively through airflow and are analyzed using dilution of food dye in the water (instead of air). The model room had (0.3 x 0.3) m^2 dimensions, and a water depth of 0.22 m. The door dimensions were (0.15 x 0.08) m^2. Figure 1-10 shows a sequence of false color images that show the exchange flow direction caused by a door opening and closing (with red on the right-hand side and blue on the left-hand side). The isolation room is at the right-hand side. When the door is opened, two vortices of opposite directions are created near the door inside and outside the isolation room. The vortex in the right-hand side moves to the inside of the isolation room due to ventilation. Closing the door results in the generation of a high-speed jet propagating along the wall inside the isolation room. The vortex on the left-hand side propagates to the outside until it breaks down.

Larger droplets and particles (> 40 µm) do not move in a passive way as small particles. They move relative to the airflow. Their movement within a turbulent flow is studied numerically. Results show that mean fall

velocity of particles is largely unchanged. However turbulence significantly enhances horizontal and vertical dispersion.

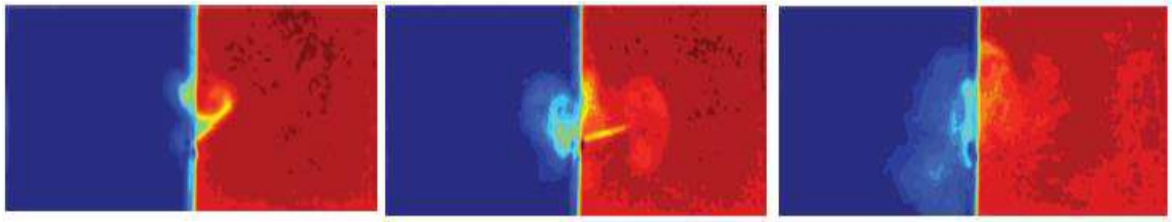

(1) (2) (3)

Figure 1-10 False color images showing time sequence of a door exchange flow in the plane view. (1) – (2) correspond to when the door is opening, and (3) corresponds to when the door is closed. (Eames, 2009)

Chen et al. (Chen, 2011) investigated numerically the bioaerosol (SARS) dispersion and transmission through patient rooms. They found that air exchange due to small temperature differences between isolation rooms played a major role in SARS transmission. Shih et al. (Shih, Chiu, & Wang, 2007) used the computational fluid dynamics (CFD) method to investigate the effects of a moving person and the opening and closing of a sliding door within an isolation room air distribution, including velocity, pressure and contaminant fields. Tung et al. (Tung, 2009) proposed a design of ventilation system to control air flow rate for containing airborne contaminant and preventing its spread to the adjacent rooms when the door to the isolation room is opened and closed. The studied model includes an anteroom (cleaner area) of dimensions (2.5 x 2.5 x 1) m^3, and an isolation room (contaminated area) of dimensions (2.5 x 2.5 x 3.7) m^3 respectively separated by a door of 2 m height. They employed a CFD approach to examine the concentration maps of CO_2 airborne contaminants and the airflow patterns between the two rooms while varying the ventilation flow rate. Airflow patterns are analyzed to be affected by ventilation rates and air temperature differentials. Results showed that an air velocity above 0.2 m/s via a doorway effectively prevents the spread of airborne contaminants out of the isolation room in the state of door opening. Hang et al. (Hang, et al., 2015) performed full-size experiments and CFD simulations to study potential inter-cubicle airborne transmissions through a shared anteroom due to the hinged door opening.

Kalliomaki et al. examined (Kalliomaki, Saarinen, Tang, & Kosk, 2016) airflow patterns across the isolation room doorway induced by the operation of single hinged and sliding doors with simulated human passage. The doorway presented the (2.06 x 1.1) m^2 surface with both door types. Smoke visualizations (Figure 1-11) show leakage of pollutants outside the isolation room with single hinged door through manikin passage. They demonstrated that the hinged door opening generated a greater flow across the doorway than the sliding door. Tracer gas measurements showed quantitatively that the door operation induced substantial air exchange through the doorway with both door types. Overall, the sliding door performed better in all tested scenarios.

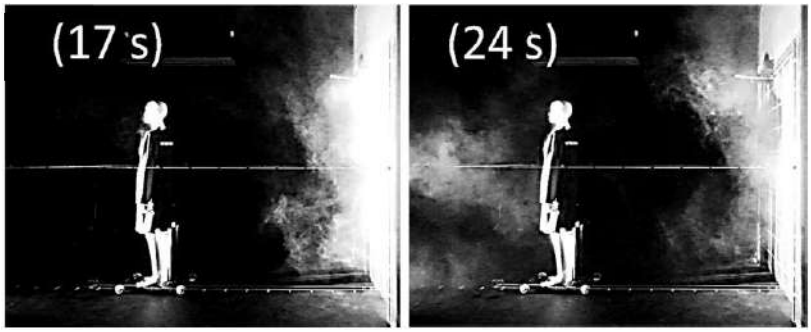

Figure 1-11 Smoke visualization (anteroom side-view) of the single hinged door and manikin passage induced airflow patterns. The time in the parenthesis denotes the time elapsed since the door started opening (Kalliomaki, 2016).

Works on moderate openings size in fume cupboards and gloves boxes

Fume cupboards and gloves boxes are considered as partial enclosures. They are widely used in laboratories to prevent the diffusion of dangerous pollutants from the inside of the enclosure into the laboratory and then to protect workers. The fume cupboard shown in Figure 1-12(left) contains an adjustable rectangular window of 0.685 m height on its lower part allowing the worker to get access by its arms to the enclosure. The gloves box shown in Figure 1-12(right) contains two circular opening (diameter 0.265 m) connected to two gloves where the worker can get access to the box.

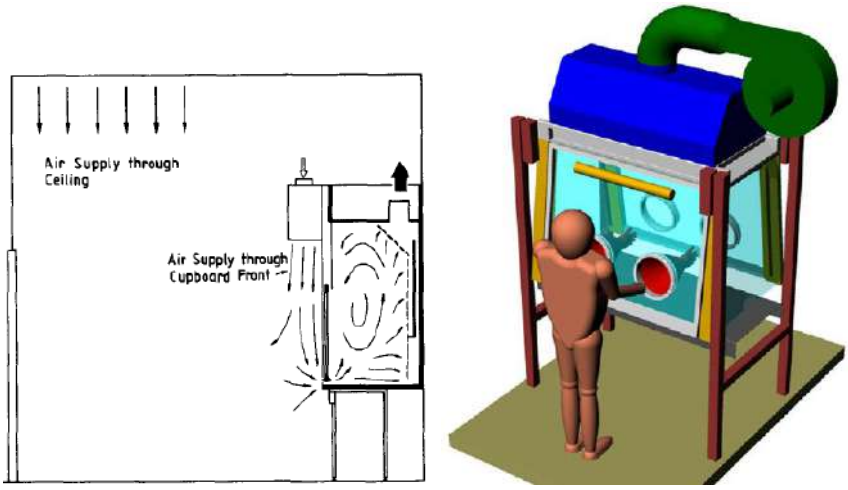

Figure 1-12 (Left): Air supply system to laboratory in a fume cupboard (Durst & Pereira, 1991), (Right): General view of a ventilated gloves box (Cruz, 2011)

V. Cesard et al. (Cesard, 2011) (Cesard, 2012) (Cesard, 2013) studied the efficiency of a dynamic containment of a Type II Microbiological Safety Cabinet (fume cupboard) through simultaneous emission of nanoparticle saline aerosol and a tracer gas (SF_6). Three enclosure operating configurations were tested: one without any disturbance, a second one simulating an operator in front of the enclosure using a mannequin and a third on highlighting the human movement by using a plate moving in front of the enclosure. For each configuration, the authors calculated a local transfer coefficient in order to quantify the protection level of the enclosure with respect to each airborne contaminant. They found that the

behavior of the nanoparticles aerosol and the gas are similar. However, the ventilated enclosure offers an average protection level for the nanoaerosol that represents the twice of that obtained for the gas.

Durst et al. (Durst & PEREIRA, 1991) performed experimental tests on a fume cupboard to test the containment performance when the front window was opened then closed. Measurements were done using SF_6 gas tracer connected to an infrared device using to acquire the gas concentration near the window opening. They founded that the performance of fume cupboards does not necessarily improve if the air renewal rate from the laboratory through the cupboard to the exhaust system is increased. For many cupboards, increased safety was achieved by reducing the air renewal rate to an optimal value. Simultaneously they performed numerical investigations inside the cupboard in order to interpret the experimental results.

Johnson et al. (Johnson & Fletcher, 1996) studied the effect of the presence of an operator at the cupboard frontal opening to the containment performance using SF_6 gas tracing technique. They highlighted the blockage and thermal effects due to the operator that could induce the leakage of tracer gas to its breathing zone. Chern et al. (Chern & Cheng, 2007) investigated numerically, using the standard k–ε turbulence model, airflow motions and associated pollutant distributions in fume hoods in the case of the presence of an operator near the frontal opening. Karaismail et al. (Karaismail & Celik, 2010) investigated numerically the recirculating flow structures formed in the wake of a worker standing in front of an enclosing fume hood using three Unsteady Reynolds Averaged Navier Stokes (URANS) models. They found that the performance of SST k − ω model to capture the anticipated unsteady and recirculating flow field in the wake of the worker was promising for further applications of CFD to worker exposure problems.

In the context of nuclear safety, many studies have been interested in quantifying the intensity and the kinetics of propagation of polluting agents that results from the breakage of static or dynamic containment in nuclear ventilated systems, for example in the case of fume cupboards or gloves boxes (Prevost & Lacan, 2003), (Prevost, Bouilloux, & Lacan , 2005), (Colin & Prevost, 2006). They most often applied gaseous and aerosol (0.18 µm and 5 µm) tracers in order to determine local transfer coefficients of various pollutants in many configurations. They also implemented optical techniques (Particle Imaging Visualization and Laser Doppler Anemometry) in order to understand the air flow structure and his behavior near the opening. The results highlighted the presence of a significant backflow of gaseous and particulate pollutants even sometimes by applying the recommendations of standards and ventilation guides.

In context of product protection in food-processing industry, the airflow observed in an enclosure equipped with glove-boxes, disturbed by operator's arms and the motion of a conveyor, was characterized by laser visualizations and PIV as well as by a three-dimensional CFD approach (Cruz, 2011). Firstly, the presence of operator's arms considered as objects, leads to the appearance of recirculating zones under each arm. Experimental and numerical results highlighted the appearance of unsteady phenomena: three-dimensional vortices which continuously grow under each operator arm and are released with a symmetrical evolution along the worktable (Figure 1-13). Simultaneously, Prevost's (Prévost, 2000) performed experimental study on a fume cupboard of a window dimensions of (1.2 m × 0.4 m) using PIV technique. Figure 1-14 shows horizontal PIV field in the right side of the hood near an operator. They detect the presence of vortex inside the cupboard near the window opening that propagates to the outside of the enclosure.

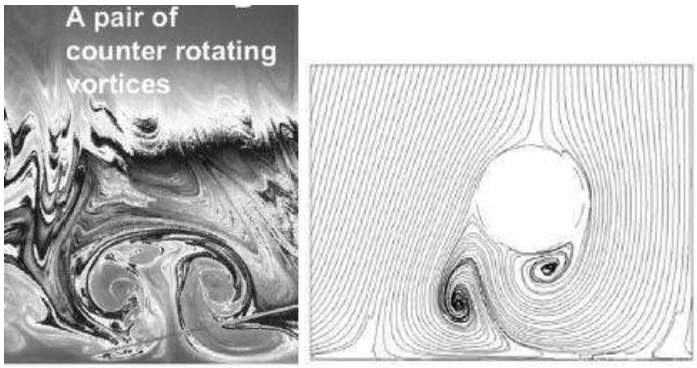

Figure 1-13 Flow visualization (left) and LES numerical simulation for vortex formation (right) near the operator arm (Cruz, 2011)

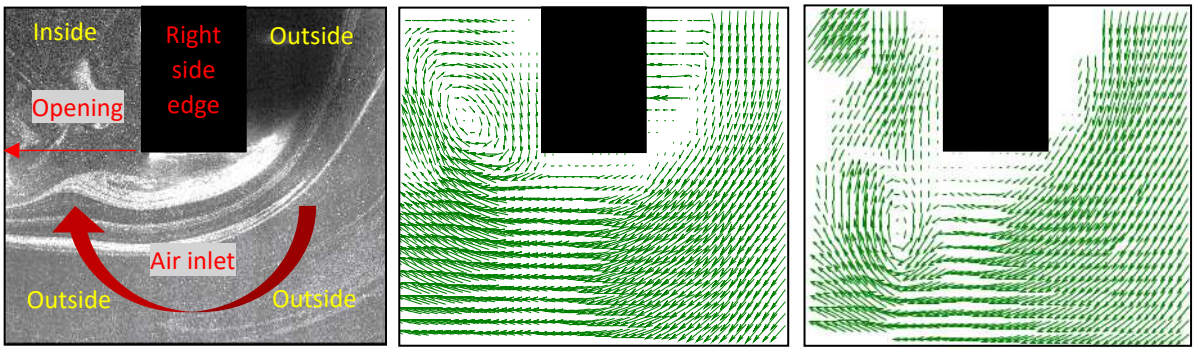

Figure 1-14 Horizontal PIV field at the right side of the fume cupboard (Prévost, 2000)

Works on small openings in nuclear field

To ensure the non-backflow of aerosol or gas, the CEA organization aimed to define a criterion that is straightforward to implement to guarantee the dynamic containment of an intervention airlock (Ducos, 2016). They used gaseous tracing technique using SF_6 on vinyl airlock (Figure 1-15).

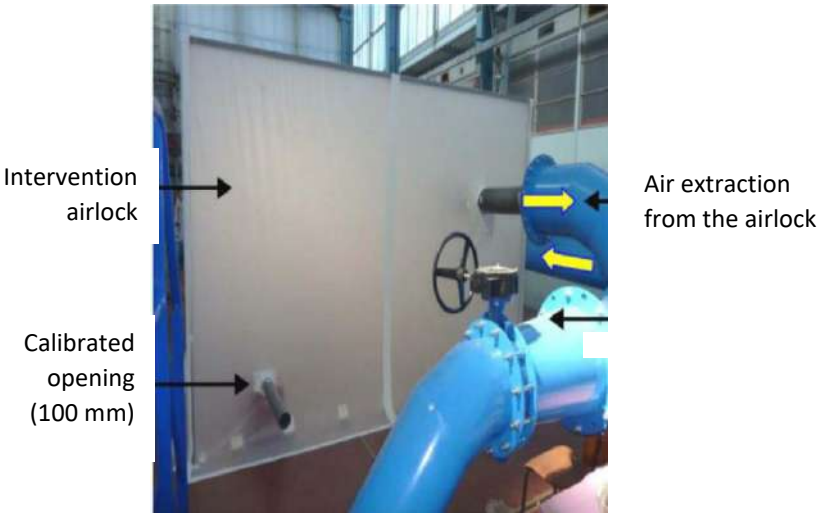

Figure 1-15 Intervention airlock with a calibrated opening of 100 m (Ducos, 2016)

They performed experiments of different scenarios of operators entry/exit movement in the personal airlock, material airlock and/or intervention airlock, in order to identify the optimal velocity within the calibrated opening that guaranteed an efficient containment and that prevented the gas tracer leakage outside the airlock. The criterion retained following the tests was an air inflow velocity ≥ 1 m/s (value easy to remember) at an opening of a diameter of 100 mm. This criterion is also recognized by IRSN.

Due to its complexity and the varieties of disturbance types, as well as the small size of our studied opening, this phenomenon was not well investigated in the literature. Unlike most investigations on the aerodynamic configurations described above that deal with large openings, our study is focusing on airflow dynamics through small openings, such as a rectangular orifice whose hydraulic diameter does not exceed ten centimeters. Our study is the continuation of S. Kaissoun study that handled the gaseous backflow subject through a small opening potentially created in the case of nominal or accidental operations on vinyl airlocks.

During S. Kaissoun study, a small-sized experimental enclosure of dimensions ($1.2 \times 0.5 \times 0.5$) m^3, with a rectangular opening on the frontal wall of dimensions (0.1×0.1) m^2, was designed in order to study the backflow phenomenon near the opening. The rigid walls enclosure is suitable for reproducing many disturbing dynamics configurations by using a rectangular injection nozzle (0.1×0.01) m^2. Laser visualization fields showed that a disturbing flow either internal or external to the enclosure is likely to induce air leakage through the opening (Figure 1-16). The author implemented the gaseous tracing technique in order to quantify the backflow near the opening under the effect of different disturbing jet configurations and to test the dynamic containment efficiency. She highlighted that the pollutant backflow was mainly controlled by the ratio V/U_{ope} that represented the velocity of the disturbing jet near the opening to the inflow velocity at the opening, and not only by the air inflow velocity U_{ope} through the opening: a minimum critical ratio (V/U_{ope}) was defined for each disturbing configuration beyond which the backflow phenomenon was triggered, as mentioned in the chapter 2 later in this report.

Figure 1-16 Laser visualizations of the vertical plane outside the enclosure under the influence of an external parietal disturbance, showing the tracer backflow near the opening (Kaissoun, 2018)

Simultaneously she performed numerical simulations on a small-sized enclosure using U-RANS and LES models in order to identify which model was suitable for the detection of flow inversions near the opening under the effect of a countercurrent internal free jet. Additionally, as continuation for S. Kaissoun works, M. Tsongo Kighoma (Kighoma, 2018) tested the ability of two other turbulence models to restitute the backflow: the model SAS-SST and the hybrid model DES.

Figure 1-17 shows the vertical profiles of the gaseous tracer flow when a countercurrent disturbance was applied, with the different turbulence models tested at a specific time t = 9 s. S. Kaissoun found that using U-RANS (SST k–ω) model, the flow converged to steady state form and could then provide information about global flow patterns such as mean velocities. But U-RANS calculations were not able to restitute the turbulence structure of the flow near the opening or to detect flow leakage through the opening. However using LES model, the flow tracer was going outside the enclosure in the form of eddy structures: LES computations were more suitable to describe the flow inversions and vortex structure of the flow.

As shown in Figure 1-17, the URANS model could not restitute the backscatter phenomenon near the opening; however the phenomenon was observed in the LES model by the presence of the unsteady vortices outside the enclosure and near the opening. The models SAS-SST and DES succeeded to restitute the backscatter effect near the opening. Finally, the resolution of the turbulence increased from URANS, through SAS-SST and DES to LES where the turbulence resolution was higher than the others.

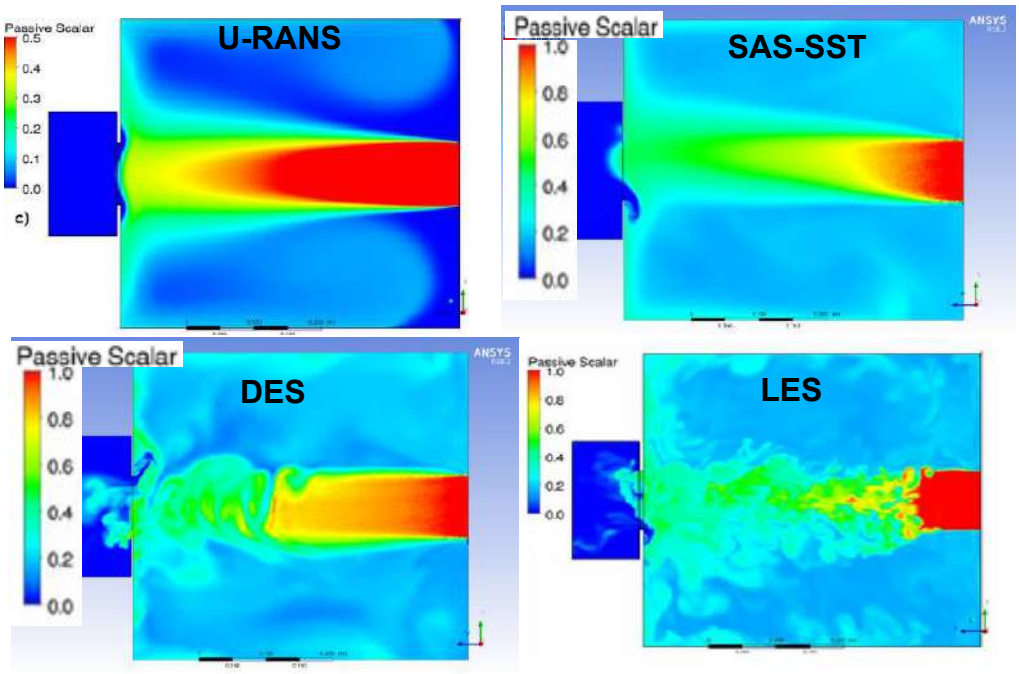

Figure 1-17 Vertical profiles of the gaseous tracer flow for different turbulence models: U-RANS and LES (S. Kaissoun) and hybrid models SAS-SST and DES (M. Tsongo Kighoma, 2018) at t = 9 s

We should mention that testing other models such as the SAS-SST and the hybrid model DES was important in order to find an alternative model that can restitute the backflow phenomenon and that consume less simulation time and memory requirements than the LES model. The calculation times per iteration and per mesh (assuming a single processor) are 7.10^{-6} s for LES model, 9.10^{-8} s for DES model and 7.10^{-8} s for SAS-SST model. Finally, in our study, we adopt the DES hybrid model since the turbulence is better resolute than the SAS-SST model, and the calculation times between the two models are comparable.

The main objectives of our research work are to study experimentally the airflow dynamics of gaseous and particulate pollutants around the openings under the effect of two different disturbing configurations inside the enclosure and to check the ability of CFD numerical simulations to restitute the flow inversions near the openings using hybrid models. This will allow to increase the number of configurations that we

can study by means of numerical simulations without the experimental constraints. Simultaneously an analytical experimental program is conducted on an experimental model representative of a real airlock since 2021. It aims to acquire quantified data to define aeraulics criteria to respect, in order to guaranty the performance of containment in these airlocks type. Numerical simulations using a hybrid model chosen from our study will also be applied to this full-size airlock in order to compare the results with those acquired with the experimental program and validate its effectiveness.

1.2. Mixing of gases and particles in a gas flow

In contrary to S. Kaissoun's works that deal mainly with dispersion of gaseous pollutants, our study deals with gaseous and particulate pollutants dispersion in a gaseous flow. For that, we brief first the transport of gas in turbulent flows, and then we detail the particle-laden gas flow due to its complexity and wide application. We are interested in understanding the behavior between the gas and particulate pollutant in turbulent flows in order to better interpret our following results.

The dispersion of a pollutant in the form of a gas or an aerosol in another gas flow, results in microscopic and macroscopic phenomena such as molecular and turbulent diffusion (Berne, 1997). The molecular diffusion is a microscopic phenomenon and is responsible of the matter transfer by random agitation of the main flow molecules and the pollutants molecules or particles. It results in the generation of a flow from high to lower concentration regions. Following Fick's first law, the surface density of this flow is proportional to the concentration gradient. The turbulent diffusion is a macroscopic phenomenon where the turbulence of the main flow contributes in the gas or aerosol dispersion in the gas flow. The turbulent flow represents fluctuations associated with eddies of wide range of length and time scales such as vortices. Thus, two fluid elements that are initially arbitrary close will be transported by vortices in a random way and will find themselves separated by a distance. The turbulent diffusion is considered as a phenomenon of convection.

1.2.1 Mixing of gas in turbulent flow

Gaseous dispersion in a flow depends on many factors. The gas dispersion is a dynamic process that depends not only on pressure, temperature and composition, but also on the flow conditions and on the history of the process (Sheng et al., 1999a). Many numerical simulations are used to simulate gas simulation in a flow. A three-dimensional transient finite volume CFD program is used to simulate gas dispersion and explosion events (Bai, 2016). Models for passive gas and heavy gas dispersion models were described (Mannan, Volume 2, 2005).

It is important to understand experimentally and numerically the ability of turbulent flows to effectively mix entrained fluids to a molecular scale. Fluid introduced in a turbulent region is dispersed into the fluid by motions of largest to smallest eddies, where molecular diffusion enhance mixing. Turbulent flow with high Reynolds number generates large interfacial surface area and accelerates the slow molecular mixing. When fluid is entrained at the largest scales of the flow, scalar dispersion and mixing are provided by the full scale spectrum of the turbulence cascade. Many flows exhibit qualitatively different behavior beyond a transitional Reynolds number (Dimotakis P. , 2000). This transition occurs in shear and boundary layers of the flow (jet and pipe flows). Experiments show that when Reynolds number becomes higher than the transitional Reynolds number, its effects on flow dynamics and mixing become substantially weaker.

Mixing in turbulent flows presents three levels (Dimotakis, 2005). Level-1 mixing is the simple case where mixing is passive and occurs between passive scalars. Dispersion and mixing are driven by turbulent flow and do not influence the flow dynamics. They are referred to molecularly mixed fluid. This mixing level occurs between density-matched gases, for dispersion of nonreacting trace markers (pollutants, small temperature differences, small-particle smoke or ink) and low-concentration dyed in a liquid. Level-2 mixing alters the flow dynamics. It is characterized by the generation of vorticity resulted from differences between pressure and density gradients or temperature and entropy gradients in the flow. Vorticity generated controls internal Kelvin-Helmholtz layers and instability to enhance mixing and homogenize density variations in the flow. Examples are mixing of stratified fluids or variable-density fluids subjected to imposed pressure gradients or acceleration/gravitational fields as in Rayleigh-Taylor (Rayleigh, 1883), (Taylor, 1950) instability flows. Level-3 mixing generates changes to the fluid coupled to dynamics such as its composition, density, enthalpy release and pressure increase. This mixing level includes combustion phenomena, supernova explosions imposing additional time/space scales and dynamics complexity to numerical approaches (Colgate & RH., 1966).

The study of Level-1 turbulent mixing is very developed with high Reynolds number flows such in channel flows, pipe flows free shear layers and jets. Da Silva et al. (Da Silva, 2015) performed direct numerical simulations DNS and large-eddy simulations (LES) of spatially developing turbulent planar jets with a passive scalar to study the characteristics of the spreading rates of the velocity and passive scalar fields as shown in Figure 1-18. However, Level-2 and Level-3 mixing are less developed and represent an open research topic nowadays.

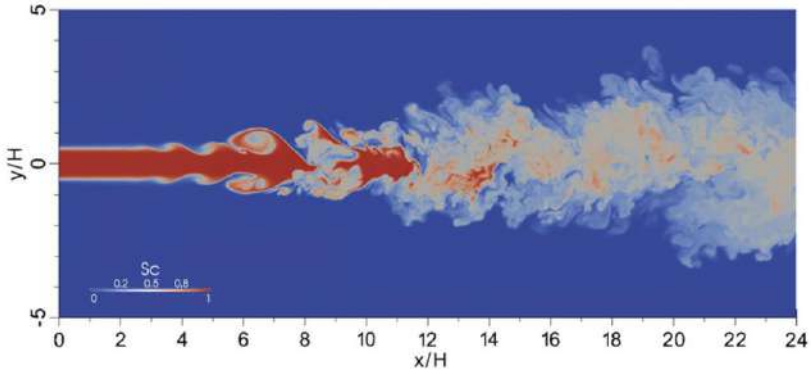

Figure 1-18 Contours of passive scalar plane for the DNS of a turbulent planar jet (Da Silva, 2015)

1.2.2 Particle-laden flows

Dispersed multiphase flows are common in many engineering and environmental applications, and they are often turbulent (Maxey & Corrsin, 1986) (Glawe & Samimy, 1993) (Lazaro & Lasheras, 1989) (Ishima, , 1993b).These flows are thus characterized by a dispersed phase such as particles, droplets, or bubbles that is dispersed within a carrier phase in the form of gas or liquid. The inherent stochastic nature of the carrier-phase turbulence is complicated by non uniform spatial distribution of the dispersed phase (Renoux & Boulaud, 2003). The presence of the dispersed phase makes both experimental measurements and numerical simulations of turbulent multiphase flows far more difficult than those of single-phase flows.

1.2.2.1 Characterization of the aerosol

An aerosol is the suspension of liquid and / or solid particles in a gaseous medium and having a very small settling velocity. The behavior of aerosol particles depends essentially on the movement and characteristics of the carrier gas. They are present in many natural phenomena such as formation of clouds and precipitations, and in industrial phenomena such as the spray formation, room with controlled dust, etc. They are considered as the principle causes of pollution due to exhausted gas and atmospheric radioactivity.

Due to their complex shape, it is rather difficult to know the actual size, shape and density of aerosol particles. In nuclear facilities, the aerosol description in the installations and the environment is described based on the aerodynamic diameter (d_{ae}) which corresponds to the diameter of a sphere having the same settling velocity as the particle and a density of 1000 $kg.m^{-3}$. It is involved in the processes of particle deposition, filtration, etc… It describes the aerodynamic behavior of an aerosol. It is given by the following relation:

$$d_{ae} = d_{ev} . \left(\frac{\rho_p}{1000 . \chi} \right)^{1/2}$$

Where ρ_p represents the density of the particle considered ($kg.m^{-3}$), d_{ev} is the equivalent diameter in volume which corresponds to the diameter of a sphere having the same mass m and the same density ρ_p as the particle considered and χ the dynamic shape factor that is equal to 1 for a sphere.

Many forces are acting on an aerosol in particle-laden flows that can lead to the drift of aerosols in the carrier gas and their deposition on surfaces. We can mention the Brownian motion between particle and fluid molecules, sedimentation resulting from balance between buoyancy and drag forces, thermophoresis, photopheresis, electrostatic effect, impaction under the effect of centrifugal force: is due to a deviation of the particles with respect to the curved fluid streamlines, due to their inertia and the presence of a wall on this new path. Other forces are due to the fluid turbulence, such as turbulent impaction and turbulent diffusion. Due to turbulent impaction, a particle receives sufficient quantity of energy from a surrounding turbulent structure can be projected, thanks to this energy input, until it meets a wall. The turbulent diffusion is due to transport of particles by turbulent structures of the fluid in the boundary layer, through the buffer zone, to the surface (upper limit) of the viscous sublayer. The particles then pass through the viscous sub-layer, mainly by Brownian motion. This phenomenon should not be confused with the turbulent impaction: in the case of turbulent diffusion, the particles follow the vortices until the latter bring the particle into the viscous sub-layer, while in the case of turbulent impaction, the particle instantly leaves the energy-carrying vortex to impact.

1.2.2.2 Classification of two-phase turbulent flows

The particle-laden turbulent flow can be classified into different regimes depending on their volume fraction and Stokes numbers (Elghobashi, 1994).

1.2.2.2.1 Based on their volume fraction

Figure 1-19 presents the map of possible interactions between particles and turbulence depending on their volume fraction (Elghobashi S. , 1991).

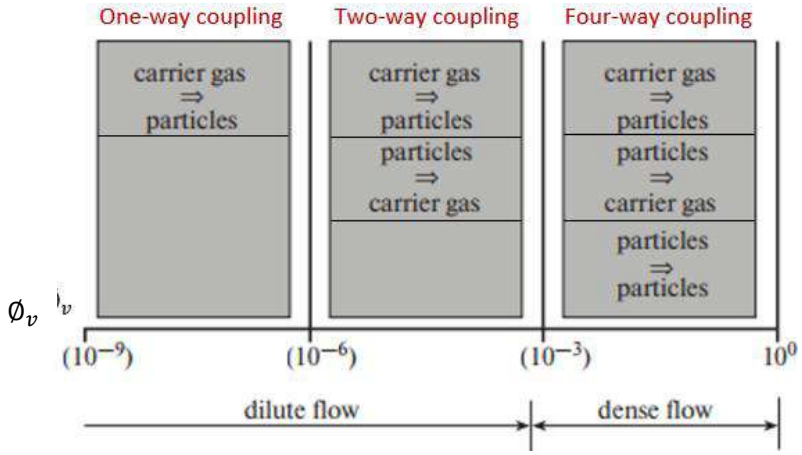

Figure 1-19 Map of interactions between particles and turbulence depending on the particles volume fraction (Elghobashi S., 1991)

One-way coupling: When particle mass loading ratio (the ratio of particle mass flux to the carrier phase mass flux) and volume fraction of dispersed phase are low ($\emptyset_v \leq 10^{-6}$), their time average effect on the flow of the carrier fluid is negligible. The particles are affected by the turbulent flow field, but particles themselves do not affect turbulence. The determining interaction is represented by the effect of the carrier phase on suspended particles, which controls all of their characteristics (averaged and fluctuation velocities and temperatures, local fraction, etc.). This regime is referred to as a one-way coupling regime.

Two-way coupling: When volume fraction increases ($10^{-6} < \emptyset_v \leq 10^{-3}$), the dispersed phase in turn begins to generate a feedback on the carrier medium. The particle mass loading ratio is relatively high, but the volume fraction of the dispersed phase is low. In this regime, the particles influence the turbulence and the turbulence affects the particle motion. The momentum transfer from the particles is large enough to alter the turbulence structure. This interaction is called two-way coupling.

Flows in the two regimes discussed above are often referred to as dilute suspensions. Heterogeneous flows of these two types ($10^{-9} < \emptyset_v \leq 10^{-3}$) are often referred to as dilute flows.

Four-way coupling: In the case of a dense flow ($\emptyset_v > 10^{-3}$), where both the particle mass loading ratio and the volume fraction of the dispersed phase are high, the inter-particle interaction becomes important. Here, in addition to the two-way coupling between suspended particles and the carrier phase, particle/particle collision takes place (which represents two supplementary interactions of the particles on each other), hence the term four-way coupling. As $\emptyset$ approaches 1, we obtain a granular flow in which the influence of fluid is weak and contact or friction between particles are dominating.

The behavior of particles in turbulent flows with one-way coupling is reasonably understood, at least in unconfined homogeneous flows. The limitation to this understanding relies mainly from the incomplete understanding of turbulence itself even in particle-free flows. On the other hand, flows in the two-way or four-way coupling regimes are still at the infancy stage of understanding due to highly nonlinear nature of interactions in these flows.

1.2.2.2.2 Based on their Stokes number

The Stokes number,Stk, is a dimensionless number characterizing the dynamic response of particles in a fluid flow. It is defined as the ratio of the particle response time to the flow characteristic time scale:

$$Stk = \frac{\tau_p}{\tau_f}$$

With τ_p the relaxation time of the particle and τ_f the characteristic time scale of the flow.

τ_p represents the time required by a particle, released from rest in an uniform flow, to reach 63% of the flow velocity assuming Stokes drag law is applicable (Reynolds number of the particle is less than unity). For a spherical particle in a gas, it is given by $\tau_p = \frac{\rho_p {d_p}^2}{18\,\mu_f}$, where ρ_p is the particle density, d_p is the particle diameter and μ_f is the viscosity of the carrier fluid.

Since we are studying jet type disturbances, τ_f represents the characteristic timescale for large vortex structures in the jet mixing layer and is defined as $\tau_f(x) = \frac{\delta(x)}{U(x)}$, where $\delta(x)$ is the eddy length scale. For a free mixing jet, it represents the measure of the local thickness of the jet mixing layer, which increases as the mixing layer grows. $U(x)$ is its characteristic jet velocity at distance x from the nozzle. In the case of jet from a pipe flow: $\tau_f = \frac{D}{U_0}$, where D is the pipe diameter and U_0 is the centerline velocity of the jet at pipe exit.

Thus the Stokes number at the jet exit is given by the equation below:

$$Stk = \frac{\rho_p {d_p}^2 U_0}{18\,\mu_f D}$$

In a turbulent jet, the Stokes number characterizes the ability of large-scale structures for moving particles laterally in mixing region. For particle-laden turbulent flow, this number at the jet exit is an important parameter. This parameter allows also to characterize the capacity of particles to behave like a tracer. The greater the Stokes number, the less they follow the airflows. We can distinguish three types of particle-laden flows that are summarized in Figure 1-20:

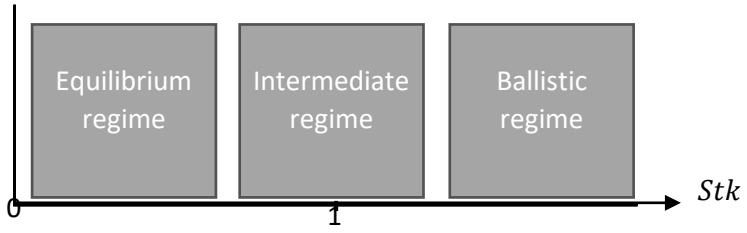

Figure 1-20 Regime distribution depending on Stokes number

Equilibrium flow regime (Stk <<1)

Particles with Stk << 1 have sufficient time to respond to fluid fluctuations and follow the fluid streamlines. They are able to adjust quickly to any changes in the flow. They follow completely the turbulent fluctuations of the carrier gas velocity and their averaged velocity profile is similar to that of carrier phase. This regime is known as Stokes regime. These particles are used as tracer particles for many optical devices, such as LDA and PIV, to determine the velocity of the turbulent fluid flow. For accurate tracing, particle response time should be faster than the smallest time scale of the flow.

Quasi-equilibrium flow (Stk ≈1) – Intermediate regime

Particles with $Stk \approx 1$ are in the intermediate regime. Heterogeneous flows of this type are characterized by the equality of averaged velocities of the carrier and dispersed phases. However, particle inertia will be sufficient to induce differences between fluctuation velocities of the gas and suspended particles. Particles respond partially to fluid fluctuations. They may be dispersed faster than the fluid and their trajectories are altered by fluid fluctuations. Flow in this regime is the most poorly understood and therefore the most difficult to model.

Preferential accumulation phenomenon of particles is often observed. Researches show that particle concentration in turbulent flows may be highly non-uniform with local regions of anomalously high or low concentration. Vortex structures can preferentially concentrate dense particles within specific regions because the particle inertia prevents them from following curved streamlines (Eaton & Fessler, 1994) (Chung & Troutt, 1988). Particles tend to move away from areas of high vorticity such as vortex cores, and to accumulate in regions of low vorticity and high strain rate. Then preferential concentration results in centrifuging of particles away from vortex cores and an accumulation of particles in convergence zones. Particles could be trapped in rings around vortices (Wicker & Eaton, 2000). Particle interactions are illustrated in two-dimensional flows in Figure 1-21(left). The picture at the bottom left corresponds to a particle moving near a vortex. Particle cannot follow the curved streamline and spirals away from the center of the vortex. The picture at the top left shows a particle moving to a converging flow region of high strain rate and low vorticity. In many cases of preferential concentration, Longmire & Eaton (1992) found that for Stokes numbers between 1 and 10, vortex rings concentrate particles in high strain rate regions surrounding the vortex and the cores of the rings are essentially devoid of particles as shown in Figure 1-21(right). Particles are pulled out of the streaming regions inside the vortex rings and pushed into regions downstream of the cores where the clusters appear.

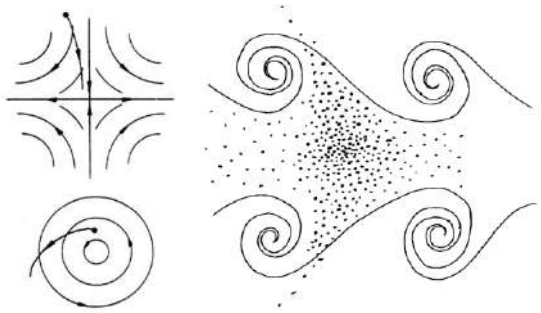

Figure 1-21 (left) Particle interaction with simple two-dimensional flows, (right) Cartoon of particles interacting with vortex ring (LONGMIRE 1992)

Flow with large particles (Stk >>1) - ballistic regime

Particles with Stk >> 1 have a relaxation time that exceeds significantly the characteristic time of large-scale turbulent eddies. They will not have sufficient time to respond to fluid fluctuations and continue along their initial trajectories (in nearly rectilinear course). Particles would take a longer time to adjust to the flow. They are dominated by their inertia and are dispersed less than the fluid.

1.2.2.3 Works on particle-laden flows

Longmire et al. (Longmire & Eaton, 1992) studied experimentaly the behaviour of glass particles in a jet dominated by vortex ring structures from a nozzle of an exit diameter D of 2 cm. The jet was forced over a range of frequencies to produce different sizes of vortex rings in the axisymmetric shear layer (Schmidt

number St_D=0.43 for a frequency of 364 Hz; St_D=0.93 for a frequency of 794 Hz). Figure 1-22 shows instantaneous photographs from visualization studies of a smoke-marked single-phase flow (top) and its corresponding particle-laden flow for St_D=0.43 (middle) and St_D=0.93 (down) respectively and Re_D = 23000.

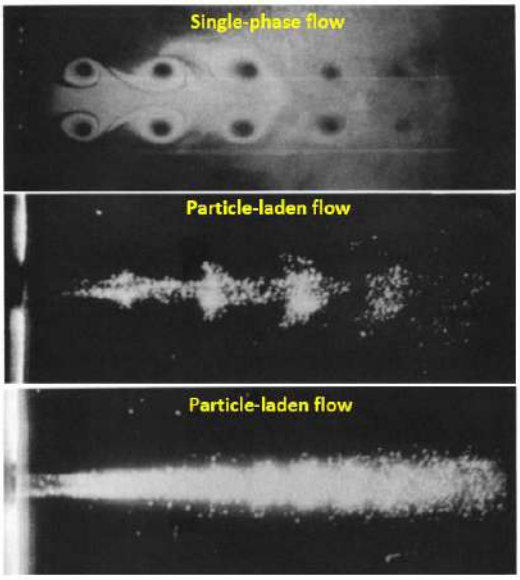

Figure 1-22 Single-phase (top) and particle-laden flow (middle) St_D=0.43, Re_D=23000; particle-laden flow (down) St_D=0.93, Re_D=23000 (Longmire & Eaton, 1992)

The single-phase flow was seeded with smoke particles of diameter of 1 µm in order to visualize the jet flow. The smoke particles appeared to follow all scales of the fluid flow and corresponds to the equilibrium regime. The particle-laden flows in the two other images are seeded with glass particles having a diameter of 55 µm. The second image highlight the preferential phenomenon where dense clusters of particles are located in regions of high strain and low vorticity immediately downstream of vortex rings. Increasing the jet frequency in the third image, particle-laden flow does not contain distinct clusters and particles dominated by their inertia leave the nozzle in a nearly rectilinear trajectory, corresponding to flow with particles in the ballistic regime.

Chung et al (Chung & Troutt, 1988) analyzed numerically the particle dispersion in an axisymmetric jet by following particle trajectories in a jet flow at a pipe exit. A Lagrangian approach is followed to predict particle motion in the jet flow simulated by discrete vortex rings. They found that particle dispersion depends strongly on Stk. Particles with Stk = 0.05 are dispersed at approximately the same dispersion rate as the fluid tracers. Particles with Stk = 1 may be dispersed faster than the fluid and are flung out of the large vortex structures. Particles with large Stk of 10 and 100 values are dispersed less than the fluid. Particles don't respond to fluid fluctuations and continue their initial rectilinear path.

Physical mechanisms of additional dissipation and generation of turbulence in heterogeneous flows are shown schematically in Figure 1-23 (Varaksin, 2007). It is important to note the dissipative effect of fine particles to laminarize the flow (Varaksin & Zaichik, 1998), the effect of large particles to generate additional turbulence due to formation of a wake, and the combined effect of both mechanisms on a turbulent flow of gas in a pipe. Early studies of heterogeneous jets revealed that the presence of low-inertia particles leads to a decrease in the intensity of turbulence of carrier gas. The energy in large eddies is spent to provide momentum to particles in fluctuation motion, leading to the suppression of high-

frequency content in the energy spectrum of turbulence. However, large particles tends to increase turbulence generation in the flow, by generating additional turbulence in their wakes.

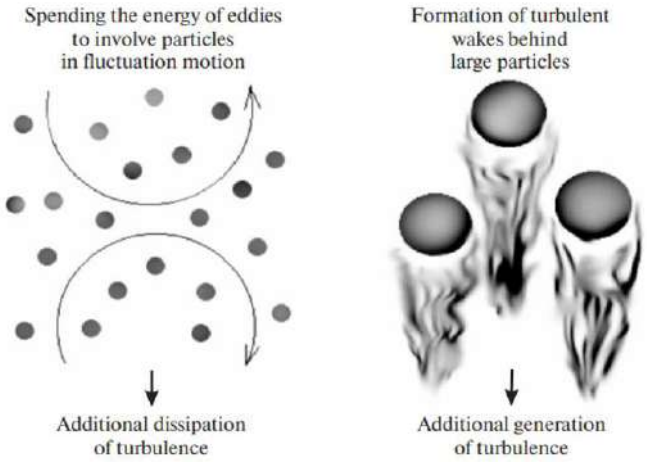

Figure 1-23 Basic physical mechanisms of modification of turbulent energy in gas flows with low-inertia and large particles (Varaksin, 2007)

Gore & Crowe (1989) (Gore & Crowe, 1989) reviewed early work on jet and pipe flows and plotted the percentage change in the turbulence intensity versus the ratio of particle diameter to a turbulence integral scale as shown in Figure 1-24. They found that particles larger than approximately 1/10 of the integral scale increase turbulence intensity, whereas smaller particles damp fluctuations.

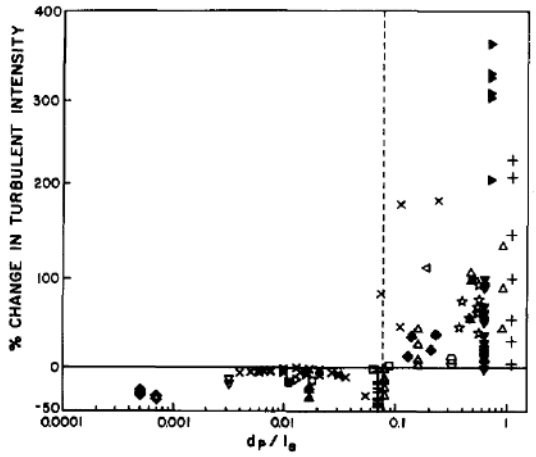

Figure 1-24 Change in turbulent intensity as function of length scale ratio (Gore 1989).

Wang et al. (Wang & Maxey, 1993) performed direct numerical simulations to investigate the motion of heavy particles in isotropic homogeneous turbulence. The preferential sweeping is illustrated by Figure 1-25 where a heavy particle settles through a flow region of three vertical structures. Due to its inertia, the particle does not follow the vortex streamline but rather continue its path along the periphery of the vortex. The combined effect of inertia bias and preferential sweeping may lead particles to move away from the vortex in downward direction. They form regions of high particle concentration that appears as long connected patches aligned vertically, and seems to be broken by stretching and rotation of vortical region. It results in an increase of 50% in particle mean settling velocity.

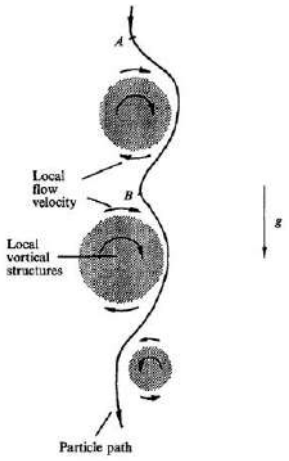

Figure 1-25 (left): Sketch showing the preferential sweeping mechanism for a heavy particle interacting with local flow vertical structure (Wang & Maxey, 1993)

1.3. Numerical simulations for turbulence

Since our study contains an important numerical part in order to simulate the backflow of gaseous and particulate pollutants from a ventilated enclosure, we are interested to detail different numerical modeling for turbulence and different approaches for particle-laden flows that exist in literature.

Turbulent flows have a wide range of characteristic scales of length, velocity and time. For high Reynolds number flows, there is a cascade of energy from large scales where turbulence is produced towards small scales where turbulence is dissipated (Richardson, 1922), (Kolmogorov, 1940). Along Kolmogorov cascade, large structures are decomposed into finer structures and energy injected into large structures is transferred to finer structures before being dissipated in heat in Kolmogorov structures. The local equilibrium hypothesis expresses the equality between the production of kinetic energy and the dissipation rate.

1.3.1 Turbulence modelling:

The averaged Navier-Stokes equations for an incompressible turbulent fluid are shown in Eq. 1.1 and Eq. 1.2.

$\frac{\partial \overline{u_i}}{\partial x_i} = 0$ continuity equation (Eq. 1.1)

$$\rho\left[\frac{\partial \overline{u_i}}{\partial t} + \overline{u_j}\frac{\partial \overline{u_i}}{\partial x_j}\right] = -\frac{\partial \bar{p}}{\partial x_i} + \frac{\partial}{\partial x_j}\left(\mu\frac{\partial \overline{u_i}}{\partial x_j} - \rho\overline{u_i' u_j'}\right)$$ momentum equation (Eq. 1.2)

Where ρ and P are respectively the density and the pressure. μ is the dynamic viscosity. $\overline{u_i}$ represents the average component of the instantaneous velocity and u_i' is its fluctuating component.

$-\overline{\rho\, u_i'\, u_j'}$ is the Reynolds stress tensor that can be totally resolved with the DNS (Direct Numerical Simulation) method, partially resolved with the LES (Large Eddy Simulation) and hybrid methods or modelled with the RANS (Reynolds-averaged Navier–Stokes) method as shown in Figure 1-26.

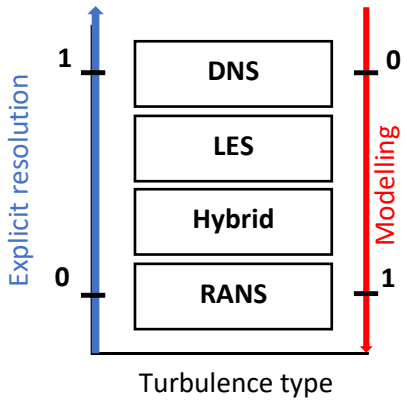

Figure 1-26 Scheme of different turbulence numerical types

1.3.1.1 Unsteady Reynolds-averaged Navier–Stokes (URANS) modelling

The turbulent flow is totally modeled with RANS method. While turbulent flow is based on an average and a fluctuating part, this method consists in modelling the fluctuating part of the fluid and only resolve the average flow equations. This average statistical method requires the closure of equations system governing the mean motion. The first order models follow the Boussinesq concept (Boussinesq, 1877) that considers that turbulent flow is strongly dominated by mixing of large structures. The turbulent viscosity μ_t is then linearly linked to Reynolds tensor by Eq. 1.3.

$$-\rho\overline{u_i'u_j'} = \mu_t \left(\frac{\partial \overline{u_i}}{\partial x_i} + \frac{\partial \overline{u_j}}{\partial x_i}\right) - \frac{2}{3}\rho\bar{k}\delta_{ij} \qquad \text{(Eq. 1.3)}$$

Where k is the turbulent kinetic energy and δ_{ij} is the Kronecker symbol (= 0 or 1).

Many closure models for the calculation of μ_t are as follows.

k – ε closure model

The turbulent viscosity μ_t is written by combining the turbulent kinetic energy k and the dissipation rate ε. It is given by the Eq. 1.4 (Jones & Launder, 1974):

$$\mu_t = C_\mu \rho \frac{\bar{k}^2}{\bar{\varepsilon}} \qquad \text{(Eq. 1.4)}$$

k and ϵ are both estimated by their transport equation.

This model is based on local and linear dependence of turbulent stresses on the average field. As a result, the model tends to overestimate turbulent stresses and turbulent viscosity in high shear zones (boundary layer, mixing layer). On the other hand, this linearity means that this model has almost no chance of reproducing complex flows, in particular three-dimensional flows.

k – ω closure model

This model was proposed by Wilcox in 1988 (Wilcox, 1998) and is based on the use of turbulent frequency vortices $\omega=\varepsilon/k$, and on an assumption of linearity between the turbulent viscosity and the shear of mean field. The turbulent viscosity is given by Eq. 1.5.

$$\mu_t = \alpha \frac{k}{\omega} \qquad \text{(Eq. 1.5)}$$

Where α is a coefficient to decrease the influence of turbulent viscosity by making a correction for low Reynolds. The values for k and ω are estimated by their transport equations.

SST k – ω closure model

The Shear Stress Transport *k* - *ω* model, proposed by Menter (Menter, 1994) is a hybrid model that uses the *k* - *ω* approach to predict flow in the viscosity-affected region and the k - ε approach for the rest of the flow. A correlation ensures the continuous transition from one model to another. This model is particularly satisfactory (at least in isothermal flow) near separation zones.

1.3.1.2 LES modelling

With large-scale simulation LES (Large Eddy Simulation) model, only largest scales are resolved explicitly, while the effect of small scales is modeled, making calculations with large Reynolds number feasible with reduced CPU ressources. This approach considers that large scales contains kinetic energy and are dependent on boundary conditions. They should be solved by filtered Navier-Stokes equations. However, it considers that small scales have a universal dissipative behavior, and then should be modeled. A filter is applied between the calculated part (average field) and the modeled part (fluctuating field).

LES methods are therefore more accurate than RANS methods since they do not model the entire fluctuating flow. However, they are more CPU demanding in terms of calculation time and memory.

1.3.1.3 Hybrid models

Hybrid LES/RANS coupling approaches are used for wall-bounded flows. Indeed, the relevant flow structures close to walls region are very small (typically smaller than the size of the opening). Applying LES model in these regions means that we need to resolve the locally most energetic vortical structures, which requires to substantially reduce the grid cell size and consequently reduce the time step. For high Reynolds number applications, the scaling of computational structures for LES is close to DNS (Frohlich, 2008). Then, a hybrid approach is necessary. Hybrid approaches combine statistical RANS methods in near-wall regions and large-scale simulation LES methods in the bulk flow far from walls, hence reducing the number of spatial-temporal scales to be resolved. The difficulty of these approaches lies in the interface between the RANS model and the large-scale LES simulations.

DES 'Detached Eddy Simulation'

The DES 'Detached Eddy Simulation' hybrid method is suitable for configurations experiencing massive flow detachments. It is an extension of RANS equations in which the model switches to a subgrid scale formulation in regions fine enough for LES calculations. Regions near solid boundaries where turbulent

length scales are smaller than the maximum grid size are assigned to RANS method. As turbulent length scale exceeds the grid dimension, regions are solved using LES method (Strelets, 2001), (Squires, 2002). Therefore, the grid resolution is not as demanding as pure LES, thereby considerably cutting down the computation cost. At high Reynolds numbers, flows around obstacles present massive flow separations and large turbulent structures and then are difficult to simulate with RANS only. The Detached Eddy Simulation (DES) (Travin, 2000) approach is suitable for separated flows with a reasonable cost. The space in the vicinity of the RANS-LES interface, known as the “grey area” (Temmerman, 2008), is one of the issues confronting the DES method (Strelets, 2016). The second serious problem raised during a DES simulation is the sensitivity to the mesh.

Spalart-Allmaras (SA) model (one equation model)

Spalart et al. (1997, 2001) exploited the Detached Eddy Simulation (DES) approach consisting of constructing a "bi-layer" approach which passes from the statistical RANS approach in the parietal zones to the LES approach in separated areas "far" from the walls. The SA formulation of Spalart and Allmaras (1992; 1994) consists in a one-equation model of transport relating to the turbulent viscosity. The SA model explicitly involves a modified distance function $\widetilde{d}$ in the destruction term which is modified to give the DES formulation to the SA model with $\widetilde{d} = \min(d, C_{DES}\Delta)$.

In this term, d is the distance to the wall, C_{DES} denotes a constant and $\Delta = \max(\Delta_x, \Delta_y, \Delta_z)$ the largest dimension of the local cell. In the zones where $d < \Delta$ (close to the walls), the DES formulation of the SA model is similar to RANS formulation and therefore the parietal zones are simulated by the RANS equations. In areas where $d > \Delta$ (far from the walls), the sink term in the transport equation has a higher level than in the RANS formulation and then the turbulent viscosity ν_t is lower than for the RANS formulation, thus giving it LES behavior.

The "simplicity" of the implementation and understanding of the DES approach on one-equation models explicitly involving the distance to the wall explains why this approach was initially limited to the SA models and Gulayev et al. (1993).

SST-DES Formulation (two transport equations)

Other approaches to determine the turbulent viscosity are based on two transport equations. The determination of the turbulent viscosity is done through solving transport equations on k and ω respectively.

The DES was extended to the most used RANS models. In particular, Strelets (2001) proposes a strategy for extending the DES approach to the SST model. This model is based on the SST formulation (ANSYS, 2020). The advantage of this combination is that accurate prediction of turbulent boundary layers up to separation and in mildly separated regions carries over from the SST model. In addition, the SST model supports the formulation of a zonal DES formulation, which is less sensitive to mesh resolution restrictions than the standard DES formulation. The idea behind the DES model (Strelets, 2016) is to switch from the SST- $k - \omega$ RANS model to an LES model in regions where the turbulent length, $L_{k-\omega}$, predicted by RANS model is larger than the local mesh spacing. In this case, the length scale used in computation of the dissipation rate in the equation for the turbulent kinetic energy is replaced by the maximum local mesh spacing, Δ. By choosing the maximum edge length in the DES formulation, this model returns to the RANS formulation in attached boundary layers.

The equation of turbulent viscosity μ_t is as follows (Eq. 1.6):

$$\mu_t = \rho \frac{k}{\omega} \quad \text{(Eq. 1.6)}$$

The k and ω equations of the SST-DES model are presented in Eq. 1.7 to Eq. 1.9 as follows:

$$\frac{\partial \rho k}{\partial t} + \frac{\partial}{\partial x_i}(\rho u_i k) = P_k - \beta^* \rho k \omega \times F_{DES} + \frac{\partial}{\partial x_i}[(\mu + \sigma_k \mu_t)\frac{\partial k}{\partial x_i}] \quad \text{(Eq. 1.7)}$$

$$\frac{\partial \rho \omega}{\partial t} + \frac{\partial}{\partial x_i}(\rho u_i \omega) = \alpha \rho S^2 - \beta \rho \omega^2 + \frac{\partial}{\partial x_i}[(\mu + \sigma_\omega \mu_t)\frac{\partial \omega}{\partial x_i}] + 2(1 - F_1)\sigma_\omega 2\rho \frac{1}{\omega}\frac{\partial k}{\partial x_i}\frac{\partial \omega}{\partial x_i} \quad \text{(Eq. 1.8)}$$

The blending function F_1 is equal to zero far from the walls, and increases to 1 at the near-wall regions.

The SST-DES modification of Strelets can be formulated as a multiplier to the destruction term F_{DES} in the k-equation (Menter, 2003).

$$F_{DES} = \max\left(\frac{L_{k-\omega}}{C_{DES}\Delta}, 1\right) \quad \text{(Eq. 1.9)}$$

where $L_{k-\omega}$ is the turbulent length scale and Δ is the maximum local grid spacing.

$L_{k-\omega}$ and C_{DES} are calculated as follows:

$$L_{k-\omega} = \sqrt{k}\ /(\beta^* \omega) \quad \text{(Eq. 1.10)}$$

$$C_{DES} = 0.78\, F_1 + 0.61\,(1 - F_1) \quad \text{(Eq. 1.11)}$$

In the attached boundary layer, $L_{k-\omega} < C_{DES}\Delta$ and the model reduces to the standard RANS model; otherwise in the separation regions, the length scale becomes grid-dependent and the model performs as a subgrid-scale version.

The numerical formulation is also switched between an upwind biased and a central difference scheme in the RANS and DES regions respectively.

$\beta^* = 0{,}09$, $\alpha = \frac{5}{9}$, $\beta = 0{,}075$, $\sigma_k = \sigma_\omega = 2$ and C_{DES}= 0,61 for homogeneous isotropic turbulence.

The C_{DES} constant is calibrated on the decaying isotropic turbulence experiment of Comte-Bellot and Corrsin (1971). This calibration adapts the level of turbulent viscosity in order to avoid the phenomena of energy accumulation at the small scales or, on the contrary, to dissipate too strongly the large scale turbulent structures.

Zheng et al. performed numerical studies of the flow near a circular cylinder at high Reynolds number using the detached eddy simulation (DES) approach. (Zheng, 2016). The DES approach has been successfully tested by various authors on configurations subject to massive flow separations (Shur, 1999), (Travin, 2000), (Strelets, 2001). In particular, these simulations show that the DES is capable of resolving the turbulent structures present downstream of a separation, which makes it possible to improve the prediction compared to a URANS approach, even on industrial configurations type.

Preliminary tests by S. Kaissoun (Kaissoun, 2018) and Tsongo Kighoma (Kighoma, 2018) on the small-size enclosure were performed using many numerical approaches. Kaissoun found that the $k - \omega$ URANS model was not able to predict the backflow near the opening. LES approach detected the backflow near the opening with an optimal resolution. However, the LES approach requires highly demanding

computational resources, then it is not suitable for a parametric study. That's why Tsongo Kighoma tested other models on the small-size enclosure in order to capture the backflow. He showed that the hybrid SST-DES model was able to predict the backflow near the opening with a good compromise between the turbulence resolution and the computational cost. Once the SST-DES model is confirmed by Tsongo Kighoma, we handled it in our study in order to quantify the backflow and perform further a parametric study.

1.3.1.4 Direct numerical simulation (DNS) method

The turbulence can be calculated explicitly using DNS. All turbulence scales are resolved numerically using Navier-Stokes equations thus eliminating the need for closure approximations (Balachandar & Eaton, 2010). However, the absence of a model requires having meshes of the order of the dissipative scales of Kolmogorov, as much as for the time step. For high Reynolds number flows, there is a broad spectrum of spatial-temporal scales to be resolved. The capacity and the performance of current calculators do not yet allow to solve explicitly complex flows.

1.3.2 Particle-laden turbulent flows approaches

A range of complementary computational approaches is available for dispersed multiphase flows. Particle-laden turbulent flows are numerically solved using turbulence closure models namely the two-fluid Eulerian (two-continuum) and the Lagrangian (particle trajectory) methods, or using the Direct Numerical Simulation (DNS) that solves the instantaneous three-dimensional Navier-Stokes equations of the carrier flow directly. We consider here dilute suspensions. Figure 1-27 shows the range of applicability of different computational approaches in terms of relative particle size and particle volumetric concentration $\emptyset_v$ (Elghobashi, 1994) (Elghobashi & Abou Arab, 1983) (Ferry & Balachandar, 2001).

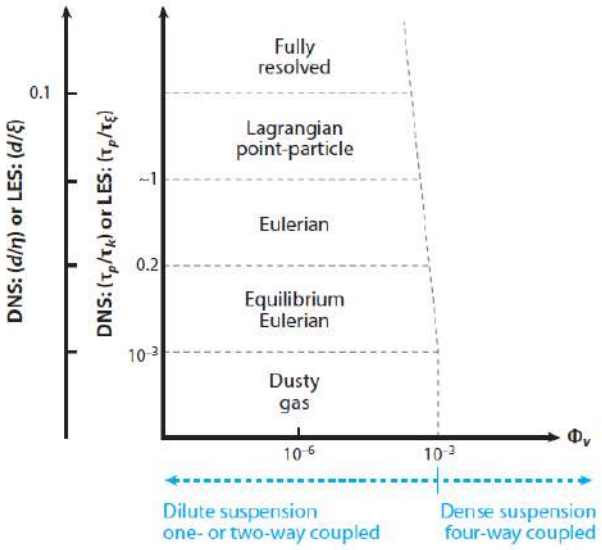

Figure 1-27 Different approaches for turbulent particle-laden flow. Their applicability is separated in terms of timescale and length-scale ratios (Balachandar & Eaton, 2010).

1.3.2.1 Dusty gas approach

This one-fluid approach is only applicable for particles with a very small relaxation time scale (Stk <<1). It assumes that particles are so small to perfectly follow the local carrier phase. Particle-laden flow is considered as single fluid whose density depends on local mass fraction of suspended particles. The most important advantage of this approach is its simplicity (Carrier, 1958) (Marble, 1970).

1.3.2.2 Equilibrium Eulerian approach

Equilibrium Eulerian approach retains the computational simplicity of dusty gas approach, but allows particle velocity to be different from the surrounding carrier phase. It assumes that particles are sufficiently small that their motion is dictated only by the surrounding fluid. The advantage of the equilibrium Eulerian approach is that it captures the relative particle motion more accurately and thereby enables important phenomena, such as preferential particle accumulation and turbophoresis (Reeks, 1991). Accurate results of turbulent flows are obtained for $Stk \leq 0.2$ (Ferry & Balachandar, 2001) (Ferry, Rani, & Balachandar, 2003).

1.3.2.3 Eulerian approach

This two-fluid approach treats the carrier and the dispersed phases as interpenetrating fluid media, and the particulate phase properties are given by an Eulerian field representation (Druzhinin & Elghobashi, 1998) (Fevrier, Simonin, & Squires, 2005). The two-fluid formulation requires additional momentum and energy equations for the particulate phase, with momentum and energy exchange between phases taken into account as source and sink terms. The advantage of the two-fluid formulation over equilibrium approximation is that restriction on the Stk number can be relaxed. Thus, the Eulerian approach is applicable for larger particles (Stk >1) (Ferry & Balachandar 2001).

Aerosol model for our study:

An Eulerian two-fluid model, which needs to solve three momentum equations for each particle size, requires large computational calculation times. However, a simplified Eulerian approach can be used for low-inertia particles significantly reducing the number of equations to be solved and then reducing computational cost. It is based on a single transport equation for each particle size.

In our study, we used a simplified Eulerian approach given by (Nerisson et al. 2011) to calculate the particulate concentrations. This approach is applicable on dilute gas-particle flows and for low-inertia particles (aerodynamic diameter less than 50 μm). Note that in our study we considered particles with aerodynamic diameter equal to 5 μm. It is based on a "diffusion–inertia" model due to the low-inertia of particles according to Zaichik et al. (Zaichik, 1997, 2003, 2004). This approach is a one-way coupling approach where the carrier gas affects the particles fluctuations but the effect of particles on the fluid and interparticle collisions are neglected. It consists of a single transport equation of aerosol considering sedimentation, deviation from fluid streamlines and migration effects (Brownian and turbulent diffusions, thermophoresis, turbophoresis).

Recalling that particles deposition on smooth surfaces is due to many physical phenomena such as:

- Deposition due to a force applied on the particle such as sedimentation, thermophoresis and electrophoresis. Electrophoresis and thermophoresis are neglected in this study.

- Deposition due to Brownian diffusion (where particles migrate from regions of high particles concentration to regions of low particles concentration) and turbulent diffusions (where particles are transported by turbulent eddies of the fluid to the fluid viscous sublayer).
- Deposition by impaction due to centrifugal effects, where particles cannot follow curved fluid streamlines due to their inertia and may impact walls.
- Deposition by impaction due to airflow turbulence, where particles receive enough energy from eddies in a turbulent flow and are projected onto a wall across the viscous sublayer.

The aerosol transport equation and deposition model given by Nerisson et al. are presented in the followings.

Aerosol transport model:

The expression for the diffusion–inertia model is given in Eq 1.12:

$$\frac{\partial C}{\partial t}+\frac{\partial}{\partial x_i}\left\{\left[U_{f,i}+\tau_p g_i-\tau_p\left(\frac{\partial U_{f,i}}{\partial t}+U_{f,k}\frac{\partial U_{f,i}}{\partial x_k}\right)\right]C\right\}$$
$$=\frac{\partial}{\partial x_i}\left[\left(D_B\delta_{ik}+D^t_{p,ik}\right)\frac{\partial C}{\partial x_k}+C\frac{\partial}{\partial x_k}\left(D_B\delta_{ik}+\frac{\Omega}{1+\Omega}D^t_{p,ik}\right)\right] \quad \text{(Eq 1.12)}$$

Where C is the particles concentration, U_f is the fluid velocity, τ_p is the particle relaxation time (s), D_B is the Brownian diffusion coefficient (m^2/s), $D^t_{p,ij}$ is the particle turbulent dispersion tensor components (m^2/s), δ_{ij} is Kronecker delta and Ω is a dimensionless turbulent Stokes number.

The left-hand-side of Eq. 1.12 considers particle sedimentation due to gravity and the particle deviation from fluid streamlines due to their inertia (the last term).

The first term in the right-hand-side of Eq. 1.12 represents the Brownian and turbulent diffusions. The second term refers to migration effects of particles due to thermophoresis (under the effect of a temperature gradient) and turbophoresis (migration of particles from high-turbulence regions to low-turbulence regions).

Aerosol deposition model:

The particle deposition flux towards the wall J (kg/ m^2/ s) is given by Eq. 1.13:

$$J = C_M u^* v_d^+ \quad \text{(Eq. 1.13)}$$

Where C_M is the aerosol concentration in the bulk airflow (outside the boundary layer) at the first calculation point (kg/ m^3), u^* is the fluid friction velocity (m/s) and v_d^+ is the dimensionless aerosol deposition velocity.

The dimensionless aerosol deposition velocity v_d^+ and the dimensionless particle relaxation time τ_p^+ are defined as follows:

$$v_d^+ = v_d \ / u^* \quad \text{(Eq. 1.14)}$$

$$\tau_p^+ = \tau_p \, u^{*2} / \, v_f \quad \text{(Eq. 1.15)}$$

Where τ_p is the particles relaxation time (s) and v_f is the fluid velocity (m/s).

The dimensionless aerosol deposition velocity v_d^+ on a vertical wall is given by:

$$v_d^+ = \left\{ \left[\left(\frac{Sc_B^{-\lambda_1}}{\lambda_0} \right)^n + \left[\frac{\tau_p^{+2n}}{\omega^n} \right]^{-1/n} + \frac{\sigma_t}{\kappa} \ln(y^+) \right\}^{-1} \qquad \text{(Eq. 1.16)}$$

Sc_B is the Brownian Schmidt number, τ_p^+ is the particle dimensionless relaxation time, σ_t is the turbulent Schmidt number, κ is the Von Karman's constant = 0.41 in our case, ω = 1700, n = 2, λ_0 = 13.7 and λ_1 = 2/3.

In this model, we identify different deposition regimes based on the value of τ_p^+ as shown in Figure 1-28. The first term in Eq. 1.16 refers to the diffusion regime, the second term refers to the diffusion impaction regime and the third term refers to the inertia-moderated regime.

As shown in Fig. 1, three deposition regimes can be described for vertical walls:

– The diffusion regime (τ_p^+< 0.1): deposition is due mainly to Brownian diffusion close to the wall, because of the very small particle size. In this region, v_d^+ seems to decrease on average when τ_p^+ increases. Here, deposition is independent of τ_p^+: it depends on Schmidt number.

– The diffusion-impaction regime (0.1 < τ_p^+ < 10): deposition increases with increasing τ_p^+. In this regime, deposition is due to turbulent diffusion and following the turbulent eddies in the fluid buffer layer, particles impact the wall.

– The inertia-moderated regime (for τ_p^+ > 10): deposition is mainly due to turbulent impaction of particles on walls due to their inertia. The amount of particles deposited remains constant when τ_p^+ increases.

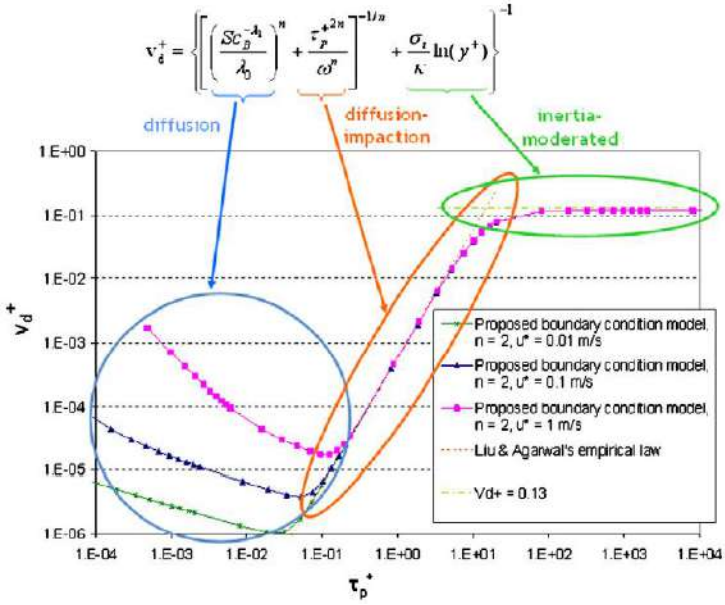

Figure 1-28 Deposition laws on vertical walls in function of the dimensionless particle relaxation time (Nerisson, 2011)

These transport and deposition models can be used for a very wide range of geometries (from elementary devices to rooms of various volumes), in industrial applications dealing with particulate pollutant. They were validated from many experimental data related to ventilated rooms.

1.3.2.4 Lagrangian point-particle approach

This approach is based on the Lagrangian tracking of the particles and solves the equations of motion to predict the position, momentum, and energy of the particles. The particulate phase is represented by a number of computational particles whose trajectories are computed by simultaneous integration. In this approach (Gosman & Ioanides, 1981) (Yuu, Yasukouchi, & Hirosawa, 1978), the conservation equations governing the motion of the carrier flow (continuity, momentum, k and ε) are integrated over a fixed mesh covering the flow domain as in the two-fluid approach. The most significant advantage of the Lagrangian approach is that there is no fundamental limitation on Stk as in Eulerian approach. Furthermore, the size of each particle is independent, and thus polydispersity can be handled easily. The differences between the Eulerian-Eulerian and Eulerian-Lagrangian approaches are shown in Figure 1-29.

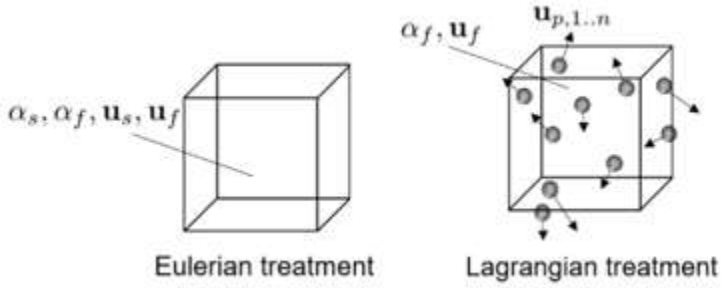

Figure 1-29 Eulerian-Eulerian and Eulerian-Lagrangian treatment for a gas-particle flow in a grid (Hirche, Birkholz, & Hinrichsen, 2019)

The Eulerian-Eulerian approach considers the gas (fluid) and the particles (solid) as two continuous fluids media of velocities u_f and u_p and volume fractions α_f and α_s respectively. However the Eulerian-Lagrangian approach considers the gas (fluid) as a continuous fluid medium of velocity u_f and volume fraction α_f and the particles (solid) as a discrete medium. Each particle (from a total of n particles) has a velocity $u_{p,(1..n)}$ and the Lagrangian approach tracks the trajectory of each particle separately.

1.3.2.5 Fully resolved approach

All the above methods both explicitly or implicitly, are based on point-particle approximation and thus are restricted to particles of size smaller than the Kolmogorov scale η, or the smallest resolved eddies in the case of LES. For particles of size comparable or larger than the smallest undisturbed flow scales of the carrier phase, the ultimate option is to perform fully resolved DNS, in which all the scales of ambient turbulence, and the flow scales introduced by the particles, are completely resolved. (Burton & Eaton, 2005) (Merle, Legendre, & Magnaudet, 2005) (Uhlmann, 2008).

Conclusion

In this chapter, we presented the state of art of our study. Our study represents the continuation of S. Kaissoun works (Kaissoun, 2018) that deal with the experimental and numerical backflow of gaseous

pollutants outside a ventilated enclosure. Our contribution added the particulate part to the study. We presented first the containment systems and the criteria recommended for an efficient dynamic containment. Concerning the backflow part, it is important to note that the backflow phenomenon near small openings in nuclear sites airlocks was not thoroughly investigated in the literature. Some studies were about the dynamic containment efficiency on moderate and large-scale openings that we showed. Then we presented the dispersion of gaseous and particulate species in a gas flow and the interaction that exists between gas and particles in particle-laden flows, in order to understand the interactions that exist between gas molecules and particles. For the numerical part, we presented different turbulence models and particle-laden approaches from the literature. The turbulence model that we used in our study is the hybrid SST-DES model and the aerosol model is a simplified Eulerian approach (Nerisson, 2011).

Synthesis of S. Kaissoun study and our study

During her study, S. Kaissoun (Kaissoun, 2018) studied the backflow of a gaseous pollutant experimentally and numerically through a small opening on a small-size enclosure. Experimentally, she used gas tracing technique and laser visualizations in order to quantify and visualize the backflow. Many disturbing configurations were tested such as counter-current internal jet, internal and external parietal jets and moving obstacle near the opening. She tested also the flexible and rigid frontal walls and changed the thickness of the opening. Numerically, she visualized the backflow near the opening using the LES model with an optimal turbulence resolution. She performed numerical simulations using the configurations of the internal counter-current and internal parietal disturbing jets. However, this model is very computational consuming. Tsongo Kighoma (Kighoma, 2018) showed that a hybrid model SST-DES was able to visualize the backflow near the opening. This model is less time consuming and is suitable for a parametric study.

In our study, that is a continuation of S. Kaissoun study, we aim to visualize and quantify the backflow experimentally and numerical, using two types of pollutants: gaseous pollutant and 5 μm aerosol pollutant. Experimentally, we used gaseous and particulate tracing techniques and laser visualizations. The numerical model is the hybrid SST-DES model (Kighoma, 2018). During our study, we handled the internal counter-current and parietal jets configurations and we tested two types of frontal wall of the enclosure: a rigid frontal wall then a flexible frontal wall. We started first by studying the backflow locally near the opening. Then, and due to limitations of sampling near the opening, we added an envelope around the small-size enclosure in order to quantify the total amount of the backflow. At the end, we performed a backflow study on a full-size airlock.

Table 1-2 Synthesis table showing parameters related to S. Kaissoun's study and our study

	Kaissoun	**Rida**
Type of pollutant	Gas	Gas, 5 μm aerosol
Numerical model	LES	SST-DES
Types of disturbance	Internal counter-current jet Internal and external parietal jets External moving obstacle	Internal counter-current jet Internal parietal jet
Type of study	Local quantification	Local quantification Global quantification
Type of enclosure	Small-size enclosure	Small-size enclosure Full-size airlock

JOURNAL OF NUCLEAR SCIENCE AND TECHNOLOGY
https://doi.org/10.1080/00223131.2021.2012288

ARTICLE

Experimental study of backflow air leakage through an opening from a depressurized enclosure

Zeinab Rida[a,b], Salima Kaissoun[a,b], Corinne Prevost[a], Thomas Gelain[a] and Eric Climent[b]

[a]Institut de Radioprotection et de Sûreté Nucléaire (IRSN), PSN-RES, SCA, Gif sur Yvette, France; [b]Institut de Mécanique des Fluides de Toulouse (IMFT) - CNRS, Université de Toulouse, Toulouse, France

ABSTRACT

In nuclear decommissioning and dismantling operations, a dynamic confinement is applied to all openings in order to prevent the transfer of pollutants outside depressurized enclosures and to insure the safety of workers. To guarantee an efficient dynamic confinement, ISO 16647 and ISO 17873 recommend to maintain a constant value for inward inflow velocity near the opening depending on the level of radioactive pollution hazard. The main purpose of this work is to identify possible conditions under which flow inversions near the opening may lead to gaseous pollutant leakage and then failure of the dynamic confinement. We aim at quantifying the amount of this backflow. Leakage from an experimental ventilated enclosure with a small opening on its frontal wall has been investigated. Laser flow visualizations and Particle Image Velocimetry (PIV) measurements showed that the presence of an additional turbulent jet flow in competition with the inward confinement flow is among the main causes leading to leakage through opening. The gas tracing technique has provided experimental data to quantify the pollutant backflow and allowed us to compare different scenarios. We conclude that a new criterion based on local aeraulic conditions near the opening is relevant to guarantee an efficient confinement.

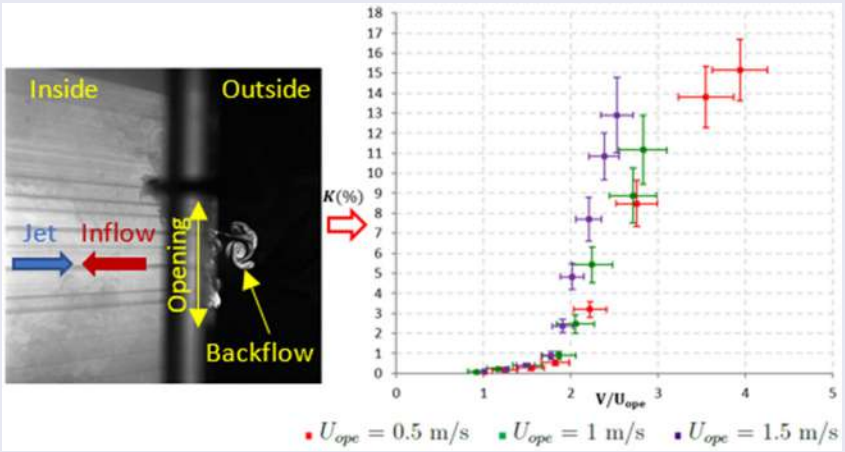

ARTICLE HISTORY
Received 1 September 2021
Accepted 22 November 2021

KEYWORDS
Dynamic confinement; flow inversion; turbulent jet; backflow pollutants

1. Introduction

Operations of decommissioning and maintenance in nuclear facilities require ventilated enclosures around contaminated equipment in order to prevent the leakage of radioactive materials towards the atmospheric environment. These enclosures are operated with a negative pressure relative to the room where they are installed. By means of extraction systems, air is sucked through openings that can be either inherent to the design of the enclosure or accidental, and generates directional airflow ensuring the dynamic confinement of hazardous material. However, due to some operating works and fluctuating differential pressure on both sides of the opening, local and unsteady flow inversions may occur, leading to the dispersion of contamination outwards, a phenomenon commonly referred to as backflow. Criteria for the conception of dynamic confinement through nominal or accidental openings in nuclear installations are presented in ISO 16647 standard [1] for decommissioning and maintenance operations and in ISO 17873 standard [2] for laboratories and factory scale. In the past, three values of inlet velocity at the opening were mentioned: 1.5 m/s for tritium, 1 m/s for plutonium 238 and 0.5 m/s for any other pollutants.

CONTACT Zeinab Rida zeinab.rida@irsn.fr PSN-RES, SCA, Gif sur Yvette Cedex, 91192France

However, the ISO 17873 standard recommends that each case must be investigated specifically, based on the potential risk of contamination and the influence of the aeraulic disturbances. ISO 16647 standard indicates the common values of criteria for an efficient confinement such as air direction, air velocity and depression level depending on the potential contamination risk. For example, areas with moderate air contamination potential have to impose an air velocity higher than 1 m/s near a calibrated opening orifice of 100 mm diameter. Areas with very high potential for atmospheric contamination are to be studied on a case-by-case basis. The current study follows the ISO standard recommendations to study each case specifically and focuses on the evaluation of the relevant criteria to guarantee an efficient dynamic confinement and then the safety of nuclear operations. To this aim, we need to identify and reproduce the aeraulic scenarios that may disturb the confinement inflow and possibly lead to backflow of a gaseous pollutant outside the ventilated enclosure through small openings. Then, we can predict and prevent them during operations in maintenance or dismantling sites. The disturbing jet is a model of accidental events that may occur near the opening during maintenance in dismantling airlocks (motion of an operator near the opening with a typical velocity of 1 m/s, blowing operations inside or outside the enclosure due to accidental disconnections of compressed air systems,. . .).

Ventilation systems are employed in many applications to maintain a directional airflow at the openings and thus to limit airborne contaminant dispersion. They are necessary with large-scale openings as large doors for different industrial purposes [3], for building entrances equipped with air curtains [4,5], for refrigerated storage spaces and cold rooms [6,7] and for hospital isolation rooms [8]. They have also been studied in food [9,10] and electronic industries [11] and for pharmaceutical applications. Tracer gas is used to calculate the dispersion rate in ventilated systems useful for the assessment of control room habitability [12]. Studies confirm that the directional airflow is disturbed by many unsteady events, such as door opening [13,14], human walking [15] and the presence of temperature gradients [16,17]. In the context of nuclear safety, many studies have been dedicated to quantifying the intensity and the kinetics of the propagation of polluting agents that result from the breakage of static or dynamic confinement in nuclear ventilated enclosures, for example, in the case of fume cupboards or glove boxes [18,19]. Tracing gas technique was used to calculate the dispersion rate in ventilated systems useful for the assessment of control room habitability [12]. Simulation method was established in order to predict the tritium behavior after the tritium leak event should happen in ventilated room [20].

Unlike most investigations on the aerodynamic confinement previously described that deal with large openings, the current study focuses on airflow dynamics through small openings, such as a rectangular slit whose hydraulic diameter does not exceed ten centimeters and where the initial air inflow is fully turbulent. Thanks to preliminary visualization tests, we have observed that the confinement flow directed from the outside towards the enclosure might be disturbed by an additional parallel or perpendicular flow created inside or outside the enclosure. This flow disturbance causes instabilities in the velocity field near the opening due to its sharp edge geometry and the turbulent nature of flows. To the best of our knowledge, this phenomenon occurring on small rectangular slit is not described yet in the literature because of the large number of possible configurations and the difficulties related to its quantification. In fact, the unsteady and three-dimensional nature of flow structures makes it very difficult to observe locally and to capture quantitatively the amount of pollutant released.

In this work, we designed a reduced size ventilated enclosure with a rectangular opening on its frontal wall as shown in Figure 1. In order to apply a dynamic containment, the enclosure is set under a negative pressure drop by means of a ventilation system that generates a directional inflow at the opening. Air enters the enclosure from the opening with a velocity U_{ope}. We control the extraction flowrate inside the enclosure in order to reach the desired velocity at the opening U_{ope} of 0.5 m/s, 1 m/s and

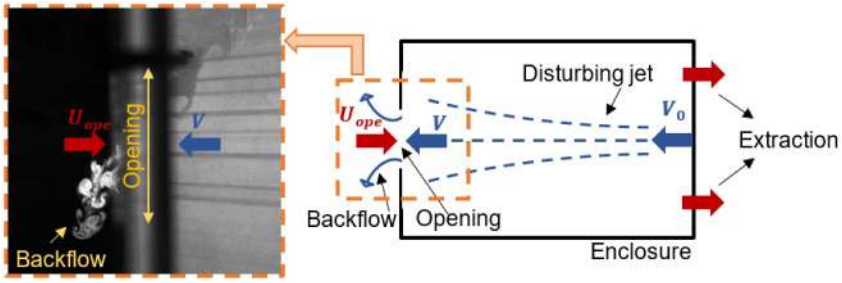

Figure 1. Scheme of the backflow scenario in a ventilated enclosure.

1.5 m/s, respectively. The perturbation is produced by a free jet of velocity V at the opening (two configurations are possible: countercurrent jet facing the opening or transverse jet). The direct competition between the inflow and the disturbing jet near the opening results in the backflow of pollutants from inside to outside the enclosure.

This paper is organized as follows: The first part is the description of the experimental setup and the methods used to measure the backflow phenomenon, namely, the visualization, the PIV, and the gas tracing techniques. The second part focuses on the qualitative results obtained from the visualization and the PIV, and finally, we comment on the quantitative results in terms of transfer coefficients. This paper closes with a conclusion and perspectives.

2. Description of experimental setup and measurement techniques

2.1. Experimental enclosure

The geometric characteristics and dimensions of the experimental enclosure have been chosen wisely. First, it should be small in comparison with the airlock workstations and without internal obstacles. Second, it must be adapted to accommodate turbulent jets far from the opening. Thus, an experimental ventilated enclosure chamber of a volume equal to 0.3 m^3 was built, as shown in Figure 2 (top). It is equipped with an airflow extraction circuit connected to a centrifugal fan.

The experimental model is a sealed and fully transparent PMMA (Plexiglass) enclosure with smooth walls, parallelepipedic shape and internal dimensions of 1.2 m $\times$ 0.5 m $\times$ 0.5 m. The enclosure depth (0.5 m) and width (1.2 m) have been carefully chosen to contain an internal additional turbulent jet located in front of the opening or perpendicular to it, to be in a fully developed regime when reaching the opening.

The enclosure is sketched with its different parts in Figure 2 (down). The front wall, of (1.06 $\times$ 0.36) m^2 area, is removable and transparent and has a thickness of 5 mm. A rectangular small opening is centered on the enclosure front wall and has a surface of (0.1 $\times$ 0.03) m^2 (the hydraulic diameter is equal to D_h = 46 mm) and a thickness of 5 mm. The rear wall is also removable for a simple access to the enclosure. It supports two identical units of square shape and dimensions (0.05 $\times$ 0.05) m^2, centered with respect to the median horizontal plane of the enclosure. They are connected to an airflow extraction circuit in order to ensure a homogenous internal pressure field and a directional inflow. The enclosure is depressurized by a centrifugal extraction fan (VSB-14 Plastifer) equipped with a 0–50 Hz frequency converter. The

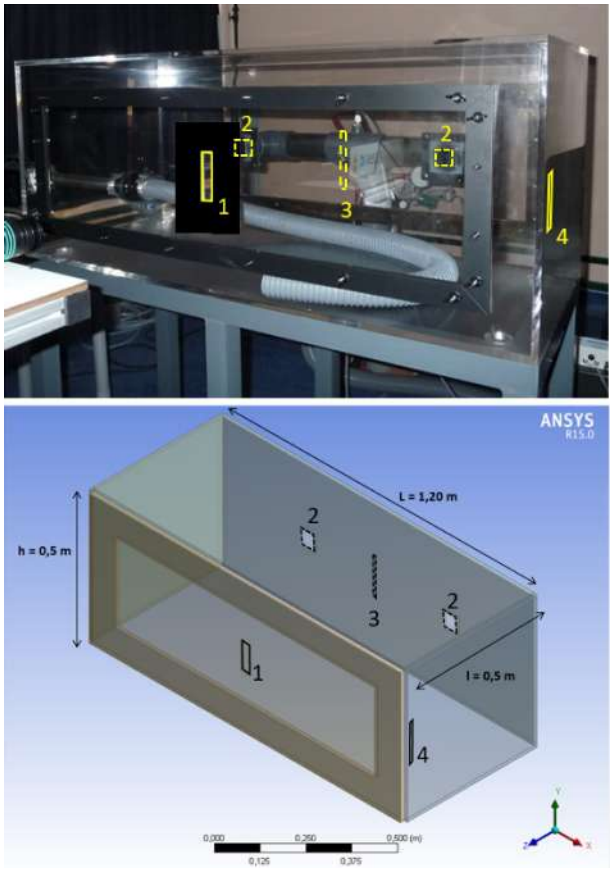

Figure 2. Top: Frontal view of the experimental enclosure showing the opening. Bottom: Sketch of the experimental enclosure with its different parts (CFX scheme). (1): opening, (2): extraction units, (3): countercurrent disturbance orifice and (4): parietal disturbance orifice.

extraction rates of the enclosure are fixed depending on the incoming flowrateimposed at the opening (the maximum flowrate is of the order of 100 $m^3.h^{-1}$). Nevertheless, we will focus our study on much lower flowrates, of the order of a few cubic meters per hour. The rear wall also contains a rectangular orifice of (0.1 $\times$ 0.01) m^2 centered with respect to the median horizontal and vertical walls of the enclosure and connected to an injection nozzle in order to produce an internal countercurrent turbulent jet injected towards the opening.

Apart from the frontal wall, the enclosure walls have a thickness of 12 mm, which ensures their mechanical resistance in the face of significant depression. Note that all the walls of the enclosure are sealed, except the front and rear walls. The right-hand side wall is equipped with a circular hole of 8 mm diameter for the tracer gas injection and a circular passage of 40 mm diameter for the extraction of the disturbance. It is also equipped with a rectangular orifice of (0.1 $\times$ 0.01) m^2 connected to an injection nozzle used in the case of internal parietal disturbing jets. Pressure taps are distributed over the enclosure wall and connected to a probe for the continuous monitoring of the depression inside the enclosure.

2.2. Generation of the flow perturbation

Our study aims to put into interaction two different flows: the flow passing through the opening due to the dynamic confinement of the enclosure and the aeraulic disturbance originating from a turbulent jet. Three types of aeraulic disturbances have been studied. Due to the enclosure dimensions, they reach the opening in a fully developed regime.

- The transverse disturbance is a jet flow propagating along the frontal wall and perpendicular to the direction of the inflow entering the opening. It may be located outside the enclosure in the case of an external transverse jet (Figure 3(a)) or inside the enclosure (injected from the side wall on the right) in the case of the internal transverse jet (Figure 3(b)).
- The countercurrent internal disturbance is a turbulent free jet originating from the rear wall facing the inflow at the opening. The two flows are in opposite directions at the opening (Figure 3(c)).

Devices producing the internal disturbance are integrated into the system as a closed-circuit (shown in red on Figure 4) in order to keep the enclosure under negative differential pressure.

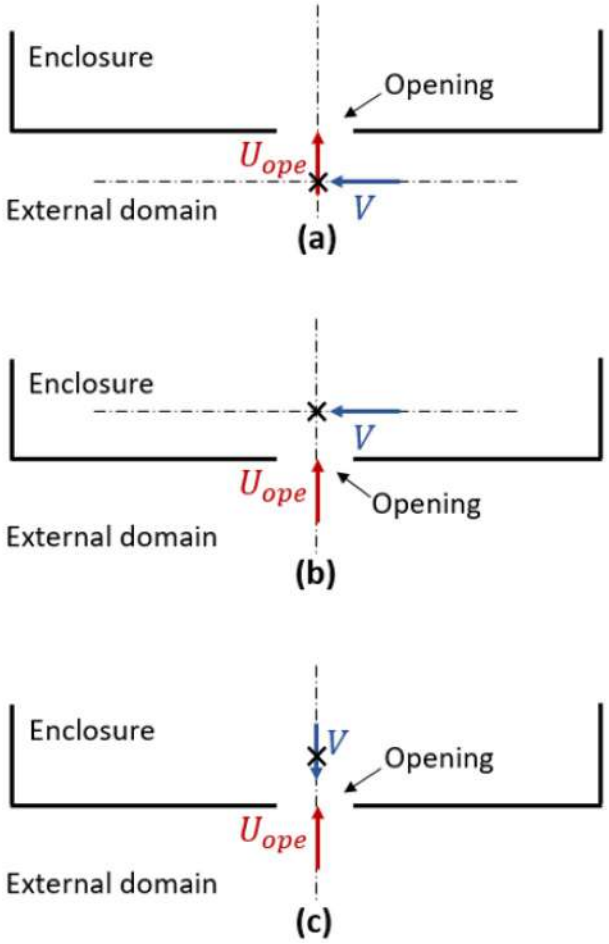

Figure 3. Sketches of the disturbance flow directions in the case of external transverse jet (a), internal transverse jet (b) and internal countercurrent jet (c). The symbol " × " in each sketch corresponds to the measurement location of the velocity V.

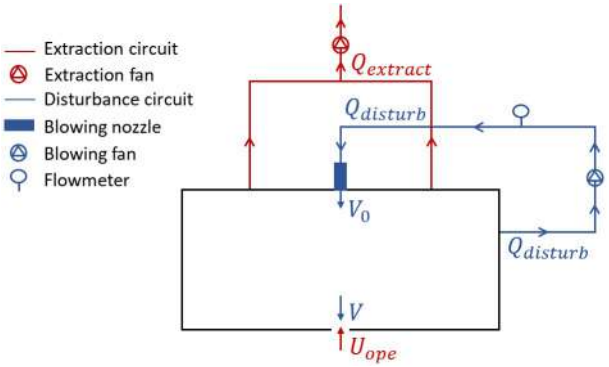

Figure 4. Scheme of the closed circuit of the internal countercurrent disturbing jet.

A centrifugal fan is connected through a duct to the side wall in order to continuously extract part of the flow, which is reinjected into the enclosure through the injection nozzle (0.1×0.01) m^2 located on the rear wall. A valve is added between the fan and the nozzle in order to vary the disturbance flowrate inside the enclosure. The fan can reach a maximum flowrate of about 130 $m^3.h^{-1}$.

2.3. Visualization technique

Visualization methods are applied to observe the flow inversions on both sides of the opening in the presence of a countercurrent jet flow. The double pulsed laser/CCD camera facility is set in order to first visualize the flow by laser tomography images and second to obtain the velocity fields near the opening from PIV post-processing. Particle image velocimetry (PIV) is a non-intrusive method, which consists in capturing two images in two separate frames and performing multistep cross-correlation analysis to obtain the Eulerian velocity fields of the flow [21] on a cartesian grid.

A thin (1–3 mm) light sheet is oriented vertically towards the opening axial plane. Acquisition devices are presented in Figure 5. The gas phase is seeded with smoke oil particles of 1 micron diameter, as fluid flow tracer particles, produced by SAFEX F2001 Plus particle generator supplied by Dantec Dynamics. 1 micron particles are very small and they follow the gas streamlines. They have the same velocity as the gas and are used as tracers for PIV applications. The light source is a dual-cavity double Nd:YaG pulsed laser emitting at 532 nm, with a maximum energy of 800 mJ per pulse and a maximum frequency of 15 Hz. The image acquisition equipment includes a Flowsense EO 4 M digital camera equipped with a CCD sensor of 2048 × 2048 pixels and an objective of 50 mm (pixel size is 7.4 μ m). The camera buffer has a maximum acquisition frequency of 10 Hz and is triggered in synchronization with each pulse of the laser. The control, the synchronization of the laser-camera system and the post-

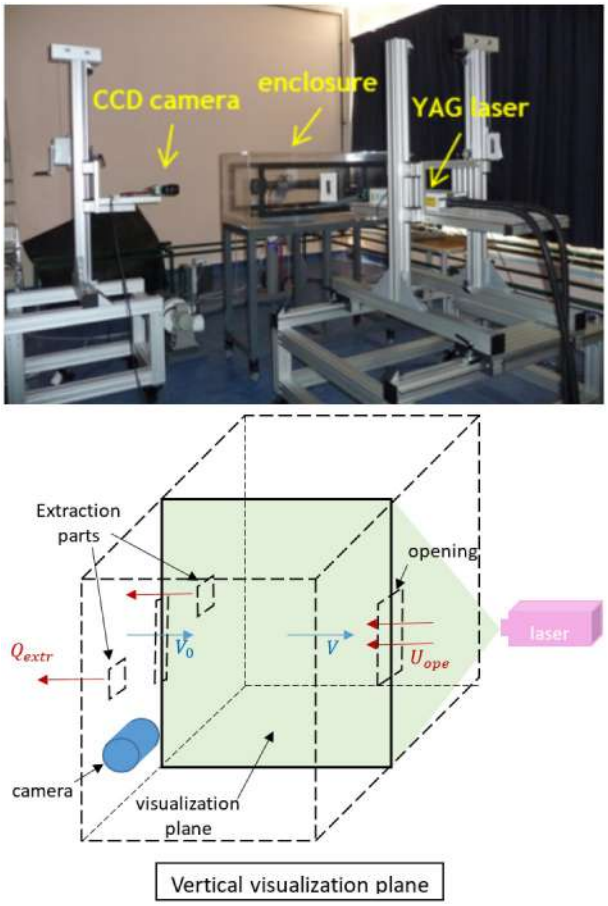

Figure 5. Top: Acquisition devices required for the visualization and PIV measurements. Bottom: Scheme of visualizations and PIV devices in the vertical plane on the enclosure for a countercurrent disturbance.

processing of images are carried out using the Dynamic Studio V5 software, which provides instantaneous 2D velocity vector fields in the illuminated cross-section of the flow.

2.4. Determination of the backflow factor

In order to quantify the amount of gaseous pollutant backflow at the opening, a characteristic factor K is defined [22]. It is the ratio between the mean tracer concentration in the air/tracer mixture backflowed locally at the opening outside the enclosure $\overline{C_{out_{eq}}}$ and the tracer concentration in the air/tracer mixture present inside the enclosure $\overline{C_{in_{eq}}}$ at equilibrium (measured at the extraction outlet). This coefficient is expressed as a percentage and is defined by Equation (1),

$$K = \frac{(\overline{C_{out_{eq}}} - C_{air})}{(\overline{C_{in_{eq}}} - C_{air})}, \quad (1)$$

where C_{air} is the concentration of the gaseous tracer naturally present in ambient air (5 $\pm$ 2 ppm for the case of helium). The concentrations are expressed in volume parts per million (ppm.v). The backflow factor K gives a common reference to the quantity of backflowed pollutant and consequently allows us to compare all tests among one another. The backflow factor K is directly related to the dynamic containment efficiency E by Equation (2),

$$E = 1 - K. \quad (2)$$

We stress that, in nuclear safety, a transfer coefficient k (s/m^3) (Equation (3)) is commonly used to quantify the backflow phenomena that occur during a dynamic containment.

$$k(s/m^3) = \frac{(\overline{C_{out_{eq}}} - C_{air})}{q_0}, \quad (3)$$

where q_0 is the volume flowrate of the gas tracer injected into the enclosure.

Additionally, we introduce a non-dimensional aeraulic parameter, allowing us to characterize the aeraulic conditions at the opening. It is defined as the ratio between the disturbance velocity at the opening V and the local flow of dynamic confinement at the opening U_{ope}: V/U_{ope}. We note that U_{ope} and V are measured independently: U_{ope} is measured when the disturbance flow is stopped and V is measured when the air extraction is stopped. We will show that, contrary to the criteria used commonly in the ISO standards (minimum velocity at the opening and/or minimum pressure in the enclosure), the dimensionless V/U_{ope} ratio is more appropriate as a relevant parameter to characterize the onset of the pollutant backflow at the opening regardless of the type of aeraulic disturbance.

In the following results section, we comment on the evolution of the backflow factor K (%) versus of this dimensionless aeraulic parameter V/U_{ope}.

2.4.1. Determination of the characteristic flow velocities

2.4.1.1. Determination of the velocity at the opening, U_{ope}. The extraction flowrate applied to the enclosure Q_{ext} and consequently the flow velocity at the opening U_{ope} are determined using the gas tracing technique. It consists of three parts: the injection circuit, the detection device and the acquisition system. The principle is shown schematically in Figure 6(top). Initially, a constant and controlled tracer gas flow q_0 $(Nl.h^{-1})$ is injected continuously into the enclosure from a compressed pure helium reservoir equipped with a BROOKS 5850E volume flowmeter (0–45 $Nl.h^{-1}$).

At equilibrium, the concentration $\overline{C_{in_{eq}}}$ of air/tracer is homogenous inside the enclosure and is measured in the extraction circuit as follows. An air/tracer sample is pumped to an Alcatel model ASM 102 mass spectrometer for analysis. A LabVIEW acquisition system insures the continuous monitoring of the helium concentration $\overline{C_{in_{eq}}}$ during the experiment.

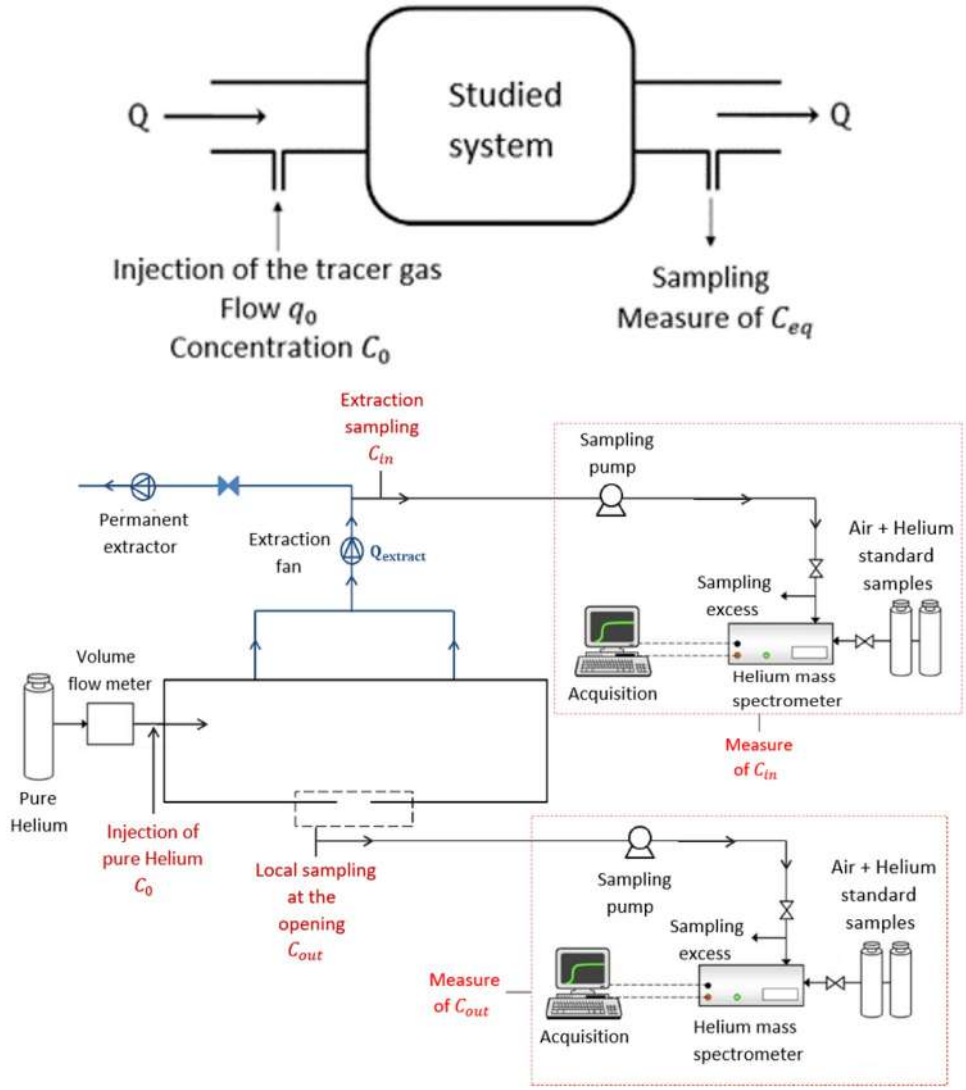

Figure 6. Top: Determination of the airflow through a ventilated system. Bottom: Scheme of the measurement of $\overline{C_{in_{eq}}}$ and $\overline{C_{out_{eq}}}$ using the gas tracing technique.

The extraction flowrate from the enclosure Q_{ext} is then obtained using tracer mass balance at equilibrium (Equation (4)),

$$Q_{ope}C_{air} + q_0C_0 = Q_{ext}\overline{C_{in_{eq}}}, \tag{4}$$

with Q_{ope} being the air flowrate entering through the opening ($m^3.h^{-1}$), q_0 the flowrate of injected gas ($m^3.h^{-1}$), $\overline{C_{in_{eq}}}$ the tracer concentration measured in the system at equilibrium (ppm.v) and Q_{ext} the gas extraction flowrate in the system ($m^3.h^{-1}$). C_{air} is the concentration of the tracer gas naturally present in the air ($C_{air} = 5 \pm 2$ ppm when the tracer gas is helium) and C_0 is the tracer injection concentration (ppm).

Since air admission into the enclosure is only possible through the opening (assuming negligible leaks) and q_0 is negligible compared to Q_{ope} and Q_{ext}, the flow velocity at the opening U_{ope} could be deduced from the extraction flowrate from the enclosure Q_{ext} ($m^3.h^{-1}$), which is obtained from Equation (5),

$$Q_{ext} = Q_{ope} = U_{ope} \times S, \tag{5}$$

where S (m^2) is the surface of the opening.

2.4.1.2. Determination of the resulting disturbance velocity V at the opening. The aeraulic parameter related to the perturbation flow is the resulting velocity V at the opening. It results from the spatial decay of the turbulent jet velocity of the disturbance along its axis. The latter is measured locally at the opening in the median horizontal plane. The position of the measuring point varies from one disturbance to another (internal/external wall jet, internal countercurrent free jet). For the internal countercurrent free jet, the measuring point is inside the enclosure in the plane perpendicular to the frontal wall at 3 cm from the opening. For the case of an internal transverse jet, it is located inside the enclosure at the plane parallel to the frontal wall at 3 cm from the opening. For the case of an external transverse jet, it is located outside the

enclosure in the plane parallel to the frontal wall at 3 cm from the opening. The measurement is carried out using an hot-wire sensor of KIMO VT210TF type. The position of the hot-wire sensor used for the measurement of the velocity V for each disturbance type is denoted " × " in Figure 3. Note that these velocities V are measured in the absence of the frontal wall of the enclosure for the case of the internal countercurrent free jet and in the presence of the frontal wall of the enclosure for the case of the internal and external transverse jets. Indeed, for the case of the countercurrent disturbing jet, it was difficult to perform velocity measurements with the presence of the frontal wall. The actual velocity values with the presence of the frontal wall should be lower than our measured values without the frontal wall but more representative of the real situation.

2.4.2. Determination of $\overline{C_{in_{eq}}}$ and $\overline{C_{out_{eq}}}$ using the gas tracing technique

The measurement of $\overline{C_{in_{eq}}}$ and $\overline{C_{out_{eq}}}$ is carried out using the gas tracing technique as shown in Figure 6 (down).

2.4.2.1. Determination of $C_{in_{eq}}$. A first sampling probe is located downstream in the extraction of the enclosure, at a convenient distance to obtain a homogeneous air/helium mixture. A mass spectrometer is added to measure the helium concentration of the air/helium gas mixture in the enclosure. Once equilibrium of the helium concentration is reached in the enclosure and then in the extraction ducts, the signal remains steady and the average equilibrium value of the helium concentration inside the enclosure is noted $\overline{C_{in_{eq}}}$ (ppm). This concentration is measured before the generation of the disturbance.

2.4.2.2. Determination of $\overline{C_{out_{eq}}}$. The second measurement is an average of many samplers; it records the helium concentration of the air/helium gas mixture backflowed outside the enclosure near the opening, due to the disturbance. The number and the spatial arrangement of samplers located on the periphery of the opening are optimized in order to capture the backflowed gas tracer for each disturbance while preventing the promotion of the backflow due to their presence. In the case of countercurrent perturbation, we added 16 samplers of 3 mm diameter placed on the frontal wall at 3 mm away from the edges of the opening, and 3 samplers uniformly spaced and located in front of the opening at 2.5 cm outside the enclosure, as shown in Figure 7. In this case, the analysis of the backflowed gas mixture concentration is carried out using an Alcatel model ASM100 mass spectrometer and gives a fluctuating signal. The temporal mean backflowed helium concentration over the samplers is noted $\overline{C_{out_{eq}}}$.

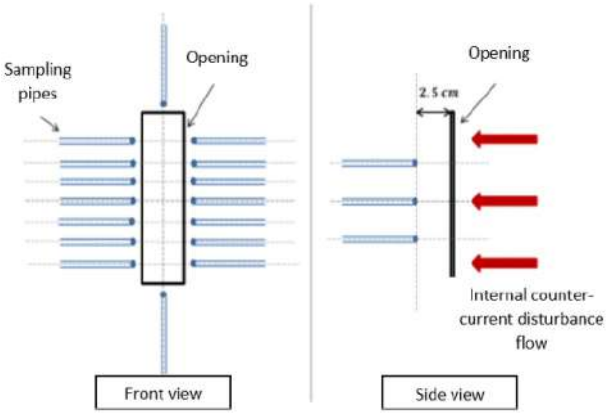

Figure 7. Scheme of the frontal and side views of the samplers positions around the opening.

2.4.3. Estimate of uncertainties

The $U_{r(K)}$ uncertainty is an expanded relative uncertainty, expressed as a percentage, with a coverage factor of 2 corresponding to 95% confidence interval.

The expanded relative uncertainty on the backflow factor K and the ratio V/U_{ope} is given by Equations (6) and (7), respectively,

$$U_{r(K)} = \pm 2\sqrt{\left[\frac{U_{r(\Delta C_{ineq})}}{2}\right]^2 + \left[\frac{U_{r(\Delta C_{outeq})}}{2}\right]^2}, \quad (6)$$

$$U_{r(V/U_{ope})} = \pm 2\sqrt{\left[\frac{U_{r(U_{ope})}}{2}\right]^2 + \left[\frac{U_{r(V)}}{2}\right]^2}. \quad (7)$$

The origins of uncertainties for $\Delta C_{in_{eq}}$ and $\Delta C_{out_{eq}}$ are the temporal drift of the spectrometers between two calibrations, the uncertainty of the instrumentation (spectrometer/acquisition/software unit), the uncertainty associated with the standard mixtures of air/helium bottles and the dispersion of the sampled concentration from the mean value. The uncertainty related to U_{ope} is based on the uncertainty of the injection flowmeter and $\Delta C_{in_{eq}}$. The uncertainty related to V is based on the uncertainty of the hot wire anemometer. Uncertainties will be added to plots with error bars.

3. Observation of leakage and flow measurements

Experiments presented below highlight the competition between the existing air inflow at the opening and the turbulent jet created outside or inside the enclosure, which induces unsteady flow dynamics in the vicinity of the opening. First, we present the results obtained for an external transverse jet flow and then those obtained for an internal countercurrent jet flow. In both cases, the confinement inflow has been set at

Table 1. Velocities V_0 at the outlet of the nozzle and V at 3 cm from the opening for each disturbance.

Countercurrent internal free jet		Internal transverse wall jet		External transverse wall jet	
V_0 (m/s)	V (m/s)	V_0 (m/s)	V (m/s)	V_0 (m/s)	V (m/s)
1.8	0.5	6.7	1.9	5.8	1.7
3.2	0.9	8.4	2.6	9.8	2.5
5.5	1.6	10.5	3.0	14.1	3.8
7.7	2.1	13.3	3.6	17.4	4.6
9.5	2.8	15.5	4.1	20.1	5.8
11.6	3.2	17.9	4.6	24.0	6.9
14.1	3.9	21.2	5.4	25.8	7.5

the opening to a level corresponding to the velocity U_{ope} = 1 m/s (mean extraction flowrate of 10.8 $m^3.h^{-1}$).

Table 1 shows the velocities V_0 at the outlet of the nozzle for each disturbance and their corresponding velocities V at 3 cm from the opening. These values are strictly used to plot the evolution of the backflow factor K(%) in section 4.

3.1. Visualization of the backflow

3.1.1. External transverse wall jet

Considering the case of an interaction between the confinement air flow and an external transverse turbulent jet flow, two experimental campaigns have been conducted. The injection velocity of the perturbation jet from the nozzle was fixed to V_0 = 25.5 m/s outside the enclosure. Two distances between the opening center and the injection nozzle were chosen: 45 cm and 24 cm. In this way, the turbulent jet reaches transversally the opening with two velocities, V = 5 m/s and V = 6.8 m/s respectively. These two values were measured at the opening central point by a hot-wire anemometer without any extraction flowrate in the enclosure. Figure 8 shows the behavior of the gas tracer at the opening due to the interaction between the confinement inflow and the external transverse turbulent jet for each flow velocity, on a vertical plane at the opening outside the enclosure. The cropped visualization field is a (16 × 16) cm^2 square. According to the corresponding flow visualization, leakage is detected in both cases. While comparing Figure 8(a,b), we found that more vigorous vortices are observed in the case where the injection nozzle is located closer to the opening Figure 8(b), hence when V is higher. We should mention that the backflow phenomenon has an intermittent behavior. The tracer diffuses outside the enclosure near the opening, and then part of it is taken back to the inside of the enclosure.

3.1.2. Internal countercurrent perturbation

In this case, we show the interaction between the initial airflow at the opening and four configurations of internal countercurrent turbulent jets

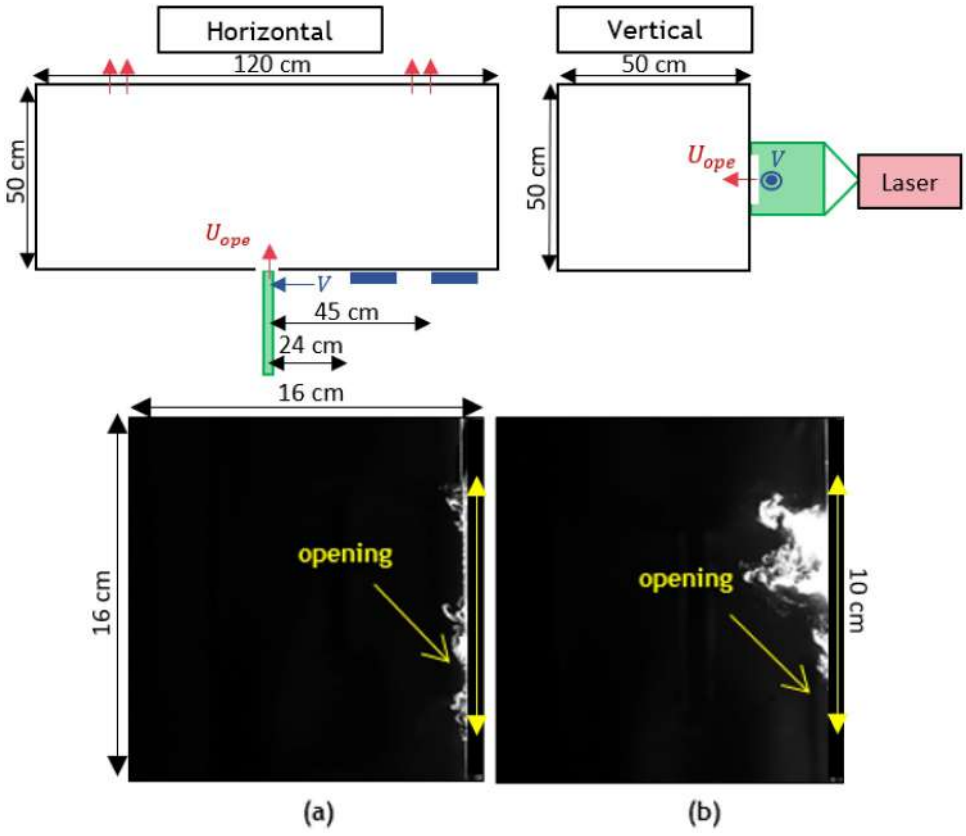

Figure 8. Top: Schemes of the external wall jet perturbation in the horizontal and vertical planes. Bottom: Laser tomography visualization of tracer leakage in the vertical plane outside the enclosure in the case of external transverse jet of velocity: (a) V = 5 m/s, (b) V = 6.8 m/s for U_{ope} = 1 m/s.

corresponding to three velocities at the nozzle exit that are V_0 = 3 m/s, 6 m/s, 8.4 m/s and 11.7 m/s, respectively. The countercurrent internal jet disturbance was generated from the nozzle facing the opening inside the enclosure as described in section 2.2 Figure 9 illustrates instantaneous laser tomographic visualizations of the flow tracer in the median vertical plane of the opening. Note that the inside of the enclosure is at the left of each figure, while the outside of the enclosure is at the right of each figure. The visualization zone corresponds to a surface of (30 × 30) cm^2.

We note that for a turbulent jet of 3 m/s velocity at the nozzle exit, as shown in Figure 9(a), there is no leakage of the tracer to the outside of the enclosure. The external air continues to enter the enclosure through the opening, resulting in a small region free of tracer inside the enclosure near the opening. The dynamic confinement succeeds in preventing gas backflow. While applying a jet with a velocity of 6 m/s as shown in Figure 9(b), the leakage of the tracer to the outside of the enclosure starts to occur: we observe vortex shedding close to the opening. This backflow phenomenon appears in the form of random puffs with resumption of the majority of the tracer to the inside of the enclosure. The dynamic confinement efficiency starts to break up. For a higher velocity of 8.4 m/s as shown in Figure 9(c), there is a continuous leakage of the tracer to the outside of the enclosure

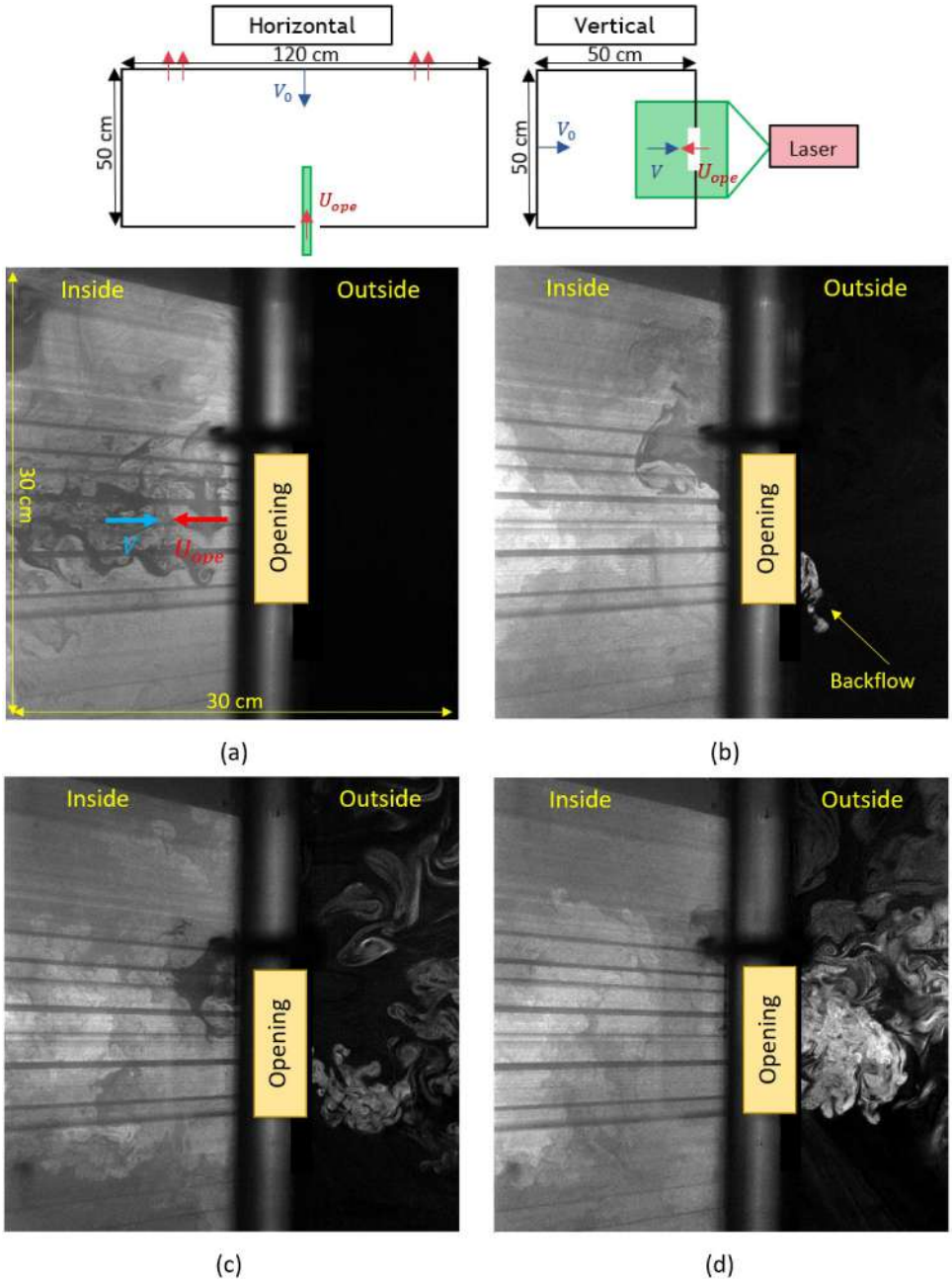

Figure 9. Top: Schemes of the internal countercurrent disturbance in the horizontal and vertical planes. Bottom: Laser tomography visualization of tracer leakage at the vertical median plane at the opening in the case of an internal countercurrent jet velocity: (a) V_0 = 3.2 m/s, (b) V_0 = 6 m/s, (c) V_0 = 8.4 m/s and (d) V_0 = 11.7 m/s for U_{ope} = 1 m/s.

with strong vortex shedding at the opening. While increasing the velocity to 11.7 m/s as shown in Figure 9(d), the continuous dispersion of the tracer to the outside of the enclosure is enhanced. The dynamic confinement fails to protect the environment outside the enclosure in these cases ((c) and (d)).

3.2. Flow velocity measurements

3.2.1. Internal countercurrent perturbation

PIV measurements presented here show the interaction between the confinement inflow and an internal countercurrent turbulent jet, at the vertical median plane of the opening inside the enclosure. Four configurations of nozzle jet velocities V_0 (3.2 m/s, 6 m/s, 8.4 m/s and 11.7 m/s) were studied. The time between two laser pulses for each configuration is set to Δ t = 1 *ms*. The inter-correlation algorithm applies an adaptive PIV method with a grid step size of 64 × 64 pixels, a minimum interrogation area size of 64 × 64 pixels and a maximum interrogation area size of 128 × 128 pixels. A statistical average is carried out on 400 images for each configuration of the flow and their corresponding mean velocity fields in the vertical median plane of the opening are shown in Figure 10.

For a countercurrent turbulent jet velocity V_0 = 3.2 m/s (Figure 10(a)), the mean flow inside and outside the enclosure near the opening is oriented horizontally towards the inside of the enclosure. The velocity near the opening inside the enclosure has a value close to 0.5 m/s, and outside the enclosure, it is about 0.1 m/s. In this case, there was no backflow outside the enclosure as already observed in the corresponding visualization fields in Figure 9(a). For a countercurrent turbulent jet velocity V_0 = 6 m/s as shown in Figure 10(b), the direction of the mean flow

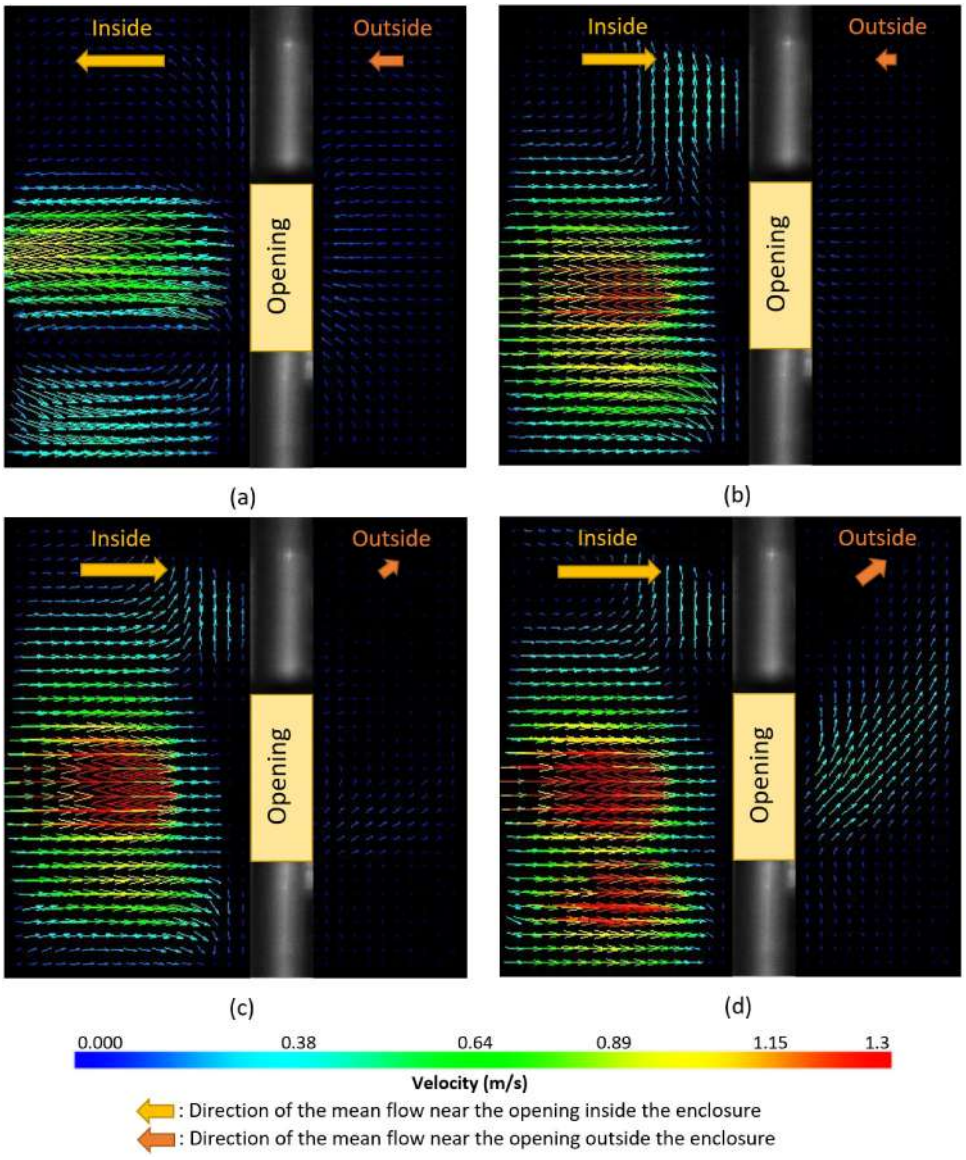

Figure 10. Time-averaged velocity fields in the vertical median plane of the opening inside and outside the enclosure representing the interaction between the inflow and an internal countercurrent disturbance jet. Velocity at the nozzle outlet: (a) V_0 = 3.2 m/s, (b) V_0 = 6 m/s, (c) V_0 = 8.4 m/s and (d) V_0 = 11.7 m/s for U_{ope} = 1 m/s.

near the opening inside the enclosure is horizontally towards the outside of the enclosure with a mean velocity of about 0.6 m/s. For the region outside the enclosure, the direction of the mean flow near the opening is towards the inside of the enclosure and is about 0.07 m/s. Here, the corresponding visualization fields indicate the occurrence of weak tracer backflow (Figure 9(b)), but the majority of the tracer is taken back to the inside of the enclosure. For V_0 = 8.4 m/s (Figure 10(c)), the mean flow direction inside the enclosure is towards the outside of the enclosure and of the order of 0.9 m/s. For the region outside the enclosure, the mean flow is towards the outside of the enclosure and has a mean velocity of 0.12 m/s. In this case, the countercurrent turbulent jet is strong enough to overcome the dynamic air inflow and leads the tracer to the outside of the enclosure. As we increase the countercurrent turbulent jet velocity V_0 to 11.7 m/s as shown in Figure 10(d), the mean velocity field is towards the outside of the enclosure and is of the order of 1 m/s inside the enclosure and 0.3 m/s outside the enclosure. There is a continuous dispersion of tracer outside the enclosure.

Figure 11 shows the instantaneous velocity fields in the vertical median plane corresponding to the interaction between the inflow and the internal countercurrent disturbance jet. These velocity fields show the presence of vortices near the opening inside and outside the enclosure. These vortices highlight the turbulence created due to the competition between the inflow and the disturbing jet. Vortices are more likely to occur inside the enclosure for the disturbing jet velocities of V_0 = 3.2 m/s and V_0 = 6 m/s. For these cases, we did not detect a continuous leakage phenomenon outside the enclosure. However, for the case of disturbing jet velocities of V_0 = 8.4 m/s and V_0 = 11.7 m/s, vortices start to occur outside the enclosure, where the continuous leakage exists. When backflow occurs, the leakage is produced by the presence of vortices outside the enclosure. This phenomenon is

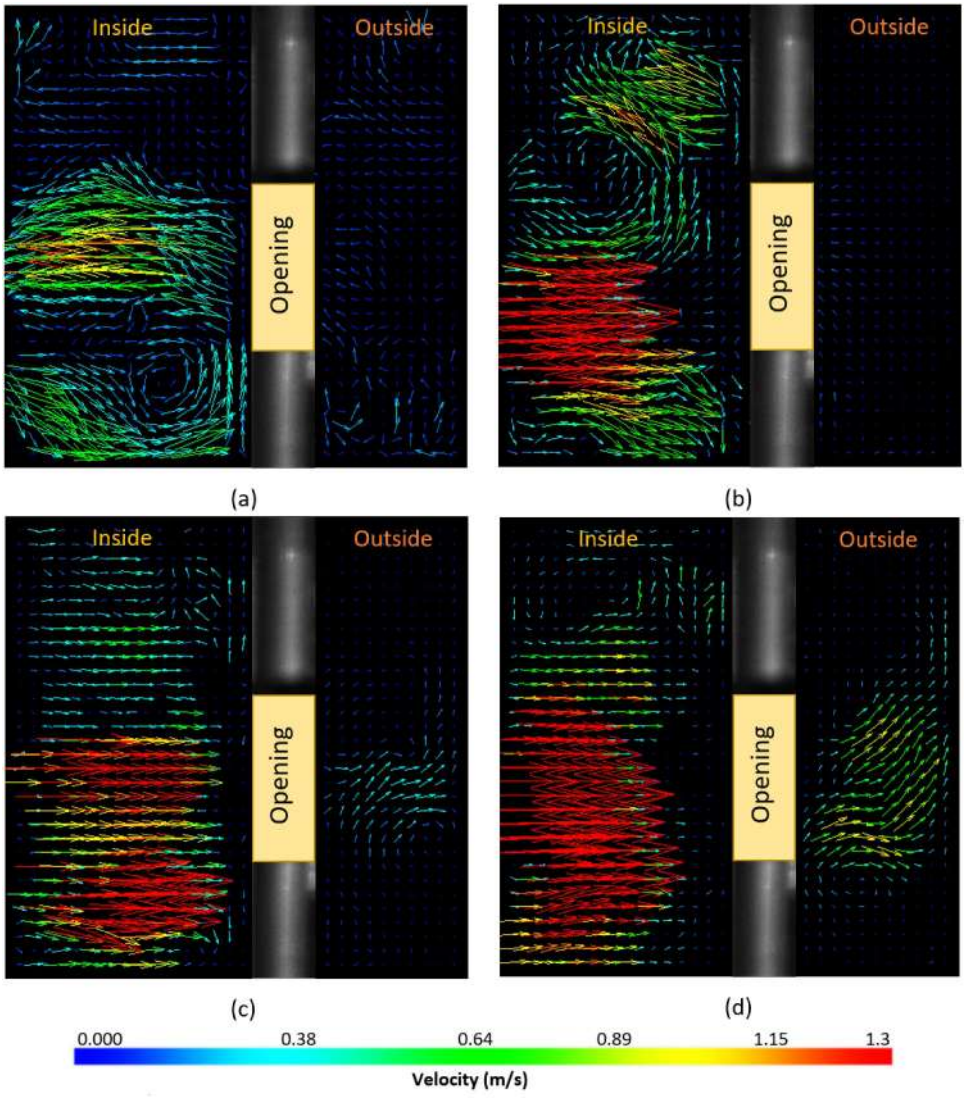

Figure 11. Instantaneous velocity fields in the vertical median plane of the opening inside and outside the enclosure representing the interaction between the inflow and an internal countercurrent disturbance jet. Velocity at the nozzle outlet: (a) V_0 = 3.2 m/s, (b) V_0 = 6 m/s, (c) V_0 = 8.4 m/s and (d) V_0 = 11.7 m/s for U_{ope} = 1 m/s.

highly intermittent and both internal and external vortices disappear in Figure 10 due to the time-averaging procedure.

4. Comments on backflow measurements

In the following, we comment on pollutant dispersion in terms of the backflow factor evolution. However, we assumed in our study that C_{air} is negligible compared to $\overline{C_{in_{eq}}}$ (typically $C_{air}/\overline{C_{in_{eq}}}$ is less than 1%) and that the flowrate of the injected tracer q_0 is negligible compared to the extraction flowrate of the enclosure Q_{ext} (typically, q_0/Q_{ext} is less than 0.1%). Based on these assumptions, the transfer coefficient k (s/m^3) can be directly calculated from our backflow factor K using Equation (8),

$$kQ_{ext} = K. \tag{8}$$

The evolution of the backflow factor K (%) according to V/U_{ope} has been studied for three different configurations of the disturbance jet: internal countercurrent free jet, internal or external transverse wall jet. Three flowrates through the opening, corresponding to flow velocities U_{ope} equal to 0.5 m/s, 1 m/s and 1.5 m/s, have been tested for a range of disturbing velocities at the opening V ranging from 1.3 m/s to 9 m/s depending on the direction of disturbance. The repeatability of the measurements has been verified: each measurement point of the backflow evolution was systematically obtained from an average over two repetitions. The reproducibility of the results was also verified over different days during which the experimental conditions varied slightly (variation of the ambient temperature, recalibration and control of the drift of mass spectrometers, restart of all measuring devices, repositioning of the measuring points, etc.). The detection threshold of the backflow is defined when a minimum helium concentration of air/helium mixture detected at the opening, outside the enclosure, is $\overline{C_{out_{eq}}} - C_{air}$ = 1 ppm ($\pm$ 50%). The minimum backflow factor, which can be measured, is of the order of K = 0.1% ($\pm$ 50%).

4.1. Countercurrent internal free jet disturbance

The evolution of the backflow factor K (%) as a function of V/U_{ope} is studied in the case of the disturbance produced by a countercurrent internal free jet for three inflows at the opening: U_{ope} = 0.51 m/s ($\pm$ 7.72%), U_{ope} = 1.04 m/s ($\pm$ 18.14%) and U_{ope} = 1.56 m/s ($\pm$ 5.4%), for a range of disturbing flowrates at the opening corresponding to V between 1.5 m/s and 4 m/s.

The evolution of the backflow factor K (%) as a function of the dimensionless parameter V/U_{ope} is presented in Figure 12 for the different flowrates entering

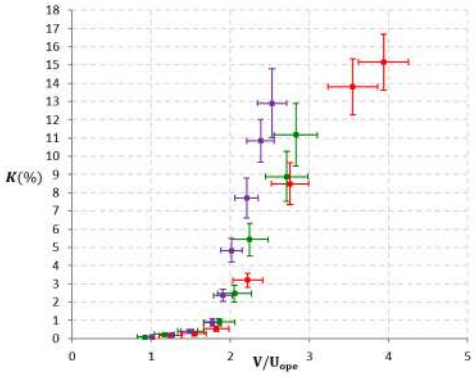

$U_{ope} = 0.5$ m/s $U_{ope} = 1$ m/s $U_{ope} = 1.5$ m/s

Figure 12. Evolution of the backflow factor K (%) as a function of V/U_{ope} for an internal countercurrent free jet disturbance.

at the opening. It can be observed that regardless of the magnitude of confinement velocity at the opening, the backflow phenomenon occurs for a perturbation velocity of the same order as U_{ope} corresponding to the ratio $V/U_{ope} \approx 1$. We can also note that the three evolution curves are overlapped for $V/U_{ope} \leq 1.8 \pm 0.2$. Beyond this value, for $2 \leq V/U_{ope} \leq 4$, the measuring points are progressively scattered.

For the three cases, the part of the graph corresponding to $V/U_{ope} \leq 2$ clearly shows that the occurrence of the backflow phenomenon is determined by a critical threshold V/U_{ope}, within uncertainties, regardless of the flowrate of the dynamic confinement imposed on the opening. Note that in this part of the evolution, the backflow factor does not exceed 1%.

4.2. Internal transverse wall jet disturbance

In Figure 13, the evolution of the backflow factor K (%) as a function of the dimensionless aeraulic parameter V/U_{ope} in the case of a transverse internal wall jet disturbance is presented for three inflows at the opening: U_{ope} = 0.52 m/s ($\pm$ 5.4%), U_{ope} = 1.03 m/s ($\pm$ 6.4%) and U_{ope} = 1.52 m/s ($\pm$ 5.58%), for a range of disturbance velocities V at the opening ranging from 1.3 m/s to 8 m/s.

The onset of backflow is observed for the three flowrates at V/U_{ope} = 3.5 $\pm$ 0.2 with a good overlap beyond that point. Under these flow conditions, the occurrence of leakage at the opening and dispersion of the pollutant are adequately rationalized by V/U_{ope} for $V/U_{ope} \leq 4$. Beyond this value, the curves are no longer overlapping and there are non-negligible differences in the backflow intensity. For example, for the same ratio V/U_{ope} = 5.2, the backflow factor is more important when the flowrate is smaller, which means that the measured quantity of pollutant outside the enclosure is more effective.

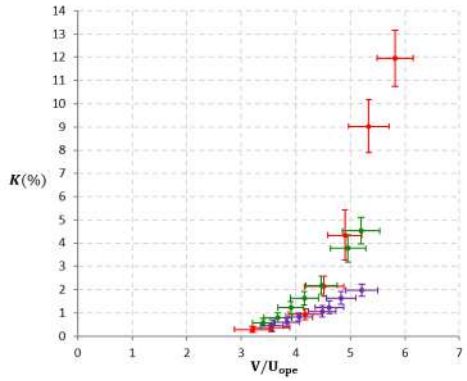

• $U_{ope} = 0.5$ m/s • $U_{ope} = 1$ m/s • $U_{ope} = 1.5$ m/s

Figure 13. Evolution of the backflow factor K (%) as a function of V/U_{ope} for the case of internal transverse wall jet disturbance.

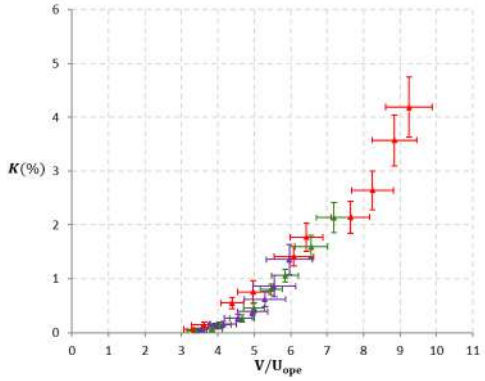

▲ $U_{ope} = 0.5$ m/s ▲ $U_{ope} = 1$ m/s ▲ $U_{ope} = 1.5$ m/s

Figure 14. Evolution of the backflow factor K (%) as a function of V/U_{ope} for transverse external wall jet disturbance.

4.3. External transverse wall jet disturbance

The evolution of the backflow factor K (%) as a function of V/U_{ope} is studied for the case of the transverse external wall jet for three inflows at the opening corresponding to U_{ope} = 0.49 m/s (± 8.4%), U_{ope} = 1.03 m/s (± 5.3%) and U_{ope} = 1.55 m/s (± 8.3%). The range of disturbance velocities at opening V that we tested is between 1.6 m/s and 9 m/s and corresponds to the results of Figure 14.

We can clearly observe that the three sets of data for the backflow factor K (%) are overlapped (within uncertainties of experimental measurements) for the range of studied experimental conditions. The onset of the backflow phenomenon is around V/U_{ope} = 3.5 ± 0.25. We can conclude that the effect of aeraulic opening conditions on the backflow factor is adequately characterized by the dimensionless parameter V/U_{ope} over the whole range of V/U_{ope} that we studied.

As we can expect, the external disturbance jet presents much less backflow compared to the internal disturbance configuration. Indeed, in the case of internal jets, the disturbance comes from a closed aeraulic network connected to the enclosure filled with helium during the test. At equilibrium, the jet produced by this aeraulic network is charged with helium, which implies that the tracer concentration in the internal zone near the opening remains homogeneous over the duration of the test. In the case of an external perturbation, the jet is made of ambient air. Therefore, the external area close to the opening is continuously swept with fresh ambient air free of helium, which reduces the leakage of pollutants compared to internal perturbations.

5. Conclusion

The transfer of gaseous pollutants outside a ventilated enclosure through existing or accidental openings is commonly referred to as backflow. This phenomenon is more likely to occur for enclosures under low pressure compared to their external environment, such as maintenance or dismantling airlocks implemented in nuclear facilities. Because very few investigations were carried out on characterizing flow inversion phenomena at rectangular slits in depressurized enclosures, the approach that we adopted was to reproduce the phenomenon in different controlled configurations and to measure the intensity of gas tracer as a surrogate for pollutant dispersion. To this aim, we performed experiments on an experimental enclosure to which an aeraulic disturbance system was added to generate internal or external disturbances. It has been observed that an additional turbulent flow (typically a jet) either inside the enclosure or outside can cause leakage at the opening.

Visualization techniques offer the opportunity to detect the leakage of gas tracer in the presence of turbulent jets and visualize the inversion due to unsteady vortices near the opening. The PIV technique provides information on the local flow structure and magnitude of the velocity of the turbulent flow near the opening in the presence of the disturbance jet. It also gives quantitative information on the velocity V of the perturbation flow near the opening. Our aim is to determine the conditions that are prone to generate backflow for different types of disturbances. The observations help to conclude that two conditions must be met in order to yield significant backflow phenomena at openings: the presence of specific aeraulic conditions as well as the presence of continuous supply of tracer in the vicinity of the internal side of the opening.

The gas tracing technique was applied to quantify the backflow phenomenon for different scenarios of external or internal disturbance turbulent jet. The

evolution of the backflow factor K as a function of the dimensionless aeraulic parameter V/U_{ope} for different dynamic confinement flowrates through the opening U_{ope} showed that this dimensionless velocity was relevant to characterize the effect of the aeraulic conditions on the onset of backflow. This was done for all three types of turbulent jet disturbances we tested.

The ISO standards [1,2] recommendation relies on a constant inflow velocity at the opening whatever the operating conditions, depending only on the nature of the pollutant species. Simultaneously, the ISO standards indicate that each scenario must be studied specifically. Our study has shown that the constant inflow velocity at the opening recommendation does not provide a conservative prediction of the gaseous pollutant backflow phenomenon. Indeed, depending on the direction of flow perturbation, the critical conditions for the onset of pollutant dispersion are characterized by a specific value of V/U_{ope}. This means that for a fixed value of the confinement velocity U_{ope}, backflow of pollutants will occur if the perturbation velocity is large enough. This typical value is $V/U_{ope} = 1$ for a countercurrent jet and $V/U_{ope} = 3.5$ for transverse flows. Above this critical value, the amount of backflowed gas also depends on the type of perturbation, with the countercurrent jet being the most dangerous. Comparison transverse jet configurations showed that internal perturbations are more prone to generate outward dispersion of tracer gas. Measurements concerning the external jet have resulted in lower intensity of pollutant dispersion.

The perspectives of this work are to study the backflow phenomenon of a particulate pollutant, as well as to test the backflow of pollutants through a flexible wall in order to predict and prevent them on a real dismantling site. Simultaneously, we aim to test the ability of CFD simulations to reproduce the backflow phenomenon through openings. These works are currently in progress.

Acknowledgments

The present work was equally supported by IRSN and EDF in collaboration with IMFT in the context of nuclear safety of maintenance and dismantling sites. The authors would like to thank Luc Lafanechere, Marjorie Jacqueline and Audrey Amphoux for their special assistance and insightful comments. The contribution of Laurent Ricciardi from IRSN is gratefully acknowledged, particularly for fruitful discussions. Nadia Liatimi from IRSN is also acknowledged for her technical support.

Disclosure statement

No potential conflict of interest was reported by the author(s).

Nomenclature

Variables		
C	Tracer concentration	ppm
$\overline{C}$	Mean concentration	ppm
k	Transfer coefficient	(s/m^3)
K	Backflow factor	%
P	Pressure	Pa
P_{atm}	Atmospheric pressure	Pa
q	Flowrate of tracer	m^3.h^{-1}
Q	Extraction flowrate	m^3.h^{-1}
S	Area of the opening	m^2
U_{ope}	Velocity at the opening	m/s
U_r	Relative uncertainty	%
V	Disturbance velocity at the opening	m/s
V_0	Disturbance velocity at the nozzle	m/s
Abbreviations		
2D	Two-dimensional	
CCD	Charge-Coupled Device	
ISO	International organization for standardization	
LDV	Laser Doppler velocimetry	
PIV	Particle image velocimetry	
PMMA	Poly-methyl methacrylate	
Subscripts		
0	Relative to the origin	
ext	Relative to the extraction	
in	Rrelative to inside the enclosure	
eq	Relative to the equilibrium	
ope	Relative to the opening	
out	Relative to outside the enclosure	

References

[1] ISO 16647. Nuclear facilities — criteria for design and operation of confinement systems for nuclear worksite and for nuclear installations under decommissioning. 2008.
[2] ISO 17873. Nuclear facilities — criteria for the design and operation of ventilation systems for nuclear installations other than nuclear reactors. 2004.
[3] Valkeapaa A, Anttonen H. Draught caused by large doorways in industrial premises. Int J Vent. 2004;3(1):41–51.
[4] Wang L, Zhong Z. An approach to determine infiltration characteristics of building entrance equipped with air curtains. Energy Build. 2014;75:312–320.
[5] Goubran S, Qi D, Saleh WF, et al. Experimental study on the flow characteristics of air curtains at building entrances. Build Environ. 2016;105:225–235.
[6] Foster AM, Swain MJ, Barrett R, et al. Effectiveness and optimum jet velocity for a plane jet air curtain used to restrict cold room infiltration. Int J Refrig. 2006;29:692–699.
[7] van Belleghem M, Verhaeghe G, T'Joen C, et al. Heat transfer through vertically downward-blowing single-jet air curtains for cold rooms. Heat Transf Eng. 2012;33:1196–1206.
[8] KalliomDELaki P, Saarinen P, Tang JW-T, et al. Airow patterns through single hinged and sliding doors in hospital isolation rooms. Int J Vent. 2015;14:111–126.
[9] Rouaud O. Etudes numeriques et experimentales de dispositifs de protection contre la contamination aeroportee dans les industries alimentaires [PhD thesis]. Nantes: Universite de Nantes, ENITIAA; 2002.

[10] Havet M, Rouaud O, Solliec C. Experimental investigations of an air curtain device subjected to external perturbations. Int J Heat Fluid Flow. 2003;24:928–930.
[11] Hu SC, Chuah YK, Yen MC. Design and evaluation of a minienvironment for semiconductor manufacture processes. Build Environ. 2002;37:201–208.
[12] Song D, Lee J, Ha S, et al. Assessment of control room habitability and unfiltered air inleakage test of the OPR 1000 NPP. J Nucl Sci Technol. 2015;52:905–911.
[13] Hayden CS II, Johnston OE, Hughes RT, et al. Air volume migration from negative pressure isolation rooms during entry/exit. Appl Occup Environ Hyg. 1998;13:518–527.
[14] Kalliomaki P, Saarinen P, Tang JW-T, et al. Airflow patterns through single hinged and sliding doors in hospital isolation rooms - effect of ventilation, flow differential and passage. Build Environ. 2016;107:154–168.
[15] Chang L, Tu S, Ye W, et al. Dynamic simulation of containment in leakage produced by human walking into control room. Int J Heat Mass Transf. 2017;113:1179–1188.
[16] Chen C, Zhao B, Yang X, et al. Role of two-way airflow owing to temperature difference in severe acute respiratory syndrome transmission: revisiting the largest nosocomial severe acute respiratory syndrome outbreak in Hong Kong. J R Soc Interface. 2010;8:699–710.
[17] Hang J, Li Y, Ching WH, et al. Potential airborne transmission between two isolation cubicles through a shared anteroom. Build Environ. 2015;89:264–278.
[18] Prevost C, Lacan J. Etude de l'effcacite de confinement d'une boite a gants en situations accidentelles de fonctionnement. CFA Conference. Paris; 2003.
[19] Prevost C, Bouilloux L, Lacan J. Etude de l'effcacite de confinement assure par une boite a gants en situations accidentelles de fonctionnement. SFRP Conference. Nantes; 2005.
[20] Iwai Y, Hayashi T, Yamanishi T, et al. Simulation of tritium behavior after intended tritium release in ventilated room. J Nucl Sci Technol. 2001;38:63–75.
[21] Cao X, Liu J, Jiang N, et al. Particle image velocimetry measurement of indoor airflow field: a review of the technologies and applications. Energy Build. 2014;69:367–380.
[22] Cesard V, Belut E, Prevost C, et al. Assessing the containment efficiency of a microbiological safety cabinet during the simultaneous generation of a nanoaerosol and a tracer gas. Ann Occup Hyg. 2013;57:345–359.

3. Experiments

In this section related to the experimental setup, we divide our chapter into two parts: the first one is dedicated for the characterization of the local backflow phenomenon near the opening and the second one for measurements of global backflow using an envelope. We remind that chapter 2 presents the experimental setup and results for the local backflow of gaseous pollutant related to S. Kaissoun's works. In the first part of this chapter related to local backflow, we show first the results of laser visualizations and PIV in order to detect the backflow near the opening. Then we show the experimental procedure to quantify the gaseous and particulate pollutants concentrations near the opening. Results showing the evolution of the local backflow coefficient are presented for different disturbing jet types and frontal wall types. In the second part related to global quantification, we start first by verifying the impact of the envelope on flows near the opening. Then we checked the gaseous and particulate concentrations decay curves of the envelope in order to access to the renewal rates for each of them. After that, we explained the procedure to determine the global backflow coefficient for gaseous and particulate pollutants. We displayed results for the evolution of global backflow coefficients for different configurations. And lastly, a synthesis of the local and global backflow results is illustrated at the end of this chapter.

Experiments for local and global backflow were performed on two types of disturbances: the counter-current internal disturbing jet and the parietal internal jet, and on two types of frontal wall: a rigid frontal wall and a flexible frontal wall.

<u>Determination of the disturbing jet velocity near the opening</u>

It is important to remind that in the following, we changed the method of determination of the disturbing jet's velocity near the opening that S. Kaissoun used (Kaissoun, 2018). Recalling that the mean velocity *V* of the disturbing counter-current internal jet is measured at 3 cm from the opening inside the enclosure using an anemometer. S. Kaissoun performed the measurement of this velocity *V* without the presence of the frontal wall of the enclosure as we see in Figure 3-1 (a). However, our measurements of the velocity of the disturbing jet, denoted V_{dist} in our case, were done in the presence of the frontal wall of the enclosure as we see in Figure 3-1 (b). PIV measurements, in addition to anemometer measurements, were done in our case in order to sample the disturbing jet velocity V_{dist}. The sampling location of the disturbing jet near the opening is denoted '×' on Figure 3-1.

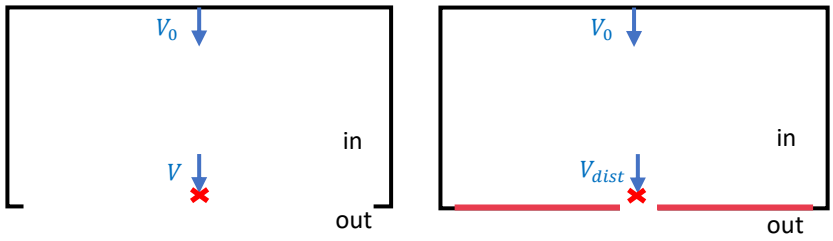

Figure 3-1 Schemes showing the sampling method of the disturbing jet velocity: (a) V without the presence of the frontal wall (S. Kaissoun) and (b) Vdist, with the presence of the frontal wall in our case

Figure 3-2 shows the evolution of the velocity of the disturbing jet near the opening: V without the presence of the frontal wall (S. Kaissoun) and Vdist in the presence of the frontal wall in our case in function

of the disturbing jet velocity at the nozzle's outlet V0. As we see in Figure 3-2, the evolution of the disturbing jet velocity V without the presence of the frontal wall (S. Kaissoun) is above the data of Vdist in the presence of the frontal wall in our case. Then for the same value of V0, V without the presence of the frontal wall is larger than Vdist in the presence of the frontal wall, since the frontal wall is an obstacle on which the jet is impacting, resulting in the decrease of the mean velocity near the opening.

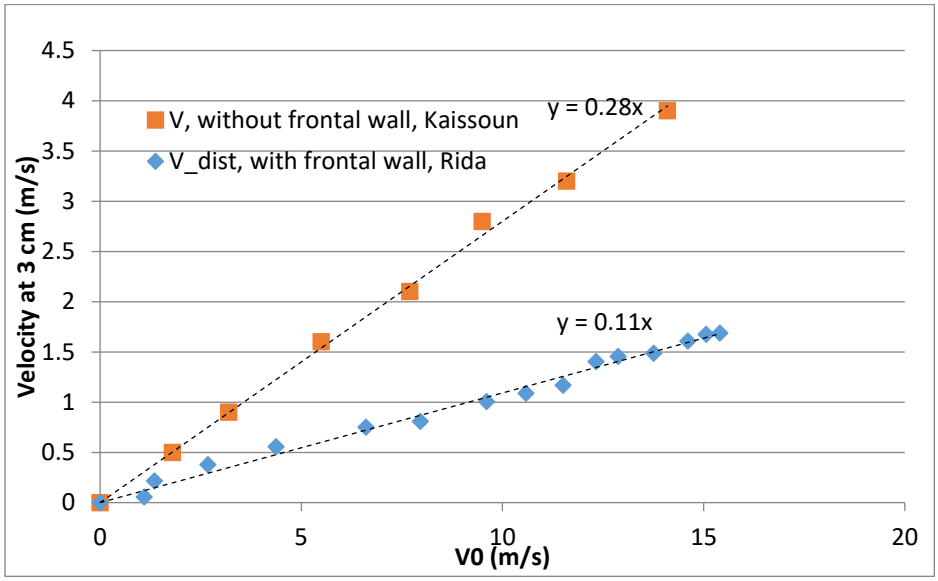

Figure 3-2 Evolution of the velocity of the disturbing jet at 3 cm from the opening in function of velocity of the disturbing jet at the nozzle's outlet V_0

Comparison of the local gaseous backflow coefficients with respect to S. Kaissoun results

Since the sampling of the disturbing jet velocity near the opening was not performed under the same conditions as S. Kaissoun, we cannot compare the results of evolution of the backflow coefficient *K* of S. Kaissoun in function of V/U_{ope} (Figure 12 in chapter 2) with our results in function of V_{dist}/U_{ope} (Figure 3-23). However, in order to compare the results, we plotted the evolution of the backflow coefficient *K* (%) in function of V_0/U_{ope} for the two configurations since the presence or absence of the frontal wall should not have an impact on the velocity at the nozzle's outlet V_0. Figure 3-3 shows the evolution of the backflow coefficient *K* (%) in function of V_0/U_{ope} for the gaseous pollutant for the three inflow velocities (0.5, 1 and 1.5 m/s), related to our results and those of S. Kaissoun.

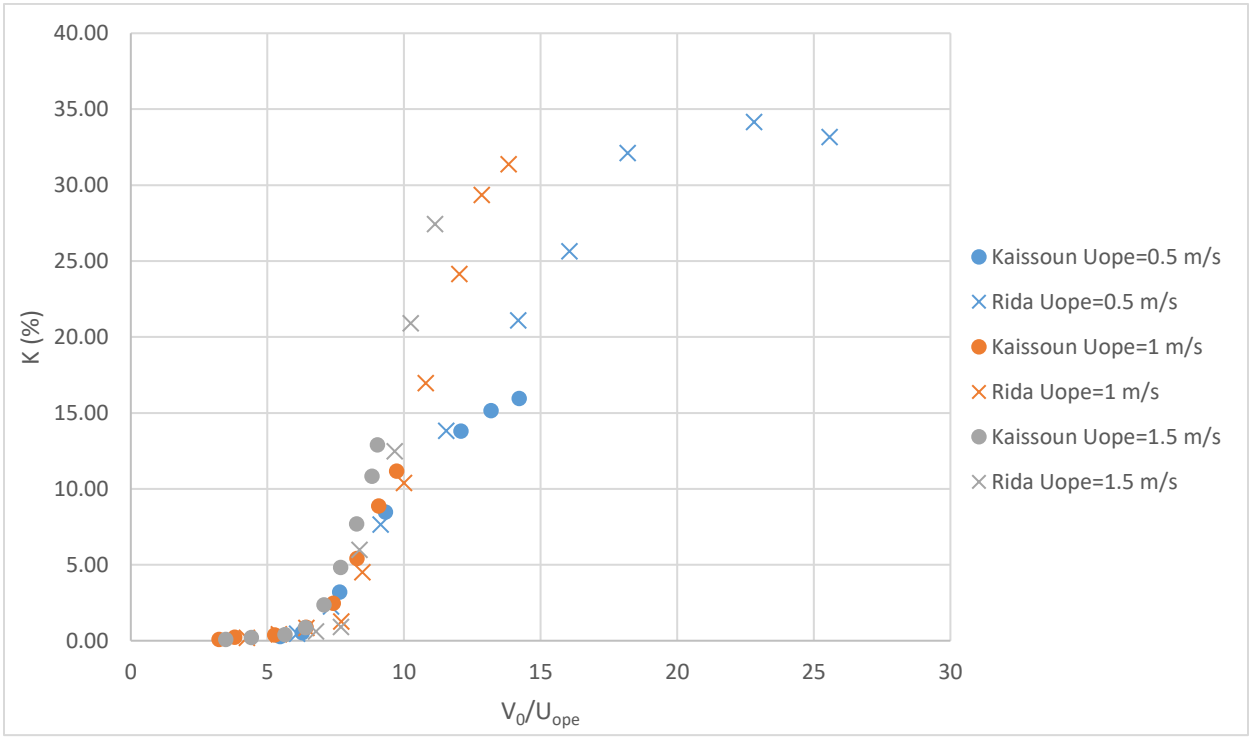

Figure 3-3 Gaseous backflow coefficient K (%) versus V_0/U_{ope} for the three values of the inflow velocity at the opening (0.5, 1 and 1.5 m/s) in comparison with S. KAISSOUN's results

As we can see in Figure 3-3, for V_0/U_{ope} between 3 to 10, the backflow coefficients related to our results and those of S. Kaissoun are similar validating the experimental procedures used by both authors. Then, there is no impact of the frontal wall on the evolution of *K* versus V_0/U_{ope}. As we can see also, our experiments covered a higher range of V_0/U_{ope}.

Description of the disturbance types

Experiments were carried out on two distinct configurations: the counter-current internal jet and the parietal transverse internal jet as shown in Figure 3-4 and Figure 3-5. A detailed description of material and methods for these two configurations is mentioned in chapter 2. As explained earlier, the extraction circuit corresponding to the flowrate $Q_{extraction}$ generates the desired velocity at opening U_{ope} (0.5 m/s, 1 m/s or 1.5 m/s). The counter-current and the parietal disturbing circuits ($Q_{disturbance}$) generate each a velocity V_0 at the nozzle exit, which corresponds to velocity V_{dist} at 3 cm from the opening. The competition between U_{ope} and V_{dist} may lead to the backflow phenomenon near the opening.

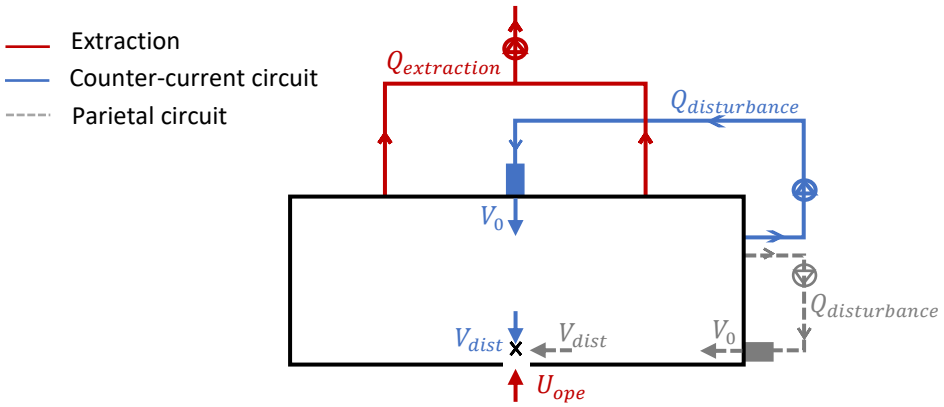

Figure 3-4 Scheme of the two disturbance configurations: counter-current disturbing jet and parietal transverse disturbing jet

U_{ope} is the mean inflow *velocity* of the dynamic containment and V_{dist} is the disturbing flow velocity at 3 cm from the opening. They are determined independently of each other: the disturbance flowrate is no activated when U_{ope} is measured and inversely, the extraction flowrate is stopped when V_{dist} is measured. The main difference of the determination of the disturbance velocity between our results and those of S. Kaissoun is that in our case, the measurements of the velocity V_{dist} were done in the presence of the frontal wall, unlike S. Kaissoun's measurement where this velocity V was measured without the frontal wall. In our case, the mean velocity V_{dist} of the disturbing counter-current internal jet is measured at 3 cm from the opening in the presence of the flexible frontal wall using the PIV technique. Simultaneously, we performed measurements for the velocity V_{dist} with a hot-wire anemometer in order to locally confirm our PIV results. For the internal parietal disturbing jet, the velocity V_{dist} is measured at 3 cm from the opening with an anemometer fixed in the horizontal median plane of the opening, in the presence of the rigid frontal wall. The position of the hot wire sensor used for the measurement of the velocity V_{dist} for each disturbance type is denoted "×" on Figure 3-4.

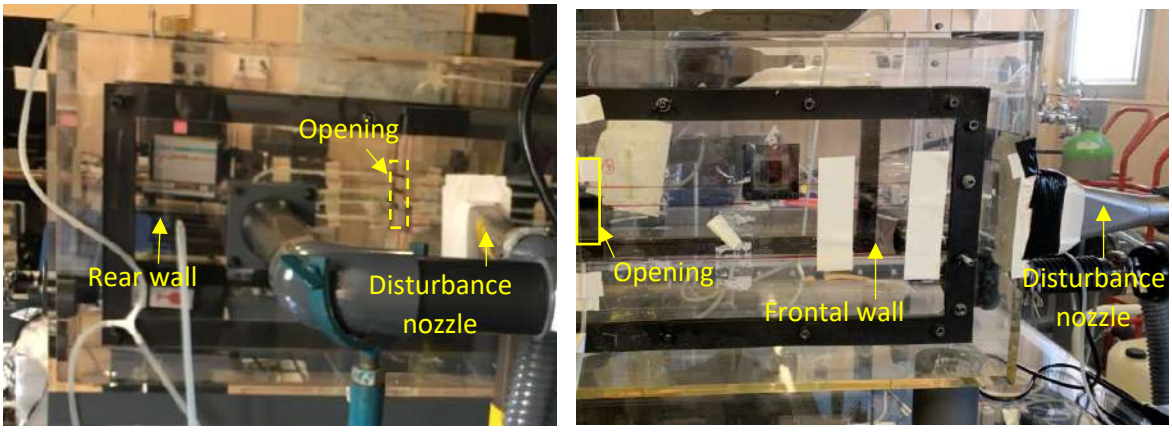

Figure 3-5 Pictures for counter-current disturbance configuration (left) and parietal disturbance configuration (right)

The Reynolds number (Re) is the ratio between inertial and viscous effects within a fluid as shown in Eq. 3-1 For low values of Reynolds number, the flow tends to be laminar. For higher values, the flow tends to be turbulent.

$$\text{Re} = \frac{u\,L}{\nu} \qquad \text{(Eq. 3-1)}$$

where u is the flow velocity (m/s), L is a characteristic length (m) and v is the kinematic viscosity of the fluid (m^2/s).

The Reynolds numbers at the opening corresponding to the inflow velocities of 0.5 m/s, 1 m/s and 1.5 m/s are respectively about 1500, 3000 and 4500. The velocity in Eq. 3-1 corresponds to the inflow velocity (U_{ope}) ranging from 0.5 m/s to 1.5 m/s, the characteristic length corresponds to the hydraulic diameter of the opening (0.046m) and the kinematic viscosity of air at 25°C is about 1.57×10^{-5} (m^2/s).

The Reynolds number corresponding to the internal disturbing jet ranges between 3.5×10^3 and 1.6×10^4. The velocity in Eq. 3-1 corresponds to the nozzle inlet velocity (V_0) of the disturbing jet ranging from 3 m/s to 14 m/s, the characteristic length corresponds to the hydraulic diameter of the disturbance orifice (0.018m) and the kinematic viscosity of air at 25°C is about 1.57×10^{-5} (m^2/s).

The flow configurations are always corresponding to a turbulent regime and we expect strong vertical structures to develop both in the free jet and close to the opening justifying an hybrid approach for CFD.

Description of the frontal wall types

Experiments were done on two types of frontal wall of the enclosure: enclosure with a rigid frontal wall and enclosure with flexible frontal wall as shown in Figure 3-6. The rigid frontal wall is made of transparent Plexiglass® type of a 5 mm thickness. The flexible frontal wall is made of pink vinyl of a 1 mm thickness. We should note that the remaining enclosure's walls were kept rigid and transparent during experiments. We did only change the type of the frontal wall.

Figure 3-6 The enclosure with rigid frontal wall (left) and flexible frontal wall (right)

Each disturbance configuration (counter-current jet/parietal jet) is applied on the enclosure first with the rigid frontal wall enclosure then with the vinyl frontal wall.

3.1 Local backflow

In this part, we describe the visualization of the backflow phenomenon near the opening using laser visualizations and PIV. Material and methods are detailed in chapter 2 as well as part of visualization results for the counter-current disturbing jet of the enclosure with a rigid frontal wall. In the following, we completed the chapter 2 with additional results for the same configuration, and then we modified, the types of the disturbance and the frontal wall. Secondly, in the section related to quantitative measurements, we added the aerosol pollutant to the procedure described in chapter 2. Procedure and results for gaseous backflow were shown in chapter 2. We detail here the materials used to quantify the backflow of the aerosol, and then we compare results of gaseous and particulate backflow for each disturbance type and each frontal wall type.

3.1.1 Visualization of the backflow

3.1.1.1 Materials and methods

Materials and methods for the visualization of the backflow and PIV measurements are detailed in chapter 2. We were interested in visualizing the median vertical and horizontal planes of the enclosure passing through the opening. We start first by showing complementary results of the counter-current internal disturbing jet in the enclosure with its rigid frontal wall, then with it flexible frontal wall. In a second time, we show results corresponding to the parietal internal jet in the enclosure with its flexible frontal wall.

Laser visualizations fields in the median horizontal and vertical planes in the opening of the enclosure with its rigid and flexible fontal wall for the counter-current and parietal internal disturbing jets are presented in appendix 1. In the following, we show a summary of the results.

We mention that preliminary works on Background Oriented Schlieren (BOS) technique were done in order to visualize the backflow near the opening as showed in appendix 4.

3.1.1.2 Counter-current internal disturbing jet

Experiments presented below highlight the competition between the existing inflow at the opening and the counter-current turbulent jet created inside the enclosure, which induces turbulent flow structures in the near field of the opening. We present first the configuration of the enclosure with its rigid frontal wall, then the configuration with its flexible frontal wall.

3.1.1.2.1 Rigid frontal wall

Laser visualizations in the vertical plane

Figure 3-7 corresponds to vertical median plan visualization images acquired at the opening corresponding to an inflow velocity at the opening U_{ope} = 1 m/s and in the presence of a counter-current internal turbulent jet with U_{ope} = 1 m/s and V_0 = 6 m/s, then with U_{ope} = 0.5 m/s and V_0 = 3.2 m/s.

Figure 3-7 Laser visualization images in the vertical plane of the opening corresponding to: (a,b) an inflow velocity U_{ope} = 1 m/s and a counter-current internal turbulent jet of V_0 = 6 m/s and (c) an inflow velocity U_{ope} = 0.5 m/s and a counter-current internal turbulent jet of V_0 = 3.2 m/s

As we can observe in Figure 3-7, there is a leakage of tracer to outside the enclosure. Flow inversions are detected near the opening. More laser visualizations of the backflow in the vertical median plane passing through the opening are found in chapter 2 and in appendix 2-B.

Several laser visualizations corresponding to three inflows through the opening that are U_{ope} = 0.5 m/s, 1 m/s and 1.5 m/s are performed to detect the velocity of the internal counter-current turbulent jet for the onset of backflow. Finally, we found that V_{dist}/U_{ope} corresponding to the initial stage of the backflow was about 0.68 ($\pm$ 0.06) for the three inlet velocities.

Laser visualizations in the horizontal plane

Appendix 1-A shows all the visualizations fields in the median horizontal plane at the opening of the enclosure with its rigid frontal wall and in the presence of a counter-current internal disturbing jet.

Figure 3-8 shows laser visualizations in the median horizontal plane in the opening of the enclosure with its rigid frontal wall corresponding to U_{ope}= 1 m/s and with a counter-current internal disturbing jet of velocity near the opening V_{dist} = 0.39 m/s, 0.58 m/s, 0.9 m/s and 1.52 m/s respectively. Figure 3-9 shows their corresponding PIV fields.

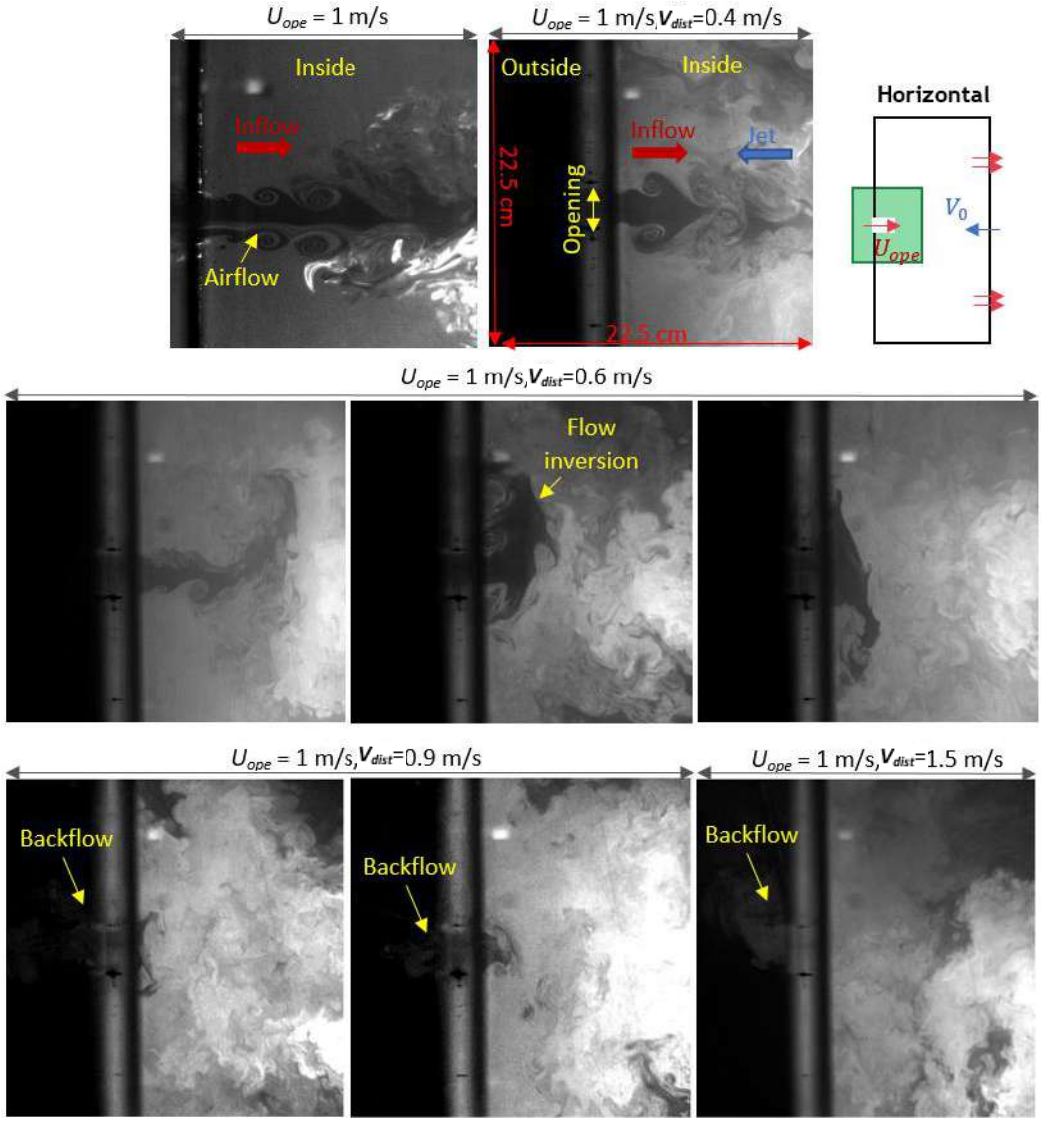

Figure 3-8 Laser visualizations in the median horizontal plane at the opening of the enclosure with its rigid frontal wall corresponding to U_{ope} = 1 m/s and with a counter-current internal disturbing jet of velocity near the opening V_{dist} = 0.4 m/s, 0.6 m/s, 0.9 m/s and 1.5 m/s respectively

The top left image of Figure 3-8 corresponds to the horizontal visualization field of an inflow of U_{ope} = 1 m/s without the presence of a disturbing counter-current jet. The dark color inside the enclosure corresponds to the air flow stream that enters the enclosure from outside through the opening, and that generates vortices near the opening field due to edge effects of the opening.

The top right image corresponds to the horizontal visualization field of an inflow of U_{ope} = 1 m/s and with a frontal disturbing jet of V_0 = 3.2 m/s (V_{dist} = 0.4 m/s). The presence of the disturbing jet starts to disturb the flow stream of air near the opening and generates additional turbulence. Here, the velocity of the disturbing jet is low and does not result in a complete breakup of the inflow air stream, and then there is no leakage of the pollutants to outside the enclosure.

As we increase the disturbing jet velocity to V_0 = 5 m/s (V_{dist} = 0.6 m/s), we can see a direct competition of the inflow and the disturbing jet. The inward and outward flows are facing in opposite directions which leads unstable aerodynamic configuration. This phenomenon results in the oscillation of the air flow in right-and-left directions inside the enclosure near the opening. We still observe some vortices near the opening edge due to the turbulence created. We do not detect leakage near the opening in this horizontal visualization plane.

For the case of the visualization fields of an inflow velocity U_{ope} = 1 m/s and a disturbing jet of velocity V_0 = 8.4 m/s (V_{dist} = 0.9 m/s), the disturbing jet has enough momentum to reach the opening and the air flow stream is quasi breaked up. However, we still see some vortices of the air stream near the opening. Then, we can clearly detect the leakage of pollutants outside the enclosure near the opening. However, a significant part of backflowed pollutants is recovered to the inside of the enclosure through opening.

The bottom image corresponds to the visualization fields acquired for an inflow velocity U_{ope} = 1 m/s and a disturbing jet of velocity V_0 = 14 m/s (V_{dist} = 1.5 m/s). The disturbing jet overcomes the air inflow. We do not detect significant vortex shedding near the opening in this horizontal median plane. The leakage of the pollutant appears on both sides (right and left) of the opening (see appendix 2-A). The most of the tracer leakage is recovered to the inside of the enclosure and maintains its dispersion to the outside.

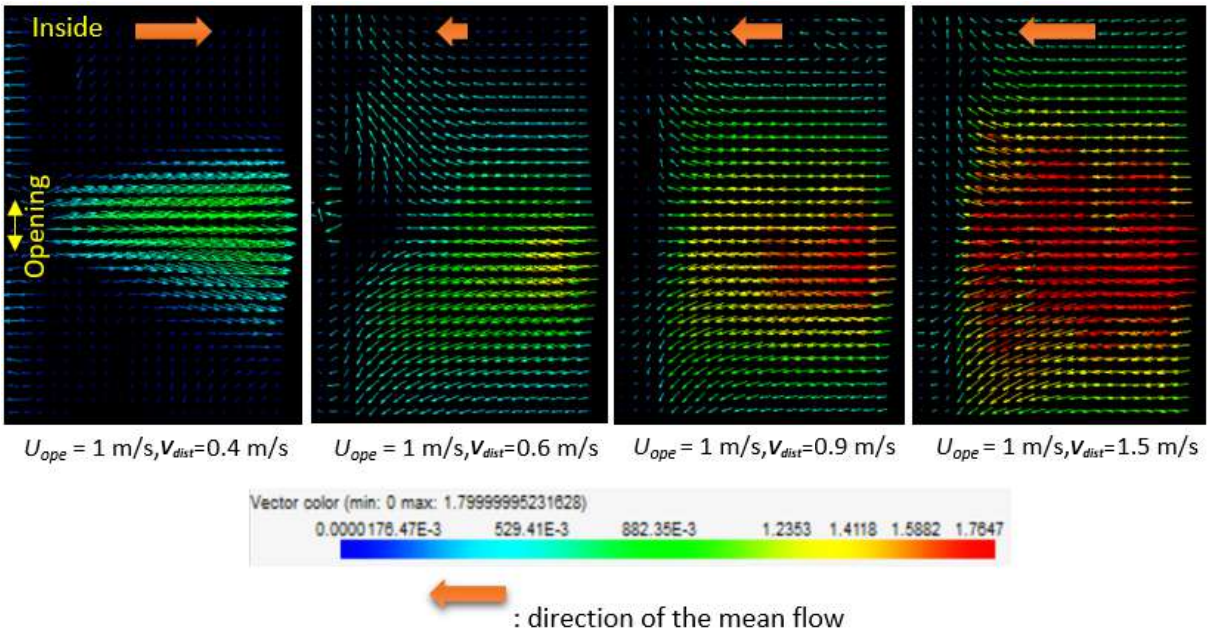

Figure 3-9 Corresponding PIV fields in the median horizontal plane at the opening of the enclosure with its rigid frontal wall for U_{ope} = 1 m/s and with a counter-current internal disturbing jet of velocity near the opening V_{dist} = 0.4 m/s, 0.6 m/s, 0.9 m/s and 1.5 m/s respectively

The corresponding PIV fields in the horizontal median plane of the opening inside the enclosure for each configuration are shown in Figure 3-9. The time between two laser pulses was set to Δt = 1 ms. The inter-correlation algorithm applies an adaptive PIV method with a grid step size of 64 × 64 pixels, a minimum interrogation area size of 128 × 128 pixels and a maximum interrogation area size of 256 × 256 pixels. A statistical average is carried out on 400 pairs of images for each configuration. The first field corresponding to an inflow of U_{ope} = 1 m/s and a disturbing jet of velocity V_{dist} = 0.4 m/s shows a mean velocity direction

near the opening directed towards inside the enclosure and of magnitude about 1 m/s. No backflow was observed in this case. The second field corresponds to an inflow of U_{ope} = 1 m/s and a disturbing jet of velocity V_{dist} = 0.6 m/s. The mean velocity direction near the opening is directed towards outside the enclosure and has a magnitude of about 0.7 m/s. We detected a zone emptied of vectors near the opening and that represents the flow inversions seen in the visualization fields resulting from the competition between the inflow and the disturbing jet. Increasing the disturbing velocity to V_{dist} = 0.9 m/s and 1.5 m/s results in the disappearance of this emptied zone near the opening. The backflow starts to appear in these cases, hence the mean flow near the opening is directed to outside the enclosure and has a value of about 1.4 m/s and 1.8 m/s respectively near the opening.

We should note that our results in the vertical median plane (appendix 1-B) at the opening of the enclosure show that for low disturbing jet velocities (3.2 m/s and 6 m/s), flow inversions appear all along the opening height and vortices are created at the top and bottom edges of the opening too. For disturbing jets of higher velocities (for 8.4 m/s till 14 m/s), we mainly detected flow vortices near the top and bottom edges of the opening inside the enclosure, highlighting the effects of the opening edges on the turbulence.

3.1.1.2.2 Flexible frontal wall

Vertical plane – outside the enclosure

Figure 3-10 presents three vertical visualization fields passing through the opening outside the enclosure with its flexible frontal wall for an inflow of U_{ope} = 1 m/s and a disturbing jet of velocity V_0 = 14 m/s (V_{dist} = 1.5 m/s). The camera was inclined in order to visualize the opening shape. Due to the opaque nature of the vinyl frontal wall, we only visualize here the outside part in Figure 3-10. The visualization field corresponds to (22.4 x 22.4) cm^2. The yellow dashes on Figure 3-10 represent the right and left sides of the opening.

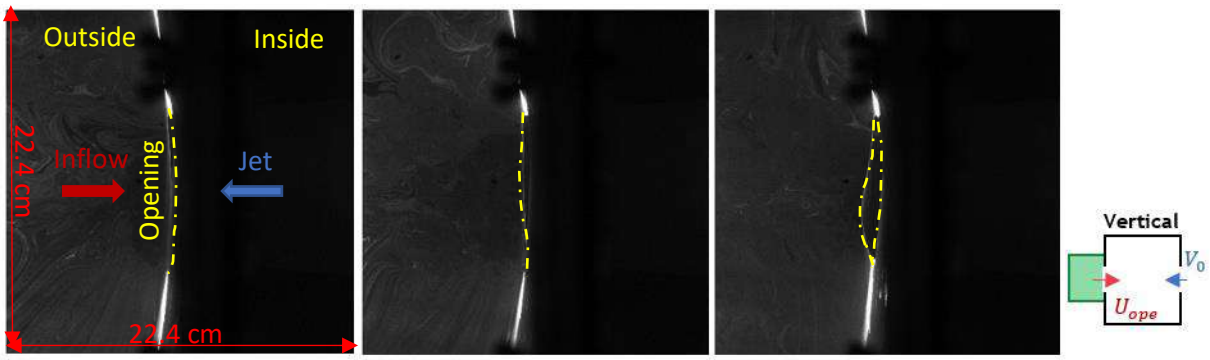

Figure 3-10 Vertical laser visualization fields with vinyl flexible frontal wall of an inflow U_{ope} = 1 m/s and a counter-current disturbing jet of V_{dist} = 1.5 m/s outside the enclosure with dt = 1 ms

We are interested in visualizing the deformation of the opening of the flexible vinyl frontal wall due to the interaction of the inflow and the counter-current disturbing jet. As we see in Figure 3-10, the opening is curved and changes its shape for different time steps. The deformation oscillation seen on this pictures is a result of the vibrations of the flexible frontal wall under the effect of the interaction between air flows at the opening. The first image represents the frontal wall that is curved to the inside owing to the

enclosure set under negative pressure, and then it starts to be curved to the outside of the enclosure in the second image and is totally distorted in the third image as the velocity of the disturbing jet is increased.

Additional laser visualization fields in the median horizontal plane at the opening of the enclosure with flexible frontal wall and with a counter-current internal disturbing jet, outside and inside the enclosure are shown in appendix 1 – C and D.

Vertical plane – inside the enclosure

Figure 3-11 presents the vertical visualization fields passing through the opening inside the enclosure with the flexible frontal wall for an inflow of U_{ope} = 0.5 m/s and disturbing jets of progressive velocity V_{dist}. The camera was inclined in order to visualize the opening shape. The visualization field corresponds to (24.3 x 24.3) cm^2. Additional visualization fields are shown in appendix 1 - E.

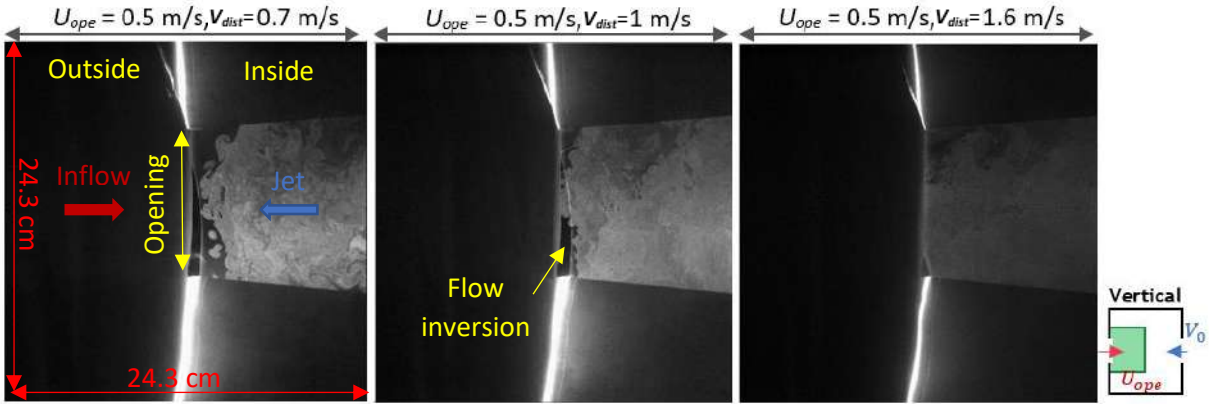

Figure 3-11 Vertical visualization fields passing through the opening inside the enclosure with its flexible frontal wall for an inflow of U_{ope} = 0.5 m/s and different disturbing jets of velocity V_{dist} = 0.6 m/s, 1 m/s and 1.5 m/s

The first image represents the vertical visualization fields inside the enclosure for an inflow U_{ope} = 0.5 m/s and V_{dist} = 0.65 m/s. Due to the competition between the air inflow and the counter-current disturbing jet, significant flow inversions are detected near the opening. When the disturbing velocity is increased to about V_{dist} = 1 m/s, flow inversions inside the enclosure near the opening start to attenuate. In this case, leakage of the pollutant is simultaneously detected outside the enclosure. For V_{dist} = 1.5 m/s, very few or no flow inversions are detected inside the enclosure. However, outside the enclosure, a continuous flow stream of pollutant escapes through the opening. We can clearly see the deformation of the opening while increasing the disturbing velocity.

Comparing qualitatively the backflow intensity for the rigid or flexible frontal wall, we did not detect a significant difference. It is true that the soft frontal wall vibrates under the interaction between the inflow and the counter-current disturbing jet, leading to the deformation of the opening shape. However, turbulence intensity generated by these vibrations is quite small compared to that generated by the disturbing counter-current jet. Apparently, the origin of backflow is mostly related to disturbing jet. On the other hand, the vibration of the frontal wall on both sides could induce the escape then the recovery of the pollutant, resulting of no significant effect of these vibrations on backflow intensity for this configuration.

3.1.1.3 Parietal internal disturbing jet

The parietal disturbance is produced with the nozzle jet located at the right side of the enclosure. This disturbance is produced via a closed circuit generating a velocity V_0 at the nozzle exit and a velocity V at 3 cm from the opening. For the laser visualizations and PIV, we tested the configuration of the enclosure with the flexible vinyl frontal wall.

Vertical plane - outside

The two images in Figure 3-12 illustrate laser visualizations fields in the median vertical plane of the enclosure with its flexible frontal wall corresponding to an inflow velocity U_{ope} = 0.5 m/s and a parietal disturbing jet of velocity V_{dist} = 0.8 m/s and 2 m/s respectively. Note that we rotate the camera at slight angle in order to detect the deformation of the opening and the associated backflow. Due to light reflections above and under the opening, we added black masks on the following visualization images. Additional laser visualization fields are shown in appendix 1 - F.

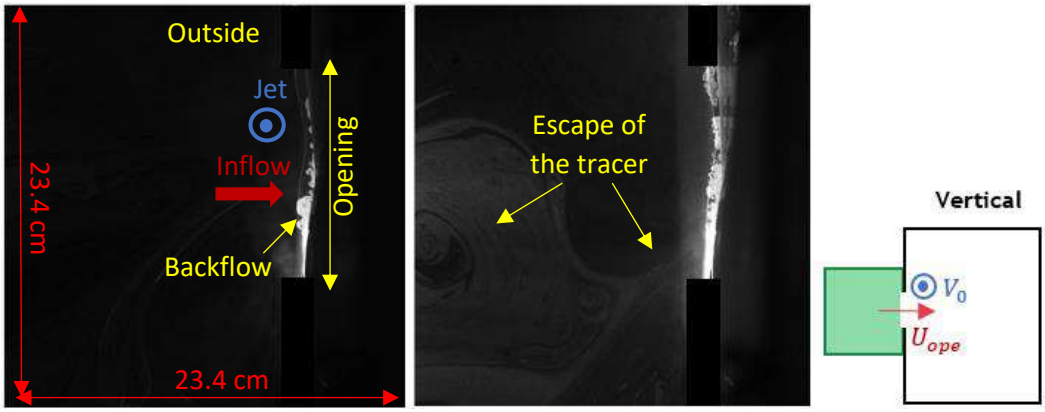

Figure 3-12 Laser visualizations outside the enclosure in the inclined vertical median plane containing the opening of the enclosure with its flexible frontal wall for an inflow of velocity U_{ope} = 0.5 m/s and a parietal disturbing jet of velocity V_{dist} = 0.8 m/s (left) and V_{dist} = 2m/s (right).

The first image corresponding to U_{ope} = 0.5 m/s and V_0 = 6 m/s (V_{dist} = 0.8 m/s) reveals weak backflow near the opening. The backflow phenomenon is located at the lowest part of the opening. For U_{ope} = 0.5 m/s and V_0 = 13.4 m/s (V_{dist} = 2 m/s), the backflow is evenly distributed along the opening height, with an intense concentration at the lowest part of the opening. Here we detect a flow stream of smoke oil particles in the form of vortex escaping the enclosure from the lowest side of the opening.

In this case, the flexible frontal wall is deformed, and under the influence of the parietal disturbing jet that flows along the frontal wall, it strikes the deformed edges of the opening and leads to the backflow outside the enclosure. Significant leakage of pollutant in the lowest side of the opening can be due to a curved shape of the frontal wall containing the opening from the opposite side wall of the disturbing jet inside of the enclosure.

However, we did not detect significant vibrations of the frontal wall or significant change in the deformation of the opening shape under the influence of the parietal disturbance.

Horizontal plane-inside the enclosure

Figure 3-13 shows the horizontal visualization fields in the median plane of the opening for the enclosure with its flexible frontal wall of an inflow U_{ope} = 0.5 m/s and a parietal disturbing jet of progressive velocities V_{dist} = 0.7 m/s, 1 m/s, 1.6 m/s and 2 m/s respectively. Here the camera was fixed above the enclosure and perpendicular to the upper wall. The horizontal bar seen on Figure 3-13 represents the edge of the upper wall of the enclosure. We can still see some parts of the vinyl frontal wall near this bar. Additional laser visualization fields are shown in appendix 1 – G. Figure 3-14 shows their corresponding PIV fields. The time lapse between two laser pulses is set to Δt = 0.7 ms. The inter-correlation algorithm applies an adaptive PIV method with a grid step size of 64 × 64 pixels, a minimum interrogation area size of 128 × 128 pixels and a maximum interrogation area size of 256 × 256 pixels. Statistical average is formed over 300 pairs of images for each configuration.

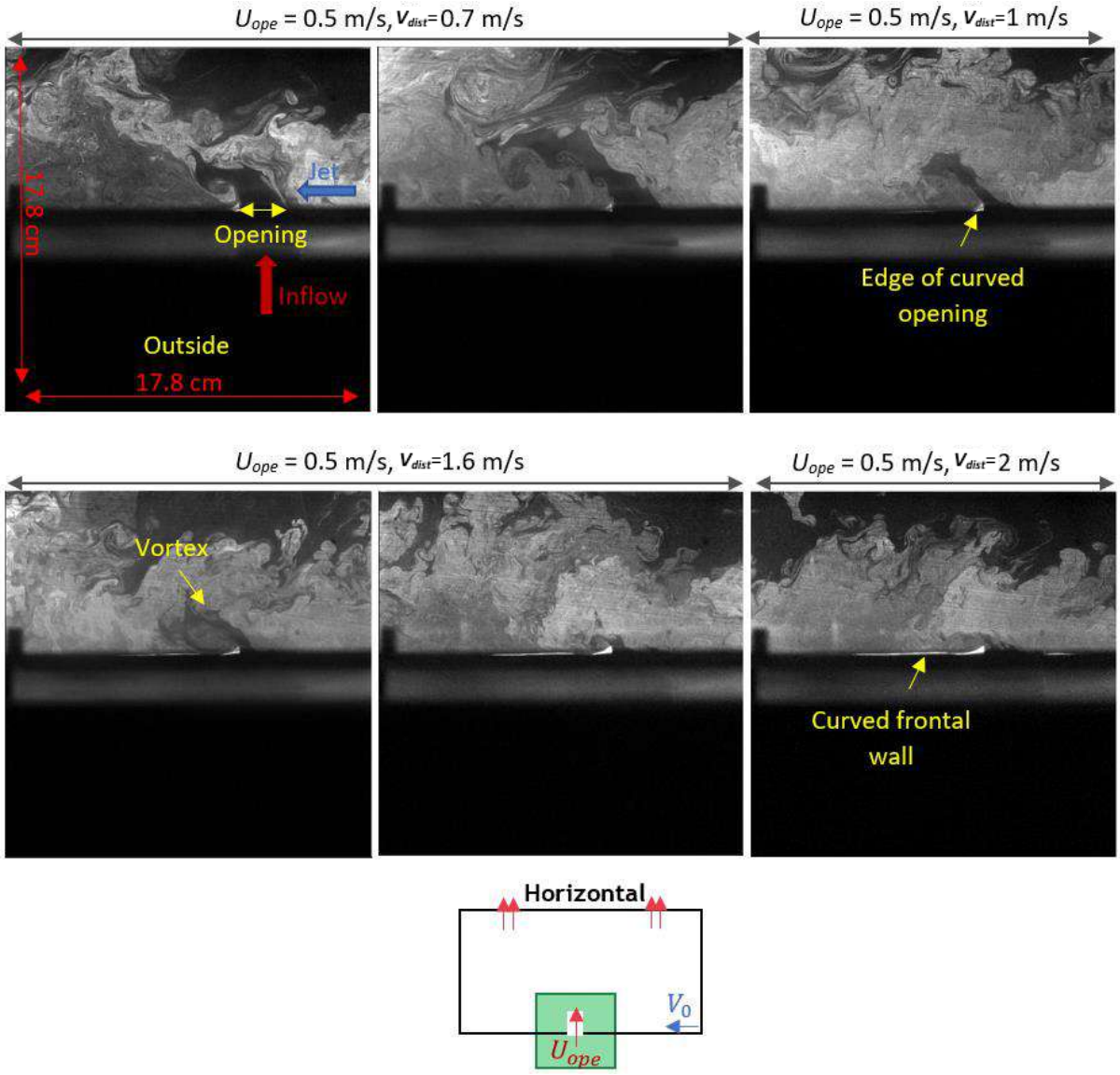

Figure 3-13 Laser visualization fields in the median horizontal plane of the opening for the enclosure with its flexible frontal wall of an inflow U_{ope} = 0.5 m/s and a parietal disturbing jet of progressive velocities V_{dist} = 0.7 m/s, 1 m/s, 1.6 m/s and 2 m/s respectively.

As we observe in Figure 3-13, the interaction between the inflow velocity U_{ope} = 0.5 m/s and the parietal internal disturbing jet of velocity V_0 = 5.6 m/s (V_{dist} = 0.7 m/s) results in significant flow inversion near the opening. An air stream inducing vortices appears near the opening and is directed to the left side of the enclosure. The presence of this flow stream prevents the backflow of pollutant to outside the enclosure. For the case of the air inflow of U_{ope} = 0.5 m/s and the parietal internal disturbing jet of velocity V_0 = 7.54 m/s (V_{dist} = 0.97 m/s), the air stream starts to reduce its extent. The flow inversions near the opening are the result of the competition between the air inflow and the parietal jet in one hand, and the crossing of the parietal jet on the edge of the curved opening on the other hand. Near the opening, very weak backflow phenomenon is detected, but most of tracer is taken back to the inside of the enclosure. Increasing the parietal jet velocity to V_0 = 11.3 m/s (V_{dist} = 1.6 m/s) results in very few inversions in the form of vortex near the opening. We should note also that the vinyl frontal wall starts to appear beyond the horizontal bar, which means that the frontal wall has moved due to vibrations. The vibrations of the frontal wall that generates the curvature of the opening is responsible of these vortices near the opening. Near the opening, we still see light backflow, with the escape of part of the tracer to the outside of the enclosure. Likewise, when we increase the disturbing jet velocity to V_0 = 13.4 m/s (V_{dist} = 2 m/s), the curvature of the frontal wall becomes significant (see Figure 3-13). The flow inversions near the opening are very low. Backflow of pollutant to the outside of the enclosure is detected. The presence of the horizontal bar does not allow to visualize the backflow towards outside the enclosure in these configurations.

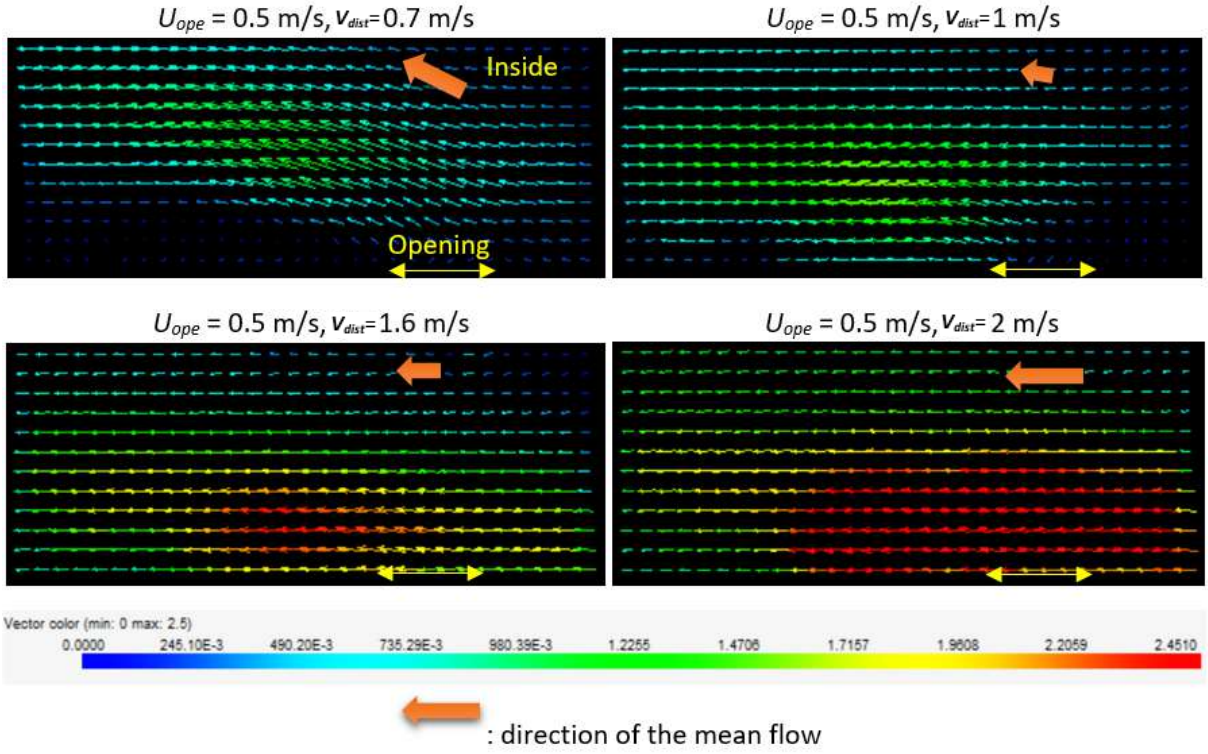

Figure 3-14 Corresponding PIV fields in the median horizontal plane of the opening with a flexible frontal wall and an inflow U_{ope} = 0.5 m/s with a parietal disturbing jet of velocities V_{dist} = 0.7 m/s, 1 m/s, 1.6 m/s and 2 m/s respectively.

In Figure 3-14, the PIV field corresponding to U_{ope} = 0.5 m/s and V_{dist} = 0.7 m/s represents a mean flow direction near the opening to the upper left side which highlights the presence of the air flow stream that prevents the backflow towards outside the enclosure. The velocity near the opening is about 0.7 m/s. In the second average field corresponding to U_{ope} = 0.5 m/s and V_{dist} = 1 m/s, the rotation of the mean velocity vector to the upper left still persists, highlighting the reduced air flow stream in this case. The mean velocity near the opening is about 1 m/s. Increasing the jet velocity to V_{dist} = 1.6 m/s makes the mean flow direction to the left side in a horizontal way. The mean velocity fields near the opening have an average of about 2 m/s. For the disturbing jet of V_{dist} = 2 m/s, the mean velocity fields are directed to the left side of the enclosure and have a value higher than 2.5 m/s near the opening.

We should note that the backflow intensity detected for the internal parietal disturbing jet is very low compared to that detected for the internal frontal counter-current disturbing jet for the similar values of V_{dist}/U_{ope}. Simultaneously, we observe the vibrations of the flexible frontal wall via the internal parietal disturbing jet are much weaker compared to the vibrations generated by the counter-current frontal jet for the same values of V_{dist}/U_{ope}.

The laser visualizations and PIV fields offer qualitative information about the amplitude of the backflow locally detected near the opening and it will be measured in the next section. Also, it allows to better understand the backflow phenomenon, and to interpret the following quantitative results of backflow phenomena.

3.1.2 Quantification of the backflow phenomenon

The quantification of the backflow coefficient locally near the opening follows the same procedure as that described in chapter 2 for the gaseous pollutant. However, in this chapter, we injected the aerosol of 5 µm aerodynamic diameter* simultaneously with helium in order to calculate the backflow coefficients for helium gas, K_{gas} (%), and for a sodium chlorure aerosol (NaCl) labeled with sodium fluorescein ($C_{20}H_{10}O_5Na_2$), $K_{aerosol}$ (%), in the same conditions. We first detail the devices used to produce and then to sample the aerosol. Then we explain the procedure for quantifying the gaseous and particulate backflow. After that, we show the results in term of backflow curves.

3.1.2.1 Material and methods (scheme procedure for gas and aerosol)

Devices used for the gaseous tracers includes: compressed pure helium and SF_6 reservoirs with a volumetric flowmeter for the injection of gases, an helium specific mass spectrometer (Alcatel analyser) with an internal pump for the detection of helium concentration, an infrared absorption analyzer (Xtream analyzer) with an external pump for the detection of SF_6 concentration and an acquisition systems (Labview Software) for the continuous monitoring of helium and SF_6. These devices are detailed in chapter 2.

Devices used for the particulate tracers includes: an aerosol generator for the continuous production of 5 µm aerosol (Sinaptec 500 kHz LIXEA device), filters (fiberglass) and filer holders connected to a piston pump (Reciprotor® model) and a volumetric meter for the aerosol sampling, a field fluorimeter (ESE analyzer) for the filtered sample concentration measurement, an aerodynamic particle sizer (APS system from TSI) equiped with air dilutor for sampling of high particles concentration according to some application.

3.1.2.1.1 Aerosol devices

Description of the aerosol generator

An ultrasonic generator (LIXEA, Sinaptec) is used to produce aerosol of a mass median aerodynamic diameter d_{ae} = 5 µm by ultrasonic spraying of the sodium fluorescein solution (Figure 3-15). The total air flow produced by this generator is fixed and equal to 10 m^3/h.

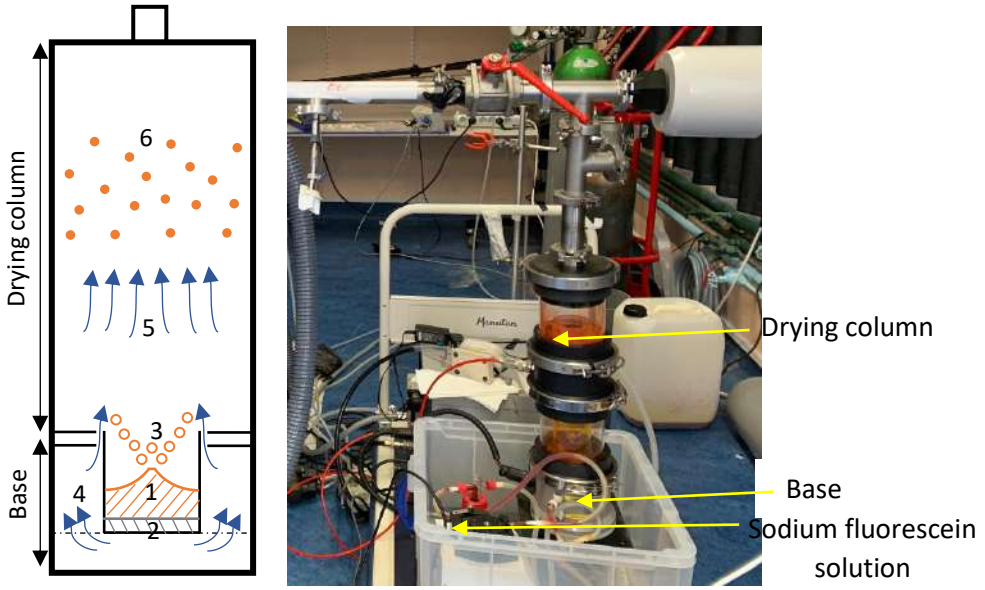

Figure 3-15 (left): Scheme of an ultrasonic aerosol generator constituted of a nebulized base and a drying column with 1: fluorescein sodium solution, 2: vibrating ceramic, 3: droplets of diameter d_g, 4: dispersion of air flow, 5: drying air flow, 6: dried particles of diameter d_p; (right): picture of particles generator LIXEA connected to the enclosure

An aqueous solution of sodium fluorescein is used as fluorescent particulate tracer in our experiments, which consists of an orange powder (sodium fluorescein commonly referred to as uranine) soluble in water with a quantity of sodium chloride (NaCl). Since no fluorescent aerosol is initially present in the ambient air, the uranine detected at a measurement point necessarily comes from the particles generator. Then, the concentration measurements are specific and not disturbed by ambient aerosol naturally present in the experimental environment.

As shown and described in Figure 3-15, the ultrasonic LIXEA generator is composed of a nebulizer base and a drying column. Fluorescein sodium solution is added on the piezoelectric vibrating ceramic located at the base of the device. The ultrasonic oscillations of the ceramic forced by a given frequency cause a fountain of liquid to form on the solution surface. A mist of droplets comes out of this fountain and is nebulized by a dry filtered air (dispersion air). To obtain the desired constant size droplets, the height of liquid above the ceramic must be kept constant during generation: the diameter d_g of the droplets formed is given by Eq. 3-2.

$$d_g = \alpha_g \left(\frac{8\pi\alpha_s}{\rho_s}\right)^{1/3} F^{-2/3} \qquad \text{(Eq. 3-2)}$$

with α_g: dimensionless constant specific to the generator; σ_s: surface tension of the solution used; ρ_s: density of the solution used; F: resonance frequency of the piezoelectric ceramic.

This equation shows that the droplet diameter d_g depends on the solution characteristics and the frequency of the piezoelectric ceramic. For our case and in order to obtain a single size of droplets of 5 µm final aerodynamic diameter, we used the sodium fluorescein solution concentrated at 25 g/L in NaCl ,and the frequency of the ceramic was fixed to about 520 Hz.

Once nebulized, droplets are entrained by drying air flow in a column to form dry particles. The volume equivalent diameter d_{ev} of a dry particles depends on the quantity of pure solid (uranine and NaCl) dissolved in a droplet, therefore on the uranine and NaCl concentration in the solution.

The volume equivalent d_{ev} and the corresponding aerodynamic diameter d_{ae} of a dry particle are given by Eq. 3-3 and Eq. 3-4 respectively.

$$d_{ev} = d_g(C_v)^{1/3} \quad \text{(Eq. 3-3)}$$

$$d_{ae} = d_{ev} \cdot \left(\frac{\rho_p}{\rho_0}\right)^{1/2} \quad \text{(Eq. 3-4)}$$

C_v denotes the volume concentration of uranine and NaCl in the solution, ρ_0 = 1000 kg.m^{-3} and ρ_p represents the produced particles density (uranine and NaCl) ($kg.m^{-3}$).

Description of the Aerodynamic Particle Sizer (APS), the granulometric device usefull to characterize the particles size and number

The aerosol particle sizer is shown in Figure 3-16.

Figure 3-16 The front face of Aerodynamic Particle Sizer (APS)

It allows real-time measurement of aerodynamic diameters of particles in the range: 0.5 µm - 20 µm. The numerical input concentration should not exceed 10^4 particles.cm^{-3}. Then, an air dilutor is provided with this device in order to dilute and measure high concentration samples. Entering the APS through an internal pump, the air carrying particles is strongly accelerated by passing through a small orifice. Due to their relaxation time τ_p, the particles will take some time to adjust their velocity to that of the carrier fluid. This adjustment delay depends directly on τ_p and therefore on d_{ae}^2. Thus, d_{ae} can be determined by measuring the velocity of each particle just after the orifice, using a split laser beam. Passing through these beams, each particle produces two light pulses, converted into electrical pulses by a photomultiplier. The time between two pulses is measured by an internal clock: it is the time of flight of the particle which allows it to go back to d_{ae}. These two quantities are indeed correlated thanks to a calibration curve. For

newer device models, the two pulses are combined into a single double peak signal. The flight time becomes the time between these two peaks (Renoux and Boulaud, 1998; APS TSI notice, 2004).

We used this device to control the particles sizes distribution generated at the exit of the generator as shown in Figure 3-17. The mass median aerodynamic diameter produced by the aerosol generator is d_{ae} = 5.50 µm. The mass median aerodynamic diameter is the value of aerodynamic diameter for which 50 % of aerosol mass represents particles smaller than this diameter and 50 % of aerosol mass represents particles larger than this diameter. The geometric standard deviation for this distribution was 1.34.

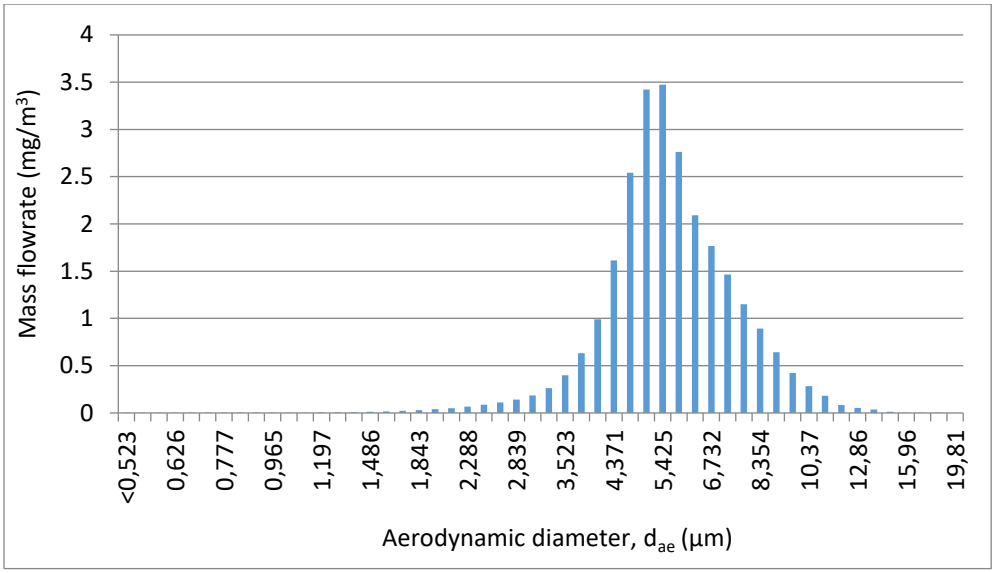

Figure 3-17 Particles sizes distribution at the outlet of the generator.

Simultaneously, we used it to quantify the number particles concentration outside the enclosure close to the opening and inside the extraction duct of the enclosure, in order to quantify the global backflow. Later, we used this device to quantify the particle deposition rate inside the envelope.

Description of the sampling devices

The sampling devices are shown in Figure 3-18 and Figure 3-19.

In order to quantify the phenomena of particulate backscattering, we distinguish several sampling points useful to measure the aerosol concentration: at the outlet of the generator, near the injection point at the entrance of the enclosure, near the opening and inside the extraction circuit of the enclosure and also in the ambiance. A sampling circuit is composed of a sampling probe, a filter media supported by a filter holder, a sampling pump, and a volumetric flowmeter. Then a fluorimeter is needed to specifically measure the concentration of the substance collected.

We should note that in order to measure correctly the aerosol concentration of a given area (in a duct, at the ambient point, ...), that is to say to be representative, the aerosol sample must respect the isokinetism rules: the fluid current lines must enter the sampling probe without being disturbed. For this, the axis of this device must be parallel to the flow. Then the velocity of the fluid in the sampling probe is equal to that of the fluid at the main flow. There is therefore no loss of particles at the inlet. In general, isokinetic sampling does not guarantee that there is no downstream loss between the inlet of the sampling device

and the collection filter or measurement system. On the other hand, it makes it possible to ensure that the concentration and the size distribution of the particles entering this device are the same as in the main flow (Hinds, 1999). If the sampling velocity is greater than the velocity of the main flow, the concentration is underestimated (superisokinetic sampling). On contrary, if the sampling velocity is lower than the velocity of the main flow, the concentration is overestimated (subisokinetic sampling) (Hinds, 1999).

In order to perform an isokinetic sample, the flow rate at the sample pump must be adjusted so that the velocity of the particle-laden flow in the outlet of the duct is similar to that in the sampling probe. The sampling flow rate is determined using the following equation (Eq. 3-5):

$$\frac{Q_{duct}}{d_{duct}^2} = \frac{Q_{probe}}{d_{probe}^2} \qquad \text{(Eq. 3-5)}$$

The filters used in our tests have a 40 mm diameter of and are supported by a filter holder. Two types of filter holders are used in our experiments such as closed and open filter holders as shown in Figure 3-18. Closed filter holders are connected via a sampling probe placed inside these measurement locations: in the generator outlet, in the entrance of the enclosure and in the extraction duct. The diameter of the sampling probe and flow rate of the sampling pump are chosen based on Eq. 3-5. In our experiments, open filter holders are placed near the opening, at the outside of the enclosure and in the ambient.

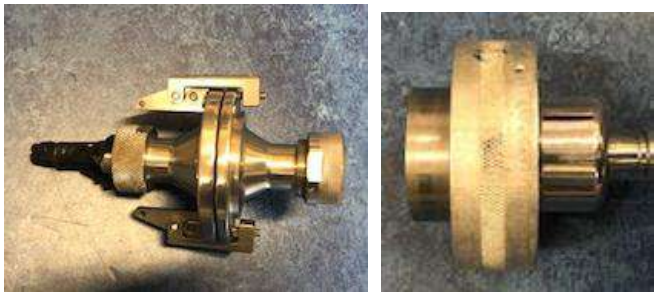

Figure 3-18 Closed filter holder (left) and open filter holder (right)

The filter holder is then connected via a pipe to a piston pump and a volumetric flowmeter as shown in Figure 3-19. The sampling is activated on a fixed duration (between 1 and 20 min in our experiments) and the obtained sampled volume is noted V_{aer}.

Figure 3-19 A volumetric flowmeter connected to a piston pump

Once the sampling is stopped, the filtered is captured to be further analyzed in order to obtain the fluorescent aerosol mass m_{aer} deposited on the filter, using a fluorimeter.

Description of the ESE fluorimeter – Determination of particles mass concentration

The filter is diluted in a volume V_w of an ammonia water. This solution is then analyzed using a fluorimeter as shown in Figure 3-20.

Figure 3-20 Fluorimeter analyzer (ESE type)

The principle consists in exciting a fluorescent solution thanks a monochromatic light corresponding to a constant wavelength of 482 nm. This wavelength is that for which the fluorescent solution exhibits the maximum absorption. The solution absorbs part of this light and re-emits on the fluorescence wavelength (520 nm). A set of filters makes it possible to selectively measure the intensity of this light. The concentration of the diluted solution is then determined using the Beer-Lambert law (Eq. 3-6):

$$I_t = I_0.e^{(-\varepsilon_s.C_f.l)} \quad \text{(Eq. 3-6)}$$

With I_t is the luminous flux transmitted by the solution, I_0 is the incident flux, ε_s is the molar absorption coefficient of the solution, C_f is the uranine concentration in the solution and l is the optical path traveled.

Knowing the solution concentration C_w and the volume of ammonia water V_w, we obtain the mass of sampled uranine m_{aer} deposited on the filter at the sampling point using Eq. 3-7:

$$m_{aer} = C_w.V_w \quad \text{(Eq. 3-7)}$$

The sampled aerosol concentration is then calculated using Eq. 3-8:

$$C_{aer} = \frac{m_{aer}}{V_{aer}} \quad \text{(Eq. 3-8)}$$

3.1.2.1.2 Scheme procedure for gas and aerosol

Our objective is to measure the quantity of gaseous and particulate pollutant emitted at opening during the backscattering phenomenon. Figure 3-21 shows the diagram of the devices used for the local quantification of the backflow. For this aim, helium and aerosol of 5 µm aerodynamic diameter are simultaneously injected in the enclosure where a dynamic containment is implemented at the opening (1), in Figure 3-21. An internal counter-current (or later a parietal) disturbance is then produced (2). At equilibrium, the pollutants concentration contained inside the enclosure (3) and those that are backflowed near the opening (4) are then measured in order to calculate the associated backflow coefficient K (%). The procedure is similar as that explained in chapter 2 for the gaseous backflow. Here, we added the aerosol part.

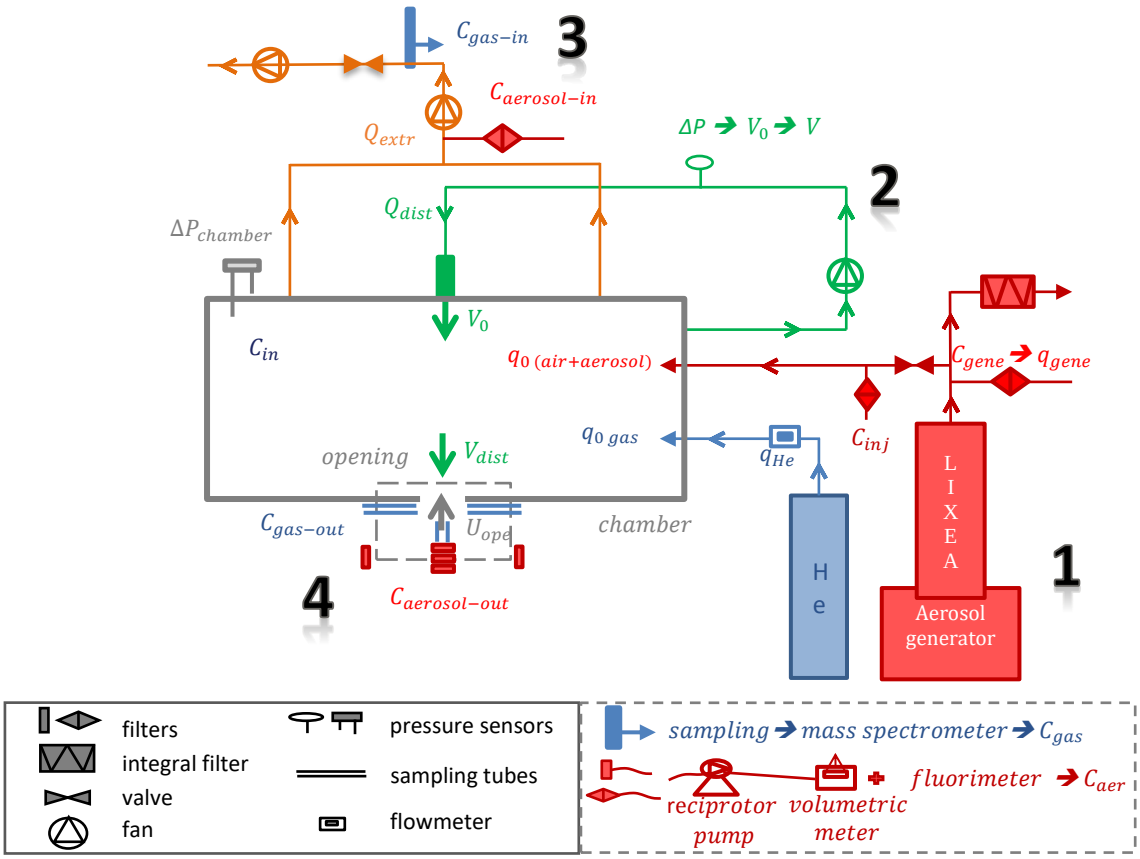

Figure 3-21 Diagram of the operating devices used for the backflow quantification in our enclosure

Successive stages were carried out to determine the backflow coefficients (Figure 3-21):

- (1) Initially, a constant and controlled tracer gas flow $q_{0\ gas}$ (Nl. h^{-1}) was injected into the enclosure from a pure helium cylinder as explained in chapter 2.

Simultaneously, a constant particulate tracer flow $q_{0\ aer}$ ($g.h^{-1}$) was injected into the enclosure from an aerosol generator (LIXEA, Sinaptec) (Figure 3-15 (right)); the mass median aerodynamic diameter of particles was about 5 µm. A valve was added to the outlet of the generator to collect only a part of the produced flow, the other part was filtered before discharge into the atmosphere. The mixture (air/ aerosol) injection rate was ranged between 2.3 m^3/h and 4 m^3/h in our experiments. Note that we adjusted the extraction flowrate of the enclosure in order to obtain the required velocity at the opening (Q_{extr}= $Q_{injection}$ + $Q_{opening}$). Given the tightness of the enclosure, except for the rectangular opening, potential leaks from the enclosure can be neglected. The generator was connected to the right side of the experimental enclosure using a Pneurop DN40 connection. A filter sampling devices respecting the isokinetic rules are added respectively at the outlet of the generator and in the injection duct of the enclosure, to check the mass flow rates of the produced aerosol q_{gene} and of the aerosol injected into the enclosure q_o (from C_{inj}).

- (2) The helium concentration inside the enclosure is controlled via a mass spectrometer connected to the extraction circuit of the enclosure. We should mention that the extraction volume flowrate corresponds to an air renewal rate of about 7 h^{-1} in the enclosure in order to obtain U_{ope} = 0.5 m/s. Then to reach the

equilibrium, we have to wait about 5 times of the renewal time of one volume, that corresponds to about 40 min. Once the equilibrium is reached inside the enclosure, the disturbing jet (counter-current or parietal jet) is initiated, generating a velocity V_{dist} at 3 cm near the opening. The velocity V_0 measured at the nozzle exit of the jet is controlled via a valve. Recalling that the disturbance circuit is a closed one and consists of a fan, a valve, a duct and a blowing nozzle.

- (3) The helium concentration at equilibrium inside the enclosure C_{gas-in}, was then measured via a gaseous sampler connected to a mass spectrometer at the extraction duct. Simultaneously, a filter sampler connected to a piston type pump was added at the extraction duct of the enclosure to measure the aerosol concentration inside the enclosure, at the equilibrium and during 1 min. A post-processing via the fluorimetric measurements gave access to the concentration inside the enclosure $C_{aerosol-in}$. Note that the gaseous and particulate measurements were done during the disturbance generation.

- (4) Near the opening, we aimed to detect the gaseous and particulate concentrations resulting from backscattering phenomena. For that, many gaseous samplers (1 mm diameter tubes) and particulate filter samplers (40 mm diameter) were placed around the opening in order to collect the amount of gas and particles diffused outside the enclosure. The number and location of the samplers is further showed. The gas samplers were connected together to a mass spectrometer to continuously acquire the helium concentration. During each disturbance generation of a known velocity V_{dist}, the helium concentration tended to stabilize over an interval of time following the disturbance. The equilibrium value was noted $C_{gas-out}$. Each particulate sampler was connected to a piston type pump that delivers air to a volumetric meter. The aerosol mass collected on the filter was then diluted in an ammonia distilled water solution and analyzed in a conventional fluorimetric analysis as mentioned above. The averaged concentration detected from the filters was written $C_{aer-out}$. The sampling time was around 20 min in our experiments.

We should note that in a first approach, the sampling of gas and particles were performed independently of each other: the gas was sampled using the tubes near the opening and the particles were sampled using the filters placed near the opening. In a second approach, we performed sampling of gas and particles at same location in order to compare them adequately: particles sampling was performed using 3 filters located near the opening and the common gas sampling tube was connected to the particulate pumps.

Then, the equilibrium mean values over the sampling time C_{gas-in}, $C_{aerosol-in}$, $C_{gas-out}$ and $C_{aerosol-out}$ were used for the calculation of the local gaseous and particulate backflow coefficients K_{gas} *(%)* and $K_{aerosol}$ *(%)* (Eq. 3-9 and Eq. 3-10).

$$K_{gas}\ (\%) = \frac{C_{gas-out} - C_{gas-ambient}}{C_{gas-in}} \qquad \text{(Eq. 3-9)}$$

$$K_{aerosol}\ (\%) = \frac{C_{aerosol-out} - C_{aerosol-ambient}}{C_{aerosol-in}} \qquad \text{(Eq. 3-10)}$$

$C_{gas-ambient}$ and $C_{aerosol-ambient}$ are respectively the concentrations of helium and aerosol measured near the opening at initial conditions before the generation of the disturbing jet. We should mention that we consider gaseous and particulate ambient concentrations for the gas and aerosol concentrations at the enclosure extraction. However, since they are negligible in comparison with the concentrations at the enclosure extraction, we did not add them in Eq. 3-9 and Eq. 3-10.

We define the gaseous and particulate backflow detection threshold for all configurations in the following by the minimum helium and aerosol concentration detected near the opening $C_{gas-out} - C_{gas-ambient}$ = 5 ppm and $C_{aerosol-out} - C_{aerosol-ambient}$ = 3.10^{-4} mg/m^3.

In order to compare various scenarios with each other and with the numerical results, we chose to draw the evolution of the backflow coefficient *K* (%) as a function of the non-dimensional V_{dist}/U_{ope} aeraulic parameter as explained earlier.

3.1.2.2 Results for internal counter-current disturbing jet of the gaseous/particulate pollutants and rigid/flexible frontal wall

3.1.2.2.1 Results of gaseous pollutant with the rigid frontal wall

First, we measured the gaseous concentration. For the gaseous pollutant, 19 gaseous samplers (1 mm diameter tubes) were disposed around and in front of the opening and connected to a mass spectrometer in order to collect the amount of helium coming from the backflow phenomenon as shown in Figure 3-22.

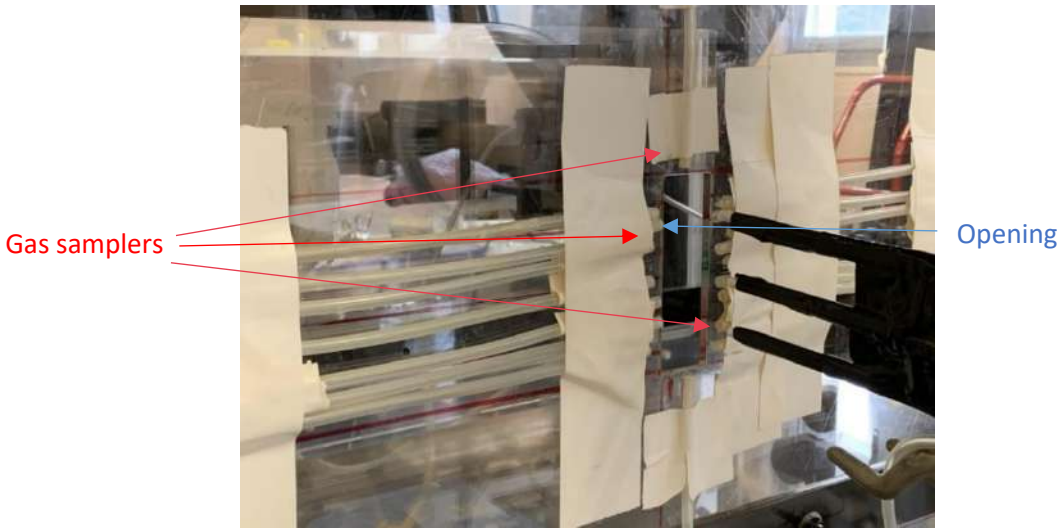

Figure 3-22 Experimental enclosure with the gaseous samplers around the opening in the case of a counter-current perturbation

Figure 3-23 shows the evolution of gaseous pollutant backflow coefficient *K (%)* versus V_{dist}/U_{ope} for the three values of inflow velocity at the opening: 0.5, 1 and 1.5 m/s. These results were obtained in the case of a counter-current internal free jet disturbance on the rigid frontal wall of the enclosure. It is reminded that V_{dist} values were measured with the presence of the frontal wall of the enclosure as mentioned before. Note these results shown below corresponds to the gas concentrations measured with the tubes around the opening independently of the aerosol samplers. The determination of uncertainties is shown in appendix 2.

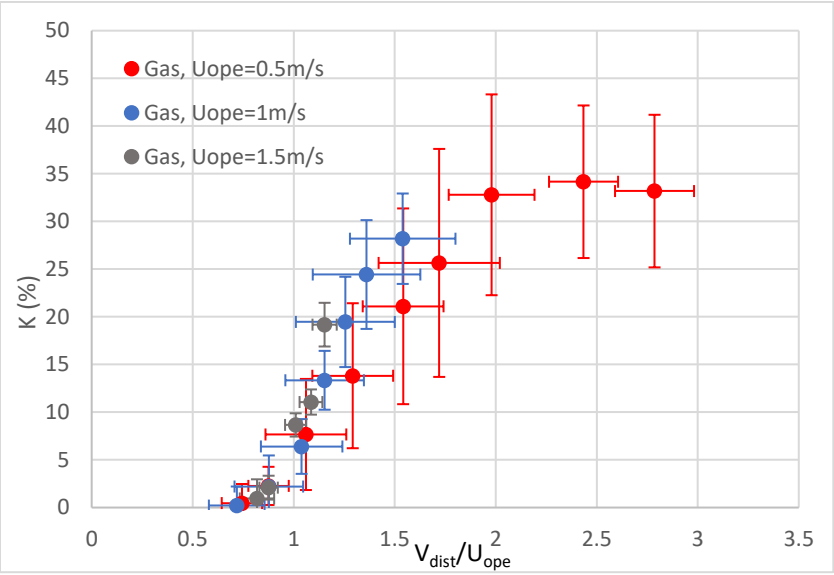

Figure 3-23 Evolution of the gas backflow coefficient K (%) as a function of V_{dist}/U_{ope} for the three values of the inflow velocity at the opening (0.5, 1 and 1.5 m/s) in the case of a counter-current internal free jet disturbance

During our experiments, we did not detect any backflow signal near the opening for V_{dist}/U_{ope} < 0.5 for each of the three inflow velocities.

The backflow phenomenon starts to appear for a disturbing velocity corresponding to the ratio V_{dist}/U_{ope} about 0.7 regardless of the value of the inflow velocity. We could also note that the three evolution curves are overlapped for $V_{dist}/U_{ope} \leq 1 \pm 0.2$. Note that in this part of the figure, the backflow rate does not exceed 1%.

Beyond this value, for $1 \leq V_{dist}/U_{ope} \leq 2$, the global trend of the three curves is an increasing backflow coefficient *K* (%) when V/U_{ope} increases. However, despite the small differences between the curves, it can be deduced that the appearance of the backflow coefficient curves is rather close, with the uncertainties, regardless of the dynamic containment velocity imposed on the opening. This part of the figure clearly shows that the curve of the evolution of the backflow coefficient *K* (%) in function of V_{dist}/U_{ope} have the same tendency regardless of the value of the inflow velocity U_{ope}.

When $V_{dist}/U_{ope} \geq 2$, the curve corresponding to U_{ope} = 0.5 m/s reaches an almost constant value, about 33 %, that reveals a quasi-stable concentration near the opening. The magnitude of the jet has no longer effect on the quantity of the tracer captured near the opening outside the enclosure, hence on the backflow coefficient. It was not possible to observe this phenomenon with higher U_{ope} (1 and 1.5 m/s) because the disturbance fan was not designed for generating higher flowrates. Later on, using numerical simulations, we will see that curves corresponding to U_{ope} = 1 m/s and 1.5 m/s reach also a constant value.

For low values V_{dist} of the disturbing jet ($V_{dist}/U_{ope} \leq 2$), the backflow phenomenon appears as transient puff induced by the competition of the inflow and the disturbing jet. The concentration of pollutants near the opening, and hence the local backflow coefficients, tend to increase when the frequency of puff and hence V_{dist} increase. For higher values of V_{dist} ($V_{dist}/U_{ope} \geq 2$), the backflow phenomenon becomes quasi-permanent and continuous. The concentration near the opening is equal to the concentration of the jet

that reaches the opening, and hence equal to that inside the enclosure, but more or less diluted by air flows near the opening. Then the local backflow coefficient tends to be stable or slowly increasing while the backflow phenomenon is continuous.

3.1.2.2.2 Results of particulate pollutant with the rigid frontal wall

For the particulate pollutant, 5 filter samplers are placed around the opening in order to collect the amount of particles coming from the backflow phenomenon as shown in Figure 3-24: at the top and bottom at about 1 cm (± 0.2 cm) from the opening edge, at the right and left at about 1 cm (± 0.2 cm) from the opening edge and facing the opening at about 6 cm (± 0.5 cm). Each sampler is then connected to a piston type pump that delivers air to a volumetric meter. The sampling velocity of these samplers is very low (between 0.22 m/s to 0.25 m/s) in order to do not disturb the flow near the opening.

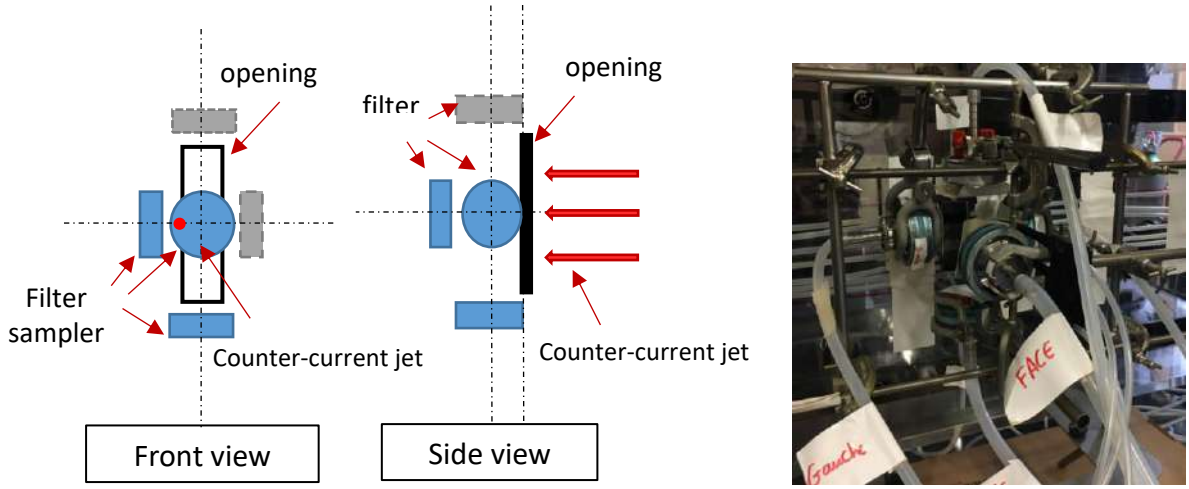

Figure 3-24 Left: diagram of the positions of the filter samplers around the opening in the case of a counter-current perturbation (front and side views) – Right: 5 filter samplers located around the opening of the enclosure

Figure 3-25 shows the evolution of the backflow coefficient *K (%)* as a function of V_{dist}/U_{ope} for the three values of the inflow velocity at the opening (0.5, 1 and 1.5 m/s) in the case of the particulate pollutant of 5 µm aerodynamic diameter. These results were obtained in the case of a counter-current internal free jet disturbance on the rigid frontal wall of the enclosure. Note that these V_{dist} values are measured with the presence of the frontal wall of the enclosure as mentioned before. Results shown below corresponds to the concentrations measured thanks to the 5 filter samplers located near the opening as mentioned earlier. The uncertainties are detailed in appendix 2.

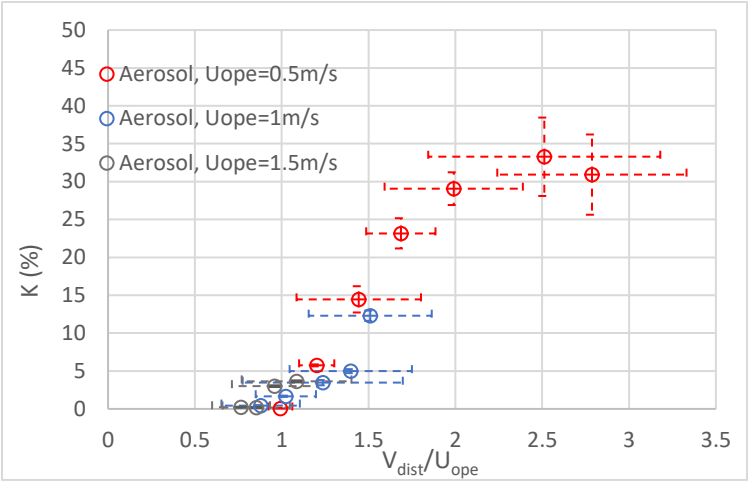

Figure 3-25 Evolution of the backflow coefficient K (%) versus V_{dist}/Uope for the particulate pollutant of 5 µm, for the three values of the inflow velocity at the opening (0.5, 1 and 1.5 m/s) in the case of a counter-current internal free jet disturbance

It can be seen that, regardless of the value of the flowrate at the opening, the backflow phenomenon occurs for a disturbing velocity corresponding to the ratio V_{dist}/U_{ope} around 0.7. For V_{dist}/U_{ope} < 0.7, no signal was detected near the opening. For 0.7 ≤ V_{dist}/U_{ope} ≤ 0.9, the backflow coefficients correspond to the trigger of the backflow and does not exceed 0.2 %. For 0.9 ≤ V_{dist}/U_{ope} ≤ 2, the global trend of the curves is an increasing *K (%)* when V_{dist}/U_{ope} increases. We can say that the appearance of the backflow rate curves is rather close, with the uncertainties, regardless of the flowrate of the dynamic containment imposed on the opening. When $V_{dist}/U_{ope} \geq 2$, the curve corresponding to U_{ope} = 0.5 m/s starts to stabilize (between 29 % and 33 %), that reveals a concentration equilibrium regime near the opening as for the case of gaseous pollutant.

We should note here that 5 sensors were located near the opening to collect the local amount of the aerosol that backflows outside the enclosure. These sensors could have an effect on the air flows produced near the opening, hence affecting the nominal situation and promoting or decreasing the backflow phenomenon. Later, the presence of the envelope around the enclosure eliminates the necessity of these sensors and will protect against the potential intrusive effect of these sensors around the opening as we will see further.

We can say that for the gaseous and particulate pollutants, the backflow coefficient *K* (%) depends on the value of the aerodynamic parameter V_{dist}/U_{ope}. Then, the form of the backflow curve is unique regardless of the value of the inflow velocity U_{ope} at the opening (for U_{ope} = 0.5 m/s, 1m/s and 1.5 m/s).

For the following results parts, we measured the gaseous and particulate concentrations at the same location in order to compare them at same conditions as shown in Figure 3-26. Then, 3 filter samplers connected to 3 pumps were placed around the opening in order to collect the amount of particles coming from the backflow phenomena; note that we added 3 filters not only to simplify but optimize the experimental setup: we have chosen the sampling points showing the most pronounced backflow effects. The collected amount of particles from the filters was noted $C_{aer-out}$. Simultaneously, a gaseous sampler was connected to the pumps in order to continuously detect the amount of helium coming from the backflow effect at the same locations near the opening.

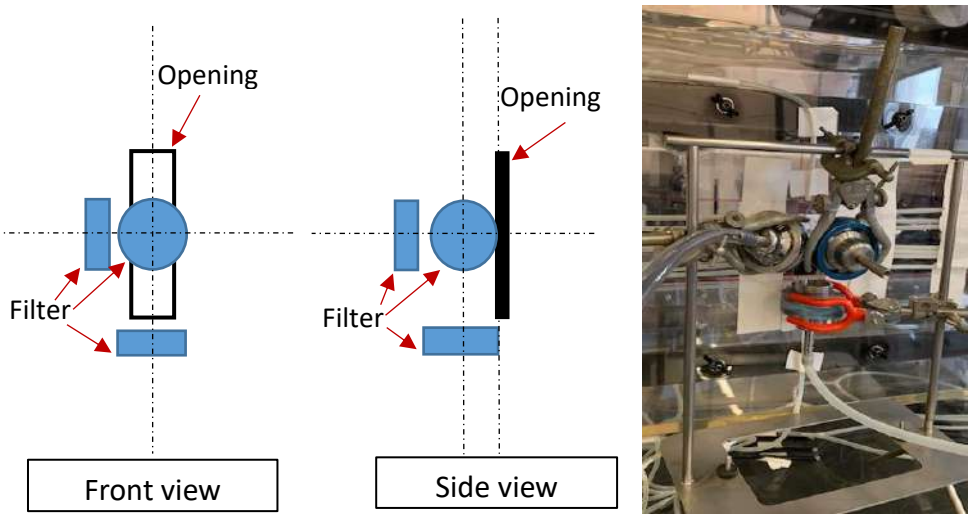

Figure 3-26 Left: diagram of the locations of the filter samplers around the opening in the case of a counter-current perturbation (front and side views) – Right: 3 filter samplers located around the opening at left, face and down positions

3.1.2.2.3 Comparison of results for gaseous/particulate pollutants within the enclosure of rigid/flexible frontal wall

In the following, experiments were done using 3 filter samplers located near the opening (left, face and down) and where the sampling of gas and aerosol was done at same location in order to compare them properly. Simultaneously, they were done first on the rigid frontal wall, then on the flexible frontal wall. Figure 3-27 shows the evolution of the backflow coefficient *K (%)* as a function of V_{dist}/U_{ope} for an entrance velocity at the opening U_{ope} = 0.5 m/s in the case of a counter-current internal free jet disturbance for the gaseous and particulate pollutant of 5 µm and for the enclosure with rigid frontal wall and soft frontal wall. The uncertainties determination is shown in appendix 2.

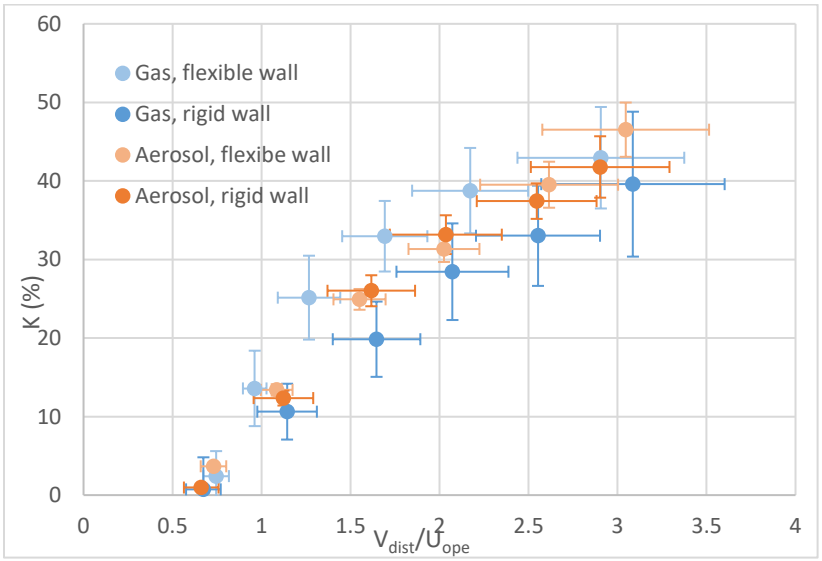

Figure 3-27 Evolution of the backflow coefficient K (%) versus V_{dist}/U_{ope} for an inflow velocity at the opening U_{ope} = 0.5 m/s in the case of a counter-current internal free jet disturbance for the gaseous and 5 µm particulate pollutants and for the enclosure with rigid frontal wall and flexible frontal wall

We can observe the four curves follow the same global tendency and the backflow phenomenon starts to appear for a disturbing velocity corresponding to the ratio V_{dist}/U_{ope} about 0.7 for all of them. For $0.65 \leq V_{dist}/U_{ope} \leq 2$, the global trend of the four curves is an increasing backflow coefficient *K* (%) when V_{dist}/U_{ope} increases. When $V_{dist}/U_{ope} \geq 2$, the four curves follow a very slowly increasing tendency. We mention that in this part, we used only 3 samplers near the opening, unlike the part 3.3.1.2.2.2 (Figure 3-24) where we used 5 samplers and where the backflow coefficient *K* (%) is quasi-constant for $V_{dist}/U_{ope} \geq 2$. This highlights the effect of the samplers number on the backflow coefficient *K* (%) (see appendix 3).

Comparing the gas and aerosol curves, we observe that the backflow coefficient is in the same order of magnitude for the gas and for the 5 µm aerosol, taking account the measurement uncertainties. We can say that the behavior of the gaseous and particulate pollutant is similar in terms of backflow coefficient for these configurations: effectively, this result is valid for our small-size geometry and for our aeraulic conditions. Taking into account the aeraulic conditions near the opening and the granulometric characteristics of the aerosol, we verified that our experimentations are done in Stokes equilibrium regime where particles follow completely the gas behavior as shown in chapter 1. We will show further in the numerical part the calculation procedure of the Stokes number in chapter 4 (4.1.3).

Comparing the results of rigid and flexible frontal wall, we observe that the backflow coefficients are similar in the two cases, taking account the measurement uncertainties. Finally, in our conditions, the backflow phenomenon does not depend on the nature of the frontal wall. These can be due to the fact that for the counter-current jet facing the opening, the flow at the opening is directed by the energy of the jet flow that could induce backflow. Moreover, the effect of the vibrations and deformation of the flexible vinyl frontal wall on the backflow is negligible compared to the influence of the vortices created by the competition between the counter-current jet and the inflow.

Comparing the four curves, we can conclude that, despite the small differences between the curves, the appearance of the backflow rate curves is rather close, taking into account the uncertainties. Then, we can clearly say that in our experimental conditions, the nature of the pollutant and of the frontal wall material have no significant effect on the backflow coefficient. We should recall that these results corresponding to the gaseous/particulate behavior and rigid/flexible frontal wall are only valid for our experimental conditions such as our small-size geometry, the nature of the disturbing jet (counter-current internal jet), the size of aerosol, the dimensions of the opening and the aeraulic conditions related to the velocity near the opening.

We should also note that the number and distance of filters to the opening do influence our experimental results. When using 5 filters near the opening, the maximum value of the particulate backflow coefficient was about 33 % and reach a stabilized value. Decreasing this number to three filters located closer to the opening, the maximum value of the particulate backflow coefficient increases to about 41 %. Simultaneously, we performed experiments using one filter placed at 3 cm facing the opening, the maximum value of the particulate backflow coefficient increases to 65 % for V_{dist}/U_{ope} of about 3. Then our local backflow results are dependent on the sampling characteristics near the opening. We should mention that these filters were positioned in optimal way to detect the backflow near the opening. However, some filters detect higher concentration than others. Then increasing the number of filters highlight the effect of concentration dilution near the opening and decreases the value of the backflow coefficient *K*. Appendix 3 shows a numerical study of the influence of the samplers number and their positions to the opening on

the backflow coefficients and recommends that numerical simulations have to be done as close as possible to experimental conditions.

3.1.2.3 *Results for internal parietal disturbing jet of the gaseous/particulate pollutants and rigid/flexible frontal wall*

In this part, the configuration of an internal parietal jet was considered. Experiments were done using 3 filter samplers located near the opening (left, face and down) in order to follow the procedure of the counter-current disturbance and to compare the results of the frontal and parietal jets properly. The sampling of gas and aerosol was done at the same locations in order to compare the behavior of the gaseous and particulate pollutants properly. Simultaneously, they were done first on the rigid frontal wall, then on the flexible frontal wall. We should mention that the velocity V_{dist} is measured locally near the opening using an anemometer, in the case of the presence of the frontal wall. Figure 3-28 shows the evolution of the backflow coefficient *K (%)* as a function of V_{dist}/U_{ope} for an inflow velocity at the opening U_{ope} = 0.5 m/s. The results concerned the configuration of an internal parietal free jet disturbance, for the gaseous and 5 µm particulate pollutants, and for the enclosure with rigid and flexible frontal walls.

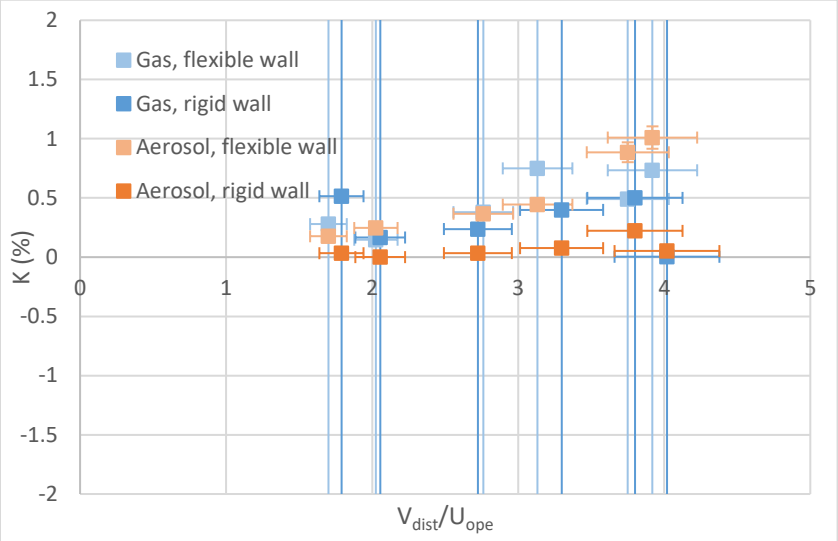

Figure 3-28 Evolution of the backflow coefficient K (%) versus V_{dist}/U_{ope} for an inflow velocity at the opening U_{ope} = 0.5 m/s in the case of an internal parietal free jet disturbance for the gaseous and 5 µm particulate pollutant and for the enclosure with rigid and flexible frontal walls respectively

Clearly, we distinguish on the Figure 3-28 that the threshold onset of the backflow phenomenon corresponding to the ratio V_{dist}/U_{ope} of about 1.7 for a parietal disturbing velocity. Beyond this value, the backflow phenomenon is still progressing but with small intensity which does not exceed 1 % for the four curves. Comparing the four curves, we observe that they are at the same order of magnitude tacking into account the large uncertainties. We can also notice that the backflow coefficients for the flexible frontal wall are little bit higher than that of the rigid frontal wall for $3 \leq V_{dist}/U_{ope} \leq 4$. We mention that uncertainties on the backflow coefficients in Figure 3-28 are about $\pm$ 5 %.

For these values of disturbance velocities, we can say that the behavior of the gaseous and particulate pollutants is similar in terms of backflow coefficients in one hand. On the other hand, the flexible frontal wall seems to induce a little more backflow than the rigid frontal wall. However, considering the small values of *K* (%) that does not exceed 1 %, we cannot predict their behaviors for higher disturbing jet

velocities. Numerical simulations on higher values of V_{dist}/U_{ope} were done for the case of rigid frontal wall that show that the backflow coefficient increases when V_{dist}/U_{ope} increases as we will see in chapter 4.

3.1.2.4 Comparison of the local backflow between the frontal and parietal disturbances for the gaseous and particulate pollutants

Here we aim to compare the results corresponding to the internal counter-current disturbing jet and the internal parietal jet. As mentioned before, the sampling of the gaseous and particulate pollutants was done at the same location using 3 filter samplers for each disturbance configuration in order to compare them in a good way. Then any difference between the results of the two disturbance configurations could only be due to the nature of the disturbing jet. In the following, we present the results related to the rigid frontal wall, since as we showed earlier, there was no significant difference between the backflow coefficients of the rigid frontal wall and those of the flexible frontal wall. Figure 3-29 shows the evolution of the backflow coefficient *K (%)* as a function of V_{dist}/U_{ope} for an inflow velocity at the opening U_{ope} = 0.5 m/s, in the case of a rigid frontal wall disturbance for the gaseous and 5 µm particulate pollutants and for the two type of internal disturbing jets.

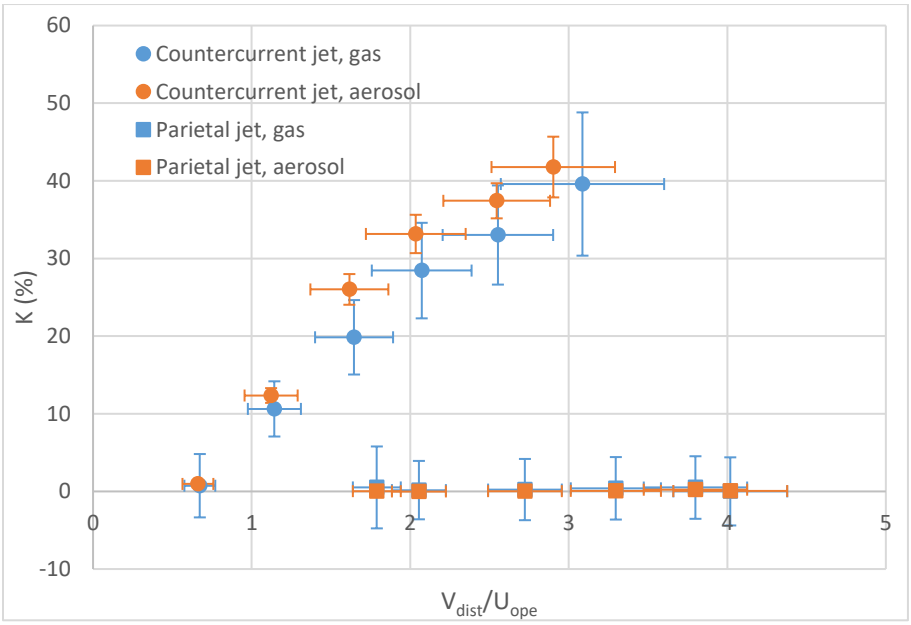

Figure 3-29 Evolution of the backflow coefficient K (%) as a function of V_{dist}/U_{ope} for an inflow velocity at the opening U_{ope} = 0.5 m/s in the case of a rigid frontal wall disturbance for the gaseous and 5 µm particulate pollutants and for the internal counter-current and parietal disturbing jet .

First of all, we compare the onset of the backflow phenomenon corresponding to the counter-current and parietal disturbing jets. The backflow phenomenon corresponding to the internal counter-current disturbing jet for the gaseous and particulate pollutants is triggered for a disturbing jet of V_{dist}/U_{ope} of about 0.7. In the case corresponding to the internal parietal jet, triggering takes place at higher value of V_{dist}/U_{ope}, of about 1.7.

Secondly, when comparing the values of the backflow coefficients for all the configurations tested, we conclude clearly that the backflow coefficients are higher for the case of the counter-current jet. Indeed,

for V_{dist}/U_{ope} = 3, the backflow coefficient corresponding to the counter-current jet reaches a maximum of about 39 % for the gaseous pollutant and 41 % for the particulate pollutant. However, for the same value of V_{dist}/U_{ope}, the backflow coefficient corresponding to the parietal disturbing jet does not exceed 0.07 % for the gaseous and particulate pollutants.

The difference between the backflow coefficients corresponding to each disturbing jet could be explained by the effect of the orientation of the disturbance jet with respect to the plane at the opening as we will further show.

3.2 Global quantification of the backflow phenomenon

In order to collect the overall quantity of the pollutants emitted outside the ventilated enclosure without the limitations of the sampling filters placed around the opening, we designed an outer envelope that we put around the current experimental enclosure. First, we describe the dimensions of this envelope. Secondly, we evaluate numerically and experimentally using PIV the impact of this envelope on the flow around the opening of the tested enclosure. Then we performed characterization of the air exchange rate and particles deposit measurement inside the envelope. After that we present the procedure for the global quantification of the backflow and the global backflow curves under the effect of a counter-current and a parietal disturbing jets. Like the previous study in the experimental enclosure, we varied the nature of the pollutant (gaseous and particulate pollutant) and the nature of the frontal wall (rigid and flexible frontal wall).

3.2.1 Description of the envelope

In our study, to collect the overall quantity of the pollutants emitted outside the ventilated enclosure, we designed an envelope that we put around the current experimental enclosure. Its dimensions should be chosen adequately to ensure that it does not perturb the flow around the opening or generates an undesirable flow.

Figure 3-30 and Figure 3-31 show respectively the global 3D view and the experimental apparatus of the ventilated enclosure surrounded by the envelope. This envelope was built, supplied and installed by YSEBAERT Company.

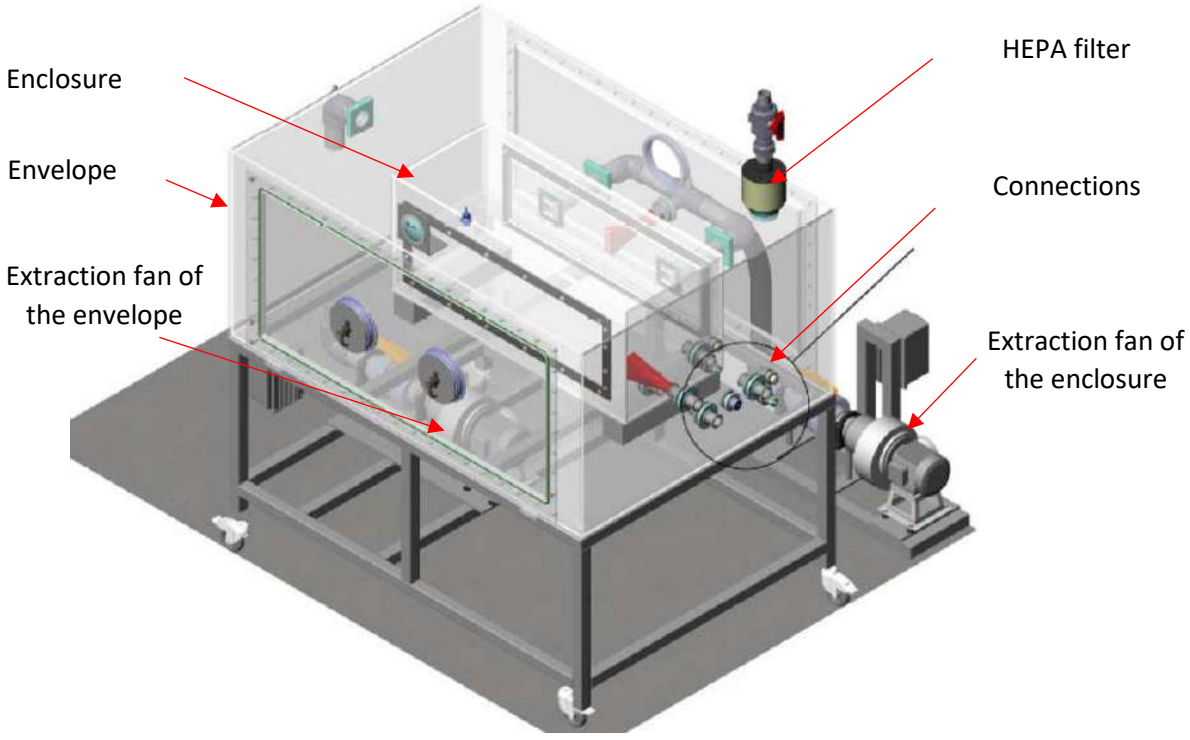

Figure 3-30 3D view of the envelope surrounding the enclosure

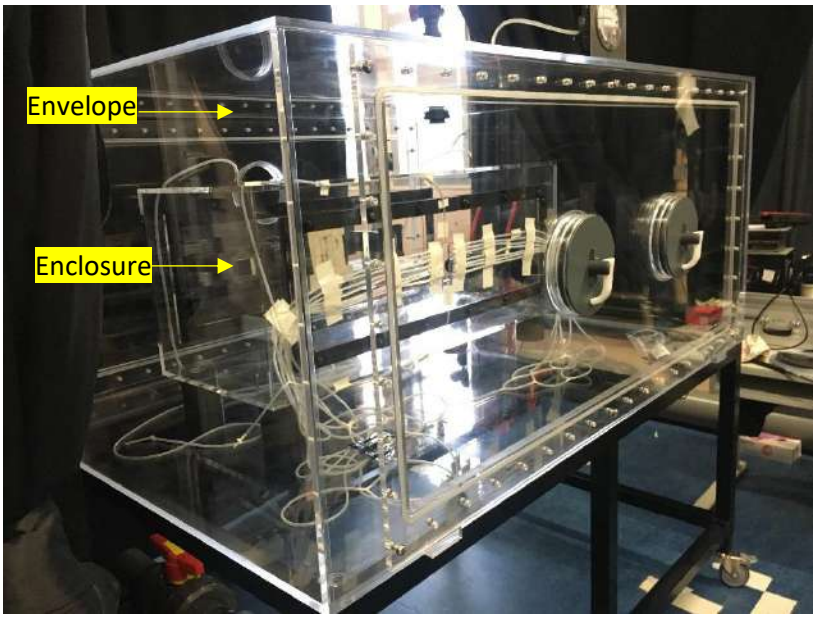

Figure 3-31 Experimental envelope surrounding the enclosure

The envelope is a gloves box body made of fully transparent bonded PMMA (Plexiglass®) walls and parallelepipedal shape. The external dimensions are (1800 × 1308 × 824) mm^3. The enclosure walls have a thickness of 12 mm. The front panel is removable allowing the implementation of the enclosure and the access to connections, and is equipped with two gloves ports (diameter 186 mm). The rear wall is also removable allowing access to the connections and is also equipped with one round of glove (diameter 186 mm). It contains two extraction units connected to the extraction units of the enclosure. The right side wall is equipped with four connections: one electric connection and three Pneurop DN 40 type connections for flow disturbances generation and aerosol injection. Each of the three connections is connected through a pipe to the enclosure. The left side wall contains a circular hole of 75 mm diameter connected to the enclosure extraction duct. The upper wall is connected to a HEPA filter holder, to ensure a clean air admission into the envelope. The nominal airflow rate is about 10 m^3/h. The pressure is monitored by a pressure sensor on the top of the envelope. Four brackets are added under the enclosure to maintain it inside the envelope. The support frame is painted of matte black color in order to prevent the laser reflections; its height is about 900 mm. The extraction duct is equipped with a control valve and a 230 V fan allowing a nominal flowrate about 50 m^3/h. The fan is implemented on the support frame under the envelope.

Recalling that the total volume of the enclosure is 0.3 m^3 and the total volume of the envelope is 1.94 m^3. Then the useful volume concerned by the renewal of air around the experimental enclosure is about 1.64 m^3.

3.2.2 Evaluation of the impact of envelope on the flow near the opening

In order to check the impact of the presence of the envelope on the flow near the opening, preliminary numerical simulations were performed that show that air exchange rate within the envelope up to 5 h^{-1} does not modify the flows profiles in the opening as we will see in the next chapter.

PIV measurements

In parallel, we used the PIV technique in order to get access to the velocity fields of the flow near the opening in the presence or not of the envelope for successive air exchange rates imposed inside the envelope. The implementation of acquisition devices around the envelope corresponding to the median vertical visualization plane of the opening is shown in Figure 3-32 and Figure 3-33.

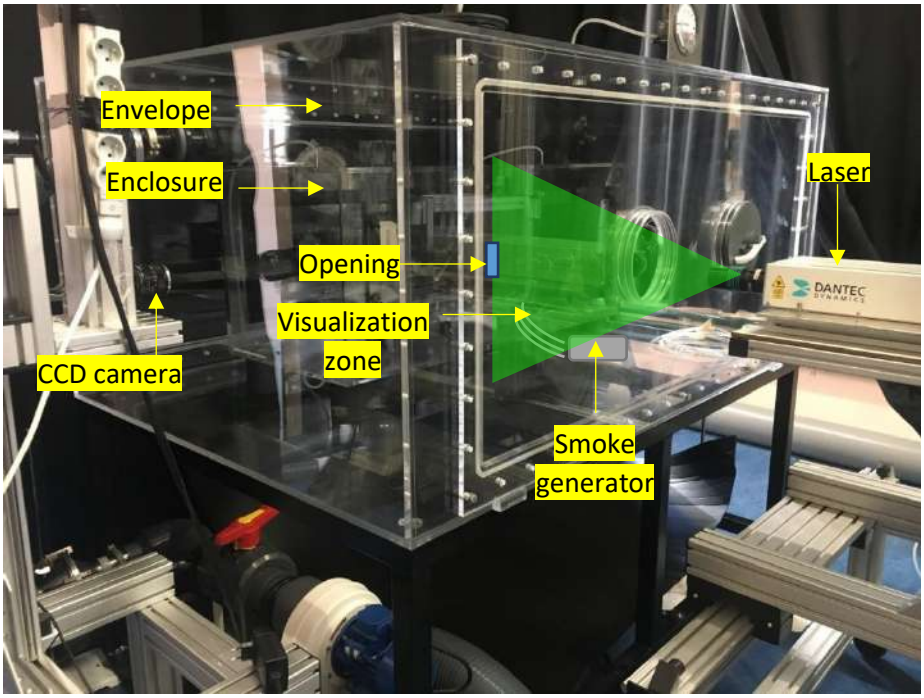

Figure 3-32 Picture of devices implementation for the PIV experiments inside the envelope

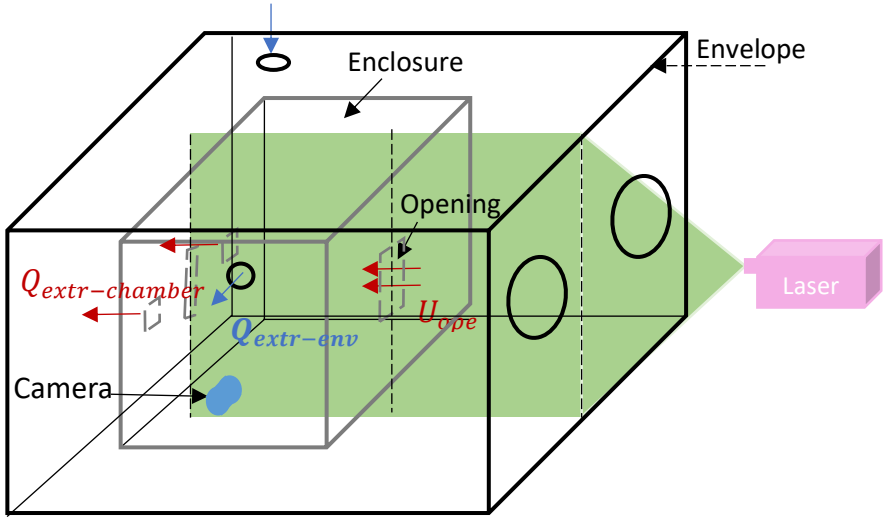

Figure 3-33 Diagram of the PIV devices used for the vertical visualization inside the envelope

A description of the PIV devices used for the acquisition and the post-processing is shown in chapter 2.

The smoke generator was placed inside the envelope near the opening of the enclosure. It generated tracer particles traveling from the envelope towards the enclosure inside by the means of the extraction

system of the enclosure. We captured visualization fields oriented through the vertical median plane of the opening. In this case, the light source were located facing the frontal wall of the envelope as shown in Figure 3-32 and Figure 3-33 and emits a thin (1-3 mm) light sheet oriented vertically towards the opening central plane of the enclosure. The camera was located facing the left side of the envelope in order to capture the vertical median plane in the envelope passing through the opening of the enclosure. The captured field of view was a square of (0.29 x 0.29) m^2.

Experiments took place in several conditions related to the envelope: first it worked without the presence of the frontal wall of the envelope, second while maintaining the presence of the frontal wall and without any air extraction in the envelope (R = 0 h^{-1}), then while varying the air exchange rate of the envelope, R = 3, then 6 and 10 h^{-1} (the volume taken into account here was the useful volume). Simultaneously, we varied the extraction rate of the enclosure corresponding to U_{ope} = 0.5 m/s, 1 m/s and 1.5 m/s.

On the Figure 3-34, time-averaged velocity fields acquired in vertical plane at the opening of the enclosure were obtained with the PIV process. Mean velocity vectors are derived from 100 images pairs analysis, corresponding to U_{ope} = 1 m/s at the enclosure opening and with an air exchange rate in the envelope fixed at 3 h^{-1}.

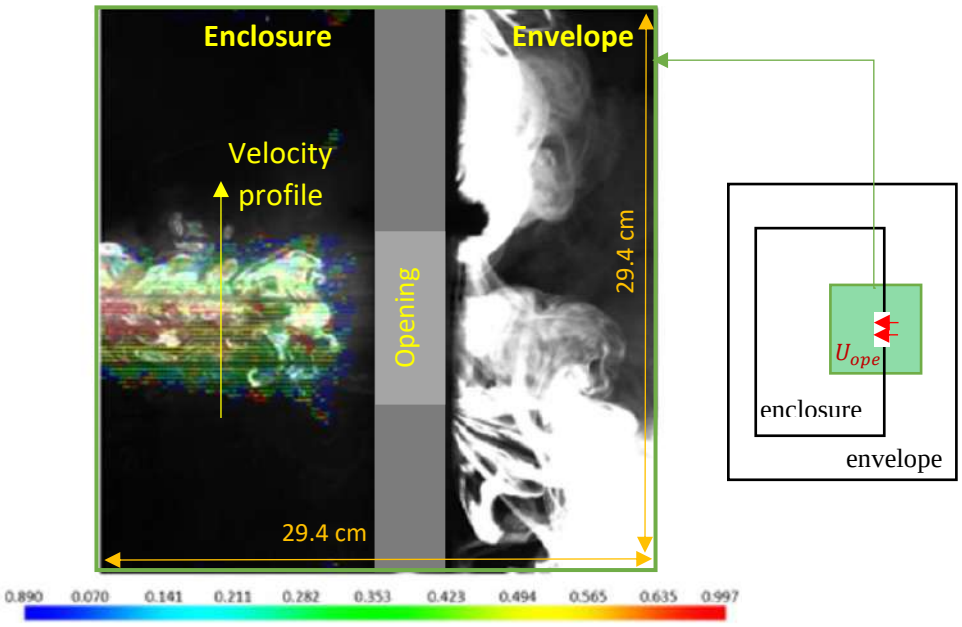

Figure 3-34 Time-averaged velocity fields acquired near the opening for an inflow velocity U_{ope} = 1 m/s and an air exchange rate of the envelope R =3 h^{-1}, in the vertical median plane (0,29 x 0,29) m^2

Velocities profiles

Due to lack of signal at the opening, the velocity profile was measured at 8 cm from the opening inside the enclosure from the vertical fields in each case of exchange rate. Figure 3-35, Figure 3-36 and Figure 3-37 show the velocities profiles deduced from the vertical velocity fields corresponding to respectively U_{ope} = 0.5 m/s, 1 m/s and 1.5 m/s and to each R value experimental case:

1) Open envelope: without the presence of the frontal wall of the envelope,
2) Closed envelope, R = 0 h^{-1}: without any extraction flow rate in the envelope,
3) Closed envelope, R = 3 h^{-1},

4) Closed envelope, R = 6 h^{-1} ,
5) Closed envelope, R = 10 h^{-1}.

Results for U_{ope} = 0.5 m/s

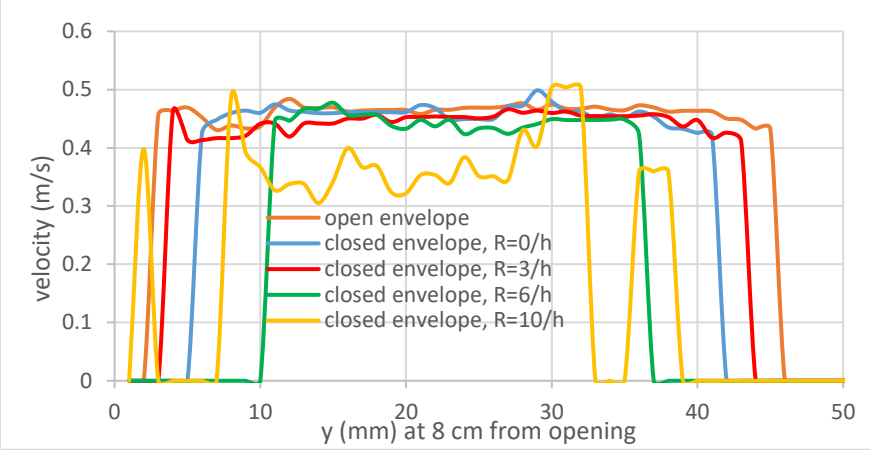

Figure 3-35 Velocity profiles deduced from the vertical velocity fields at 8 cm inside the enclosure corresponding toU_{ope} = 0.5 m/s and to each R experimental case

While comparing the curves deduced from the vertical fields as shown in Figure 3-35, we found that the curves are overlapped except for the case of an air exchange rate of the envelope corresponding to R = 10 h^{-1}. Here we can see that varying the air exchange rate of the envelope from 0 to 6 h^{-1} did not influence the velocity profile of the flow near the opening for U_{ope} = 0.5 m/s. However, the presence of the envelope with an air exchange rate of 10 h^{-1} did impact the flow near the opening for U_{ope} = 0.5 m/s. Note that the variations in the velocities near the opening borders were due to a lack of resolution and 3D effects due to our experimental conditions.

Results for U_{ope} = 1 m/s

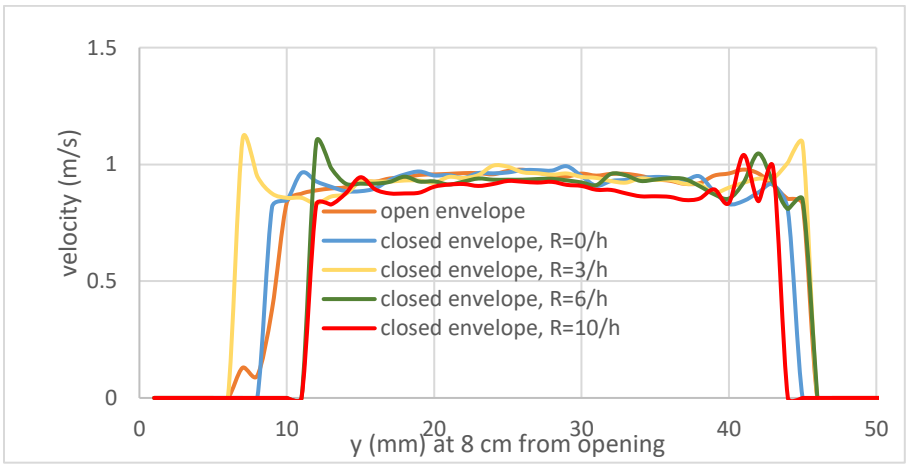

Figure 3-36 Velocity profiles deduced from the vertical velocity fields at 8 cm inside the enclosure corresponding to U_{ope} = 1 m/s and to each R experimental case

As we can see from Figure 3-36, the curves deduced from the vertical fields are quite overlapped, hence showing that neither the presence of the envelope frontal wall nor the variation of the renewal rate influenced the velocity profile of the flow near the opening for U_{ope} = 1 m/s.

Results for U_{ope} = 1.5 m/s

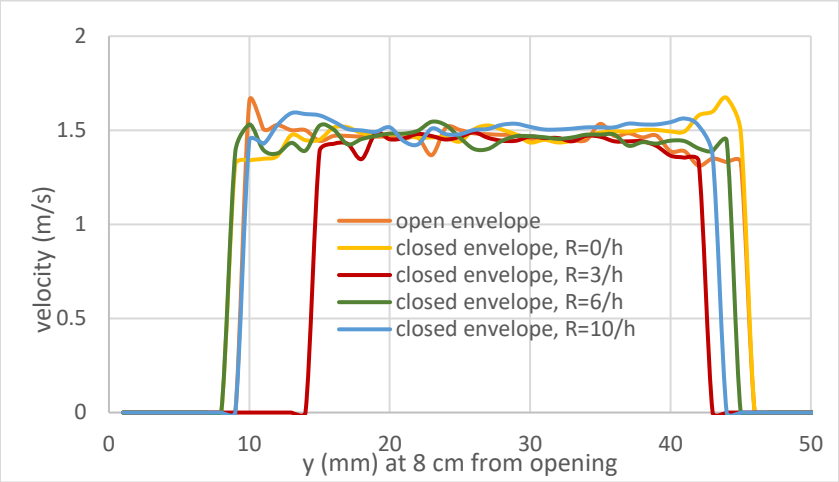

Figure 3-37 Velocity profiles deduced from the vertical velocity fields at 8 cm inside the enclosure corresponding to U_{ope} = 1.5 m/s and to each R experimental case

As we can see from Figure 3-37, the four curves deduced from the vertical *f*ields are quite overlapped, hence showing that the presence of the frontal wall of the envelope regardless the air exchange rate, did not influence the velocity profile of the flow near the opening for U_{ope} = 1.5 m/s.

Discussion

As we have seen in the vertical velocity profiles corresponding to U_{ope} = 0.5 m/s, 1 m/s and 1.5 m/s, the presence of the envelope did not influence the flow near the opening for exchange rates R = 0 h^{-1}, 3 h^{-1} and 6 h^{-1}. Concerning R = 10 h^{-1}, we found a drift of the flow only for U_{ope} = 0.5 m/s, while there was no impact on the flow for U_{ope} = 1 m/s and 1.5 m/s. Thus, in order to prevent the effect of a too strong effect of the ventilation, we limited in the following experiments, an air exchange rate of the envelope corresponding to R = 3 h^{-1}. This value corresponds to an extraction flowrate around 4.6 m^3/h considering the useful volume of the envelope.

3.2.3 Characterization of the air exchange rate and particles deposition measurement inside the envelope

In the following, we aim to characterize first the homogeneity of the ventilation inside the envelope and then the particles deposition rate in the envelope, experimentally and numerically. For this, an experiment was done where we injected simultaneously helium gas and 5 microns particles inside the envelope and we monitored their concentration in the extraction duct of the envelope. We started first by analyzing the gaseous part, then the particulate part. After that, we showed numerical simulations in order to validate our results.

3.2.3.1 *Characterization of the air exchange rate in the envelope and its homogeneity*

To check the homogeneity of the ventilation, we performed experimentally an analysis of the residence time distribution curve inside the envelope by using the gas tracing technique. An extraction flowrate through the envelope generating a velocity of around 1 m/s in the envelope outlet duct (nominal diameter DN = 40 mm), corresponds to a volumetric flowrate Q_{env} of around 4.7 m^3/h and a theoretical air exchange rate *R* about 3 h^{-1}.

Mostly, the ventilation of a room or an enclosure can be characterized from the analysis of the residence time distribution curve in the room monitoring a signal at the input of the studied system, determined experimentally by gas tracing. This method makes it possible to determine the real air renewal rate *R* of the room. During the renewal characterization tests, two situations may arise: the room is evenly or not evenly ventilated.

In the following experiment, we blocked the opening of the enclosure, thus preventing the presence of a flow passing through the enclosure. Using a calibrated flowmeter, we injected a continuous flow q_0 of helium at the inlet of the envelope. A continuous gas sample was measured at the extraction duct of the envelope and connected to a mass spectrometer, giving access to the helium concentration inside the envelope. Once the helium concentration reached the equilibrium state C_{eq} in the extraction, we stopped the injection, and the helium concentration curve began to decrease. The analysis of this decay curve gave us an information about the homogeneity of the exchange rate inside the envelope, as well as the value of the exchange rate.

In the case of a homogeneous ventilation, the concentration *C* of the gas tracer will decrease following the expression:

$$C = C_{eq}\, e^{-Rt} \qquad \text{(Eq. 3-11)}$$

Hence, R can be deduced experimentally by tracing the curve $\ln(C/C_{eq}) = f(t)$: it corresponds to the absolute value of the slope of the curve. In the case of a non-homogeneous ventilation, two (or more slopes) are obtained and R can be deduced from the values of the different slopes.

Figure 3-38 shows the time evolution of C/C_{eq} in the envelope for a closed enclosure and a theoretical exchange rate of the envelope *R* = 2.93 h^{-1}.

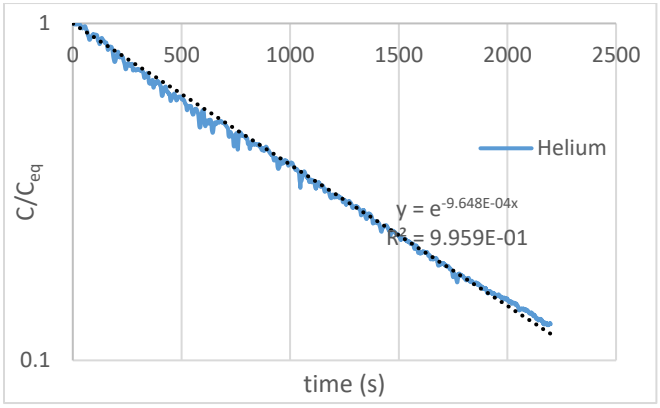

Figure 3-38 Time evolution of C/Ceq corresponding to the envelope with a closed enclosure and for a theoretical exchange rate of the envelope around 3 h^{-1}

As we see in Figure 3-38 and based on our laboratory protocol for calculating the renewal curves (Mocho, 2008), the curve represents one slope and represents a well-mixed zone inside the envelope. The experimental air exchange is deduced from the trend line and is around 3.5 h^{-1} ($\pm$ 0.3 h^{-1}) and the experimental volume flowrate of the envelope $Q_{helium,env}$ is about 5.5 m^3/h ($\pm$ 0.39 m^3/h).

3.2.3.2 Estimation of the particle deposition inside the envelope

The global quantification of the particles coming from the backflow consists in the collection of particles within the extraction duct of the envelope. However, deposition of particles inside the envelope occurs during their travel from the opening of the enclosure to the outlet of the envelope. In order to take into account this deposition of particles inside the envelope, we performed the following experiment shown in Figure 3-39.

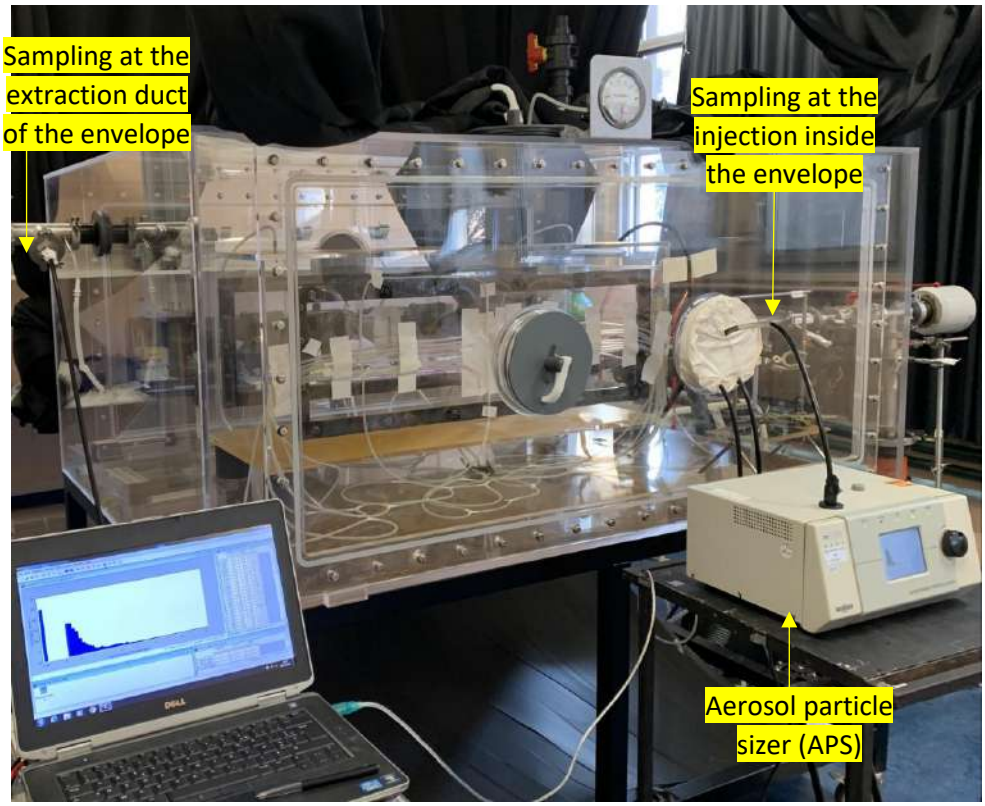

Figure 3-39 Estimation of the deposition rate of particles inside the envelope using an aerosol particle sizer

We injected 5 µm particles from an ultrasonic aerosol generator (LIXEA device) and using an injection duct of 40 mm diameter connected to the right side inside the envelope. Due to experimental restrictions, it was not possible to inject aerosol from the upper side of the envelope at the inlet. The injection flowrate was about 2.5 m^3/h. The enclosure was closed by blocking its opening. The extraction flowrate in the envelope was about 5.50 m^3/h. Using an aerosol particle sizer (APS system), we performed sampling within the injection duct in order to simultaneously measure the sampled particles size and concentration. Many samples were done at the injection with a sampling time of about 1 min for each sample; the samples mean value corresponds to $C_{injection}$. Once the equilibrium was reached inside the envelope, after about 30 min (based on the gaseous results), we performed sampling in the extraction duct of the envelope. To verify the concentrations equilibrium inside the envelope, several samplings were successively performed

in the outlet of the envelope to check the stability of the concentration within each sample. The sample time was about 2 min; the samples mean value corresponds to $C_{extraction}$. The mass concentrations for each particles diameter sampled in the injection and in the envelope extraction are given in Figure 3-40.

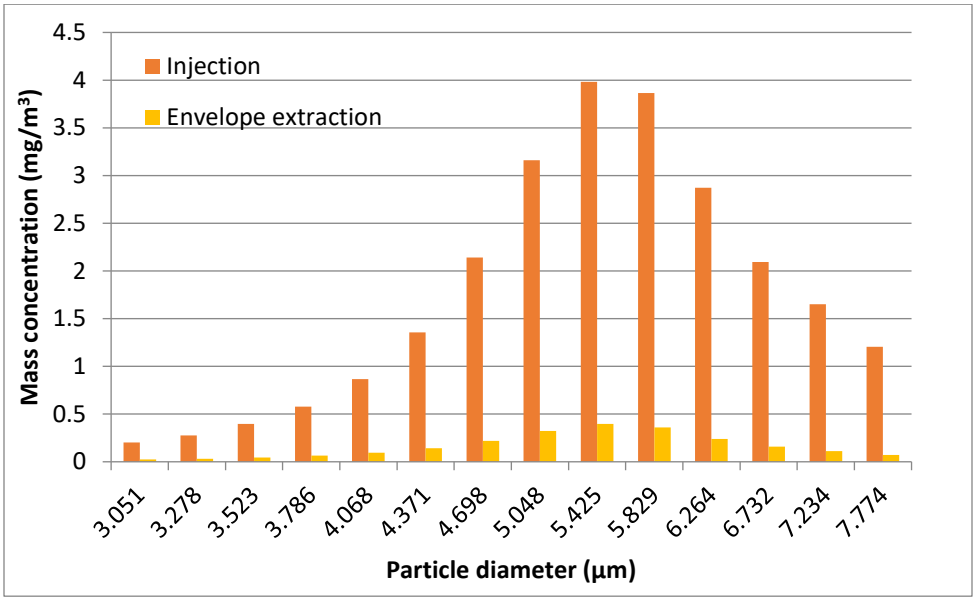

Figure 3-40 Mass concentration versus aerodynamic particle diameter corresponding to the injection outlet and the envelope extraction

According to the volume flowrates at the injection $Q_{injection}$ and at the envelope extraction $Q_{extraction,env}$ and on the mass concentrations from Figure 3-40, we deduced the corresponding particles mass flowrate $q_{injection}$ and $q_{extraction,env}$ (Eq. 3-12 and Eq. 3.13). We cumulated the mass flowrate for each particles diameter taken from the histogram of Figure 3-40.

$$q_{injection} = C_{injection} \cdot Q_{injection} \quad \text{(Eq. 3.12)}$$

$$q_{extraction,env} = C_{extraction,env} \cdot Q_{extraction,env} \quad \text{(Eq. 3.13)}$$

Then the mass deposition rate can be deduce using eq. 3-14:

$$D\ (\%) = \left(1 - \frac{q_{extraction,env}}{q_{injection}}\right) \times 100 \quad \text{(Eq. 3.14)}$$

The deposition rate was estimated to 85.2% in our case.

3.2.3.3 Experimental estimation of the gaseous and particulate decay curves within the envelope

Here, we aim to trace the particle decay curve as we did for the gaseous part in order to calculate the aerosol exchange rate $Q_{aerosol,env}$. For that, we stopped the injection of particles and we performed successive particles samplings of 5 s duration at the outlet of the envelope, using the granulometer device (APS). We plotted the evolution of C/C_{eq} versus time (s), where C_{eq} represents the concentration of particles at the extraction of the envelope, at equilibrium. Simultaneously, we stopped the gas injection inside the envelope and we monitored the helium concentration in the extraction duct of the envelope using a mass spectrometer device.

The evolution of C/C_{eq} related to helium and particles in response to time (s) are shown in Figure 3-41.

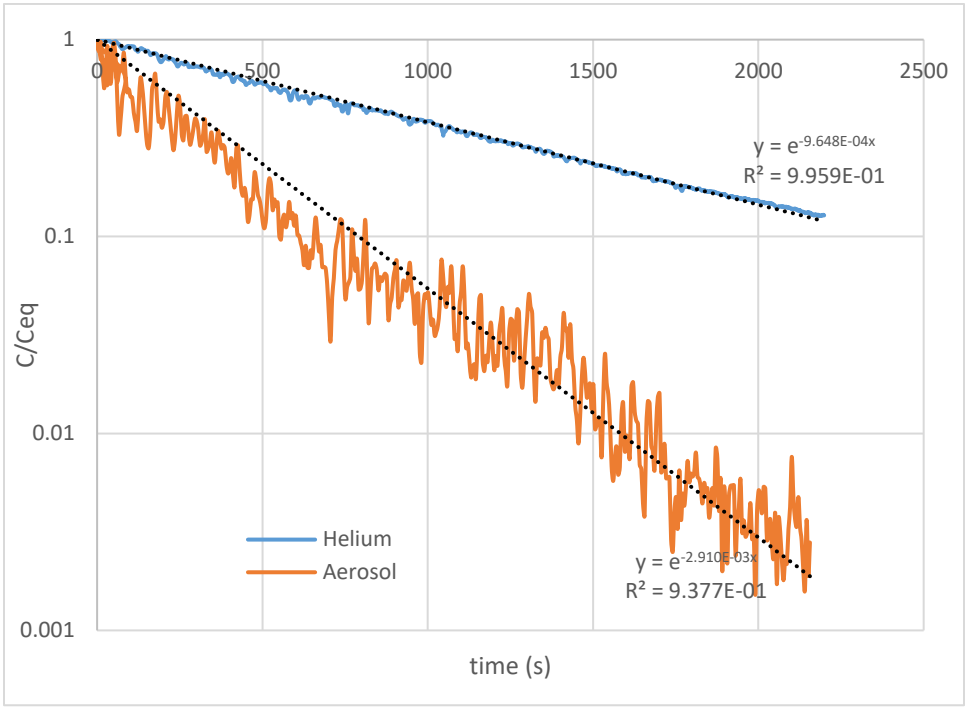

Figure 3-41 Time evolution of C/C_{eq} corresponding to the helium and 5 µm particles for a renewal rate of the envelope about 3 h^{-1}

As we see in Figure 3-41, the curves related to the particles decay are below the gas curves related to the gaseous decay experimentally and numerically, hence the decay of the particles within the extraction of the envelope is faster than those of the gas due to the particles deposition inside the envelope. The experimental aerosol exchange rate $R_{aerosol}$ is deduced from the aerosol trend line of Figure 3-41 and is around 10.5 h^{-1}, and the experimental volume flowrate of aerosol within the envelope $Q_{aerosol,env}$ is about 16.5 m^3/h ($\pm$ 3.3 m^3/h). The aerosol exchange rate and flowrate within the envelope are higher than the corresponding values for helium found above.

Unlike the gas, the aerosol decay inside the envelope depends on air extraction flowrate and on particles deposition, particularly by sedimentation, inside the envelope following Eq. 3.15.

$$C_{aerosol} = C_{eq}\, e^{-(R_{aerosol}\, t)} \qquad \text{(Eq. 3.15)}$$

$$R_{aerosol} = \frac{Q_{aerosol,env}}{V} \qquad \text{(Eq. 3.16)}$$

$$Q_{aerosol,env} = Q_{env} + K_d \,.\, S_d\, v_s \,.\, S_s \qquad \text{(Eq. 3.17)}$$

$R_{aerosol}$ represents the aerosol renewal rate within the envelope and is the slope of C/C_{eq} related to aerosol on Figure 3-41. In Eq. 3.16, V is the envelope volume. $Q_{aerosol,env}$ is the aerosol exchange rate inside the envelope. Q_{env} is air exchanger rate equal to that of helium ($Q_{helium,env}$). K_d is deposition velocity (other than sedimentation) on a surface S_d. v_s is the velocity of sedimentation on a surface S_s.

$Q_{aerosol,env}$ (16.5 m^3/h) is the sum of the air exchange rate (Q = 5.5 m^3/h), the flowrate of deposition on the envelope walls and the flowrate of sedimentation at the floor of the envelope (Eq. 3.17). The terms related to deposition and sedimentation (10 m^3/h) in Eq. 3.17 makes the decay of aerosol faster than those of gas.

In order to take into account the aerosol walls deposition and sedimentation inside the envelope in the calculation of the global backflow coefficient, we performed the following procedure.

The aerosol concentration measured at the extraction of the envelope is shown in Eq. 3.18.

$$C_{aerosol,env} = \frac{q_{backflow}}{Q_{aerosol,env}} \quad \text{(Eq. 3.18)}$$

$Q_{aerosol,env}$ depends on the deposition rate of the particles inside the envelope. If we assume that there is no deposition of particles inside the envelope, the aerosol volume flow rate within the envelope should correspond to helium flow rate (Eq. 3.19).

$$C_{(aerosol,env)without\ deposition} = \frac{q_{backflow}}{Q_{helium,env}} \quad \text{(Eq. 3.19)}$$

Then the aerosol concentration measured at the extraction of the envelope is multiplied by the ratio $\frac{Q_{aerosol,env}}{Q_{helium,env}}$ (Eq. 3.20) that corresponds to value of about 3 if we want to take into account the aerosol deposition inside the envelope in the calculation of the backflow coefficient in the following section.

$$C_{(aerosol,env)without\ deposition} = C_{aerosol,env} \times \frac{Q_{aerosol,env}}{Q_{helium,env}} \quad \text{(Eq. 3.20)}$$

3.2.4 Quantification of the global backflow phenomenon

3.2.4.1 Description of the operating procedure to collect backflow pollutants

Here we are interested in globally quantifying the gaseous and particulate pollutants that backflowed from the enclosure to the envelope by the mean of the opening. For that, specific procedures for introducing the pollutants inside the enclosure, for generating the counter-current disturbance jet inside the enclosure and for collecting the backflowed part of the pollutants at the envelope extraction are explained in the following. The global backflow coefficient K_{env} (%) is then calculated and corresponds to the ratio between the concentration of pollutants at the extraction of the envelope minus the ambient concentration measured inside the envelope before the generation of the disturbance over the concentration at the extraction of the enclosure (Eq. 3.21). K_{env} (%) depends on the pollutant concentration diluted inside the envelope and then on the volume flowrate of the envelope.

$$K_{env}(\%) = \frac{C_{out,envelope} - C_{ambient,envelope}}{C_{in,enclosure}} \times 100 \quad \text{(Eq. 3.21)}$$

Figure 3-42 shows the implementation of the experimental devices used for the global quantification of the backflow. The gaseous and particulate pollutant (helium and aerosol of 5 µm respectively) were injected simultaneously inside the enclosure at the right part of the figure. A circuit added at the extraction exit of the envelope, was set at the left part of the envelope to capture the gaseous and particulate pollutants.

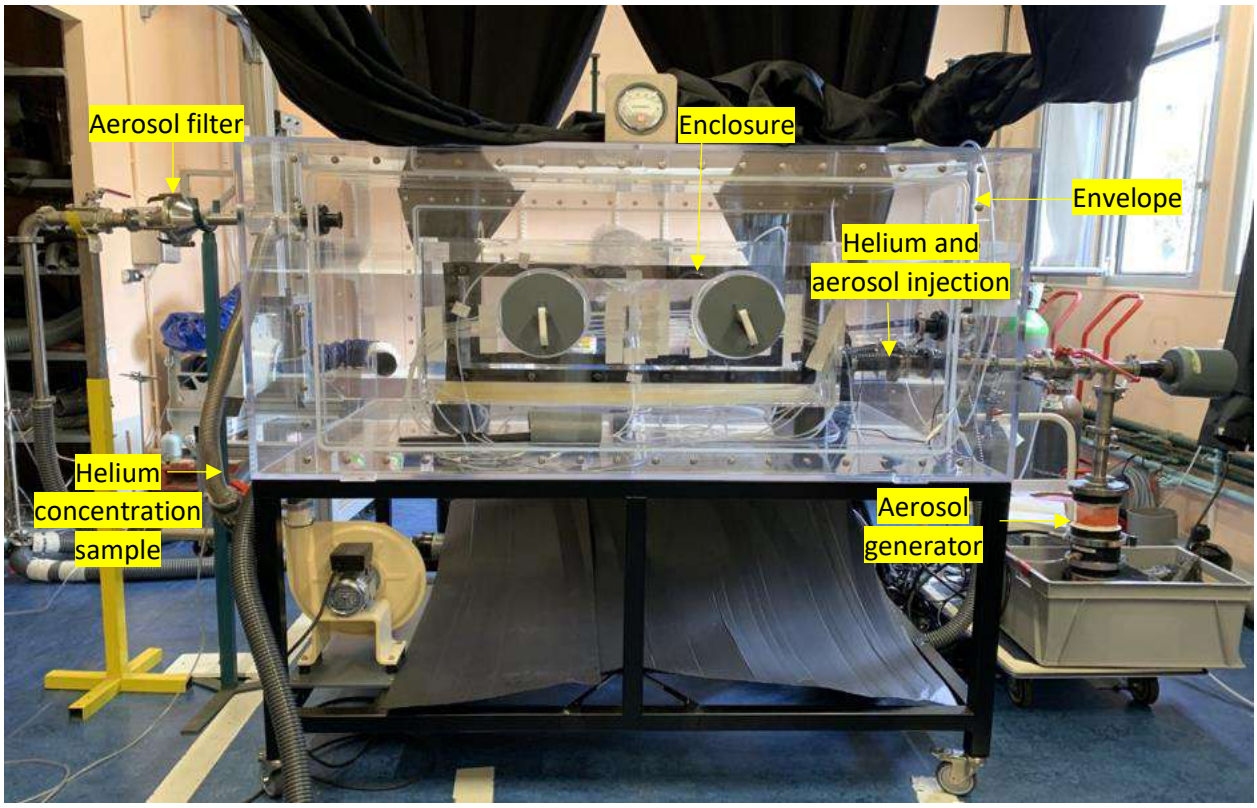

Figure 3-42 Experimental apparatus for the global quantification of the backflow

The procedure for the global quantification follows the one described for the local quantification, except for the sampling of the backflowed pollutants in the envelope. Figure 3-43 describes on a diagram the procedure to quantify the pollutant transfers in the envelope by the means of the gas and particulate tracing devices connected to its extraction duct.

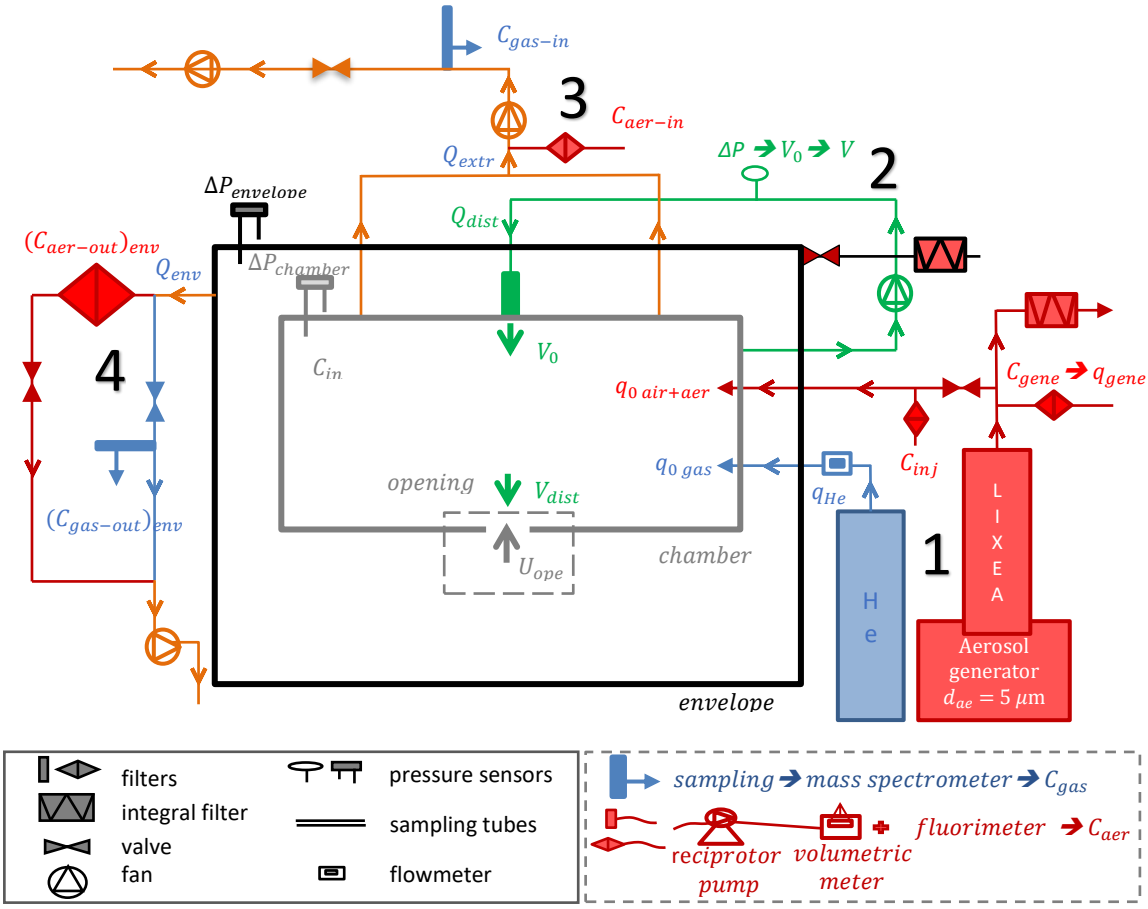

Figure 3-43 Schematic diagram of the devices used for characterizing the global backflow coefficients in the envelope

Different steps were followed to determine the backflows coefficients:

- (1) Initially, a constant and controlled tracer gas flow $q_{0\ gas}$ (Nl.h^{-1}) was injected into the enclosure. Simultaneously, a constant mixture (air/5 µm particles) flow, $q_{0\ air+aerosol}$ (g.h^{-1}), was injected into the enclosure using an aerosol generator (LIXEA, Sinaptec).

- (2) A counter-current internal jet corresponding to a velocity V_0 was initiated once the equilibrium of gas and particulate concentrations were reached inside the enclosure.

- (3) At the extraction duct of the enclosure, we measured the helium and aerosol concentrations at the equilibrium, C_{gas-in} and $C_{aerosol-in}$, respectively.

- (4) At the outlet of the envelope, a circuit was added and connected to the extraction system. A sample was fitted at the first part of the circuit connected to a mass spectrometer to continuously detect the helium concentration. A second part was connected to a filter holder and to the fan of the envelope to capture the backflowed amount of aerosol over a fixed amount of time.

A valve has been installed to the pipe upstream of each part of the envelope extraction system. Before the experiment, an air renewal rate corresponding to R = 3 h^{-1} was regulated through the extraction circuit of the envelope. First, the valve of the gas part was opened and that of the aerosol part is closed. We

continuously visualized the concentration of the helium backflowed inside the enveloppe through the signal delivered by the mass spectrometer. We waited till the backflowed pollutants were homogenized inside the envelope, about 25 min (depending on the renewal rate of the envelope), corresponding to a state of equilibrium of the helium concentrations in the envelope. This value represented $C_{gas-out}$. Secondly, we closed the gas sampling circuit valve and we opened the one corresponding to the particulate sampling circuit. The particulate pollutant has accumulated on the sampling filter for a fixed period of approximately 20 min, corresponding to this quantity represented by $C_{aerosol-out}$.

Finally, the measured values C_{gas-in}, $C_{aerosol-in}$, $C_{gas-out}$ and $C_{aerosol-out}$ were used for the calculation of the global gaseous and particulate backflow coefficients $K_{env,gas}$ *(%)* and $K_{env,aerosol}$ *(%)* (Eq. 3.22 and Eq. 3.23).

$$K_{env,gas}\ (\%) = \frac{C_{(gas-out)env} - C_{(gas-ambient)env}}{C_{(gas-in),enclosure}} \times 100 \qquad \text{(Eq. 3.22)}$$

$$K_{env,aerosol}\ (\%) = \frac{C_{(aerosol-out)env} - C_{(aerosol-ambient)env}}{C_{(aerosol-in),enclosure}} \times 100 \qquad \text{(Eq. 3.23)}$$

$C_{(gas-ambient)env}$ and $C_{(aerosol-ambient)env}$ are respectively the helium and aerosol concentrations measured inside the envelope at initial conditions (before the generation of the disturbing jet). We should mention that we take into account gaseous and particulate ambient concentrations for the gas and aerosol concentrations at the enclosure extraction. However, since the gaseous and particulate ambient concentrations are negligible in comparison with the concentrations at the enclosure extraction, we did not include them in Eq. 3.22 and Eq. 3.23.

We define the gaseous and particulate global backflow detection threshold configurations in the following by the minimum helium and aerosol concentration detected at the extraction envelope $C_{(gas-out)env} - C_{(gas-ambient)env}$ = 5 ppm and $C_{(aerosol-out)env} - C_{(aerosol-ambient)env}$ = 3.10^{-4} mg/m^3.
The figures tracing the evolution of the backflow coefficient *K* (%) versus V_{dist}/U_{ope} are further analyzed to compare the different scenarios, and to validate the numeric simulation results presented afterwards. The uncertainties are detailed in appendix 2.

3.2.4.2 Results of the global quantification for the internal counter-current free jet

3.2.4.2.1 Results for gaseous/particulate pollutants corresponding to three inlet velocities

Figure 3-44 shows the global gaseous backflow coefficients, *K* (%) versus V_{dist}/U_{ope} corresponding to successively U_{ope} = 0.5 m/s, 1 m/s and 1.5 m/s for the enclosure equipped with its rigid frontal wall, in the

case of a counter-current internal free jet disturbance. The yellow arrow on the figure corresponds to the onset of the backflow.

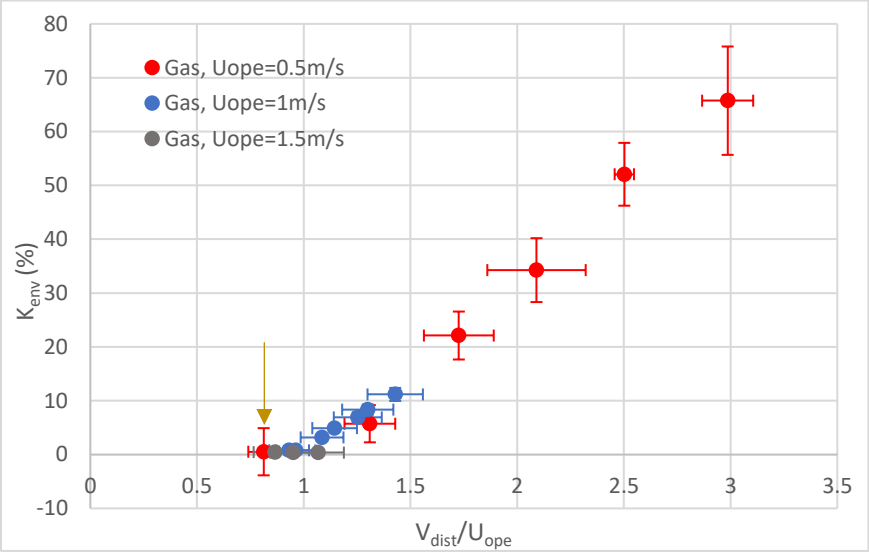

Figure 3-44 Evolution of the global gaseous backflow coefficient K (%) versus V_{dist}/ U_{ope} for the three values of the inflow velocity at the opening (0.5, 1 and 1.5 m/s) in the case of a counter-current internal free jet disturbance

As we can see, the global backflow phenomenon starts for a value of V_{dist}/U_{ope} of about 0.8 for the three inlet velocities (yellow arrow on the figure).

The three curves show an increasing trend versus V_{dist}/U_{ope}. The global backflow coefficient depends directly on the mass flowrate of the backflowed pollutant outside the enclosure. And since this backflow flowrate increases with the velocity of the disturbing jet, the global backflow coefficient increases too.

Simultaneously, the three curves are overlapped. Hence, for a given value of V_{dist}/U_{ope}, the global backflow coefficient is constant regardless of the value of the inflow velocity at the opening U_{ope}. We should note that the backflow coefficients corresponding to U_{ope} = 1.5 m/s do not exceed 0.45 % until a ratio V_{dist}/U_{ope} less than 1.1: in this case, the values of the helium concentration are very close to the ambient concentration. We should note that for U_{ope} = 1.5 m/s, we could not reach V_{dist}/U_{ope} values higher than 1.1 because V_{dist} corresponds in this case to the higher value of the volume flowrate delivered by the fan of the disturbing jet. Then, it was an experimental limit.

Figure 3-45 shows the global particulate backflow coefficient, *K* (%) as a function of V_{dist}/U_{ope} corresponding to successively U_{ope} = 0.5 m/s, 1 m/s and 1.5 m/s for the enclosure equipped with its rigid frontal wall in the case of a counter-current internal free jet disturbance. The yellow arrow on the figure corresponds to the onset of the backflow.

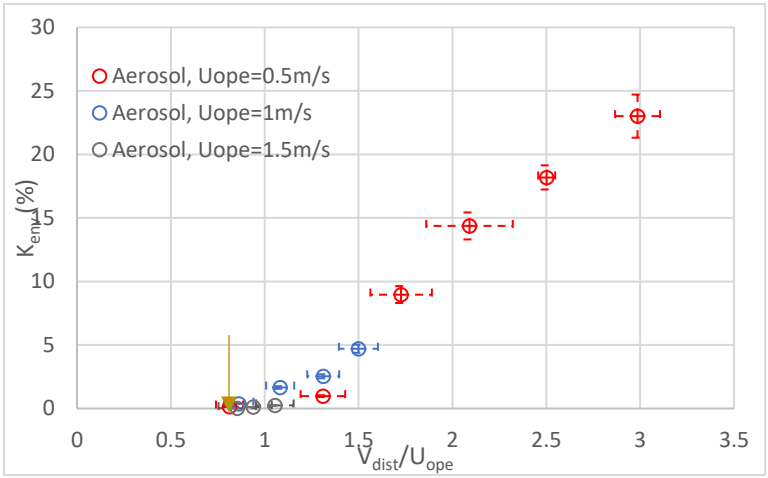

Figure 3-45 Global particulate backflow coefficient K_{env} (%) versus V_{dist}/U_{ope} for U_{ope} = 0.5 m/s, 1 m/s and 1.5 m/s in the case of a counter-current internal free jet disturbance

As we can see, the backflow phenomenon corresponding to the three inlet velocities starts at a value of V_{dist}/U_{ope} of about 0.85 similar to the onset of backflow observed for the gas. The three curves are quite overlapped and show an increasing trend. We should note that the backflow concentrations related to V_{dist}/U_{ope} values between 0.85 and 1 are very close to the ambient concentration.

We observe that the particulate backflow coefficients are lower than the gaseous backflow coefficients, due to the deposition of particles inside the envelope subjected to the sedimentation, impaction forces or to the turbulent diffusion effect. Since we did not take into account this deposition rate in the calculation of particulate backflow coefficients in Figure 3-45, these particulate coefficients are underestimated.

In order to take into account the deposition of particles inside the envelope, we corrected the above particulate backflow coefficients by the factor $\frac{Q_{aerosol,env}}{Q_{helium,env}}$ as explained above (see section 3.2.3.3): it becomes the $K_{env,corrected}$ (%) = 3. K (%). The corrected particulate backflow curves are shown in Figure 3-46. They represent the particulate backflow coefficients at the extraction of the envelope assuming that there is no deposition inside the envelope.

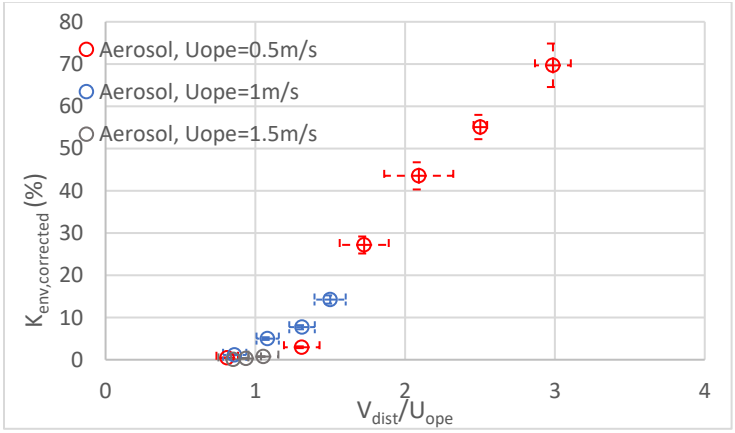

Figure 3-46 Corrected global particulate backflow coefficient $K_{corrected}$ (%) versus V_{dist}/U_{ope} for U_{ope} = 0.5 m/s, 1 m/s and 1.5 m/s taking into account the deposition of particles inside the envelope

As we see in Figure 3-46, the backflow coefficients have values higher than those in Figure 3-45 since we took into account the deposition of particles inside the envelope. The corrected particulate coefficients are at the same order of magnitude that those of the gaseous backflow coefficients revealing a similar behavior between the gas and the 5 µm particles for these aeraulic conditions.

In the following figures, the particulate coefficients are also multiplied by this correction factor; hence the particles deposition inside the envelope is taken into account.

3.2.4.2.2 Comparison of results for gaseous/particulate pollutants within the enclosure of rigid/flexible frontal wall

Figure 3-47 shows the evolution of the global backflow coefficients *K (%)* as a function of V_{dist}/U_{ope} for an entrance velocity at the opening U_{ope} = 0.5 m/s in the case of a counter-current internal free jet disturbance, for the gaseous and 5 µm particulate pollutant and for the enclosure equipped successively with its rigid and flexible frontal wall. The yellow arrow on the figure corresponds to the onset of the backflow.

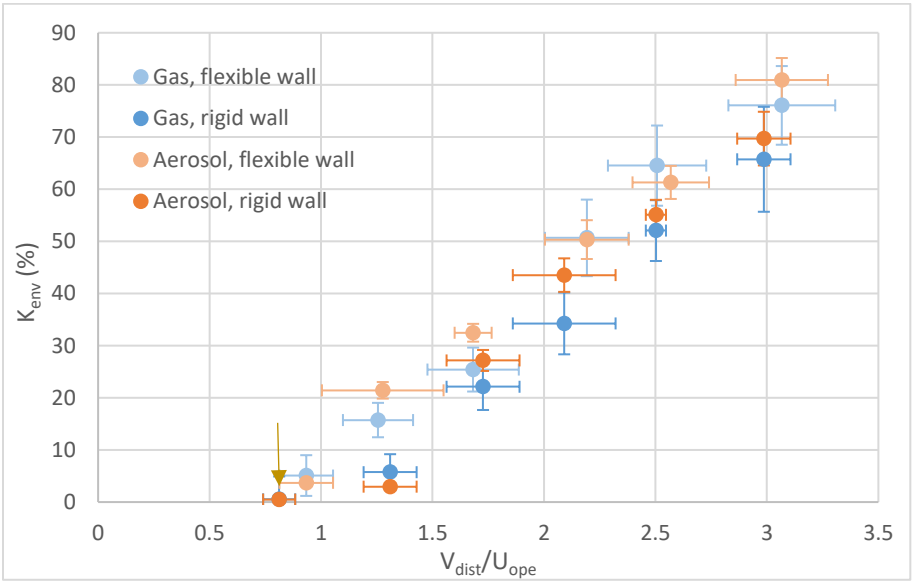

Figure 3-47 Evolution of the global backflow coefficients K_{env} (%) versus V_{dist}/U_{ope} for an entrance velocity at the opening U_{ope} = 0.5 m/s in the case of a counter-current internal free jet disturbance for the gaseous and 5 µm particulate pollutant and for the enclosure with rigid and flexible frontal wall

Following the figure, we can see that the backflow phenomenon starts to appear for a disturbing velocity corresponding to the ratio V_{dist}/U_{ope} about 0.8. The global trend of the four curves is an increasing backflow coefficient *K* (%) when V_{dist}/U_{ope} increases.

Comparing the four curves between each other, we can say that, despite the small differences between the curves, they are at the same order of magnitude. Then, two conclusions could be brought: firstly, the gas and 5 µm aerosol have a similar behavior taking into account the particles deposition inside the envelope; secondly, the backflow phenomenon is similar for the rigid and flexible frontal wall. Then the backflow phenomenon does not depend on the nature of the pollutant or of the frontal wall for our small-scale geometry and for our aeraulic conditions. These are in agreement with those observed with local backflow, obtained in the same conditions.

3.2.4.3 Results of global backflow coefficients for internal parietal free jet

In the following, we show the results related to the internal parietal disturbing jet corresponding to an inflow velocity at the opening U_{ope} = 0.5 m/s. We varied the nature of the pollutant (gas/5 µm particles) and the nature of the frontal wall of the enclosure (rigid/flexible). We show first the results of the comparison between the nature of the pollutant and the nature of the frontal wall, and then we compare the results of the local and global backflow coefficients.

3.2.4.3.1 Comparison of results for gaseous/particulate pollutants within the enclosure of rigid/flexible frontal wall

Figure 3-48 shows the evolution of the backflow coefficient *K (%)* as a function of V_{dist}/U_{ope} for an entrance velocity at the opening U_{ope} = 0.5 m/s in the case of an internal parietal free jet disturbance for the gaseous and 5 µm particulate pollutant and for the enclosure with rigid and flexible frontal wall. The yellow arrow on the figure corresponds to the onset of the backflow.

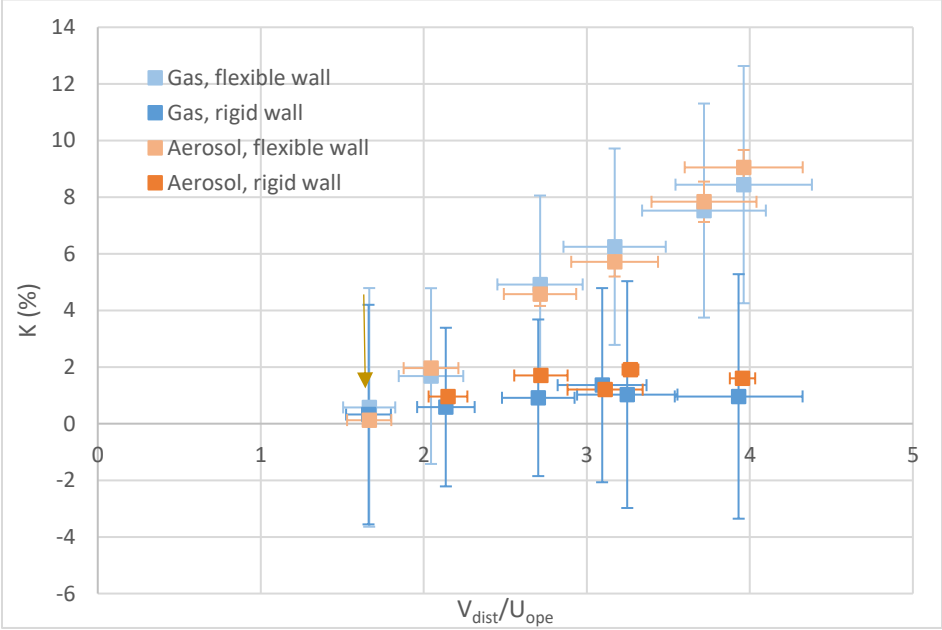

Figure 3-48 Evolution of the global backflow coefficients K (%) versus V_{dist}/U_{ope} for an entrance velocity at the opening U_{ope} = 0.5 m/s in the case of an internal parietal free jet disturbance for the gaseous and 5 µm particulate pollutant and for the enclosure with rigid and flexible frontal wall

We see on the above figure that the backflow phenomenon starts to appear for a V_{dist}/U_{ope} value of about 1.65 for the four curves.

We start first to compare the curves of the gaseous and particulate pollutants. We can clearly see that the gaseous and particulate backflow coefficients are similar for the case of the rigid or flexible frontal wall. Then the behavior of the gas and the 5 µm particles is also similar for this disturbance in our experimental conditions.

Then, we compare the curves obtained with the rigid then flexible frontal wall. We can clearly note that the backflow coefficients related to the flexible wall are above those related to the rigid frontal wall. The

curves related to the flexible frontal wall demonstrate an increasing tendency. For the case of the rigid frontal wall, the backflow concentrations at the envelope extraction is very low and close to the ambient concentration. In fact, the backflow coefficients do not exceed 2 %. We could not really say that the curves of the rigid wall have an increasing tendency. Indeed, the opening in the flexible wall is more subject to the effects of the parietal jet and therefore to the deformations produced by the jet than in the case of the rigid wall, which results in an significant increase of the backflow phenomenon (see 3.1.1.3).

3.2.5 Comparison of local and global backflow coefficients

The local concentrations used for calculating the backflow coefficients were sampled using many samplers near the opening without the presence of the envelope. However, the concentrations used for the calculation of global backflow coefficients were directly sampled in the extraction duct of the envelope. The main advantage of the envelope is that it captures the total quantity of the pollutant backflowed outside the enclosure, unlike the samplers added locally near the opening that their location and number do affect the measurements.

Indeed, we cannot perform a comparison of the local and global backflow coefficients because measurements were done independently of each other. The concentration at the opening of the enclosure takes into account the concentration coming from the backflow and the ambient concentration. The local backflow measurements were done around the opening without the presence of the envelope; hence, the leakage of pollutants was transferred to the atmosphere where the ambient concentration is very low. However, the global quantification was done using an envelope surrounding the enclosure, hence the ambient concentration inside the envelope increases with the intensity of the disturbing jet. The concentration inside the envelope and hence at the extraction circuit of the envelope depends directly on the extraction flow rate of the envelope. We are not in a case where the volume inside the envelope could be considered as infinite. If it was the case, we could say that the concentration inside the envelope and far from the opening would be negligible in comparison with the concentration near the opening; then the concentration near the opening without the envelope would be similar to that with the envelope. In our case, if local measurements were done inside the closed envelope, the sampled local concentrations near the opening could be higher because we have to take into account the ambient concentration inside the envelope. However, we could still compare the value of V_{dist}/U_{ope} at which the backflow starts to appear. It was approximately at same order of magnitude for the two types of disturbing jets.

3.3 Synthesis of experimental results

In this part, we show a synthesis of our experimental results related to the backflow of gaseous and 5 µm particulate pollutants near the opening of the rigid then flexible frontal wall, under the successive effects of a counter-current and parietal disturbing jets. We present first the local backflow results in Figure 3-49 and then the global backflow results Figure 3-50.

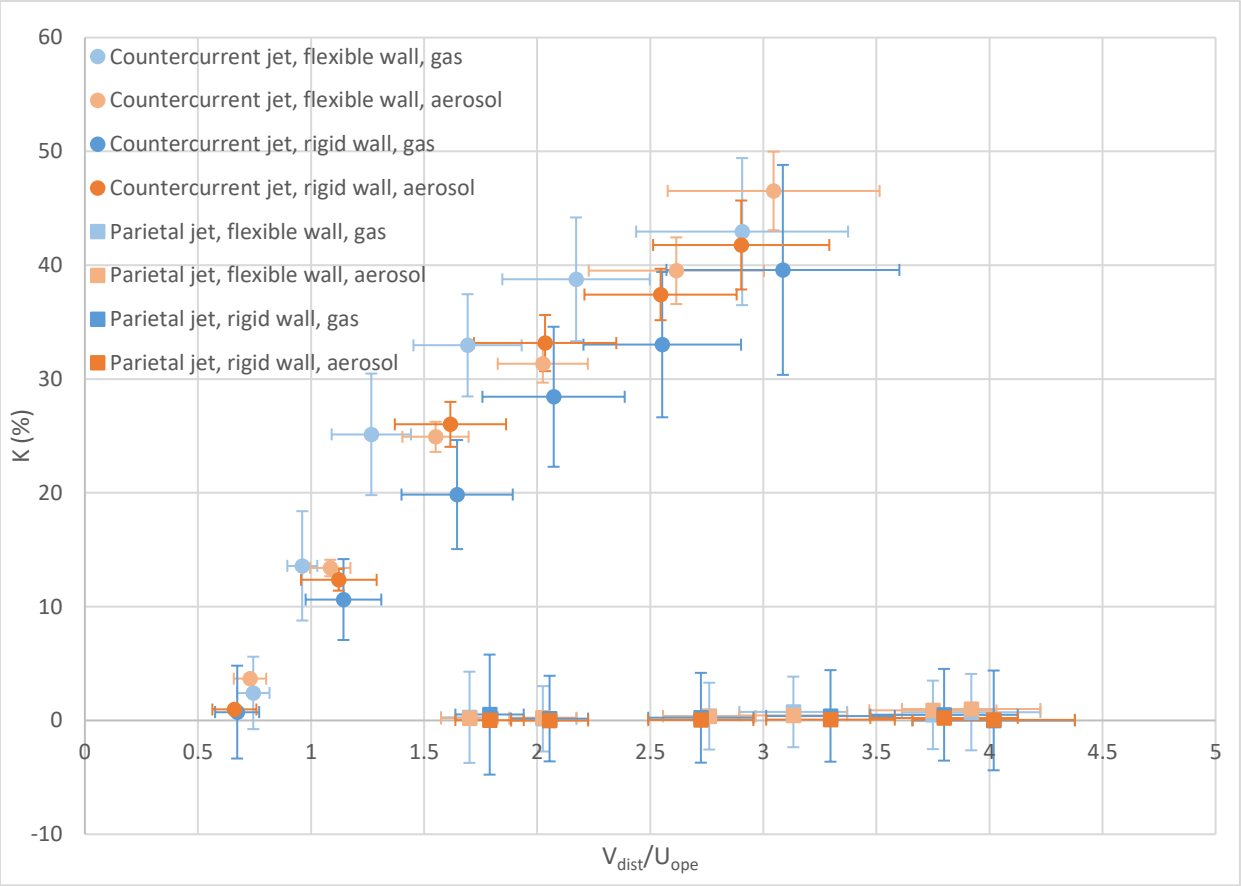

Figure 3-49 Evolution of the local backflow coefficients K (%) versus V_{dist}/U_{ope} for a velocity at the opening U_{ope} = 0.5 m/s for different disturbing jet types, frontal wall types and pollutant types

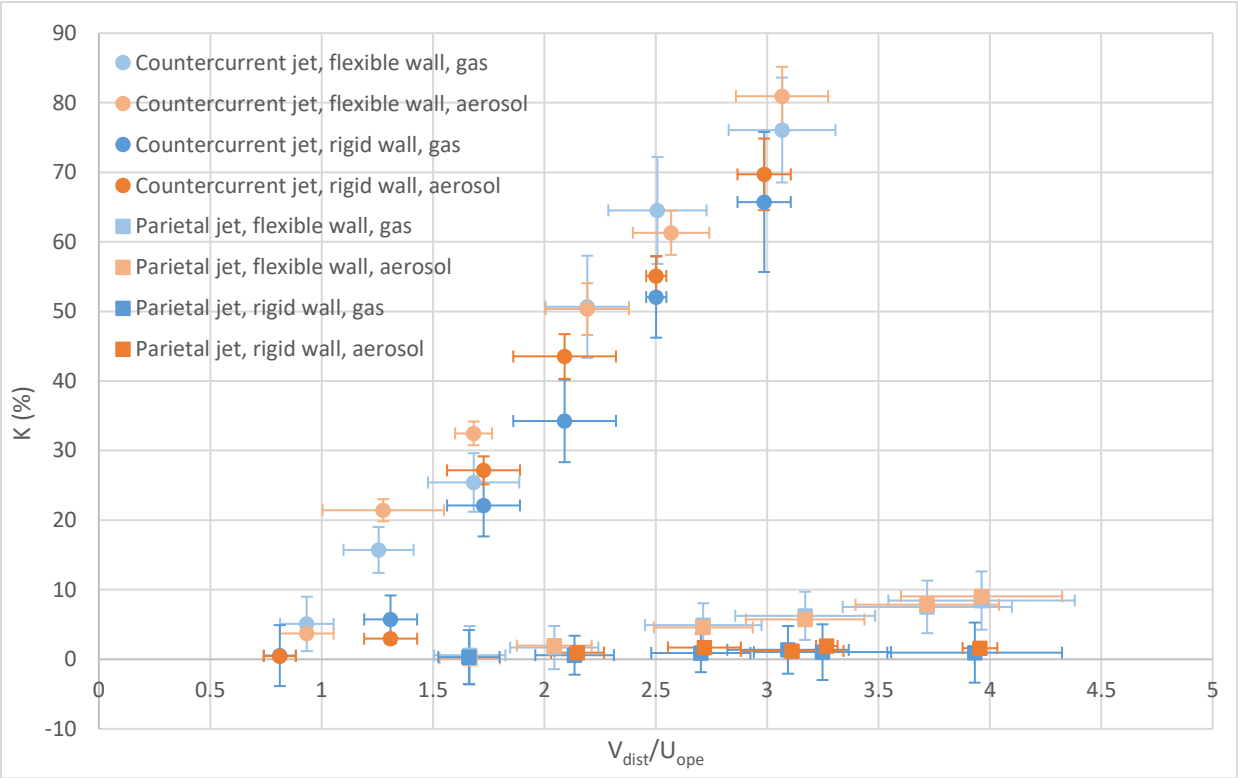

Figure 3-50 Evolution of the global backflow coefficients K (%) versus V_{dist}/U_{ope} for a velocity at the opening U_{ope} = 0.5 m/s for different disturbing jet types, frontal wall types and pollutant types

The results from the above curves could be summarized as follows:

- the gas and the 5 µm aerosol have a similar behavior, in these aeraulic and geometric conditions,
- the backflow coefficients of the counter-current disturbing jet are higher than those obtained in the case of parietal disturbing jet,
- the backflow coefficients for the flexible frontal wall are similar to those of the rigid frontal wall for the case of the internal counter-current jet, and are higher than those of the rigid frontal wall for the case of the internal parietal jet,
- the global backflow coefficients have a linear increasing trend. The local backflow coefficients tends to increase very slowly and to stabilize after V_{dist}/U_{ope} = 2.

The first conclusion is related to the nature of the pollutant. We saw that the behaviors of the gas and the 5 µm aerosol were similar in terms of backflow coefficients. This is only valid to our experimental conditions such as the geometry of the enclosure and the aeraulic conditions near the opening. This similarity of the behavior between the two pollutants could be explained by the Stokes number of the particles. In our experimental conditions, this number has a value lower than 1 (as we will see in chapter 4). Then particles are in equilibrium regime; they completely follow the gas streamlines and respond to the flow fluctuations. Hence, the particles follow the backflow behavior of the gas resulting in similarities in terms of backflow coefficients.

The second conclusion concerns the orientation of the disturbing jet. We found that the backflow coefficients of the counter-current internal disturbing jet are higher than those of the parietal internal disturbing jet. We can say that the counter-current configuration where the disturbing jet is facing the opening corresponds to the situation where U_{ope} and V_{dist} are parallel, in opposite direction and have an angle of 0°. This configuration generates the maximum backflow quantities. The large-scale turbulence generated by this disturbance type results in the creation of vortices near the opening that succeed to overcome the inlet velocity for a small value of V_{dist}/U_{ope}. This configuration is the most unfavorable configuration in terms of dynamic containment efficiency. The configuration of the parietal internal jet corresponds to the case where U_{ope} and V_{dist} are crossed perpendicularly to each other and have an angle of 90°. This configuration generates the minimum backflow quantities. Here the turbulence created by the parietal jet does not succeed to overcome the influence of the entry velocity for the tested disturbance velocities (see visualizations of the backflow in section 3.1.1). This configuration is the safest one in terms of dynamic containment efficiency. We can imagine that varying the angle between U_{ope} and V_{dist} from 0° to 90° will increase the value of backflow coefficient progressively, from a minimum value corresponding to the results of the parietal jet to a maximum value corresponding to the counter-current jet.

The third conclusion is about the nature of the frontal wall. We found that the nature of the frontal wall does not influence the backflow coefficients in the case of the counter-current disturbing jet, and then there is no need to simulate numerically the flexibility of the frontal wall in this case. However, for the case of the parietal internal jet, the backflow coefficients related to the flexible frontal wall are higher than those related to the rigid frontal wall. For the flexible frontal wall, two phenomenon could be highlighted: the vibrations of the frontal wall and the deformation of the opening shape. The vibrations of the flexible frontal wall were significant in the case of the counter-current disturbing jet. This could enhance the release and the re-training of the pollutant between the inside and the outside of the enclosure, leading no direct differences on the backflowed quantity between the flexible and the rigid frontal wall. For the case of the parietal jet, the frontal wall vibrations were very weak. Then the curved flexible frontal wall could be considered as still frontal wall and it is the deformed shape of the opening that influence directly the quantity of the backflowed pollutant. For the case of the counter-current disturbing jet, the frontal wall containing the opening is perpendicular to the jet axis. Then even if the opening is curved to the inside or outside of the enclosure, it does not have a great effect on the quantity of the backflowed pollutant. However, for the case of the parietal jet, since the frontal wall containing the opening is parallel to the axis of the parietal jet, then any deformation in the shape of the opening to the inside or outside the enclosure has a direct effect on the leakage of the pollutant. Additionally if the deformation of the frontal wall to the inside of the enclosure occurs on the left side, opposite to the injection point, it enhances the backflow under the effect of the parietal jet.

The fourth conclusion affects the appearance of the local and global backflow coefficients curves, since we demonstrate earlier that we cannot compare the values of the local and global backflow coefficients. Concerning the trend of each curve especially for the case of the counter-current disturbing jet, we should mention that the local backflow coefficient depends on the concentration near the opening and the global backflow coefficient depends on the mass flowrate of the backflowed pollutant from the enclosure. For lower values of V_{dist}/U_{ope}, the backflow phenomenon is transient and appears as puff and for higher values of V_{dist}/U_{ope}, the backflow phenomenon is continuous. The two slopes seen for local backflow coefficients correspond to these two regimes. The first slope tends to increase with the increase of V_{dist}/U_{ope} and hence with the increase of the puffs frequency near the opening. The second slope tends to increase slower and

became more or less stable since the concentration near the opening tends to be equal to the concentration inside the enclosure diluted by airflows near the opening. However, the mass flowrate of the backflow $q_{backflow\text{-}out}$ depends directly on the velocity of the disturbing jet for a given value of U_{ope}. And since the quantity $q_{backflow\text{-}out}$ increases when we increases the velocity of the disturbing jet, the global backflow coefficient increases linearly with V_{dist}/U_{ope}.

Additionally, the concentrations within the extraction of the envelope $C_{envelope}$, and hence K_{env}, depend on the extraction flowrate of the envelope $Q_{envelope}$. If we change the extraction flowrate of the envelope, these concentrations change. However, these concentrations give access to the total mass flowrate $q_{out\_backflow}$ of backflowed pollutants transmitted to outside the enclosure (Eq. 3.24).

$$q_{out\_backflow} = C_{envelope} \times Q_{envelope} \quad \text{(Eq. 3.24)}$$

In order to eliminate the dependency of K_{env} on $Q_{envelope}$, we can define a mass backflow coefficient $K_{m,injection}$ (%) that represents the ratio of the mass flowrate of the backflow $q_{out\_backflow}$ that escapes from the enclosure over the initial mass flowrate injected inside the enclosure $q_{in\_enclosure}$ (Eq. 3.25).

$$K_{m,injection}\,(\%) = \frac{q_{out\_backflow}}{q_{in\_enclosure}} \times 100 \quad \text{(Eq. 3.25)}$$

Figure 3-51 shows the evolution of $K_{m,injection}$ (%) in function of V/U_{ope}. $K_{m,injection}$ (%) for the case of counter-current disturbing jet and for the enclosure with its rigid frontal wall.

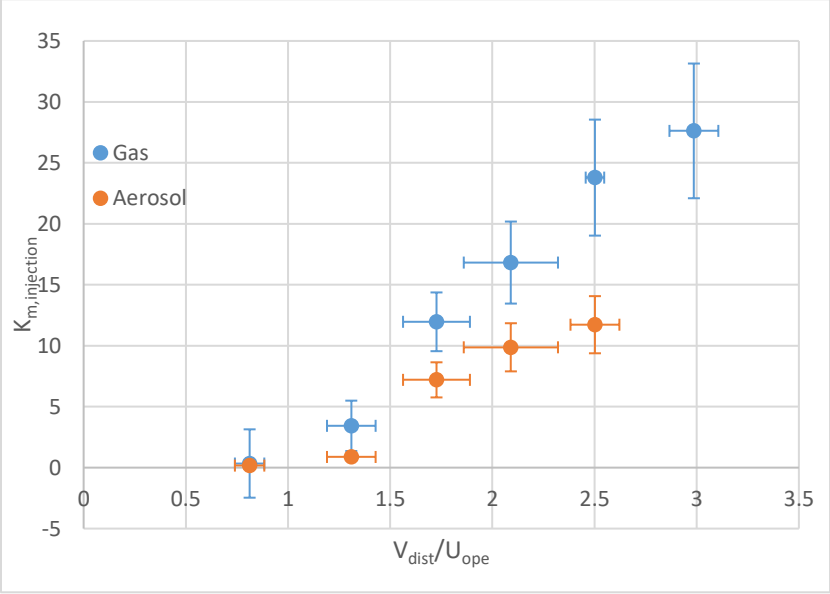

Figure 3-51 Evolution of gaseous and particulate mass backflow coefficients in function of V_{dist}/U_{ope} for U_{ope} = 0.5 m/s for the case of counter-current disturbing jet for the enclosure with its rigid frontal wall

As we see in Figure 3-51, the mass backflow coefficients $K_{m,injection}$ (%) for gaseous and 5 µm particulate pollutants have an increasing trend. For V_{dist}/U_{ope} = 2.5, we can say that about 12 % to 24 % of the initial mass flowrate of aerosol or helium respectively injected inside the enclosure escapes from the enclosure. Additionally, we notice that the mass backflow coefficients of the 5 µm aerosol are lower than the gaseous coefficients due to the deposition of particles inside the enclosure.

It is more appropriate to use this mass backflow coefficient $K_{m,injection}$ in place of global backflow coefficient K_{env} in order to eliminate the dependency of this backflow coefficient on the extraction flowrate of the envelope.

Furthermore, we can calculate a mean velocity of the backflow ($V_{backflow}$) over the opening surface (S) using the mean concentration measured using samplers near the opening ($C_{opening}$) and the mass flowrate of the backflow ($q_{out\_backflow}$) as shown in Eq. 3.26.

$$q_{out\_backflow} = C_{opening} \times V_{backflow} \times S \quad \text{(Eq. 3.26)}$$

Figure 3-52 shows the evolution of the mean backflow velocity near the opening $V_{backflow}$ in function of ($V_{disturbance}$ - U_{ope}) for the counter-current disturbing jet of the enclosure with its rigid frontal wall.

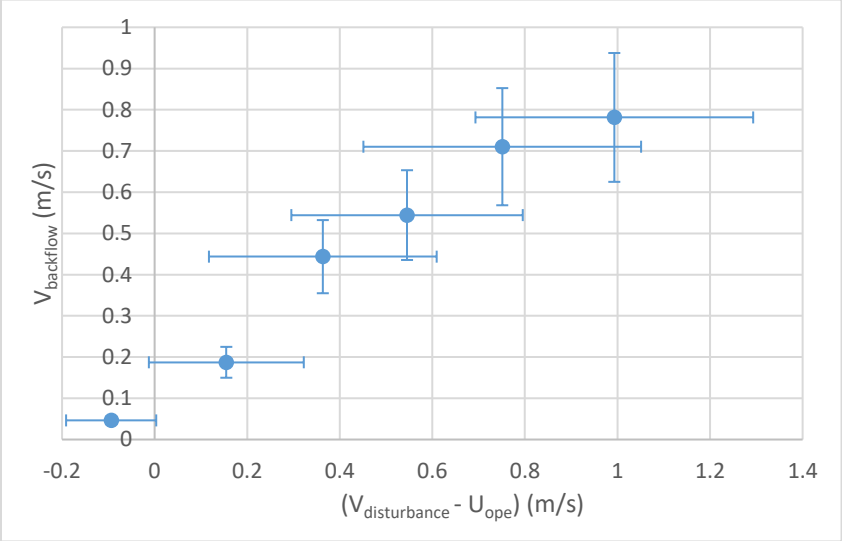

Figure 3-52 Evolution of the mean backflow velocity near the opening $V_{backflow}$ in function of ($V_{disturbance}$ - U_{ope}) for the counter-current disturbing jet

As we see in Figure 3-52, the evolution of the mean backflow velocity near the opening $V_{backflow}$ in function of ($V_{disturbance}$ - U_{ope}) has an increasing tendency. The backflow phenomenon appears for ($V_{disturbance}$ - U_{ope}) = -0.1, and hence when the disturbance velocity near the opening $V_{disturbance}$ is about the same order of magnitude of the inflow velocity U_{ope}. The backflow velocity $V_{backflow}$ continues to increase as the disturbance velocity $V_{disturbance}$ increases. The backflow velocity $V_{backflow}$ seems to at the same order of magnitude, with uncertainties, than ($V_{disturbance}$ - U_{ope}): for example for ($V_{disturbance}$ - U_{ope}) = 0.75 m/s, the backflow velocity $V_{backflow}$ = 0.7 m/s.

Once we showed our experimental results, we aim to perform a numerical validation for our backflow results. The main purposes of further numerical simulations are to find the local gaseous and particulate concentrations near the opening, and then calculate their corresponding local backflow coefficients on the one hand. On the other hand, we want to find the overall concentration values measured at the extraction of the envelope and simultaneously the global backflow coefficients. Additionally we want to check the possibility to find the mass flow rate of the gaseous and particulate pollutants backflow. Once the numerical validation of our experimental results is done, then it would make it possible to consider taking into account various risks of backflow scenarios on full-scale sites by means of numerical tools.

4 Numerical simulations validation

In this chapter, we propose comments on our numerical simulations into two parts: the local backflow quantification corresponding to the backflow phenomenon near the opening and the global backflow quantification corresponding to backflow measurements using the envelope added around the enclosure. Our numerical simulations were performed using ANSYS CFX software. Based on preliminary works (shown in chapter 1), the turbulence model selected for the quantification of the backflow in our study is the hybrid SST-DES model. In the section on local backflow, we show first the results corresponding to the visualization fields using a passive scalar then using helium and 5 microns particles. Later, we present the quantitative results in terms of gaseous and particulate backflow coefficient evolutions. For both parts, we compare our experimental and numerical results. For the global backflow quantification, we performed firstly numerical simulations in order to verify the impact of the envelope on the flow near the opening while varying the air exchange rate within the envelope. Then, we investigated the homogeneity of the flows inside the envelope and we compared the experimental and numerical rates of decay of helium concentration and aerosol of 5 microns diameter. Finally, we present the results of visualization and global quantification of the backflow phenomenon. In order to reduce the simulation time, a special procedure consisting of following the mass flow rate inside the enclosure gives access to the total amount of pollutants released outside the enclosure. As a summary, we compare our experimental and numerical global backflow coefficient results.

4.1 Local backflow

Following the experimental procedure, the local backflow analysis consists in following the backflow features near the opening of the enclosure by using samplers located near this opening. We are presenting results into two parts: visualization and quantification of the backflow. The visualization of the backflow is performed using passive tracer in preliminary tests, then by injecting the helium and aerosol of 5 m diameter as in our experimental procedure. The results are presented through passive tracer fields or helium and aerosol concentration fields. The quantification part consists in calculating the backflow coefficient near the opening under the presence of a counter-current or parietal internal jet. Comparison of experimental and numerical results are shown for each part. At the end, the effect of the Stokes number is studied for particles with different diameters.

The hybrid model DES-SST was chosen based on preliminary tests presented in chapter 1.

Geometry

The simulation domain, as shown in Figure 4-1, is closely matching the experimental enclosure with the following geometric characteristics:

- an internal domain of dimensions (1.2 × 0.5 × 0.5) m^3 corresponding to the experimental enclosure described above, including the two extraction units of dimensions (0.05 × 0.05) m^2 and the injection orifice of dimensions (0.1 × 0.01) m^2 arranged on the rear wall facing the opening in the case of the counter-current disturbance and on the right side wall in the case of the parietal disturbance;

- an opening of dimensions (0.1 × 0.03 × 0.005) m^3 connecting the internal and the external domains;

- an external domain around the opening of dimensions (0.23 × 0.23 × 0.1) m^3 in order to detect the flow inversions near the opening.

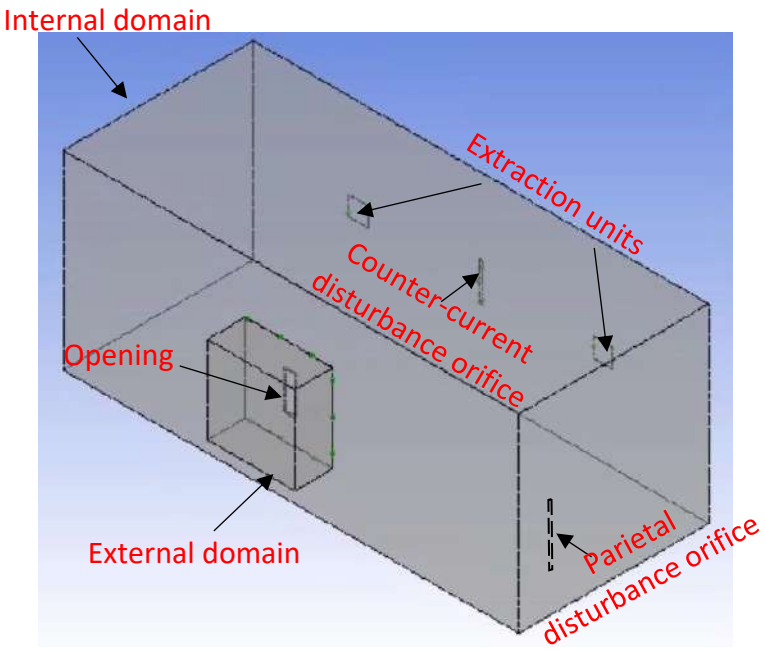

Figure 4-1 Geometry of the simulation domain

Meshing

The mesh is composed of 426 063 nodes and 2 250 433 tetrahedral elements in the case of counter-current disturbing jet, as shown in Figure 4-2. It is composed of 647 126 nodes and 3 700 471 tetrahedral elements in the case of the parietal disturbing jet. The mesh is refined in the regions of interest: around the opening, the extraction units, the injection orifice, and throughout the zone of the jet between the opening and the injection orifice.

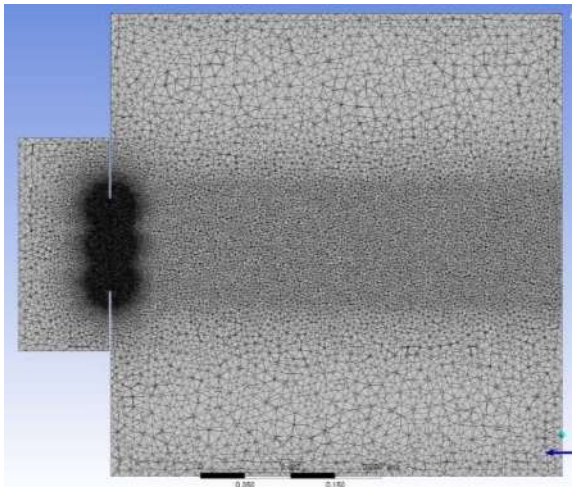

Figure 4-2 Experimental chamber meshing in the vertical plane in the case of counter-current disturbing jet

Simulation time

In the following simulations, the initial conditions were obtained using RANS simulations and the unsteady simulations were carried out using DES-SST simulations. The simulations were led: first using a passive tracer and then injections of He and aerosol are operated simultaneously.

Our simulations were launched on 4 calculation nodes (with a total of 48 cores). RANS simulations required 4 hours and 30 minutes, for 5000 iterations. DES-SST simulations using the passive tracer required 4 days and 14 hours; while those with He and aerosols simultaneously injected require 5 days and 7 hours, for a physical simulation time of 20 s.

4.1.1 Visualization of the backflow phenomenon

In order to visualize the backflow phenomenon, we applied two types of numerical procedure. First of all, we start by visualizing the disturbing jet and the backflow local features by using a passive tracer that follows completely the fluid flow. After that, we tried to follow the experimental procedure. That's why we injected two types of pollutants inside the enclosure: the gaseous pollutant and the aerosol pollutant of 5 m aerodynamic diameter. In both cases we are interested in detecting flow inversions near the opening.

4.1.1.1 Preliminary works using a passive tracer

Our preliminary visualizations aim to visualize the disturbing jet and its impact on the opening. A passive tracer that simulates a gaseous (neutrally buoyant) pollutant of the flow is added and injected through the orifice of the disturbance. This part aims principally to visualize the backflow characteristics near the opening.

4.1.1.1.1 Boundary conditions and simulation characteristics of the transient model

Boundary conditions

The boundary conditions are shown in Figure 4-1 and are related to an open-circuit where a disturbance flowrate is injected from the rear wall and then collected by the extraction of the enclosure. The simulated fluid is air at 25°C (density = 1.185 kg.m^{-3}). We introduce an additional variable Φ and solve a convection-diffusion transport equation of the passive tracer. The molecular diffusivity of the passive tracer is D_Φ= 10^{-5} m^2.s^{-1} and the number of turbulent Schmidt number, defined as the ratio of turbulent viscosity to turbulent diffusivity $Sc_t = \nu_t / D_t$, is set to Sc_t = 0.9. The passive tracer is injected at the injection orifice of the disturbing flow.

The boundary conditions fixed during the simulations are summarized in Table 4-1.

The average value of the incoming velocity at the opening is determined by the flowrate that is imposed at the extraction. As we want to study a flowrate at the opening corresponding to a velocity U_{ope}= 1 m. s^{-1} ($Q_{opening}$= 10.8 m^3.h^{-1}) and an average injection velocity, V_0 = 10 m.s^{-1} at the jet nozzle ($Q_{disturbance}$ = 36 m^3.h^{-1}), the extraction flowrate of the enclosure, $Q_{extract}$, is calculated by the expression: $Q_{extraction} = Q_{opening} + Q_{disturbance}$ = 46.8 $m^3.h^{-1}$. The volumetric flowrates are shown in Figure 4-3.

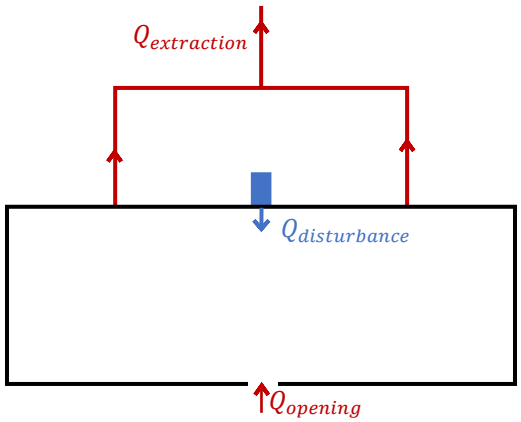

Figure 4-3 Horizontal plane crossing the opening showing the volumetric flowrates for the numerical simulations

Table 4-1 Boundary conditions for the DES simulations

Boundary conditions	Type and value
Injection orifice	Inlet, V_0 = 10 m/s, concentration Φ_{tracer} = 1 $k = \frac{3}{2}(I\,U)^2, \varepsilon = C_\mu \rho \frac{k^2}{\mu_t}, \omega = \frac{\varepsilon}{k}$ $\mu_t = 1000 I\mu\ (I = 3{,}7\%)$
Extraction units	Outlet, $U_{extraction}$ = 2.6 m/s corresponding to U_{ope}=1m/s
External domain	Opening, P = 0, concentration Φ_{tracer} = 0
Other	Wall, no slip wall condition + automatic wall law

Simulation characteristics

In this study, the turbulence model is the hybrid model SST-DES. An advection scheme of type 'central difference' and a 'second order backward Euler' transient scheme are applied. The time step is set to 0.001 s and the simulation time is 20 s. The simulation characteristics are summarized in Table 4-2.

Table 4-2 Numerical parameters for the DES modelling

Model	SST-DES
Fluids	Air and He (passive scalar)
Advection scheme	Central difference
Transient scheme	Second order backward Euler
Time step	0.001 s
Simulation time	20 s

4.1.1.1.2 Initial conditions related to steady state conditions

The initial flow conditions correspond to the stationary solution of RANS simulations applied on the chamber, and represents the initial flow field of the enclosure under negative pressure drop, where the flow enters at the opening with no disturbance applied. The extraction units are of type outlet and have a velocity $U_{extraction}$ = 0.6 m/s, which corresponds to a velocity at the opening equals to U_{ope} = 1 m/s. Since there is no disturbance applied for initial conditions, the injection orifice is considered as a wall. Boundary

conditions are presented in Table 4-3. The fluid injected is air at 25°C. The turbulence model used is SST k-ω with high resolution numerical scheme and a time step of 0.01s.

Table 4-3 Initial conditions for the RANS simulation

Boundary Conditions	Type and value
Extraction	Outlet, $U_{extraction}$ = 0.6 m/s
External domain	Opening, P = 0
Other	Wall

The vertical and horizontal velocity fields in the median plane of the opening are shown in Figure 4-4. The RANS solution will be further used as the initial condition for the SST-DES simulations.

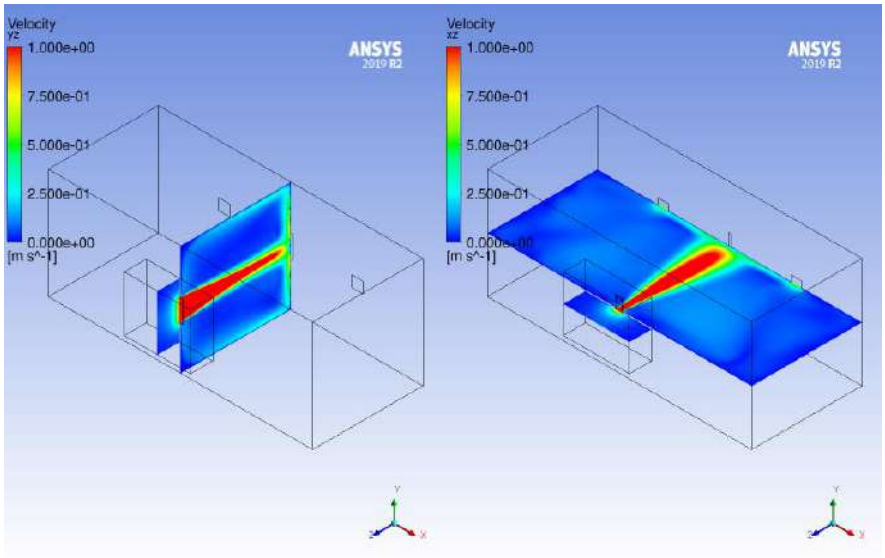

Figure 4-4 Velocity field in the vertical (left) and horizontal (right) median planes crossing the opening for RANS simulations

4.1.1.1.3 Transient results using SST-DES hybrid model (passive scalar fields)

Figure 4-5 and Figure 4-6 show respectively the passive tracer fields in the vertical and horizontal median planes crossing the opening corresponding for an inflow velocity U_{ope} = 1 m/s and a disturbing jet of velocity V_0 = 10 m/s at the nozzle outlet for different simulation times for DES-SST modelling.

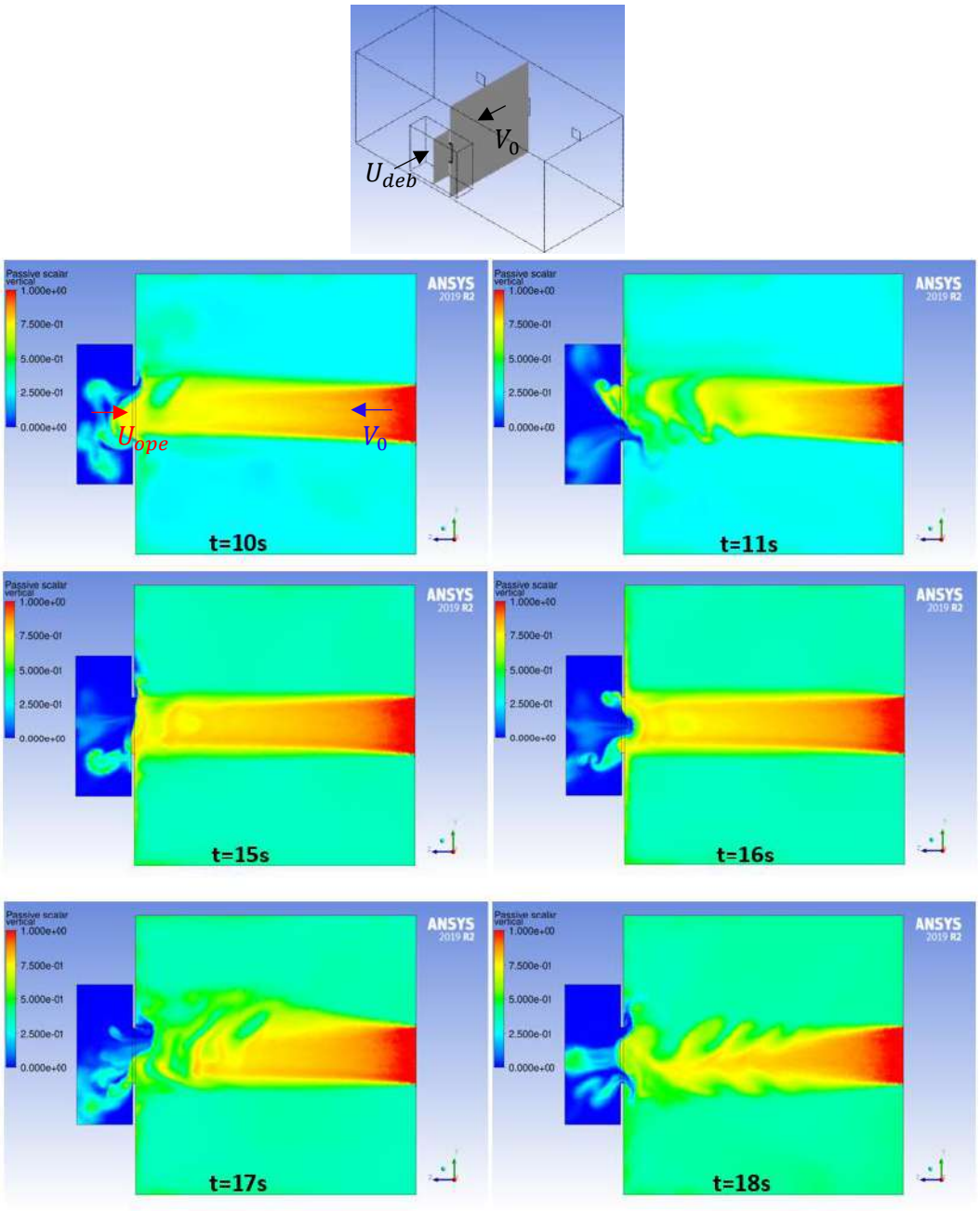

Figure 4-5 Passive tracer fields of concentration in the vertical median plane of the opening for the SST-DES simulation for U_{ope} = 1m/s and V_0 = 10 m/s for different times

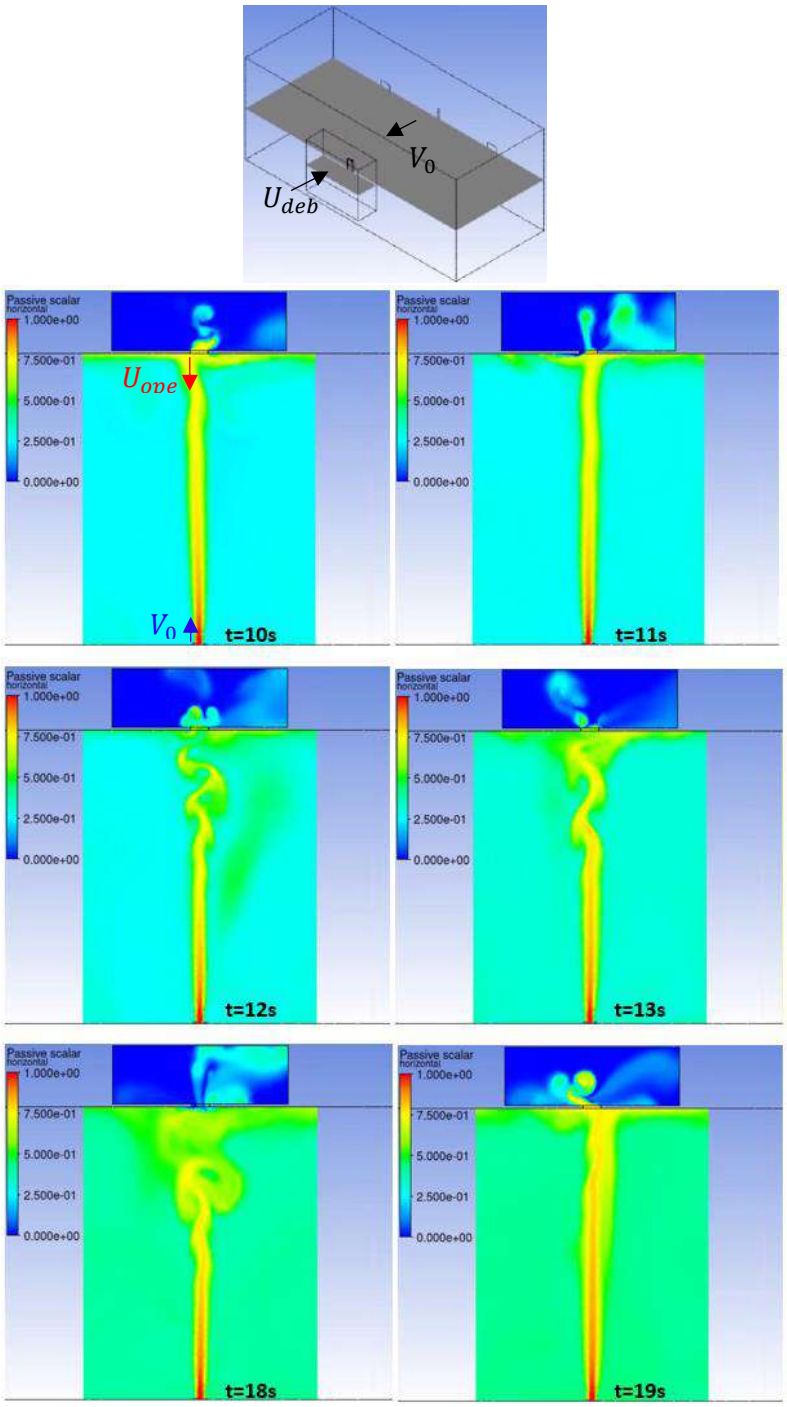

Figure 4-6 Passive tracer concentration fields in the horizontal median plane of the opening for the SST-DES simulation for U_{ope} = 1 m/s and V_0 = 10 m/s for different times

Eddy structures are detected particularly in the fully developed zone that occurs upstream of the opening. The passive tracer concentration fields in the vertical median plane in Figure 4-5 show that the tracer escapes the enclosure in the form of vortices near the opening. Vortices sways outside the enclosure near the center of the opening or at top and bottom regions of the opening (upper and lower edges of the opening). Inside the enclosure, we observed zones that are empty of tracer near the opening. This is due

to the occurrence of tracer taken back to inside the enclosure near the upper and lower edges of the opening. Simultaneously, the passive tracer fields in the horizontal median plane in Figure 4-6 show the leakage of the tracer to the outside of the enclosure swaying between the right, center and left sides of the opening. However, inside the enclosure and near the opening, we did not really found zones that are free of tracer as in the vertical plane. This could be due to the fact that the return of the tracer is especially occurring near the upper and lower edges of the opening. These visualizations highlight the importance of the opening edges on the backflow. We should also mention that the backflow phenomenon is not a periodic phenomenon nor a steady phenomenon. It is considered as an intermittent phenomenon occurring at irregular intervals and at different locations.

4.1.1.1.4 Comparison between experimental and numerical visualization fields

In this part, we compare the tracer fields obtained from our experimental laser visualizations to those obtained from the SST-DES numerical simulations in the vertical median plane of the opening. The tracer used to follow the fluid flow is composed of smoke oil particles (d_{ae} lower than 1 µm) in the case of laser visualizations and to passive tracer in numerical simulations. We applied an inflow near the opening of U_{ope} = 1 m/s and a counter-current internal turbulent jet of velocity V_0 at the nozzle outlet.

Figure 4-7(top) shows the vertical tracer fields obtained from the laser visualization for an inflow U_{ope} = 1 m/s and for three values of V_0: 3.2 m/s, 6 m/s and 11.7 m/s respectively. Figure 4-7 (bottom) shows the vertical tracer fields obtained from numerical simulations for an inflow U_{ope} = 1 m/s and for three values of V_0: 3 m/s, 6 m/s and 12 m/s respectively.

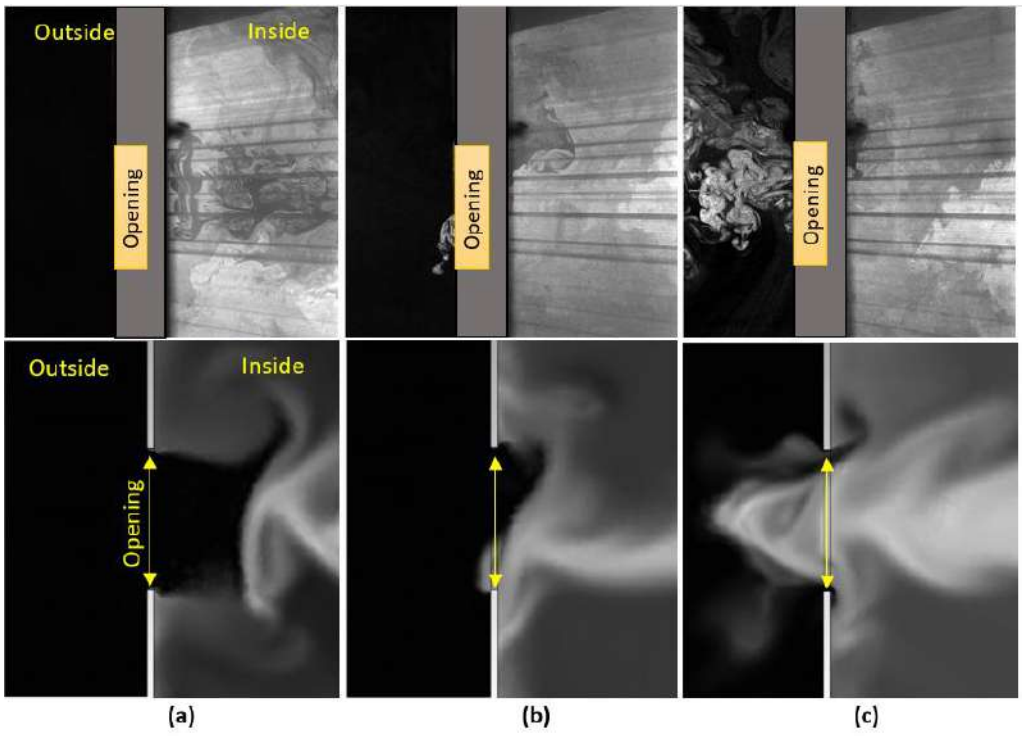

Figure 4-7 Top: laser visualization fields in the vertical median plane for an inflow of U_{ope}= 1 m/s and for three values of V_0: 3,2 m/s (a), 6 m/s (b) and 11,7 m/s (c) respectively. Bottom: numerical simulations of tracer in the vertical median plane for an inflow U_{ope} = 1 m/s and for three values of V_0 : 3 m/s (a), 6 m/s (b) and 12 m/s (c) respectively at different times

For V_0 = 3 m/s, we can see on tracer fields from laser visualization and numerical simulation in Figure 4-7(a) that there is no pollutant backflow near the opening. The dynamic containment succeeds to prevent the leakage of the tracer to outside the enclosure. For V_0 = 6 m/s, there is a leakage of a small quantity of tracer to the outside of the enclosure with a capture of part of it to inside the enclosure. Flow inversions are occurring near the opening. This phenomenon is observed simultaneously with the laser visualization and with the numerical vertical field as seen in Figure 4-7(b). For V_0 = 12 m/s, there is leakage of a significant quantity of the tracer to outside of the enclosure as we can see in both cases in Figure 4-7(c). In this case, the dynamic containment failed to prevent the leakage of the tracer.

Here, we can say that the SST-DES model using a passive tracer was able to reproduce the qualitative aspect of the backflow phenomenon of gaseous and pollutant composed of small particles with d_{ae} lower than 1 µm.

4.1.1.2 Visualizations using two-phase flow matching our experimental procedure

In order to reproduce the experimental conditions, we used a closed-circuit for producing the disturbance. We inject the pollutants (helium and 5 µm particles) by adding a pointwise source in the center of the enclosure. Part of the mixture (air/ helium/ 5 µm particles) is extracted from a sink point located at the right side of the enclosure, then reinjected at the injection orifice in the rear wall facing the opening for the case of counter-current internal jet or at the right side wall for the case of the parietal internal disturbing jet as shown in Figure 4-8.

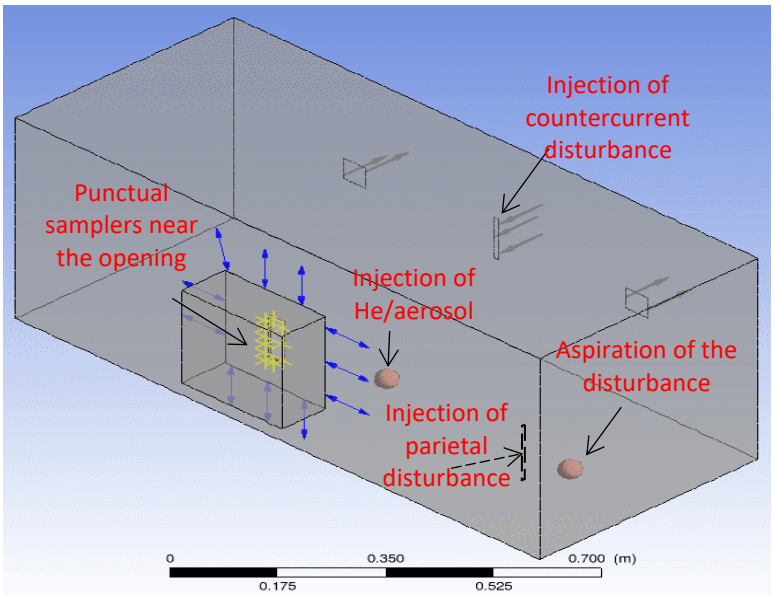

Figure 4-8 Boundary conditions for the numerical model of the enclosure in the case of counter-current disturbing jet

4.1.1.2.1 Boundary conditions and simulation characteristics of the unsteady regime

Boundary conditions

The boundary conditions for the numerical simulations shown in Figure 4-8 are presented in Table 4-4.

Table 4-4 Boundary conditions for the DES modelling

Boundary conditions	Type and value
Disturbance injection	Inlet, q_{inlet} (corresponding to the mass flowrate extracted at the disturbance sink point for V_0 = 16 m/s) $k = \frac{3}{2}(I\ U)^2, \varepsilon = C_\mu \rho \frac{k^2}{\mu_t}, \omega = \frac{\varepsilon}{k}$ $\mu_t = 1000 I \mu\ (I = 3{,}7\%)$
Extraction units	Outlet, $U_{extraction}$ = 0,6 m/s corresponding to U_{ope} = 1 m/s
External domain	Opening, P_{rel} = 0 Pa, Φ_{He} = 0, $\Phi_{aerosol}$ = 0
Other	Wall, no slip wall condition, aerosol deposition flux
Helium and aerosol injection	Source point, q_{He} = 1.66 g/h, $q_{aerosol}$ = 6.10^{-3} g/h
Disturbance source	Sink point, -q_{inlet}, at the right side of the enclosure corresponding to the extraction of a volumetric flow rate Q_{inlet} of the mixture (air/ helium/ 5 µm particles).

Simulation characteristics of the unsteady regime

In this study, the turbulence model used in simulations is SST-DES. The fluids are: air at STP (standard temperature and pressure) which constitutes the continuous phase and the constraint component for the mass balance, He gas at STP which follows a classical variable transport equation and 5 µm particles which are described using an algebraic equation. This algebraic equation is given by the simplified Eulerian transport model (diffusion-inertia model) (Nerisson et al, 2011) as shown in chapter 1. We should note that these fluids conditions are further used for numerical simulations of the envelope in global quantification part (section 4.2). An advection scheme of type 'central difference' for LES-like simulation and a 'second order backward Euler' transient scheme are applied for the numerical parameters. The time step is 0.001 s (the turbulence time scale (k/ε) is typically of the order of 10^{-2} s) and the simulation time is 20 s. The simulation characteristics are summarized in Table 4-5.

Table 4-5 The simulation characteristics used for the DES simulation

Model	DES-SST
Fluids	Air at STP (constraint)
	He at STP (transport equation)
	Particles (algebraic equation)
Advection scheme	Central difference
Transient scheme	Second order backward Euler
Time step	0.001 s
Simulation time	20 s

4.1.1.2.2 Initial conditions related to steady state conditions

First, we filled out the chamber with helium and 5 µm aerosol particles from the source point. The initial flow conditions correspond to the steady solution of a RANS simulation of the flow within the chamber, where the flow enters at the opening without disturbance applied. The extraction units are of type outlet

and have a velocity $U_{extraction}$ = 0.6 m/s which corresponds to a velocity at the opening equals to U_{ope} = 1 m/s. The injection orifice of the disturbance is considered as a wall. Boundary conditions are presented in Table 4-6. The fluid injected is a mixture of air, helium and 5 µm particles at STP. The turbulent model used is SST k-ω with high resolution and a time step of 0.01 s.

Table 4-6 Initial conditions for the RANS simulation

Boundary Conditions	Type and value
Extraction	Outlet, $U_{extraction}$ = 0.6 m/s
External domain	Opening, P_{rel} = 0 Pa, Φ_{He} = 0, $\Phi_{aerosol}$ = 0
Other	Wall, no slip wall condition
Helium and aerosol injection	Source point, $q_{He,injection}$, $q_{aerosol,injection}$

The helium molar fraction and particle mass concentration fields in the horizontal median plane of the opening are shown in Figure **4-9**. A mixture of air, helium and particles of 5 µm are injected from the source point and are then homogenized in the enclosure as shown in Figure **4-9**. We monitor the concentration of helium and aerosol at the extraction units in order to deduce their corresponding concentrations at the equilibrium state C_{He_in} and $C_{aerosol\_in}$. The RANS solution is further used as initial condition for DES simulations.

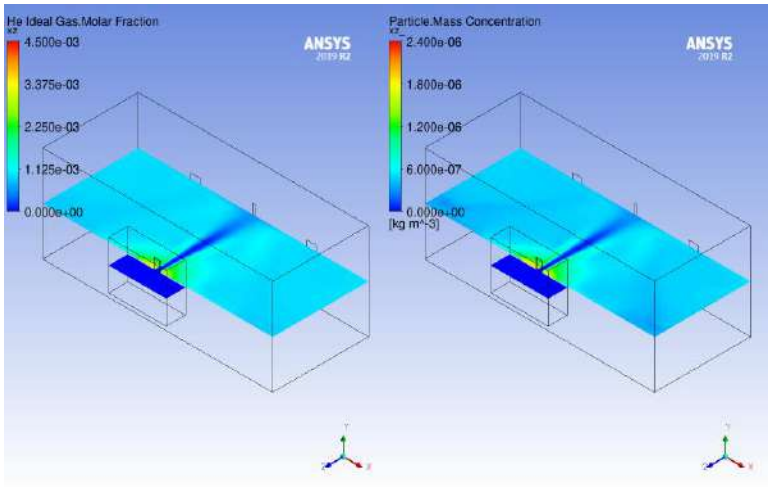

Figure 4-9 Helium molar fraction (left) and particles mass concentration (right) fields in the horizontal median plane of the opening for the URANS initial conditions

4.1.1.2.3 Helium and aerosol transient simulations

4.1.1.2.3.1. Visualization results with a counter-current internal disturbing jet

Figure 4-10 and Figure 4-11 show the helium molar fraction and particulate mass concentration fields in the vertical and horizontal median planes from the opening corresponding to U_{ope} = 1 m/s and a counter-current internal jet of V_0 = 16 m/s at different times.

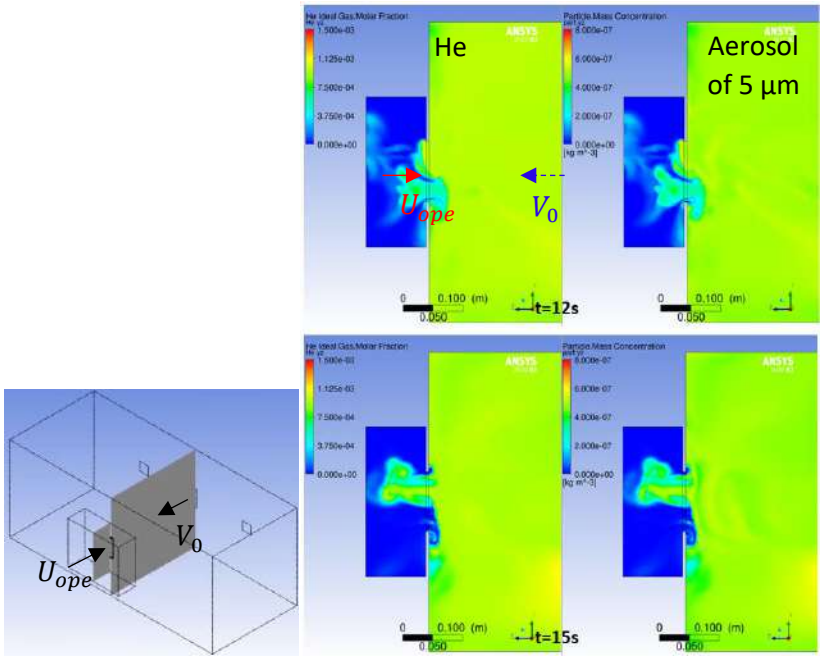

Figure 4-10 Helium molar fraction (left) and particles mass concentration (right) fields in the vertical median plane of the opening for U_{ope} = 1 m/s and V_0 = 16 m/s for the counter-current disturbing jet

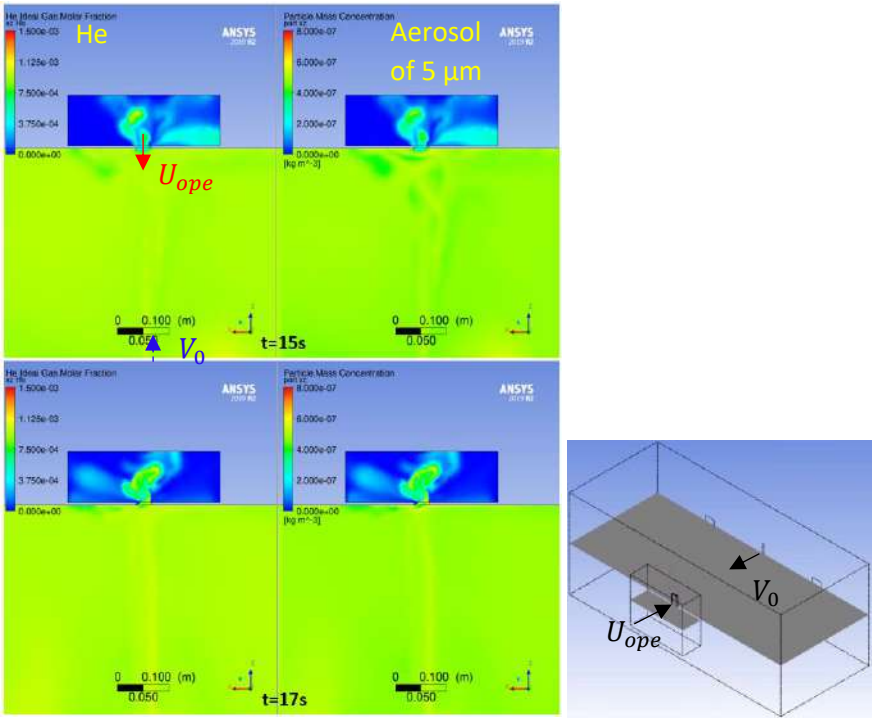

Figure 4-11 Helium molar fraction (left) and particles mass concentration (right) fields in the horizontal median plane for U_{ope} = 1 m/s and V_0 = 16 m/s for the counter-current disturbing jet

As we can note in Figure 4-10 and Figure 4-11, there is a leakage of helium and aerosol to outside the enclosure under the effect of the counter-current internal jet. The backflow near the opening occurs in all directions. The behaviors of gas and aerosol seems to be very similar along the jet and near the opening.

4.1.1.2.3.2. Visualization results of parietal internal disturbing jet

This part concerns the results corresponding to the parietal internal jet. As mentioned above, part of the mixture is extracted from a sink point and then reinjected at the injection orifice located at the right-side wall in the case of parietal internal jet. Figure 4-12 and Figure 4-13 show the helium molar fraction and particulate mass concentration fields in the vertical and horizontal median planes from the opening corresponding to U_{ope} = 1 m/s and an internal parietal jet of V_0 = 40 m/s, at different times. Figure 4-14 shows the velocity and helium molar fraction fields in the horizontal median plane of the opening corresponding to U_{ope} = 1 m/s and V_0 = 40 m/s for the case of parietal internal disturbing jet for t = 9s.

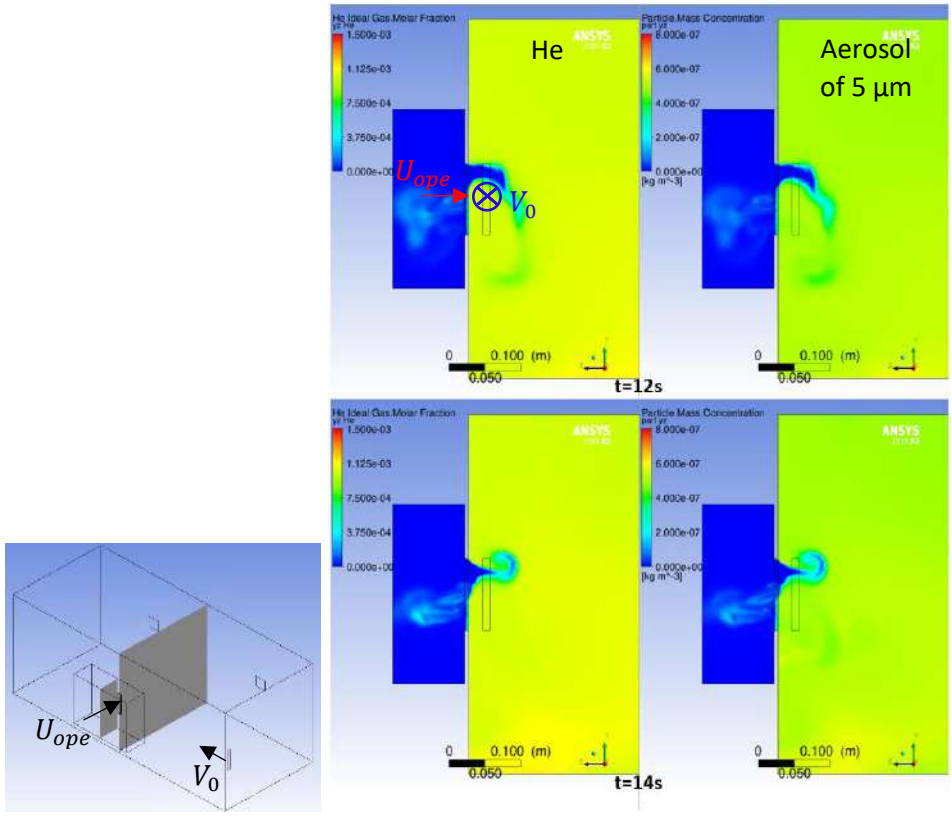

Figure 4-12 Helium molar fraction (left) and particles mass concentration (right) fields in the vertical median plane of the opening corresponding to U_{ope} = 1 m/s and V_0 = 40 m/s for the case of parietal internal disturbing jet

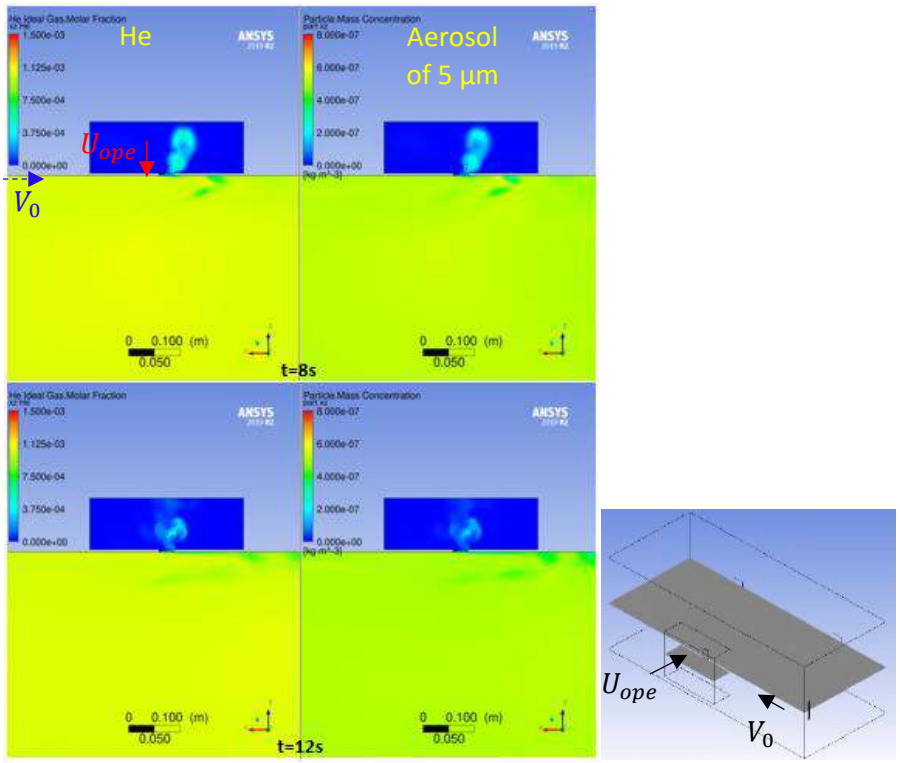

Figure 4-13 Helium molar fraction (left) and particles mass concentration (right) fields in the horizontal median plane of the opening corresponding to U_{ope} = 1 m/s and V_0 = 40 m/s for the case of parietal internal disturbing jet

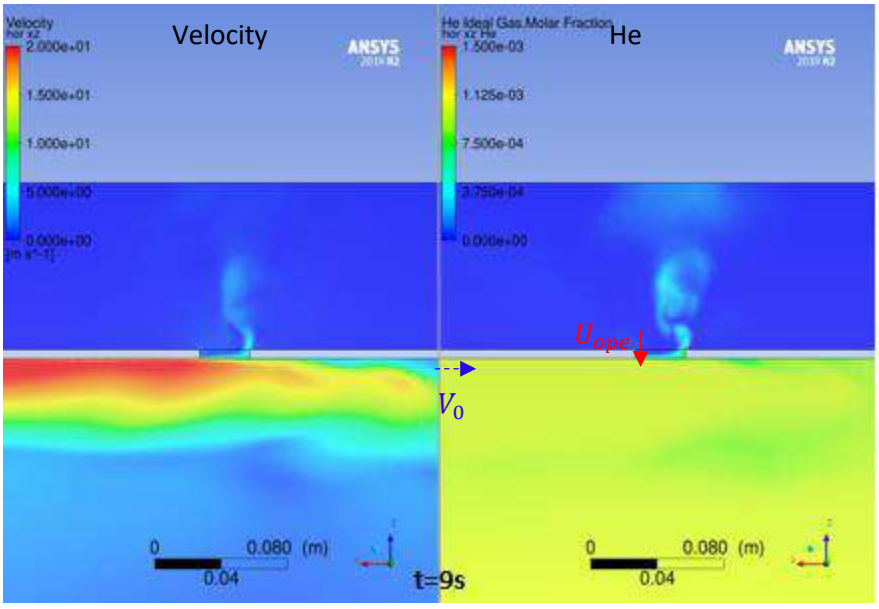

Figure 4-14 Velocity magnitude (left) and helium molar fraction (right) fields in the horizontal median plane of the opening corresponding to U_{ope} = 1 m/s and V_0 = 40 m/s for the case of parietal internal disturbing jet for t = 9s

As we see in Figure 4-12 and Figure 4-13, flow inversions are detected near the opening with leakage of the tracer to outside the enclosure. Following the horizontal plane, we find that the backflow phenomenon is present near the opening at the opposite direction of the jet. The velocity field in Figure 4-14 shows that the fluid flows from the right-side wall along the frontal wall and the parietal jet hits the edge of the left side of the opening, resulting in a significant backflow of pollutants along this edge. Again, we can observe that the gas and aerosol behaviors are very similar near the opening.

4.1.2 Quantification of the local backflow using two-phase flow simulations

4.1.2.1 Procedure

As explained above, in order to quantify the backflow and to be representative of our experimental conditions, we injected helium gas and 5 µm particles inside the enclosure. Once the enclosure is filled with the pollutants in the RANS initial conditions (Figure **4-9**), we monitor the pollutant concentration in the extraction units at equilibrium $\overline{C_{He\_in}}$ and $\overline{C_{aerosol\_in}}$. Then, for our SST-DES simulations, part of the mixture is taken from a sink in the enclosure and then reinjected through the orifice of the disturbance. We added 11 pointwise samples surrounding the opening at the top, down, right, left and facing sides as shown in Figure 4-15 in order to monitor the helium and aerosol concentrations due to backflow near the opening. The mean values of helium and aerosol over these pointwise samplers over the simulation time represent $\overline{C_{He\_out}}$ and $\overline{C_{aerosol\_out}}$ respectively. The simulation time of 20 s is quite enough for the concentration near the opening to reach a steady value.

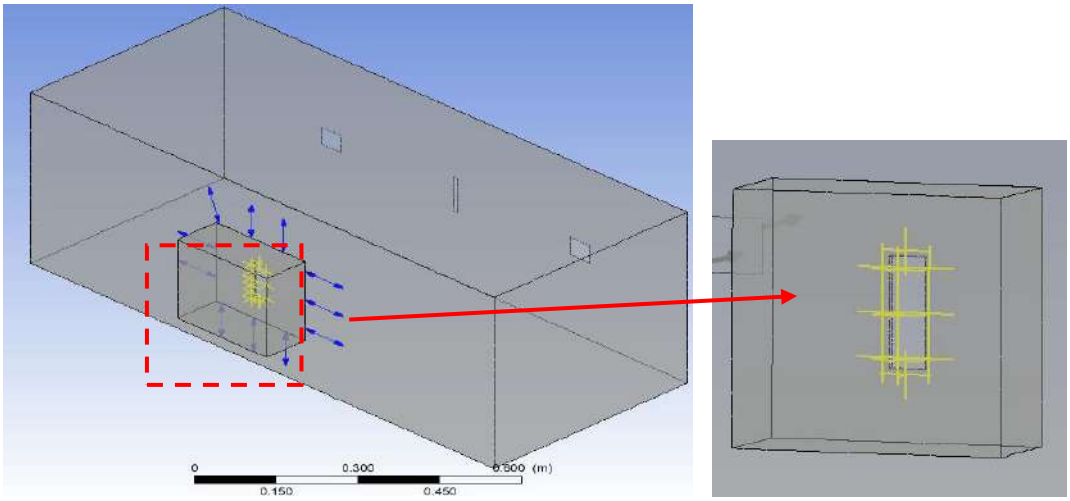

Figure 4-15 Pointwise samplers near the opening to monitor the pollutants concentration

Then we calculate the gaseous and particulate backflow coefficients. The gaseous backflow coefficient is calculated through the expression *K* (%) = $\overline{C_{He\_out}}$ / $\overline{C_{He\_in}}$ for helium. Likewise, the particulate backflow coefficient is calculated through the expression *K* (%) = $\overline{C_{aerosol\_out}}$ / $\overline{C_{aerosol\_in}}$ for 5 µm particles. The uncertainty on the backflow concentration corresponding to $\overline{C_{He\_out}}$ is calculated as the ratio of the standard deviation $\sigma_{C_{He\_out}}$ over the mean value $\overline{C_{He\_out}}$ at the 11 pointwise samplers, and that on the initial concentration at steady state corresponding to $\overline{C_{He_in}}$is calculated as the ratio of the standard deviation $\sigma_{C_{He\_in}}$ over the mean value in the extraction units $\overline{C_{He\_in}}$. The total uncertainty $U_{r\,(K)}$ related to *K* (%) is the combination of these two uncertainties as shown in Eq. 4.1.

$$U_{r\,(K)} = \left(\frac{\sigma_{C_{He\_in}}}{C_{He\_in}} + \frac{\sigma_{C_{He\_out}}}{C_{He\_out}} \right) \quad \text{(Eq. 4.1)}$$

4.1.2.2 *Backflow coefficients for gaseous and particulate release due to counter-current internal disturbing jet*

We performed SST-DES simulations for three values of inflow at the opening: U_{ope} = 0.5 m/s, 1 m/s and 1.5 m/s. We varied the velocity of the counter-current disturbing jet V_0 from 3 m/s to 14 m/s for the case of U_{ope} = 0.5 m/s, from 6 m/s to 28 m/s for the case of U_{ope} = 1 m/s and from 9 m/s to 42 m/s for the case of U_{ope} = 1.5 m/s. Note that the disturbing velocities V_0 range in our experimental conditions is between 3 m/s to 14 m/s.

Figure 4-16 shows the evolution of the gaseous backflow coefficient *K* (%) as a function of V/U_{ope} corresponding to the three inflow velocities U_{ope} = 0.5 m/s, 1 m/s and 1.5 m/s respectively obtained from SST-DES simulations in the case of counter-current internal disturbing jet.

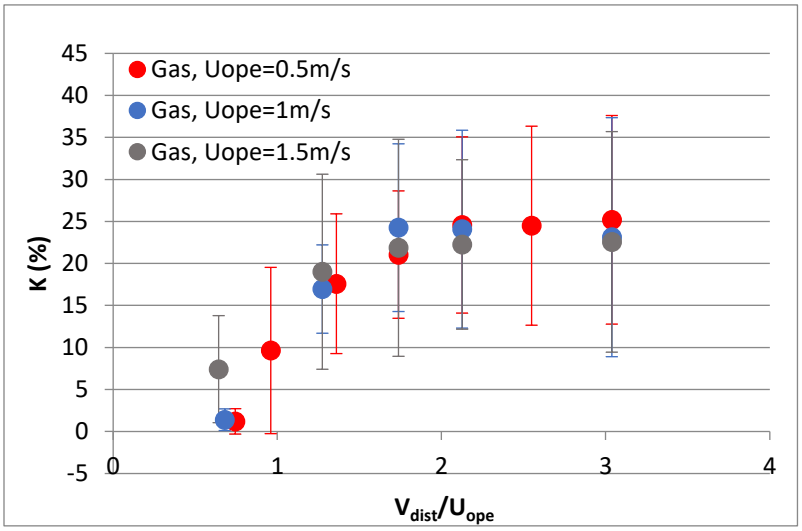

Figure 4-16 Evolution of the gaseous backflow coefficient K (%) as a function of V_{dist}/U_{ope} corresponding to U_{ope} = 0.5 m/s, 1 m/s and 1.5 m/s respectively obtained from SST-DES simulations in the case of counter-current internal disturbing jet

As we see in Figure 4-16, the three gaseous backflow curves corresponding to the three inlet velocities U_{ope} = 0.5 m/s, 1 m/s and 1.5 m/s are overlapped. The backflow phenomenon starts to occur for V_{dist}/U_{ope} = 0.7 for U_{ope} = 0.5 m/s and 1 m/s and a little bit earlier for U_{ope} = 1.5 m/s but remains within uncertainties. They show an increasing trend with V_{dist}/U_{ope} until a plateau value of K ~ 25% for V_{dist}/U_{ope}=2.

Figure 4-17 shows the evolution of the particulate backflow coefficient *K* (%) as a function of V_{dist}/U_{ope} corresponding to the three inflow velocities U_{ope} = 0.5 m/s, 1 m/s and 1.5 m/s respectively obtained from DES simulations in the case of counter-current disturbing jet.

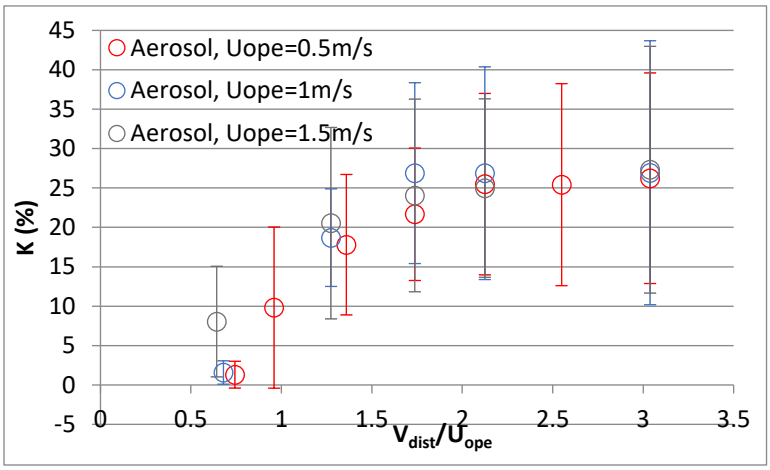

Figure 4-17 Evolution of the particulate backflow coefficient K (%) as a function of V_{dist}/U_{ope} corresponding to U_{ope} = 0.5 m/s, 1 m/s and 1.5 m/s respectively obtained from SST-DES simulations in the case of counter-current internal disturbing jet

Similarly, to gaseous pollutant, the three particulate backflow curves in Figure 4-17 corresponding to the three inlet velocities are overlapped and show an increasing trend with V_{dist}/U_{ope}. They reach a plateau value of K ~ 27% for V_{dist}/U_{ope} = 2.

We note that due to experimental limitations, it was not possible to reach high values of V_{dist}/U_{ope} for the case of U_{ope} = 1 m/s and 1.5 m/s to verify if the gaseous and particulate backflow coefficient evolutions reach a constant value as seen for U_{ope} = 0.5 m/s. However, thanks to numerical simulations in Figure 4-17 and Figure 4-18, we validate that the curves corresponding to U_{ope} = 1 m/s and 1.5 m/s reach the same constant value of *K* (%) as for U_{ope} = 0.5 m/s.

Figure 4-18 shows the comparison between backflow coefficients *K* (%) of gaseous and 5 µm particulate pollutants versus V_{dist}/U_{ope} for the inflow velocity at the opening fixed at 0.5 m/s, in the case of a counter-current internal free jet disturbance obtained from our numerical simulations.

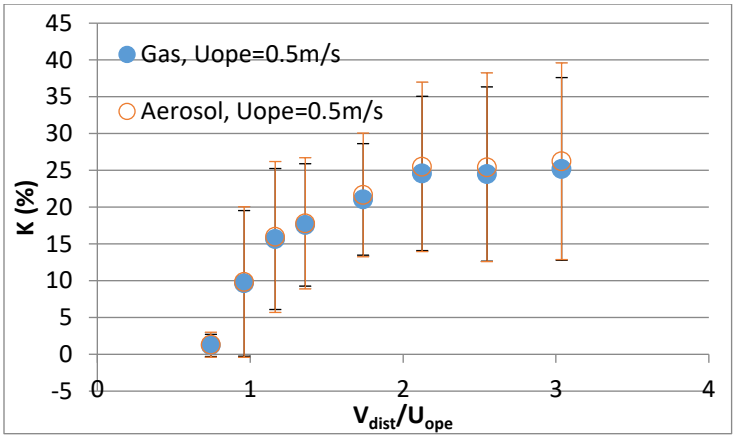

Figure 4-18 Comparison of the gaseous and particulate pollutant backflow coefficient K (%) versus V_{dist}/U_{ope} for the inflow velocity 0.5 m/s at the opening in the case of a counter-current internal free jet disturbance obtained from the DES simulations

As we see in Figure 4-18, the curves corresponding to helium and aerosol of 5 µm are overlapped for counter-current internal disturbing jet and for the inflow velocity U_{ope} = 0.5 m/s; we mention that the gaseous and particulate curves corresponding for each of the inflow velocities U_{ope} = 1 m/s and 1.5 m/s are also overlapped. Thus, the gaseous and aerosol behaviors are similar in terms of backflow for the three inflow velocities and for V_{dist}/U_{ope} ranging between 0.7 and 3.

We also note that in order to compare the experimental and numerical quantitative results, the pointwise samplers were substituted by circular filters placed near the opening. We performed a study on the sensibility of the backflow coefficient K (%) on these circular filters (see appendix 3). We found that the backflow coefficient depends essentially on the position and on the number of the samplers near the opening. For the local bakflow part and in order to validate our numerical results with the experimental results, filters should be positionned at the same locations. However, this dependancy of the backflow concentration on the sampler positions lead to find another way to quantify the backflow phenomenon based on the total mass flux of pollutants due to backflow. This justifies the addition of the global envelope around the enclosure, where pointwise samplers are no longer present near the opening. In this way, the overall quantity of the pollutants is captured in the extraction circuit of the envelope.

4.1.2.2.1 Comparison of experimental and numerical quantitative results corresponding to counter-current internal disturbing jet

In this part, we compare gaseous and particulate backflow coefficients from numerical and experimental works for U_{ope} = 0.5 m/s and for a counter-current disturbing jet, in the case where we located five samplers then three samplers near the opening as shown in Figure 4-19.

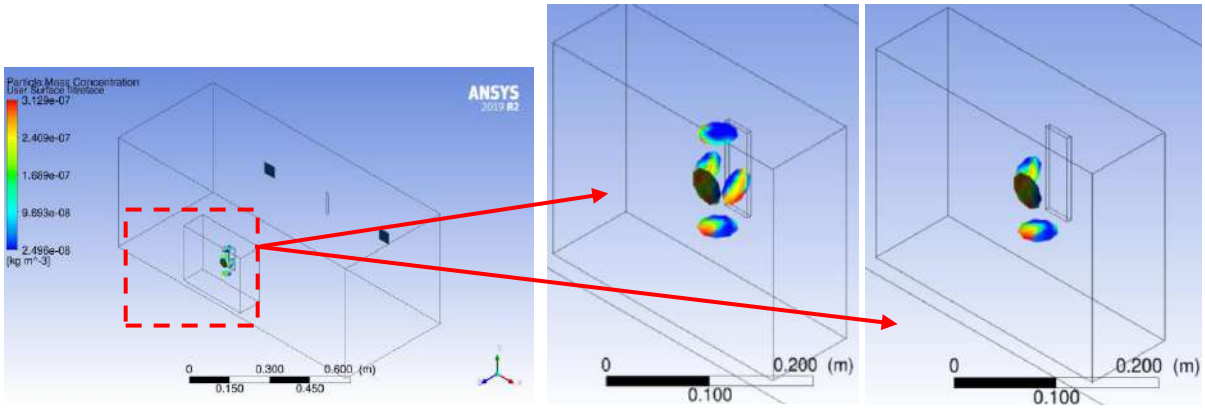

Figure 4-19 Circular samplers located near the opening for each case (5 samplers then 3 samplers)

Figure 4-20 and Figure 4-21 show the evolution of the gaseous and the particulate backflow coefficients K (%) versus V_{dist}/U_{ope} for the inflow velocity 0.5 m/s at the opening in the case of a counter-current internal jet calculated using five collectors and then three collectors respectively near the opening in experimental and numerical studies.

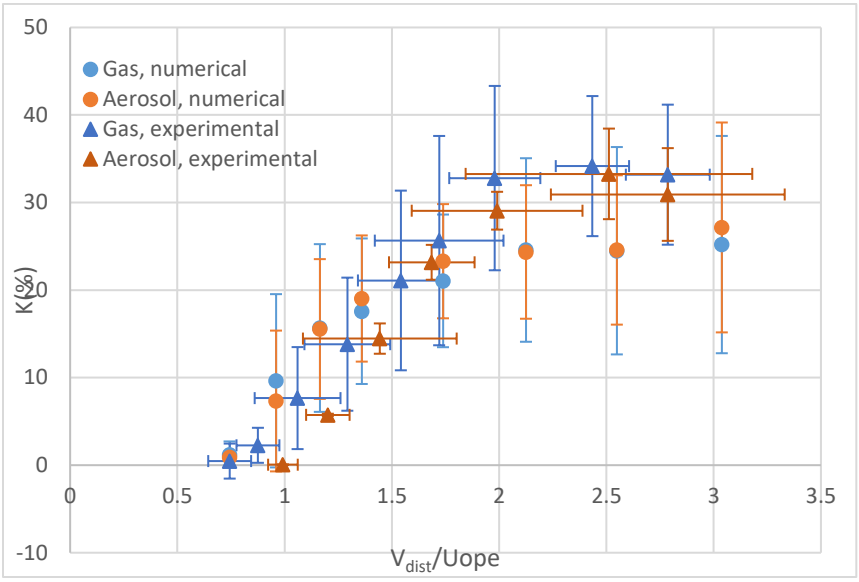

Figure 4-20 Evolution of the gaseous and the particulate backflow coefficient K (%) versus V_{dist}/U_{ope} for the inflow velocity 0.5 m/s at the opening in the case of a counter-current internal jet calculated using five collectors near the opening in experimental and numerical works

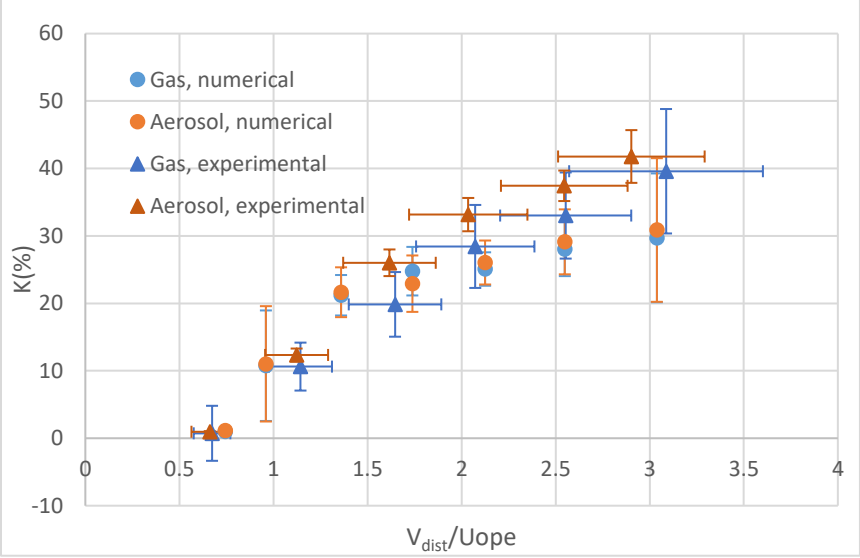

Figure 4-21 Evolution of the gaseous and the particulate backflow coefficient K (%) versus V_{dist}/U_{ope} for the inflow velocity 0.5 m/s at the opening in the case of a counter-current internal jet calculated using three collectors near the opening in our experimental and numerical works

As we can note in each of Figure 4-20 and Figure 4-21, the four curves corresponding to the gaseous and the particulate pollutants in the experimental and numerical conditions are close to each others within uncertainties. Therefore, we can conclude that the SST-DES model succeeds to predict the quantitative behavior of the backflow for the case of an internal counter-current free disturbing jet.

4.1.2.3 *Gaseous and particulate backflow coefficients of the parietal internal disturbing jet*

Similarly, to the case of a frontal disturbing jet, we calculated gaseous and particulate backflow coefficients using the SST-DES model. We chose to add three samplers near the opening as in the experimental conditions in order to compare the counter-current and the parietal internal cases in Figure 4-22. We monitored simultaneously the helium and aerosol concentrations on these samplers.

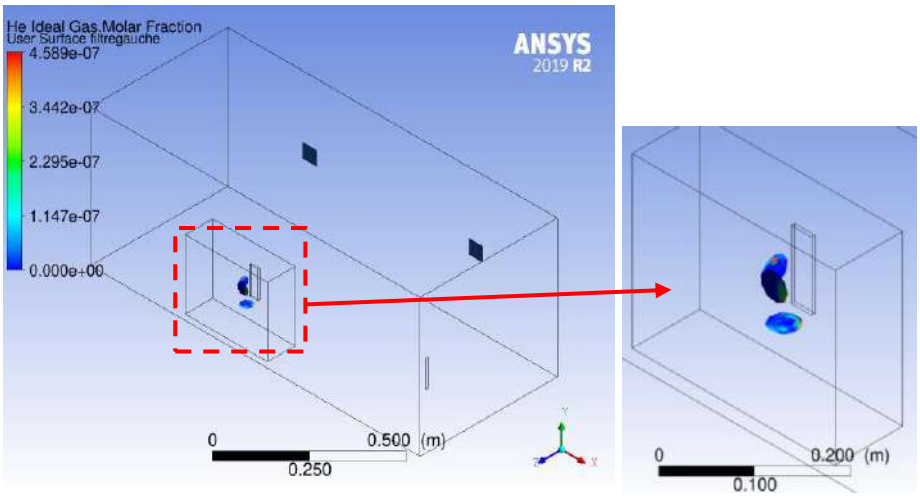

Figure 4-22 Three samplers added near the opening for the case of parietal internal jet

We performed SST-DES numerical simulations for an inflow velocity at the opening U_{ope} = 0.5 m/s and for the range of parietal internal disturbing jet V_0 from 8 m/s to 30 m/s. Simultaneously, we performed numerical simulations for inflow velocities at the opening U_{ope} = 1 m/s and 1.5 m/s corresponding to parietal internal disturbing jets V_0 of 40 m/s and 60 m/s respectively.

Figure 4-23 shows the evolution of the gaseous backflow coefficient *K* (%) as a function of V_{dist}/U_{ope} corresponding to U_{ope} = 0.5 m/s, 1 m/s and 1.5 m/s respectively obtained from SST-DES simulations in the case of parietal disturbing jet.

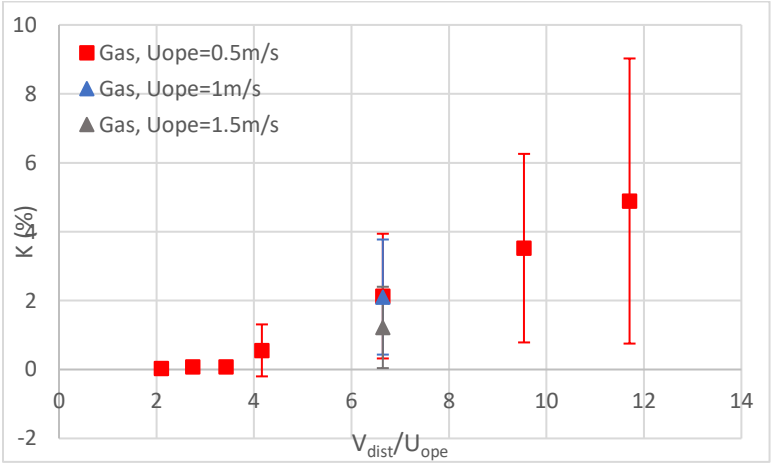

Figure 4-23 Evolution of the gaseous backflow coefficient K (%) as a function of V_{dist}/U_{ope} corresponding to U_{ope} = 0.5 m/s, 1 m/s and 1.5 m/s respectively obtained from SST-DES simulations in the case of parietal disturbing jet

As we see in Figure 4-23, we detect very low backflow coefficients (lower than 0.08 %) for V_{dist}/U_{ope} between 2 and 4. However, we observe that the onset of the backflow for the parietal internal jet is for V_{dist}/U_{ope} between 3 and 4. The backflow curve has an increasing trend. When we compare the values of *K* (%) corresponding to the inlet velocities U_{ope} = 0.5 m/s, 1 m/s and 1.5 m/s for V_{dist}/U_{ope} = 6.6, we find that they have the same order of magnitude. We note that this is also valid for the aerosol simulations.

Figure 4-24 shows the evolution of the backflow coefficient *K* (%) of the gaseous and 5 µm particulate pollutants versus V_{dist}/U_{ope} for the inflow velocity at the opening fixed at 0.5 m/s in the case of a parietal internal jet disturbance obtained from our numerical simulations.

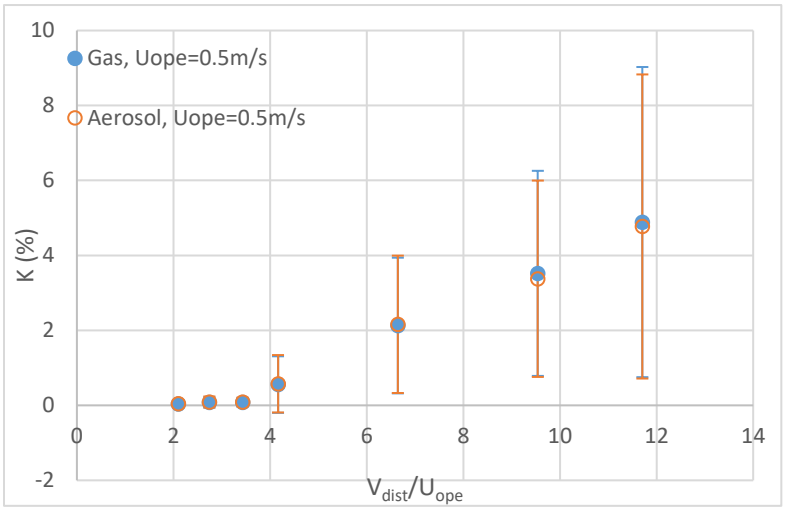

Figure 4-24 Comparison of the gaseous and the 5 µm particulate pollutant backflow coefficients K (%) versus V_{dist}/U_{ope} for the inflow velocity 0.5 m/s at the opening in the case of a parietal internal jet disturbance obtained from the DES simulations

As we see in Figure 4-24, the curves corresponding to helium and 5 µm aerosol are overlapped for the parietal disturbing jet and for the inflow velocity U_{ope} = 0.5 m/s. We can say that the behavior between the gas and the aerosol is similar in terms of backflow for the inflow velocity U_{ope} = 0.5 m/s and for V_{dist}/U_{ope} between 2 and 12. We also mention that for the two simulation points corresponding to the inflow velocities U_{ope} = 1 m/s and 1.5 m/s, the gas and aerosol behaviors were also similar in terms of backflow coefficient.

4.1.2.3.1 Comparison of experimental and numerical quantitative results corresponding to parietal internal disturbing jet

Here we compare the gaseous and particulate backflow coefficients from our numerical and experimental studies for U_{ope} = 0.5 m/s in the case where we three samplers are located near the opening for the parietal internal disturbing jet. Figure 4-25 shows the evolution of the gaseous and the particulate backflow coefficients *K* (%) versus V_{dist}/U_{ope} for the inflow velocity 0.5 m/s at the opening, in the case of a parietal internal jet calculated using first five collectors then three collectors respectively surrounding the opening for our experimental and numerical studies.

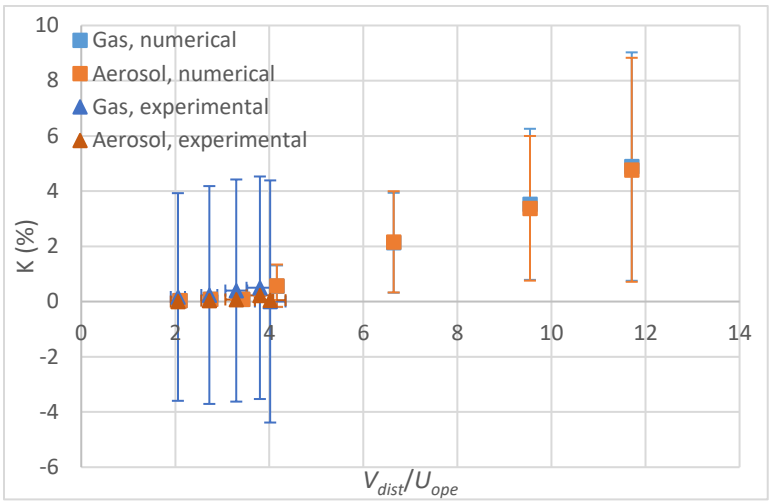

Figure 4-25 Evolution of the gaseous and the particulate backflow coefficients K (%) versus V_{dist}/U_{ope} for the inflow velocity 0.5 m/s at the opening, in the case of a parietal internal jet calculated using three samplers near the opening for our experimental and numerical studies

As we can see in Figure 4-25, the four curves corresponding to the gaseous and the particulate pollutants for experiments and numerical simulations have the same evolution within uncertainties for V_{dist}/U_{ope} between 2 and 4. However, the backflow coefficient does not exceed 0.5 %. Here we can say that the SST-DES model is able to restitute the quantitative aspect of the backflow for the case of an internal parietal disturbing jet for this range of disturbing jet velocities. Beyond this value of V_{dist}/U_{ope}, it was not possible to perform experimental measurements. However, thanks to numerical simulations, we observe that the backflow phenomenon is reinforced, but we cannot claim that the values of the backflow coefficients are consistent with experimental results.

The ability of SST-DES model to restitute the experimental qualitative results of the backflow coefficients *K* (%) is validated for the case of the counter-current and the parietal disturbing jets. The onset value of V_{dist}/U_{ope} at which the backflow phenomenon starts to occur was similar between the experiments and the numerical simulations. Additionally, the values of the backflow coefficients *K* (%) have the same order of magnitude for experiments and numerical simulations.

4.1.3 Impact of the aerodynamic diameter

In this part, we aim to comment on the results that show a similar behavior between the gas and the aerosol of 5 µm diameter. We are interested in determining the Stokes number Stk that explains the behavior between the gas and particles as shown in chapter 1. That's why we performed numerical simulations where we varied the aerodynamic diameter of particles from 5 µm to 100 µm and then the Stokes number in order to highlight the different behavior between the gas and aerosols. We neglected gravity in these simulations in order to take into account only the interactions between the gas and particles. I gravity is used large aerosols will be deposited before reaching the opening.

Figure 4-26 shows the helium molar fraction (left) and particles mass concentration (right) fields in the horizontal median plane of the opening corresponding to U_{ope} = 0.5 m/s and V_0 = 10 m/s for the case of counter-current internal disturbing jet. The aerodynamic diameter of particles is respectively 5 µm, 20 µm, 50 µm and 100 µm. The Stokes numbers related to each particle diameter are shown in

Table 4-7. They are calculated based on the definition ($Stk = \frac{\tau_p}{\tau_f}$) commented in chapter 1. The relaxation time scale of particles τ_p depends on the aerodynamic diameter ($\tau_p = \frac{\rho_p {d_p}^2}{18\,\mu_f}$). The characteristic time scale of the flow τ_f depends on the hydraulic diameter of the disturbance orifice D_h and on the velocity V at 3 cm from the opening inside the enclosure ($\tau_f = \frac{D_h}{V}$). This velocity V was recorded in numerical simulations in the presence of the inflow and the disturbing jet.

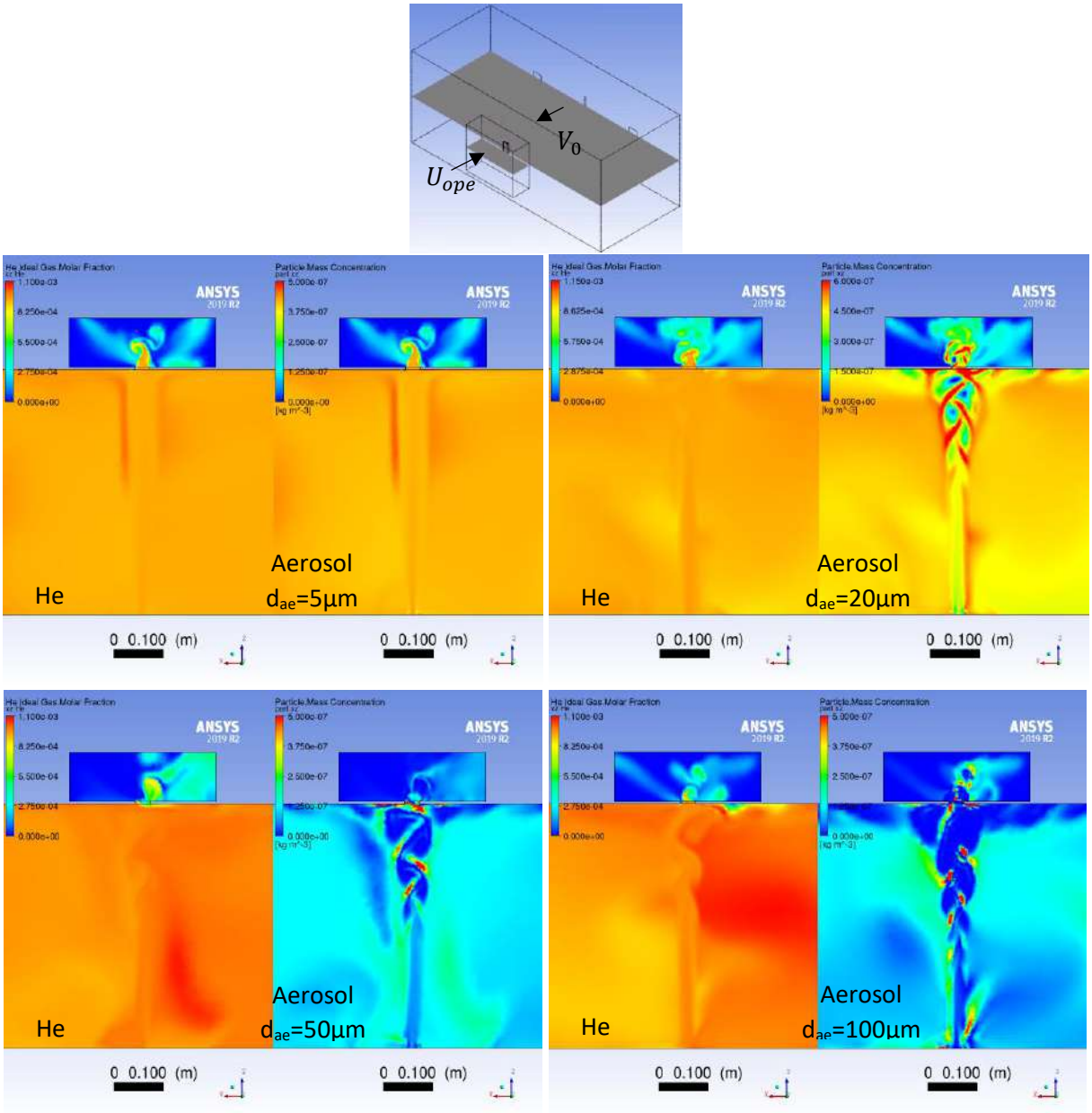

Figure 4-26 Helium molar fraction (left) and particles mass concentration (right) fields in the horizontal median plane of the opening corresponding to U_{ope} = 0.5 m/s and V_0 = 10 m/s for the case of counter-current internal disturbing jet. The aerodynamic diameter of particles is respectively 5 µm, 20 µm, 50 µm and 100 µm

Table 4-7 Stokes number related to each particle aerodynamic diameter

d_{ae} (µm)	5	20	50	100
Stk at 3 cm near the opening	0.03	0.42	2.53	13.05

As we see in Figure 4-26, the behavior of helium and aerosol of 5 microns diameter is very similar along the jet and near the opening. Unlike the helium behavior, we see that 20 µm particles diameter start to accumulate around the jet region in the form of small chains and to be progressively reduced in the core regions along the jet and near the opening. This phenomenon is enhanced for 50 µm particles, where we see regions that are totally free of particles inside the jet and near the frontal wall on one hand and regions presenting strong accumulations of particles around eddies on the other hand. Near the opening, we can easily see a vortices free of particles. For aerosol of 100 µm, we can clearly see that regions that are empty of particles are wider along the jet flow and near the frontal wall. Simultaneously, the particles accumulate at the borders; however, the particle chains start to break up. Near the opening, we also see vortices that are free of particles. The behavior between the gas and all the 20 µm, 50 µm and 100 µm particles is different in these cases.

We observe that 5 µm particles follow closely the gas behavior while 20 µm particles partially follow the gas dynamics and reveal the presence of preferential concentration regions. This phenomenon is reinforced in the case of 50 µm particles. Preferential concentrations regions start to decrease for 100 µm particles where inertial particles are almost uncorrelated with the gas behavior.

Referring to

Table 4-7 and based on chapter 1, we can interpret this behavior. Particles of 5 µm have a Stokes number of order 10^{-2}: particles are moving under the equilibrium regime and follow closely the gas behavior. Particle of 20 µm have a Stokes number between 0.1 and 1: we start to see the preferential concentrations regime. The Stokes number of 50 µm particles is of order unity: the preferential concentrations regime is clearly observed. For 100 µm particles, the Stokes number has an order of 100 : particles are in transitional regime between preferential concentrations regime and strongly inertial particle regime.

We also note that due to strong heterogeneity of 20 µm, 50 µm and 100 µm particles concentration inside the enclosure and hence in the extraction circuit, it was difficult to calculate the backflow coefficient for these cases.

4.2 Global quantification

The objective of this section devoted to global quantification is to collect the total amount of backflow that escapes from the enclosure in order to better evaluate the exposure of external environment. It consists of collecting the total quantity of gaseous tracer and particulate aerosol escaping from the enclosure for a given scenario in order to compare the experimental results with their corresponding numerical simulations. The local transfer coefficient does not provide extensive characterization of concentration values near the opening. For that, we performed numerical simulations with an additional envelope surrounding the enclosure matching the experimental setup. First, we verified the impact of the presence of this envelope on the flow near the opening while varying the air exchange rate of the envelope. Once this parameter was fixed, we analyzed the associated homogeneity of the flow within the envelope and we calculated the aerosol deposition rate inside the envelope. We compared the experimental and numerical renewal results within the envelope. After that, we carried out numerical simulations in order to visualize and quantify the backflow phenomenon. For the quantification part, we try first to control the concentration of pollutants at the extraction of the envelope in order to calculate the backflow coefficient. Then, we monitored the change in mass flow rate within the extraction of the enclosure to obtain the backflow mass flowrate. After that we proposed a comparison between the global experimental and numerical backflow coefficients.

Description of geometry and meshing

The numerical enclosure is surrounded by an envelope similarly to our experimental setup. The simulation domain contains two regions (the enclosure and the envelope) and has the following geometric characteristics as shown in Figure 4-27:

- an enclosure of dimensions (1.2 × 0.5 × 0.5) m^3 corresponding to the experimental enclosure containing the extraction units, the disturbance orifice and the opening as detailed in section 4.1.

- a surrounding envelope of dimensions (1.78 × 1.31 × 0.82) m^3. The upper wall contains a circular orifice of 60 mm diameter in order to provide air inlet to the envelope. Simultaneously, the left-side wall contains a circular orifice of 40 mm diameter where air extraction is applied to ensure the air renewal in the envelope.

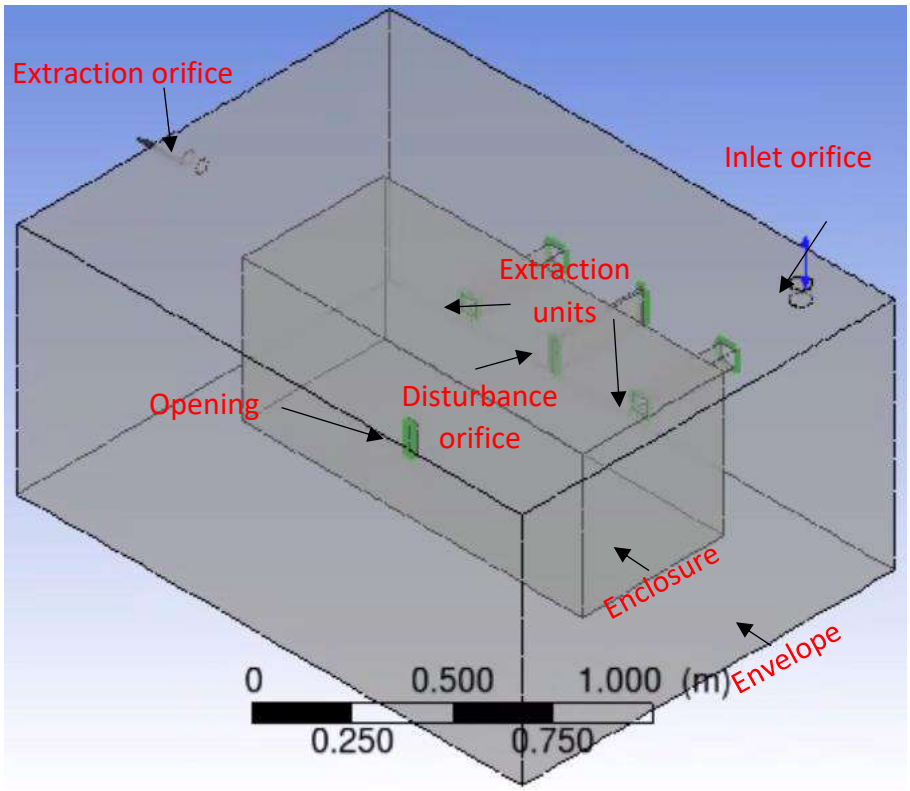

Figure 4-27 Geometry of the simulation domain

The total meshing of the simulation domain is composed of 823 613 nodes and 4 664 176 tetrahedra elements. It is refined near the opening of the enclosure, near the extraction units of the enclosure and near the orifice of the disturbing jet. Similarly, it is refined near the inlet and outlet zones of the envelope and near the opening of the enclosure. Figure 4-28 and Figure 4-29 show the mesh layout of the envelope containing the enclosure.

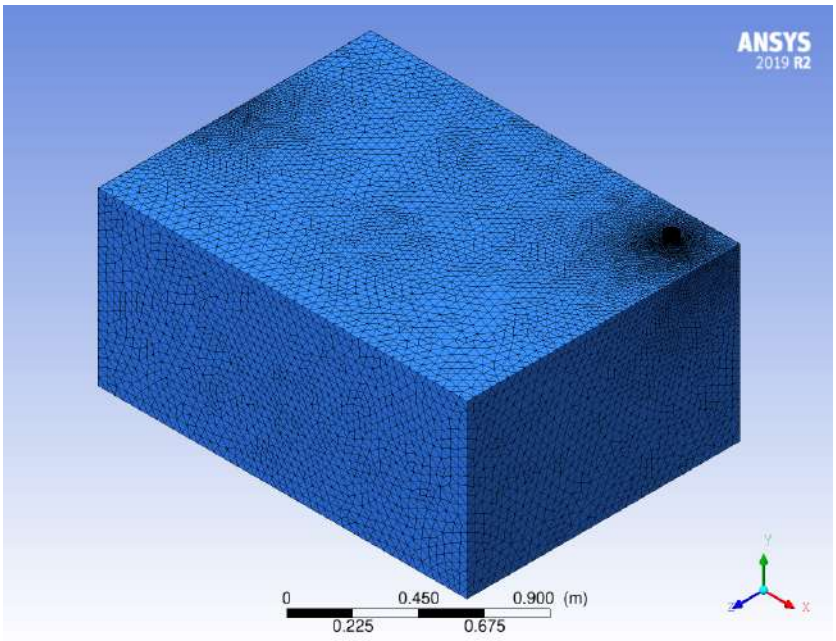

Figure 4-28 3D view of the envelope meshing

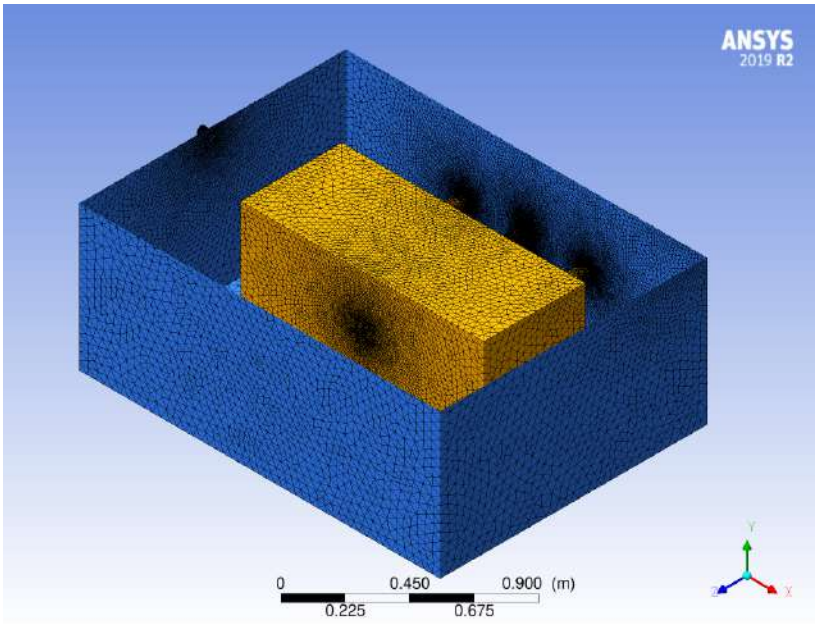

Figure 4-29 3D view of the envelope meshing containing the enclosure

4.2.1 Impact of the envelope on the flow near the opening

We performed preliminary simulations using ANSYS CFX software for the experimental enclosure surrounded by its envelope to ensure that the latter does not perturb the flows near the opening where backflow phenomenon occurs. For a ventilated enclosure with an inflow corresponding to U_{ope}=0.5 m/s near the opening , we varied the air exchange rate of the envelope from 0 to 10 h^{-1}. Using the RANS modelling with SST k-ω turbulence modelling, we analyzed the velocity profiles near the opening for each

air exchange rate. We applied an inflow velocity at the opening on the ventilated enclosure: U_{ope} = 0.5 m/s.

4.2.1.1 Boundary conditions

We remind that for our preliminary studies (before using the experimental envelope), the inlet and outlet extraction orifices were positioned on the upper wall of the envelope.

The boundary conditions fixed during the simulations are detailed in Table 4-8.

In order to obtain an inflow velocity at the opening U_{ope}=0.5 m/s, we imposed a velocity at the extraction units corresponding to $U_{extraction}$ = 0.3 m/s. We performed numerical simulations for three inlet velocities: U_{ope} = 0.5 m/s, 1 m/s and 1.5 m/s. We varied the mass flowrate at the inlet orifice q_{air} in order to vary the air renewal rate.

The tested renewal rates are the following: 0, 1, 5 and 10 h^{-1}. The mass flowrate corresponding to a renewal rate of 1 h^{-1} is q_{air} = 0.0022 kg/s.

Table 4-8: Boundary conditions for the RANS simulations

Boundary Conditions	Type and value
Extraction units of the enclosure	Outlet, $U_{extraction}$ = 0.3 m/s
Air admission orifice	Inlet, q_{air} = 0.0022 kg/s
Air extraction orifice	Opening, P = 0
Enclosure orifices and inside of envelope	Fluid-Fluid Interface Conservative interface flux
Other	Wall, no slip wall

4.2.1.2 Simulation characteristics (RANS)

For this part, we applied steady state conditions using RANS procedure. The turbulent model is SST k-ω with an advection scheme of high resolution and a time step of 1 s. The fluid injected is air at 25°C. Steady state conditions are summarized in Table 4-9. Our simulations were performed on 3 calculation nodes (60 cores total). The simulation time was about 1 hour.

Table 4-9: The simulation characteristics used for the URANS and the hybrid models

Calculation type	Steady-state
Model	SST k-ω
Fluids	Air at 25°C
Advection scheme	High resolution (first order)
Timescale control	Physical Timescale = 0.1 s
Number of iterations	2000

Figure 4-30 shows the horizontal median plane of the opening corresponding to an inflow velocity at the opening U_{ope} = 0.5 m/s and renewal rate within the envelope respectively: R = 0, 1, 5 and 10 h^{-1}.

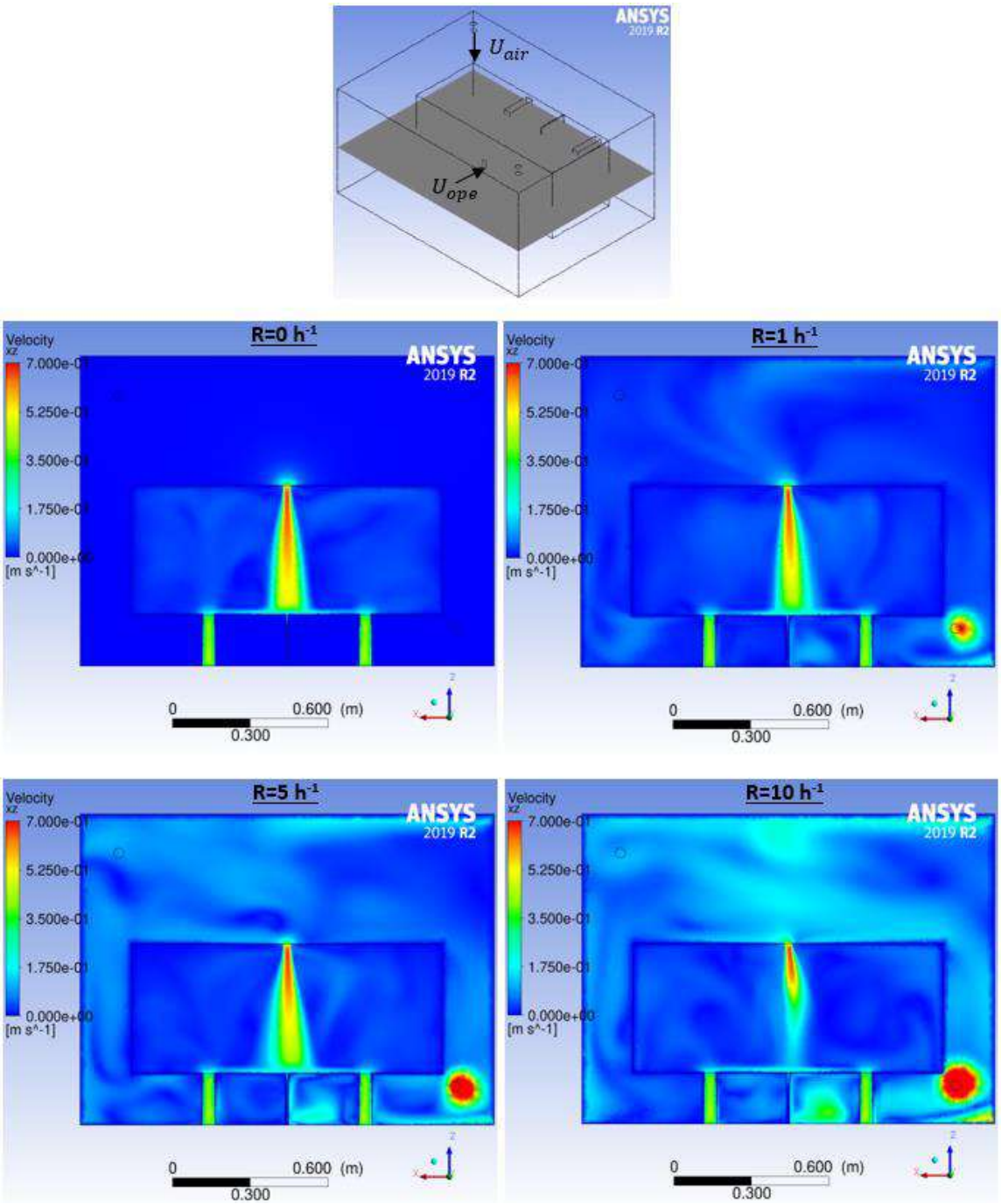

Figure 4-30 Horizontal median plane of the opening corresponding to an inflow velocity at the opening U_{ope} = 0.5 m/s and renewal rate within the envelope respectively: R = 0 h^{-1}, 1 h^{-1}, 5 h^{-1} and then 10 h^{-1}

As we see on the velocity fields presented in Figure 4-30, there are very few modifications of the jet entering the enclosure for renewal rates R = 0 h^{-1}, 1 h^{-1} and 5 h^{-1}. For these renewal rates, we may consider that the envelope does not modify the velocity profile within the enclosure. However, the velocity field corresponding to R = 10 h^{-1} shows a significant deviation of the jet inside the enclosure. For this particular case, the renewal rate within the envelope and the induced airflows do influence the velocity profile inside the enclosure.

Figure 4-32 shows the numerical horizontal and vertical velocity profiles near the opening corresponding to an inflow velocity of 0.5 m/s at the enclosure opening and for renewal rate within the envelope of following values: 0 h^{-1}, 1 h^{-1}, 5 h^{-1} and 10 h^{-1}. The locations of the vertical and horizontal velocity fields traced near the opening are shown in Figure 4-31.

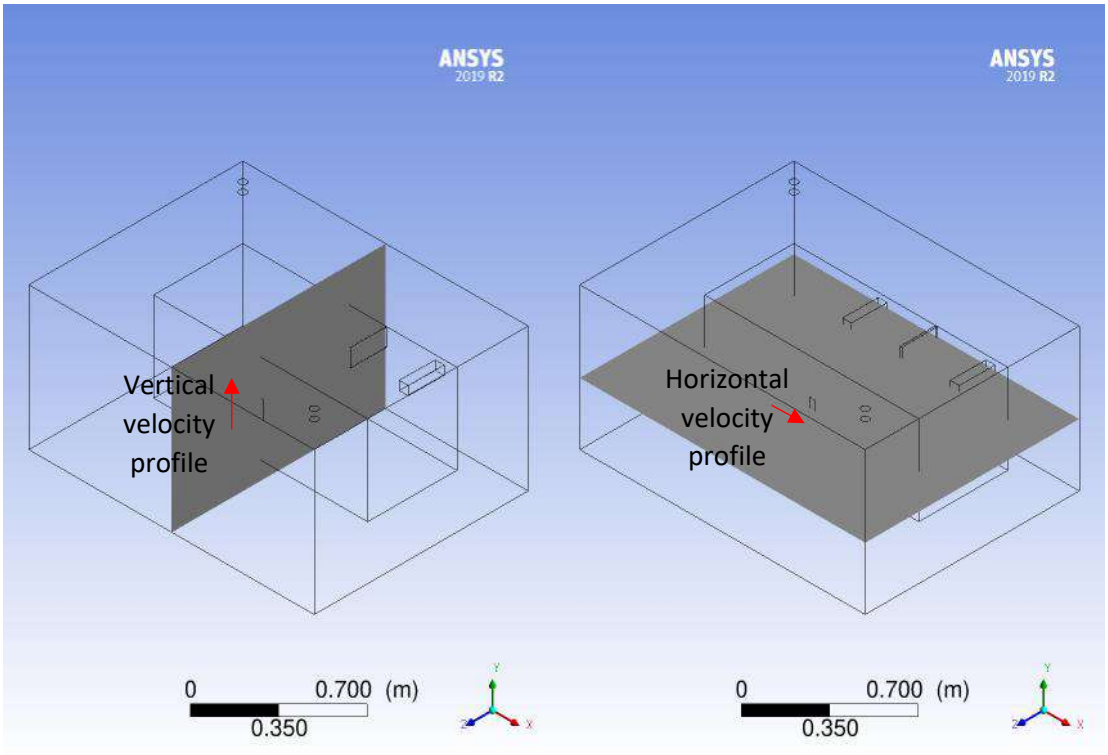

Figure 4-31 Schemes of the location of velocity profiles near the opening in the vertical (left) and horizontal (right) planes

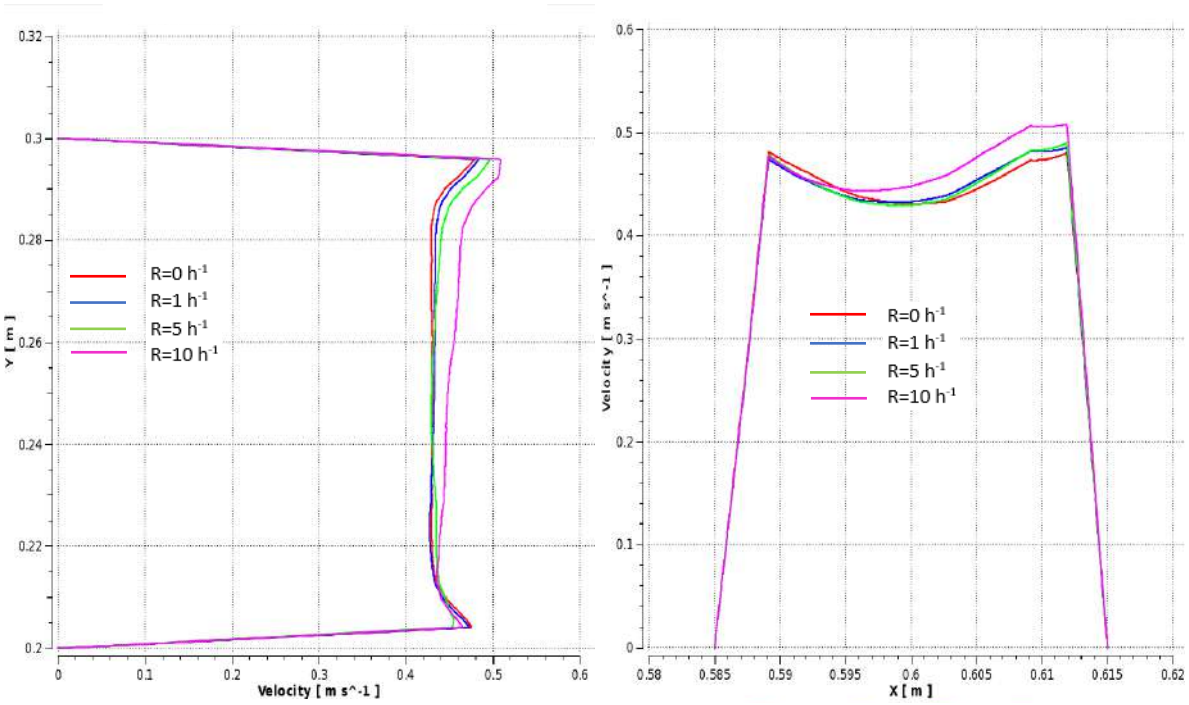

Figure 4-32 Vertical (left) and horizontal (right) velocity profiles at the opening of the enclosure for an inflow velocity of 0.5 m/s for different values of air exchange rates of the envelope

Each of the horizontal and vertical velocity profiles demonstrate the same trend for U_{ope} = 0.5 m/s: a maximum value at the opening edges and a minimum value in the middle of the opening, for all values of the envelope air exchange rate. At the same time, the horizontal velocity profiles have the same order of magnitude and are very similar when the air exchange rate of the envelope was between 0 h^{-1} and 5 h^{-1}. However, the velocity profile corresponding to an air exchange rate of 10 h^{-1} shows a significant difference. The same applies for the vertical velocity profiles. We mention that horizontal and vertical velocity profiles concerning U_{ope} = 1 m/s and U_{ope} = 1.5 m/s do not show major differences for air exchange rate between 0 and 10 h^{-1}.

In our study, the air exchange rate was fixed to ~3 h^{-1}. Then following these numerical results, the envelope should not disturb the flow around the opening.

4.2.2 Estimate of the gaseous and particulate decay evolutions within the envelope and particle deposition within the envelope

In order to verify the homogeneity of helium concentration and 5 µm particles spatial distribution inside the envelope, we investigate gaseous and particulate temporal decay curves. Once we check their homogeneity, we can say that the gaseous and particulate concentrations at the extraction of the envelope are representative of the gaseous and particulate concentrations everywhere inside the envelope. The mixture air/He/particles is injected inside the envelope similarly to our experimental setup. Once the steady state is reached, the injection is stopped and the helium and particles concentrations are monitored at the extraction of the envelope. The URANS turbulence model used is SST k-ω.

4.2.2.1 *Injection phase – equilibrium regime*

In order to match our experimental conditions, the airflows inside the enclosure were not simulated; hence, in our numerical simulations, the enclosure was considered as a solid domain with no flow and the rest of the flow in envelope was simulated as shown in Figure 4-33.

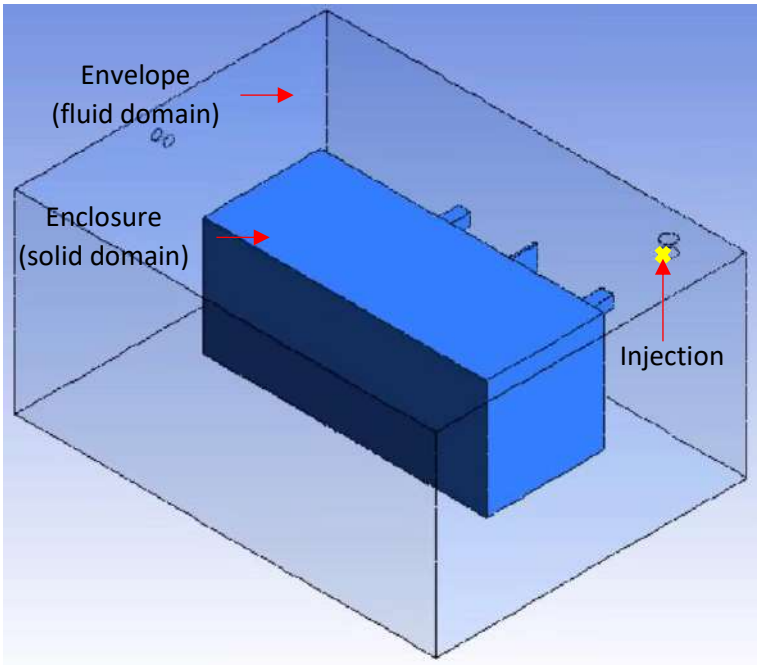

Figure 4-33 Geometry of the envelop surrounding the enclosure and simulation domain

4.2.2.1.1 Boundary conditions

The boundary conditions fixed during numerical simulations are summarized in Table 4-10.

Table 4-10 Boundary conditions for the RANS model

Boundary Conditions	Type and value
Extraction orifice of envelope	Outlet condition, $U_{extraction-envelope}$ = 1 m/s (corresponding to a renewal rate of 3 h^{-1})
Inlet orifice of envelope	Opening, *P* = 0
Helium and aerosol injection	Source point, $q_{He,injection}$= 0.83 g/h, $q_{aerosol,injection}$ = 3.10^{-3} g/h
Walls	No slip condition + aerosol deposition flux

4.2.2.1.2 Simulation characteristics (RANS)

For this part, we applied steady state conditions using RANS modelling. The turbulent model is SST k-ω with a high resolution advection scheme and a physical timescale of 1 s. The fluids injected are air at 25°C, helium at STP and 5 µm particles as shown in section 4.1.1.2. Steady state conditions are summarized in Table 4-11.

Table 4-11 The simulation characteristics used for the RANS simulations

Numerical Parameter	Value
Turbulence Model	SST k-ω
Advection scheme	High resolution (first order)
Fluid time step	1 s
Number of iterations	10000

Figure 4-34 shows the molar fraction of helium and the particles mass concentration in the vertical planes passing respectively through the envelope inlet, the injection and the envelope outlet at steady state, when the injection (pointwise source) was located near the inlet of the envelope.

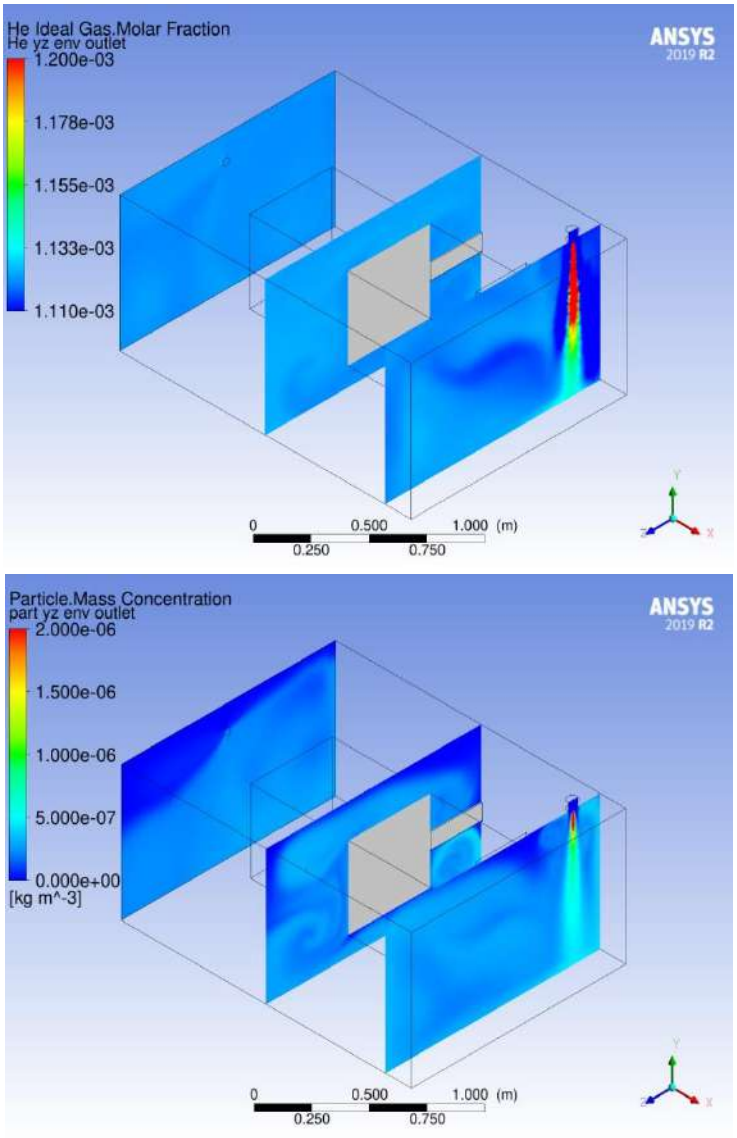

Figure 4-34 Molar fraction of helium (up) and particles mass concentration (bottom) in the vertical planes passing respectively through the envelope inlet, the injection and the envelope outlet at equilibrium when particles injection is located at the inlet of the envelope

As we see in Figure 4-34, helium and particles are homogeneously distributed inside the envelope. Some vortices are present around the enclosure due to its presence inside the envelope. These visualizations highlight that helium and 5 µm particles seem to be homogeneously distributed inside the envelope. There is no preferential accumulation of helium or aerosol inside the envelope.

In the following, we aimed to calculate the deposition rate of particles inside the envelope, in order to take it into account in further calculation of the global backflow coefficients.

Figure 4-35 shows the particle deposition presented inside the envelope. We mention that we injected helium and aerosol near the opening in order to be consistent with the backflow experimental setup.

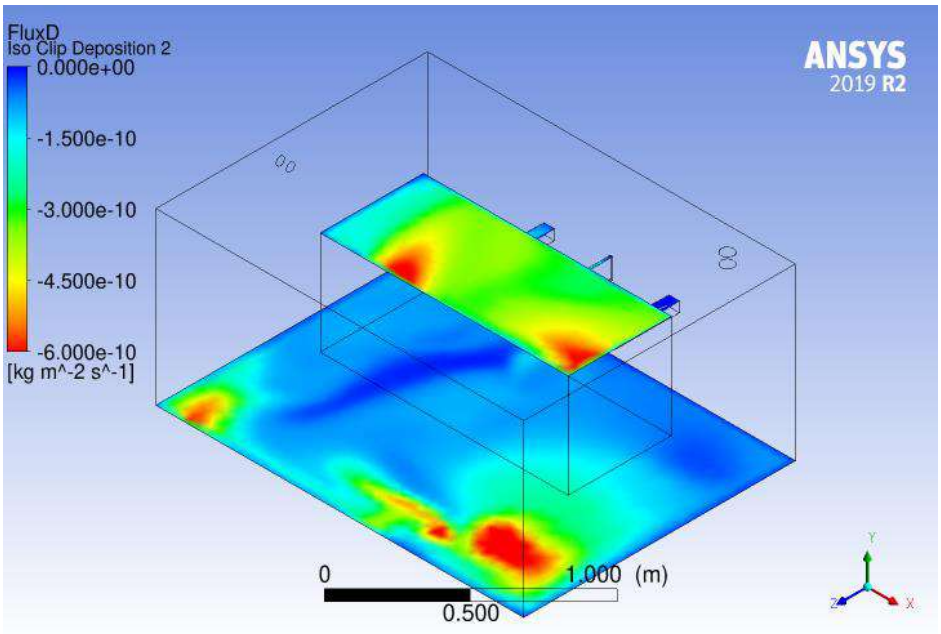

Figure 4-35 Particles deposition on the upper wall of the enclosure and at the floor of the envelope

Results from numerical simulations show that the particles deposition occurs essentially on the roof of the enclosure and on the floor of the envelope facing the enclosure as shown in Figure 4-35.

In order to calculate the mass deposition inside the envelope, we followed the mass flowrate of particles at the extraction outlet of the envelope. Once equilibrium is achieved, the mean value corresponds to q_{eq} (kg/s). Knowing the particles mass flowrate at injection $q_{aerosol,injection}$ and based on Eq. 4.2, we calculate the mass deposition rate D.

$$D\ (\%) = \left(1 - \frac{q_{eq}\ (\mathrm{mg/h})}{q_{aerosol,injection}\ (\mathrm{mg/h})}\right) \times 100 \qquad \text{(Eq. 4.2)}$$

Table 4-12 shows the experimental and numerical deposition rates of particles inside the envelope.

Table 4-12 Experimental and numerical deposition rates inside the envelope

	Experimental results	Numerical simulations
Deposition rate (%)	85.14 %	72.38%

The experimental deposition rate (85.14 %) is a little bit higher than the deposition rate (72.38 %) from simulations. This could be due to experimental uncertainties that are about 20%. However, the discrepancy between experimental and numerical results is rather moderate.

Once we showed that there is deposition of particles inside the envelope, this deposition rate should be further considered in the global backflow coefficients analysis. For this, we plotted the particulate decay curve in order to calculate the particulate exchange rate within the envelope and correct the global backflow coefficients as shown in chapter 3 (section 3.2.3.3).

4.2.2.2 Decay phase - transient regime

Once the steady state is reached (at the end of injection phase), we stopped the injection of helium and aerosol to monitor their respective decay rates. For that, we removed the injection point for the decay phase. We performed URANS simulations in order to monitor the helium and particles concentration at the extraction of the envelope.

4.2.2.2.1 Boundary conditions

The boundary conditions are similar to the injection region, except for the source point that we removed. They are summarized in Table 4-13.

Table 4-13 Boundary conditions of the decay phase

Boundary Conditions	Type and value
Extraction orifice of envelope	Outlet, $U_{extraction-envelope}$ = 1 m/s
Inlet orifice of envelope	Opening, P = 0 Pa
Walls	No slip conditions + aerosol deposition flux

4.2.2.2.2 Simulation characteristics of the unsteady regime

The turbulence model for the transient regime is SST k-ω. The fluids within the envelope are: air at 25 °C, He at STP and 5 m particles (as shown in section 4.1.1.2.). A high resolution advection scheme and a 'second order backward Euler' transient scheme are applied for the simulations. The time step is 1 s and the simulation time is 2 h. The simulation characteristics are summarized in Table 4-14.

Table 4-14 The simulation characteristics used for the URANS modelling

Numerical Parameter	Value
Turbulence Model	SST k-ω
Advection scheme	High resolution (first order)
Fluids in envelope domain	Air at 25 °C (constraint)
	He at STP (transport equation)
	Particles (algebraic equation)
Fluid time step	1 s
Fluid time step	2 h

We monitored helium and particles concentrations at the envelope extraction in order to characterize their corresponding decay rates and compare them with our experimental results. Figure 4-36 shows the helium and aerosol concentration at the extraction of the envelope in the injection and decay phases.

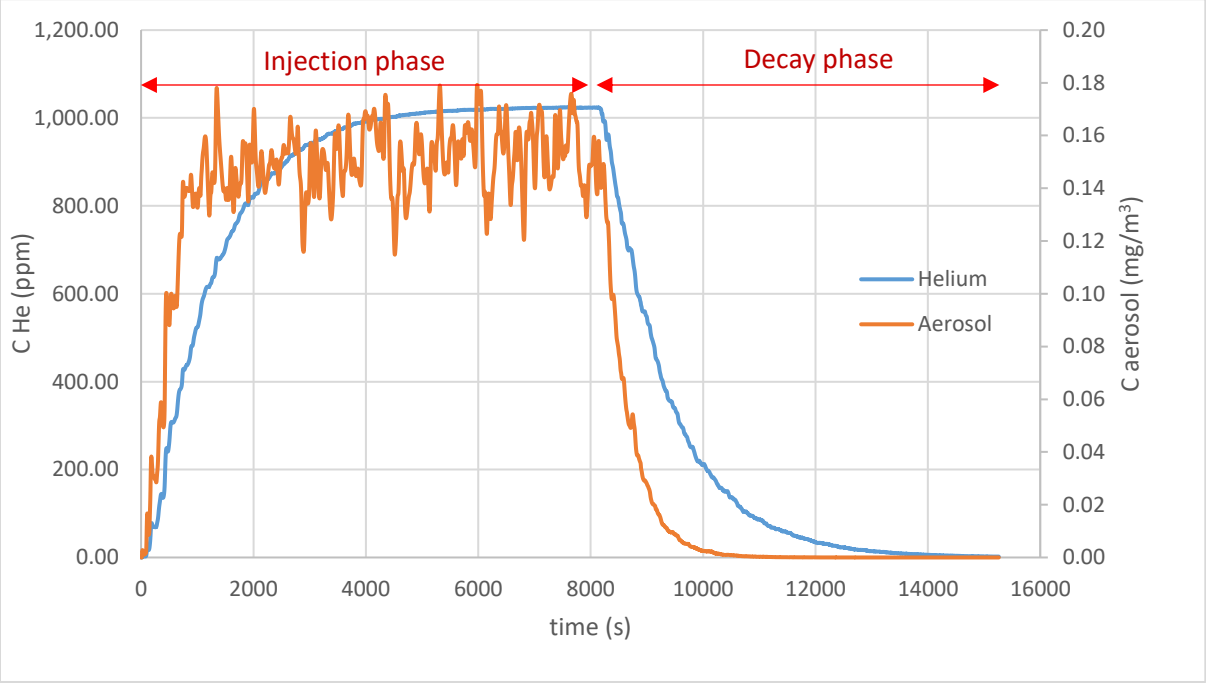

Figure 4-36 Concentration of helium and aerosol at the extraction outlet of envelope during the injection phase (0 < t < 8000 s) and the decay phase (t > 8000 s)

As we see in Figure 4-36, He concentration C_{He} increases when we inject helium inside the envelope till it reaches an equilibrium C_{eq_He} of about 1000 ppm at t ~ 5000 s. Likewise the aerosol concentration $C_{aerosol}$ increases until it reaches an equilibrium $C_{eq\_aerosol}$ at t ~ 1000 s. The aerosol distribution reaches equilibrium faster than helium. Once we stopped the injection at t = 8000 s, helium and aerosol concentrations start to decrease down to 0 at t ~ 10500 s for helium and at t ~ 14000 s for aerosol. The aerosol concentration reaches 0 faster than the helium.

We investigated the evolution of C_{He}/C_{eq_He} and $C_{aerosol}/C_{eq\_aerosol}$ in function of time (s) in the decay phase once we stopped the injection inside the envelope. The temporal evolution of C/C_{eq} related to helium and particles from our experiments and our numerical simulations are shown in Figure 4-37. The helium and aerosol exchange rates within the envelope could be deduced from the slope of each decay curve and are presented in Table 4-15.

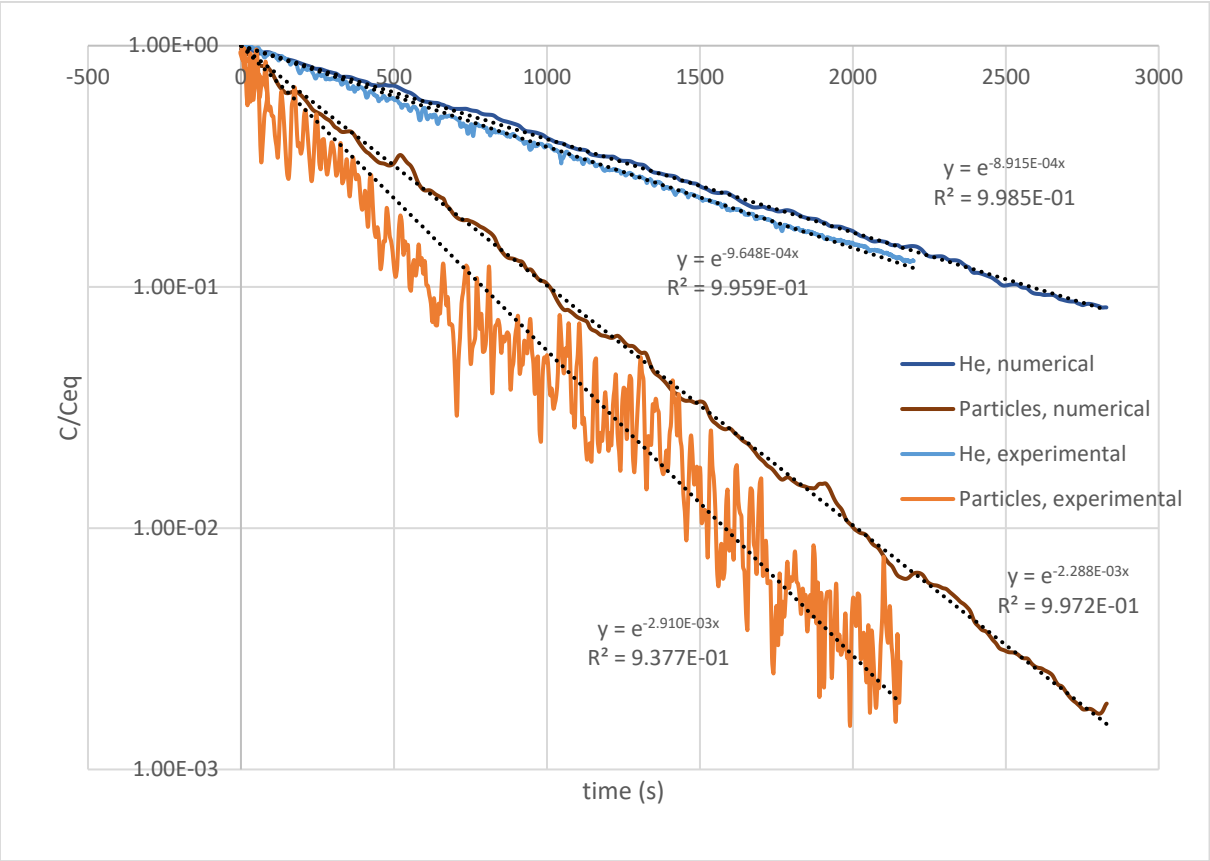

Figure 4-37 Time evolution of C/C_{eq} corresponding to the helium and the 5 µm particles from experiments and numerical simulations for an exchange rate of the envelope about 3 h^{-1}

Table 4-15 Experimental and numerical values of helium and aerosol exchange rates

	Experimentally	Numerically
Helium exchange rate	3.50 h^{-1}	3.21 h^{-1}
Aerosol exchange rate	10.60 h^{-1}	8.24 h^{-1}

As we see in Figure 4-37, all the curves have a single slope which means that the gaseous and particulate mixture is homogenous inside the envelope (see section 3.2.3. in chapter 3). The evolutions related to the particles decay are below the gas curves related to the gaseous decay experimentally and numerically, hence the decay of the particles within the extraction of the envelope is faster than that of the gas due to the deposition of particles inside the envelope. On the other way, the experimental and numerical evolutions of C/C_{eq} related to helium are very close. The numerical and experimental helium exchange rates have the same order of magnitude in Table 4-15. The numerical helium exchange rate is closer to the theoretical air exchange rate within the envelope with 3 h^{-1}. For experiments, uncertainties are present related to the measurements of the extraction flowrate of the envelope and mass spectrometer uncertainties. For the particulate pollutant, the numerical evolution is slightly above the experimental result in Figure 4-40. These results were expected since the numerical deposition rate is lower than the

experimental deposition rate of particles. The experimental aerosol exchange rate is a little bit higher than the numerical aerosol exchange rate in Table 4-15.

Here, we confirm that helium and aerosol of 5 µm are homogeneously distributed inside the envelope. Then their corresponding concentrations measured at the extraction of the envelope are representative of concentrations inside the envelope. Additionally, and since we found that there is an important deposition rate of particles inside the envelope, it should be taken into account in the calculation of the global backflow coefficient as shown in chapter 3 (section 3.2.3.3).

4.2.3 Global quantification of the backflow

In this part we aim to detect and evaluate the backflow coming from the opening and corresponding to pollutant spreading throughout the envelope. The procedure is similar to that showed in part 4.1.1.2, where we injected helium and aerosol inside the enclosure. However, here we are interested in detecting the backflow in the extraction circuit of the envelope in order to collect the total flowrate of pollutants that escape through the opening of the enclosure.

4.2.3.1 Boundary conditions

Two fluid domains are presented here: one corresponding to the enclosure and the other to the envelope. The boundary conditions related to the enclosure are similar to those detailed in part 4.1.1.2.1. The total boundary conditions are shown in Table 4-16.

Table 4-16: Boundary conditions for the DES model

Boundary conditions	Type and value
Disturbance injection inside the enclosure	Inlet, q_{inlet} (corresponding to the mass flowrate extracted at the disturbance sink point (V_0 = 6 m/s))
Enclosure extraction units	Outlet, $U_{extraction}$ = 0.3 m/s corresponding to an inflow velocity U_{ope} = 0.5 m.s^{-1}
Helium and aerosol injection inside the enclosure	Source point, $q_{He,injection}$ = 0.82 g/h, $q_{aerosol,injection}$ = 3.10^{-3} g/h
Disturbance source inside the enclosure	Sink point, -q_{inlet}, at the right side of the enclosure corresponding to the aspiration of a volumetric flow rate Q_{inlet} of the mixture (air/ helium/ 5 µm particles).
Extraction orifice of envelope	Outlet, $U_{extraction-envelope}$ = 1 m/s that corresponds to an air exchange rate of about 3 h^{-1}
Inlet orifice of envelope	Opening, P = 0
Enclosure orifices and inside of envelope	Conservative interface flux
Other (envelope walls and interface between the enclosure walls and the inside of envelope)	Wall, no slip wall + aerosol deposit flux

4.2.3.2 *Simulation characteristics of the unsteady regime*

The turbulence model is SST-DES. The fluid injected consists in a mixture of: air at STP, He at STP and 5 µm particles. An advection scheme of type 'high resolution' and a 'second order backward Euler' transient scheme are applied. The time step is 0.001 s and the simulation time is 1000 s. Simulation characteristics are summarized in Table 4-17. Our simulations were carried out on 5 calculation nodes (total 100 cores). The simulation time was between 2 and 3 months, due to the time needed to achieve the complete renewal of the envelope(~ 1.7 h).

Table 4-17 The simulation characteristics used for the DES modelling

Model	DES-SST
Fluids (in enclosure and envelope)	Air at STP (constraint)
	He at STP (transport equation)
	Particles (algebraic equation)
Advection scheme	High resolution
Transient scheme	Second order backward Euler
Time step	0.001 s
Simulation time	1000 s

4.2.3.3 *Initial conditions related to steady state*

As showed in part 4.1, the initial flow conditions correspond to steady state RANS simulations where helium is injected and aerosol of 5 µm inside the enclosure (inflow velocity is U_{ope} = 0.5 m/s enters the opening without the generation of the disturbing jet). An extraction flow is applied on the outlet of the envelope in order to obtain an air exchange rate within the envelope of 3 h^{-1}. Boundary conditions are presented in Table 4-18. The fluids injected are air, helium and 5 µm particles at 25°C. The turbulent model used is SST k-ω with high resolution and a time step of 0.1 s. Steady state conditions are summarized in Table 4-19.

Table 4-18 Initial conditions for the RANS simulation

Boundary Conditions	Type and value
Boundary conditions	Type and value
Disturbance injection inside the enclosure	Wall, no slip-wall
Enclosure extraction	Outlet, $U_{extraction}$ = 0,3 m/s
Helium and aerosol injection inside the enclosure	Source point, $q_{He,injection}$, $q_{aerosol,injection}$
Extraction orifice of envelope	Outlet, $U_{extraction-envelope}$ = 1 m/s
Inlet orifice of envelope	Opening, P_{rel} = 0 Pa, Φ_{He} = 0, $\Phi_{aerosol}$ = 0
Enclosure orifices and inside of envelope	Conservative interface flux
Other (envelope walls and interface between the enclosure walls and the inside of envelope)	Wall, no slip-wall

Table 4-19 The simulation characteristics used for the RANS

	RANS
Model	SST k-ω
Fluids	Air at 25°C, He at STP, Particles of 5 µm
Advection scheme	High resolution
Time step	0.1 s
Maximum number of iterations	8000

The helium molar fraction and particles mass concentration fields in the horizontal median plane of the opening are shown in Figure 4-38. We monitor the helium and aerosol concentrations at the extraction units of the enclosure in order to deduce their corresponding concentrations at equilibrium C_{He_in} and $C_{aerosol\_in}$. The RANS solution is further used as an initial condition for the DES simulations.

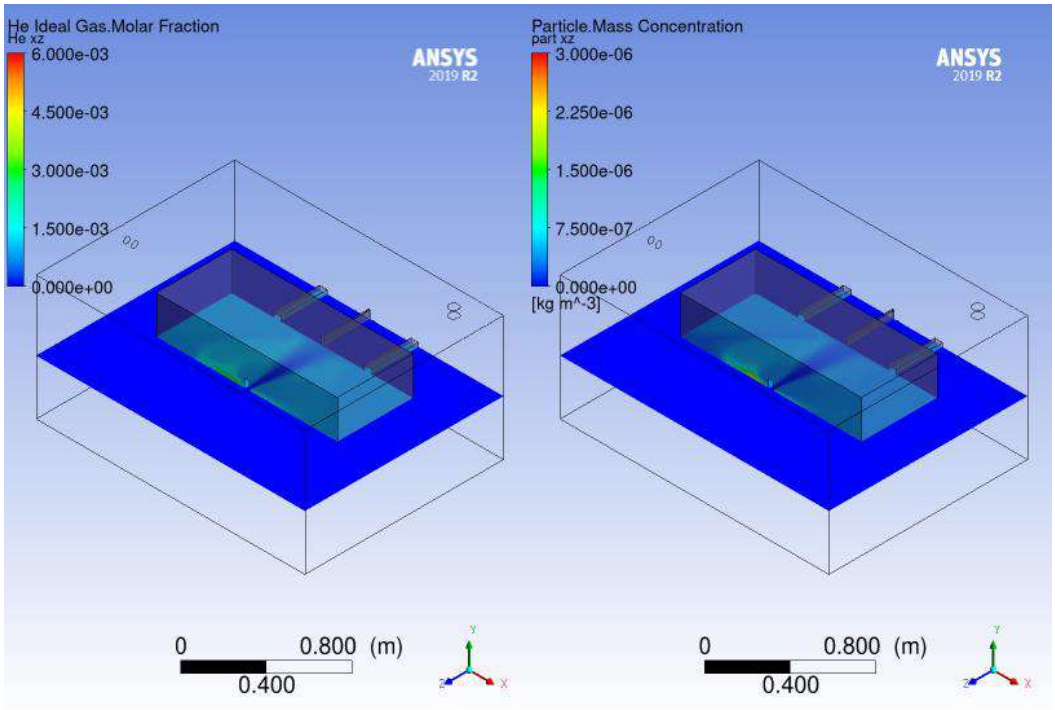

Figure 4-38 Helium molar fraction (left) and particle mass concentration (right) fields in the horizontal median plane of the opening for the RANS initial conditions

4.2.3.4 Visualization of backflow in the envelope

4.2.3.4.1 Results for helium

Figure 4-39 and Figure 4-40 show the helium molar fraction fields in the horizontal and vertical planes respectively for different times.

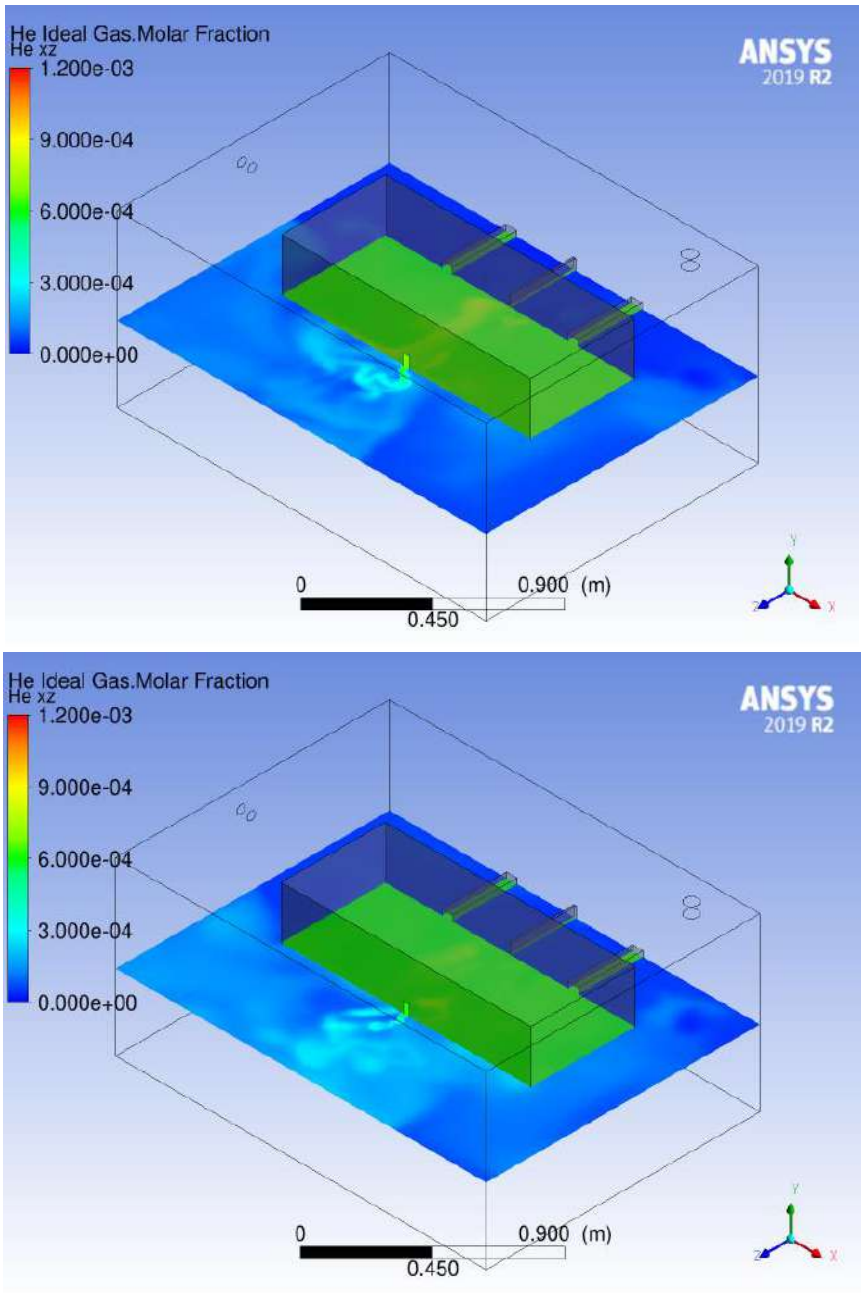

Figure 4-39 Helium molar fraction fields in the horizontal plane passing respectively through the enclosure opening for t = 208 s (top) and t = 306 s (bottom) respectively

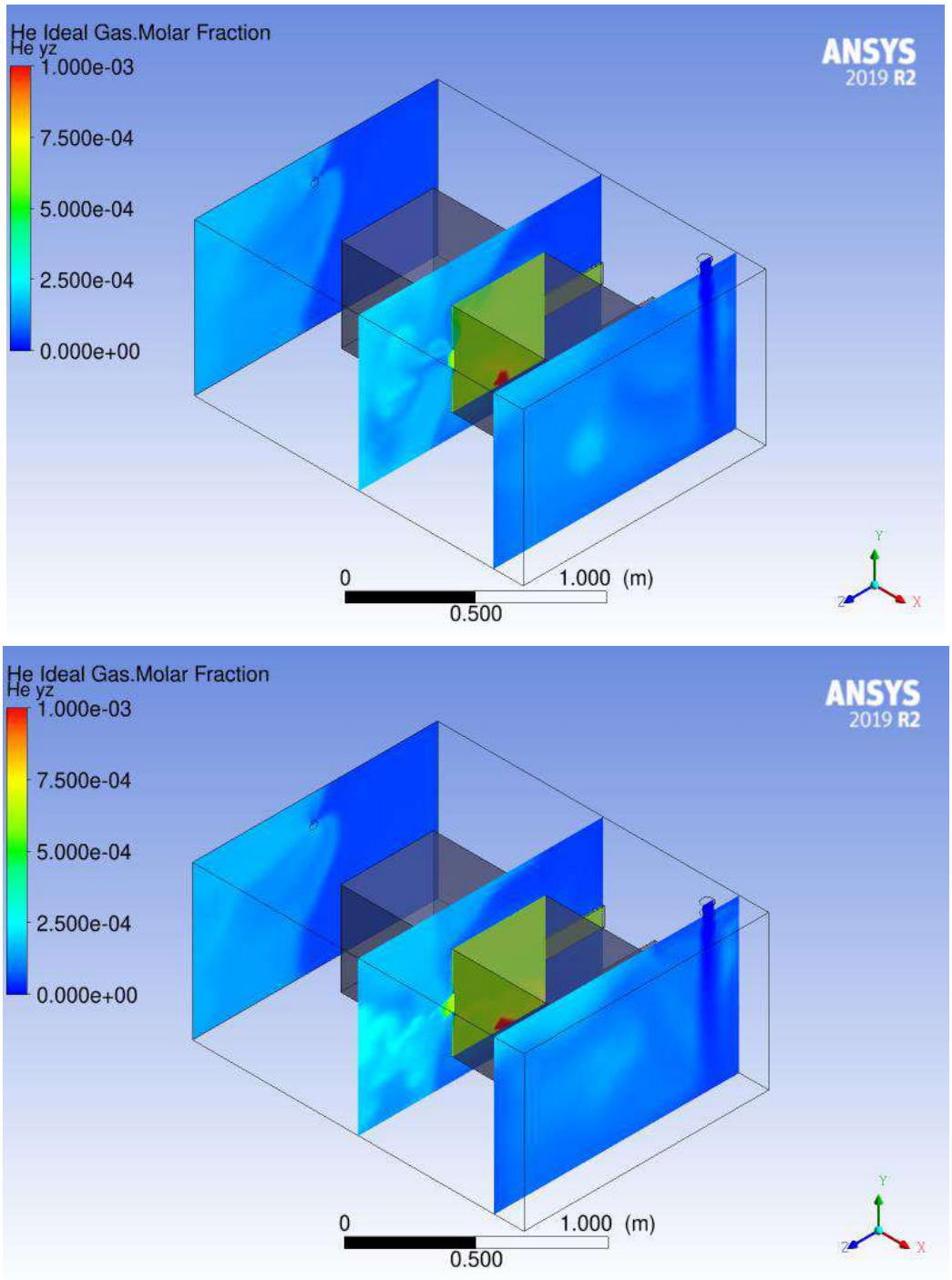

Figure 4-40 Helium molar fraction fields in the vertical planes passing respectively through the envelope inlet, the enclosure opening and the envelope outlet for t = 290 s (top) and t = 299 s (bottom)respectively

As we see in Figure 4-39 and Figure 4-40, the helium backflows through the opening of the enclosure, penetrates the envelope and is homogenized. Finally, it reaches the extraction unit of the envelope.

4.2.3.4.2 Visualization results of helium and 5 µm aerosols

Figure 4-41 and Figure 4-42 show helium molar fraction and particles mass concentration fields in the horizontal and vertical planes respectively for different times.

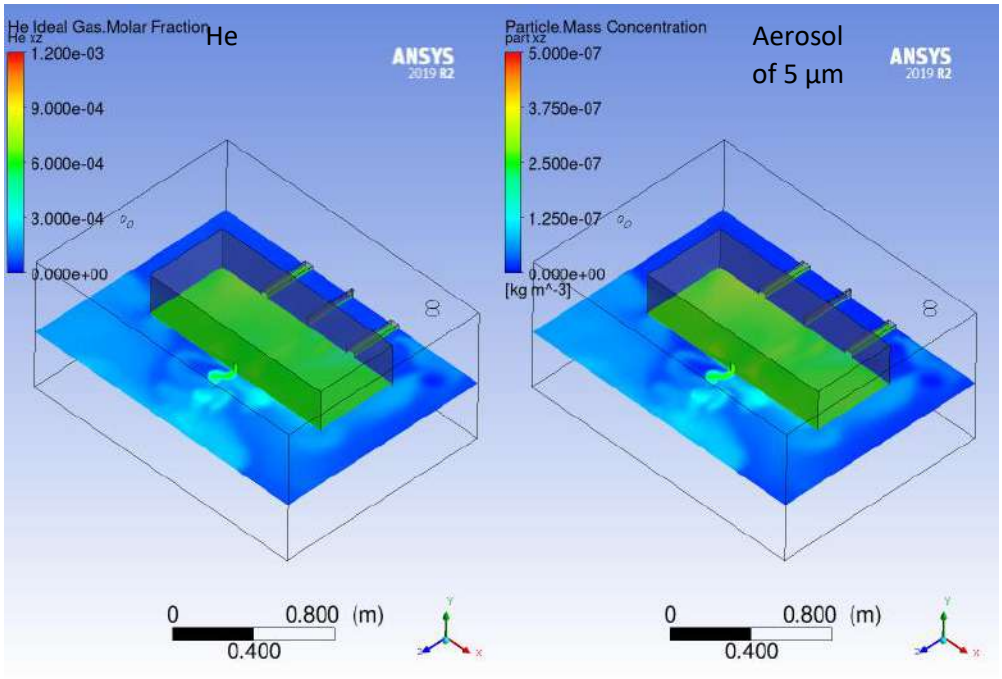

Figure 4-41 Helium molar fraction (left) and particles mass concentration (right), respectively, fields in the horizontal plane passing through the enclosure opening for t = 318 s

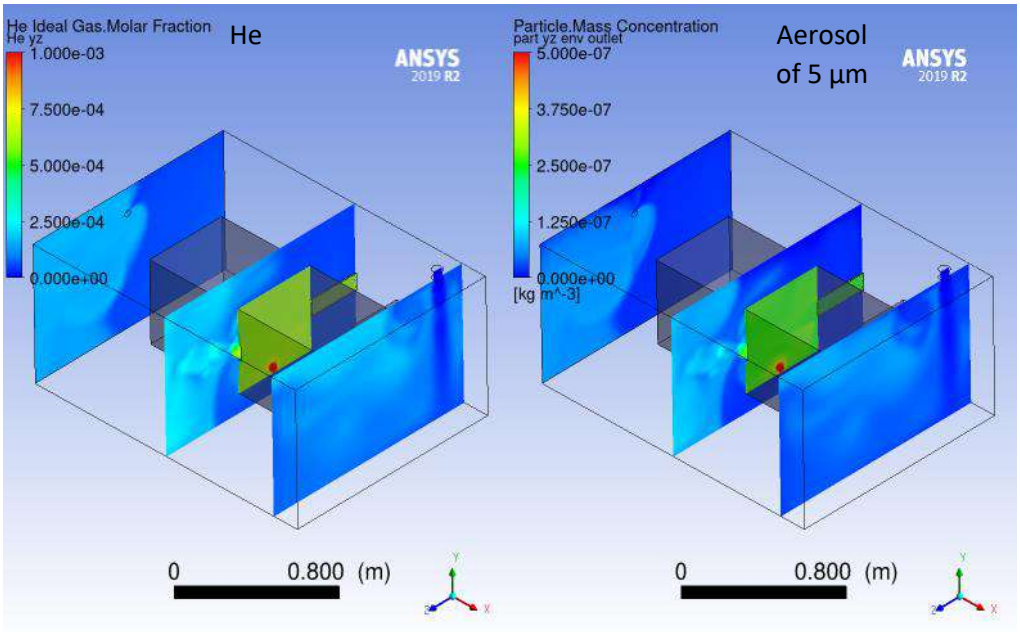

Figure 4-42 Helium molar fraction (left) and particles mass concentration (right) fields, respectively, in the vertical planes passing through the envelope inlet, the enclosure opening and the envelope outlet for t = 314 s

As we see in Figure 4-41 and Figure 4-42, 5 µm aerosol seems to have similar behavior as helium inside the envelope near the opening. This result is expected since we had already observed similar helium and aerosol behaviors locally near the opening. We expected such behavior also inside the envelope except that because of larger dimensions of the domain and lower airflow velocities the deposition of particles inside the envelope is more pronounced.

4.2.3.5 Quantitative results for the backflow phenomenon

We aim to calculate the backflow coefficient K_{env} with the envelope based on the concentration at the extraction of the envelope $C_{out\_envelope}$ over the concentration at the extraction of the enclosure $C_{in\_enclosure}$ (see Eq. 4.5). Based on the experimental procedure, we followed the concentration at the extraction of the envelope. In order to reach the equilibrium concentration at the envelope, we have to wait about 1.7 hour (since the air exchange rate within the envelope is 3 h^{-1}). However, a simulation time of 6000 s requires more than 3 months of real time simulation, which is not feasible.

Figure 4-43 shows the concentration at the extraction of the envelope for U_{ope} = 0.5 m/s and V_0 = 14m/s over a simulation time of 320 s.

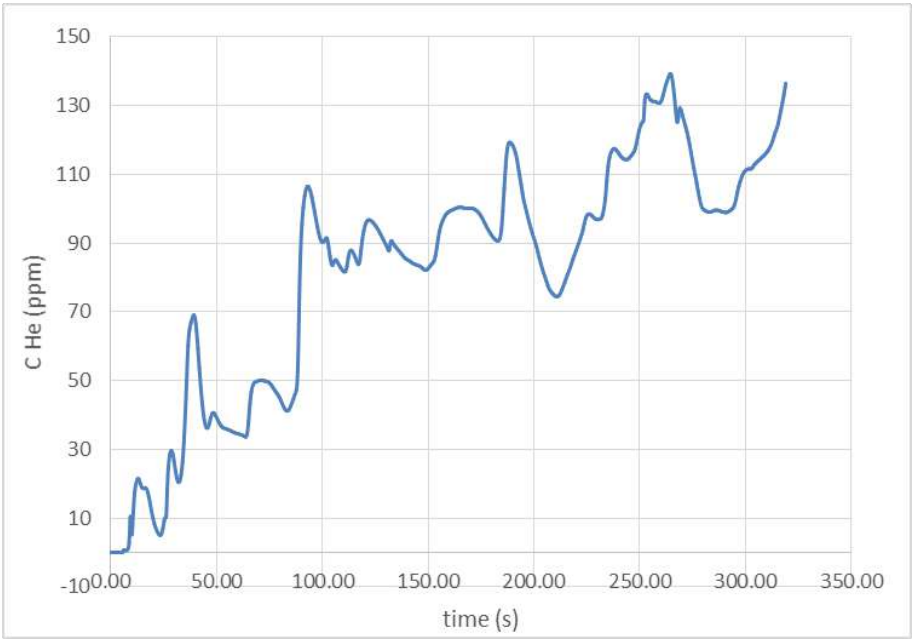

Figure 4-43 Helium concentration in the envelope outlet for U_{ope} = 0.5 m/s and V_0 = 14 m/s

As we see in Figure 4-43, the concentration at the extraction of the envelope did not reach the equilibrium yet. This numerical simulation required was about 2 months of real time simulation.

4.2.3.5.1 Determination of the global and mass backflow coefficients

In order to reduce the simulation time and to get access to the passive tracer concentration at the extraction circuit of the envelope, we chose to follow the procedure detailed below.

We monitored the helium and aerosol mass flowrates at the extraction of the enclosure during initial conditions and then during the period during which disturbance is enabled. Figure 4-44 shows helium mass flowrate in the extraction units of the enclosure at initial conditions and during the generation of the

disturbing jet. At initial conditions representing the injection of pollutants inside the enclosure, helium mass flowrate increases until it reaches an equilibrium value $q_{1,eq}$. During transient simulations and when we switch on the disturbing jet, helium mass flowrate decreases until it reaches a new equilibrium value $q_{2,eq}$ due to the loss of helium (and aerosol) outside the enclosure and within the envelope. The difference between the initial value and the new equilibrium value corresponds to the mass flowrate of pollutants outside the enclosure due to backflow: $q_{out\_backflow}$ (Eq. 4.3).

$$q_{out\_backflow} = q_{1,eq} - q_{2,eq} \quad \text{(Eq. 4.3)}$$

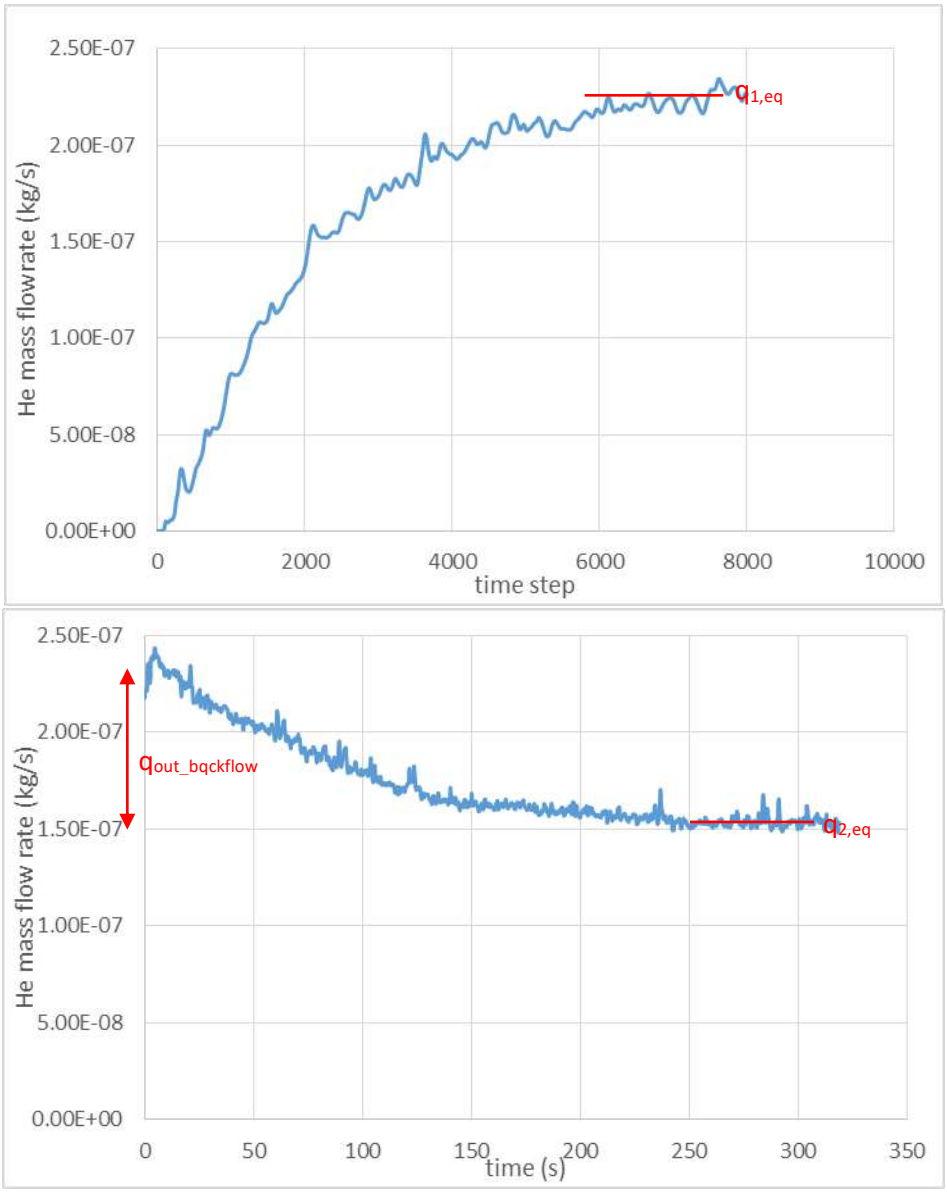

Figure 4-44 Helium mass flowrate in the extraction units of the enclosure at initial conditions (top) and during the generation of the disturbing jet (bottom)

Then the concentration at the extraction of the envelope at equilibrium due to the dispersion of pollutants within the envelope can be deduced from equation Eq. 4.4:

$C_{out\_envelope} = \frac{q_{out\_backflow}}{Q_{envelope}}$ (Eq. 4.4)

And then, the global backflow coefficient K_{env} (%) can be deduced by the ratio between $C_{out,envelope}$ and $C_{in,enclosure}$ (Eq. 4.5).

K_{env} (%) $= \frac{C_{out\_envelope}}{C_{in\_enclosure}} \times 100$ (Eq. 4.5)

The global backflow coefficients K_{env} are shown in Figure 4-45.

This way of backflow quantification reduces significantly the simulation time because we do not need to simulate the envelope anymore. Indeed, we just need to perform numerical simulations with just the enclosure for a simulation time of about 300 s (the new equilibrium regime starts to appear for a simulation time of about 250 s). This simulation procedure may require about 7 days for 6 CPU nodes (120 cores total).

The backflow coefficient K_{env} (%) in the extraction of the envelope gives indication of the concentration in the envelope under the influence of a disturbing jet. Nevertheless, this concentration depends essentially on the extraction flowrate of the envelope $Q_{envelope}$. As described in chapter 3, in order to prevent the results to depend on $Q_{envelope}$, we defined a mass backflow coefficient $K_{m,injection}$ (%) that represents the ratio of the mass flowrate of the backflow $q_{out\_backflow}$ that escapes from the enclosure over the initial mass flowrate injected inside the enclosure $q_{in\_enclosure}$ (Eq. 4.6). Results are shown below in Figure 4-46 and Figure 4-47.

$K_{m,injection}$ (%) $= \frac{q_{out\_backflow}}{q_{in\_enclosure}} \times 100$ (Eq. 4.6)

Additionally, as shown in chapter 3, we can deduce the mean velocity of the backflow ($V_{backflow}$) over the opening surface (S) using Eq. 4.7. $C_{opening}$ is the mean concentration measured near the opening and $q_{out\_backflow}$ is the mass flowrate of the backflow. Results are shown in Figure 4-48.

$q_{out\_backflow} = C_{opening} \; V_{backflow} \; S$ (Eq. 4.7)

4.2.3.5.2 Comparison of experimental and numerical backflow coefficients

Figure 4-45 shows the experimental and numerical global backflow coefficients K_{env} (%) for helium and aerosols of 5 µm in function of V_{dist}/U_{ope} for the case of counter-current disturbing jet. We mention that in the numerical analysis for V_{dist}/U_{ope} = 1.36 and 2.13, we only injected helium in the enclosure and then we have only access to the gaseous backflow coefficients for these two values.

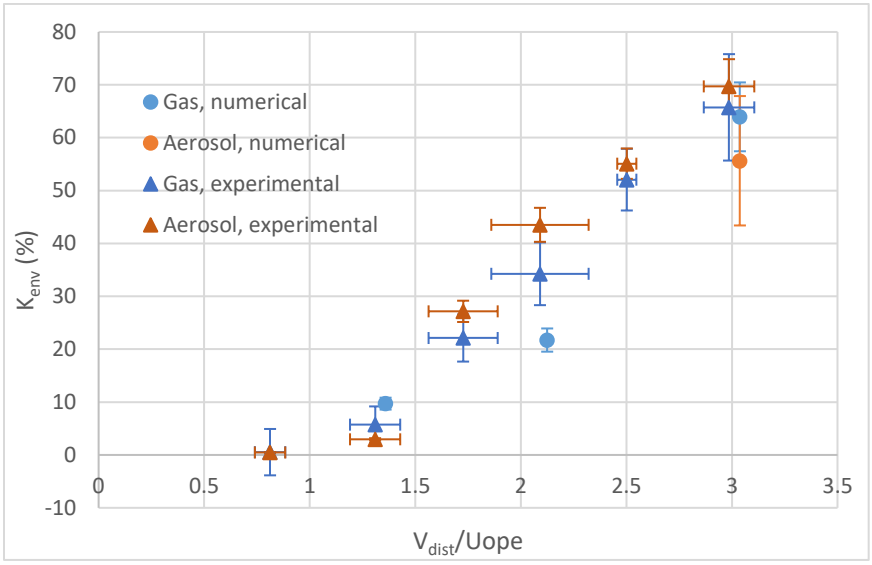

Figure 4-45 Experimental and numerical global backflow coefficients for helium and 5 µm aerosol in function of V_{dist}/U_{ope}

As we observe in Figure 4-45, experiments and simulations provide similar evolution of the backflow coefficients K_{env} (%) for both gaseous and particulate pollutants. We mention that the backflow coefficient of the second numerical point corresponding to V_{dist}/U_{ope} = 2.1 is rather underestimated since the equilibrium was not really established inside the enclosure.

Figure 4-46 and Figure 4-47 show the evolution of experimental and numerical mass backflow coefficients for the gas and 5 µm aerosol, respectively, in function of V_{dist}/U_{ope} for U_{ope} = 0.5 m/s.

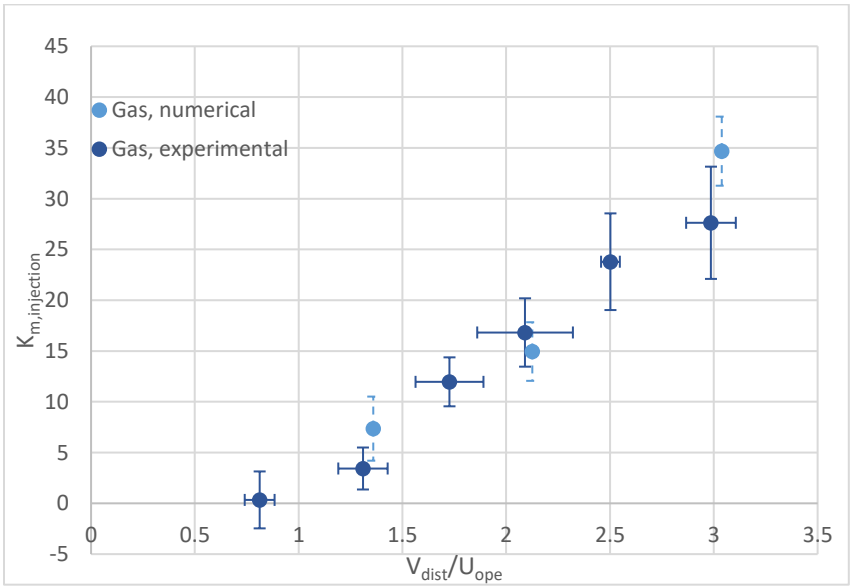

Figure 4-46 Evolution of experimental and numerical gaseous mass backflow coefficients in function of V_{dist}/U_{ope} for U_{ope} = 0.5 m/s

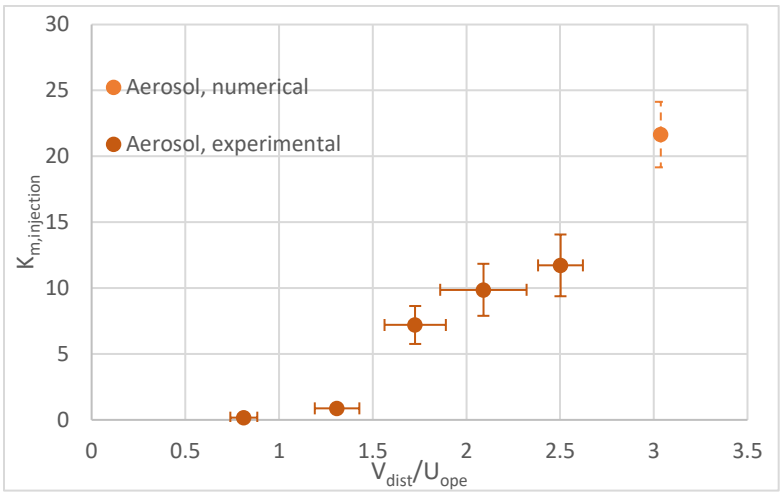

Figure 4-47 Evolution of experimental and numerical particulate mass backflow coefficients in function of V_{dist}/U_{ope} for U_{ope} = 0.5 m/s

As we see in Figure 4-46 and Figure 4-47, the mass backflow coefficients from experiments and simulations have similar order of magnitude for the gas and 5 µm aerosol, respectively. We note that the mass backflow coefficient $K_{m,injection}$ (%) gives access directly to the mass flowrate of pollutants that escapes from the enclosure and does not depend on the envelope extraction rate $Q_{envelope}$.

Figure 4-48 shows a comparison of the experimental and numerical values of the mean backflow velocities near the opening $V_{backflow}$ in function of ($V_{disturbance}$ - U_{ope}) for the case of counter-current disturbing jet.

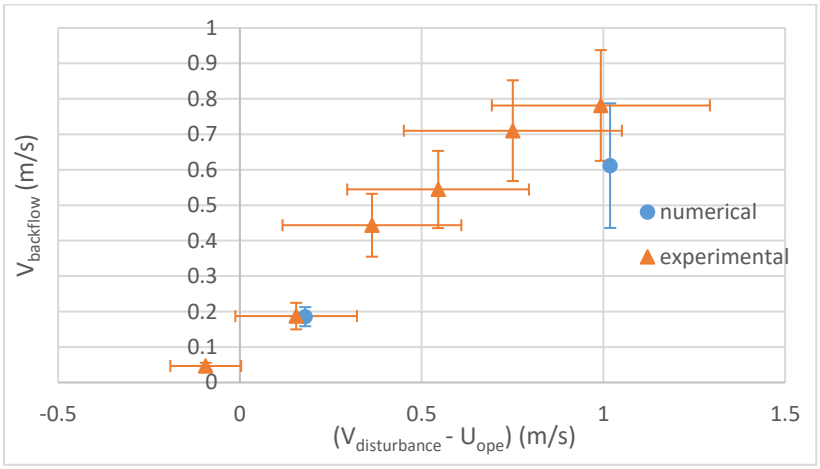

Figure 4-48 Evolution of the experimental and numerical mean backflow velocities $V_{backflow}$ near the opening in function of ($V_{disturbance}$ - U_{ope}) for the counter-current disturbing jet

As we see in Figure 4-48, the experimental and numerical evolutions of the mean backflow velocity near the opening $V_{backflow}$ in function of ($V_{disturbance}$ - U_{ope}) have an increasing trend. The numerical backflow velocities $V_{backflow}$ have the same order of magnitude and trend than the one obtained in experiments.

Finally, we can conclude that the SST-DES turbulence model succeeded to predict the global and mass backflow coefficients and the backflow velocities near the opening for the gaseous and 5 µm particulate pollutants.

Conclusion

In this chapter, we have shown that the turbulence model SST-DES is an appropriate numerical model to predict the backflow phenomenon near the opening. A comparison between experiments and visualization fields from numerical simulations have shown a very good concordance between them. At the same time, we found a good agreement between the experimental and numerical backflow coefficients near the opening under the effect of a counter-current or parietal internal turbulent jet.

The behavior of He gas and 5 µm aerosol particles is very similar near the opening. We explain this result by the calculation of Stokes number. That shows that 5 µm diameter particles were moving in the equilibrium regime for our conditions. Small particles (with low Stokes number) completely follow the gas streamlines. Increasing the particles diameter to 20 µm and more, particles start to deviate from gas streamlines and are accumulated in preferential concentration regime due to the presence of vortices in the jet.

We have given arguments to highlight that the precise value of local backflow coefficients depends primary on the number and the location of the samplers near the opening. That is why the addition of the envelope around the enclosure allows the possibility to characterize the global trend without depending on the collector type and position. This envelope gives us the ability to collect and quantify the total amount of gaseous and particulate pollutants that escape from the enclosure.

Preliminary numerical studies on the envelope have shown that the flows near the opening are not modified by the addition of the envelope, for an air exchange rate up to 5 h^{-1}. Simultaneously, we verified the homogeneity of helium distribution and 5 µm particles within the envelope. We monitored the gaseous and particulate decay rates and compared them successfully with their corresponding experimental evolutions. The deposition rate was estimated from simulations at 73 % within the envelope.

After that, we performed numerical simulations in order to visualize and quantify the backflow phenomenon. Visualization fields show a similar behavior between the gas and 5 µm aerosol inside the envelope. For quantitative characterization, the concentration of pollutant at the extraction of the envelope should be recorded in order to calculate the backflow coefficient but this procedure is highly time consuming (more than 3 months physical time of simulation). That is why we proceeded differently. We monitored the change in mass flowrate within the extraction of the enclosure, then we obtained the backflow mass flowrate and we deduced the gaseous and particulate concentrations at the extraction of the envelope. This procedure is less time consuming (about 5-7 days on 120 CPU cores) and eliminates the necessity to simulate numerically the entire envelope. Additionally, in order to eliminate the dependency of the backflow coefficient on the extraction flow rate of the envelope, we calculated the mass backflow coefficient, as suggested in chapter 3, that gives access directly to the total mass of the backflow pollutant that escapes the enclosure. Additionally, we deduced the mean backflow velocity near the opening. Numerical results for global and mass backflow coefficients and for backflow velocities are in very good agreements with the experimental results.

We mention that the local backflow coefficient K gives information on the concentrations of the pollutants resulting from the backflow near the opening. Its precise value depends on the positions of samplers near the opening. The global backflow coefficient K_{env} and the mass backflow coefficient K_m have a linear evolution with the ratio V_{dist}/U_{ope} and show an increasing trend. However, the global backflow coefficient K_{env} gives access to the concentration inside the envelope but its value depends on the extraction flowrate

of the envelope which is not representative of infinite domain. Therefore, the mass backflow coefficient K_m is more appropriate to give access directly to the mass flowrate of pollutants experiencing backflow at the opening and eliminates the dependency on the envelope aeraulic conditions.

5 Application to a full-size airlock

In this section, we carried out experimental and numerical studies on a full-size airlock (Prevost, 2020). Recalling that there is no use of similarity between the small-size enclosure and the full-size airlock.

Experimental tests were performed in the presence of counter-current or parietal disturbing jets as it may occur in real accidental situations on airlock presenting a split on its wall. Accidental situations correspond for example to a disconnection of a compressed air device used in the airlock, to a blowing produced by a particular process, or to a plume of hot air impacting the ceiling of the airlock in the case of a thermal process, etc.

Numerical simulations using the SST-DES model were performed using the counter-current disturbing jet in order to compare them with experimental results.

5.1 Experimental study

The main airlock is located inside an outer envelope ("Massale") of volume 120 m^3 that is not used in the context of our current study. The standard air exchange rates within the operational airlock are between 8 and 12 h^{-1} that correspond to volume flow rate at the airlock extraction between 120 and 180 m^3/h. Two additional airlock subdivisions are used for the access of workers and material to the operational airlock. The total volume of the three airlock subdivisions (including entrances) is equal to 18.2 m^3. The volume of the operational airlock alone is 15 m^3 with dimensions ($3 \times 2.5 \times 2$) m^3.

Figure 5-1 shows the dimensions of the real airlock located inside the envelope. Figure 5-2 shows the picture of the real airlock with its flexible vinyl walls.

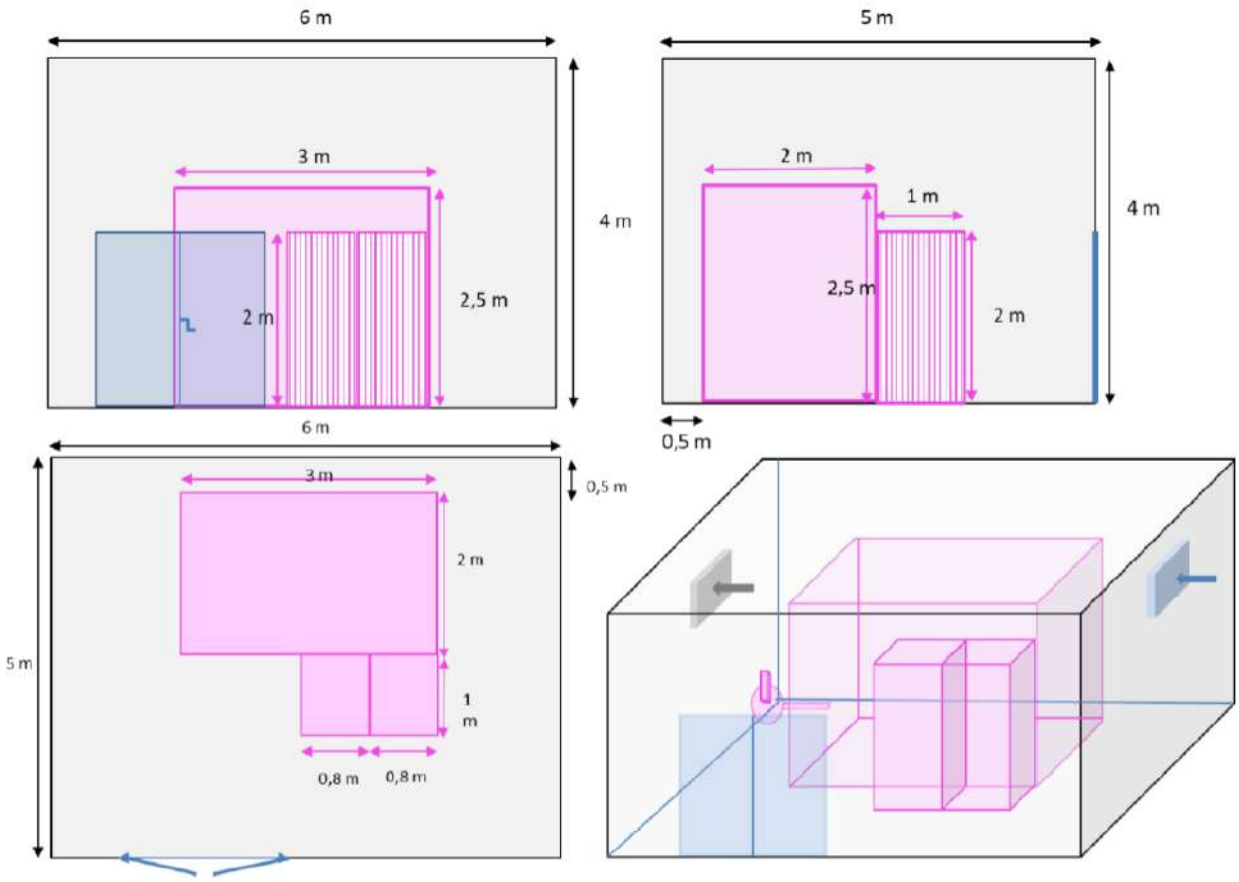

Figure 5-1 Dimensions of the airlock located inside the external envelope (Prevost, 2020)

Figure 5-2 Picture of the real airlock with its flexible vinyl walls

5.1.1 Experimental procedure

The experimental procedure of the tests is similar to that shown in chapter 3 (see Figure 5-3). An opening of dimensions (10 × 3) cm^2 is created on the flexible vinyl wall (see Figure 5-4). The aerosol generator is

located inside the airlock. Continuous generation of 5 µm particles is enabled. Simultaneously helium is injected at the outlet of the generator. The extraction within the airlock is ensured using a fan in order to have the desired velocity at the opening U_{ope} = 0.5 m/s in our case. The disturbance is produced using a blowing fan connected to a nozzle inside the airlock in order to generate a controlled velocity V_{dist} at 3 cm from the opening. The nozzle of the disturbance inside the airlock is added at 50 cm facing the opening in the case of counter-current internal disturbing jet and at 60 cm from the opening vertical axis for the case of parietal internal jet.

Aeraulic measurements

The extraction of the airlock is controlled by an extraction fan that ensures a volume flow rate of about 180 m^3/h corresponding to an air renewal rate of about 12 h^{-1}. The air in the airlock is taken from the envelope room surrounding the airlock through leaks that we generates from one of the two additional airlocks and a little part through the opening in order to obtain an inflow velocity equal to 0.5 m/s which corresponds to 5.4 m^3/h. The air volume flow rate of about 10 m^3/h generated by the aerosol generator is also taking into account in the extraction flow design. The inflow velocity at the opening U_{ope} is controlled and measured using a hot wire anemometer located at the opening.

The flowrate of the disturbing jet is controlled through a valve mounted on the upstream of the supply fan. Simultaneously, the velocities V_0 at the nozzle outlet and V_{dist} at 3 cm from the opening are measured independently from each other using a hot wire anemometer. These velocities are collected in Table 5-1 for the case of the counter-current internal disturbing jet.

Table 5-1 Values of the experimental V_0 and V_{dist} for the case of a counter-current disturbing jet

V_0 (m/s)	1.88	2.41	4.74	6.58
V_{dist} (m/s)	0.25	0.51	1.06	1.52

Backflow coefficient measurement

The sketch shown in Figure 5-3 explains the experimental procedure of our experimental tests. The extraction within the airlock is already activated and the inflow velocity at the opening is 0.5 m/s. Helium and 5 µm aerosols are injected at the same location at the outlet of the generator inside the flexible airlock. Once equilibrium of the tracers concentrations is reached inside the airlock, the aeraulic disturbance is generated. Three filter samplers are added near the opening outside the airlock at the following positions: left side, face side and bottom side of the openingFigure 5-3. The samplers are connected to three sampling piston pumps (RECIPROTOR®) in order to collect the particles. Simultaneously, the helium sampling is performed in the pumps discharge circuit, in such a way, helium and aerosol measurements are made at the same location. A post-processing procedure using the fluorimeter and mass spectrometer gives access to $C_{aerosol,out}$ and $C_{gas,out}$ respectively. Helium and aerosol concentrations inside the airlock are measured first in the extraction circuit of the airlock. Helium concentration at equilibrium corresponds to $C_{gas,in}$. Then, we added two samplers inside the airlock near the opening to be more representative of the internal concentration. The concentration on these two samplers were close to concentration in the airlock extraction circuit at equilibrium. However we decide to consider the mean concentration on these two samplers as $C_{aerosol,in}$. Additionally, the gaseous and particulate ambient concentrations are measured outside the airlock within the envelope and correspond to $C_{gas,ambient}$ and $C_{aerosol,ambient}$, respectively. Then the gaseous and particulate backflow coefficients K_{gas} (%) and $K_{aerosol}$ (%) are deduced (Eq.. 5.1 and Eq. 5.2)

from the ratio between the external concentration obtained from the backflow $C_{gas,out}$ (or $C_{aerosol,out}$) over the internal concentration $C_{gas,in}$ (or $C_{aerosol,in}$).

$$K_{gas}\ (\%) = \frac{C_{gas,out} - C_{gas,ambient}}{C_{gas,in} - C_{gas,ambient}} \times 100 \qquad \text{(Eq. 5.1)}$$

$$K_{aerosol}\ (\%) = \frac{C_{aerosol,out} - C_{aerosol,ambient}}{C_{aerosol,in} - C_{aerosol,ambient}} \times 100 \qquad \text{(Eq. 5.2)}$$

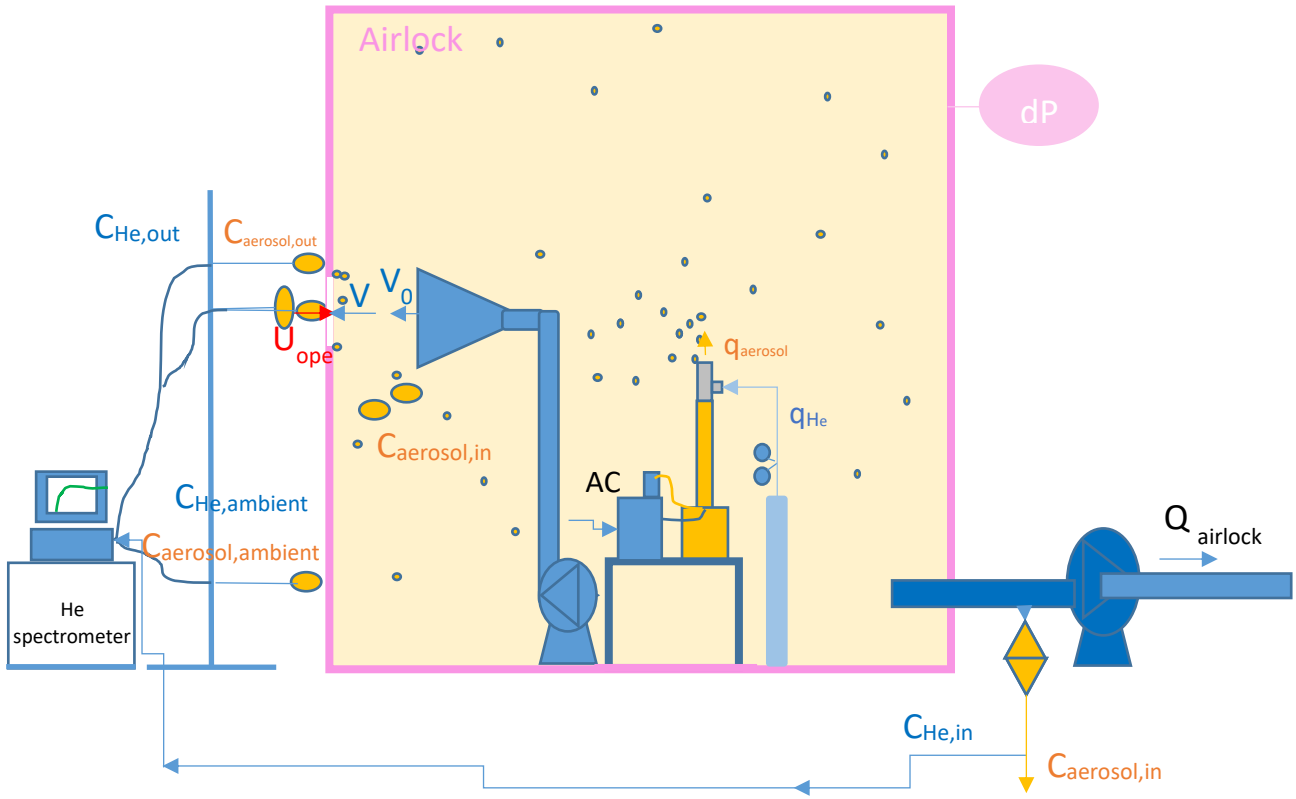

Figure 5-3 Sketch of the experimental equipments corresponding to a counter-current internal disturbing jet (Prevost, 2020)

Figure 5-4 shows the experimental device inside the airlock where the opening can be seen, the aerosol generator and the disturbance circuit (nozzle and fan) are also present on the sketch. We should mention that the positions of the aerosol generator and the disturbance were relocated during the experiments: the generator is positioned at the center of the airlock and the disturbance is positioned at 50 cm facing

the opening. The samplers are located outside and inside the airlock on eitheir side of the opening. The samplers outside the airlock are shown in Figure 5-5.

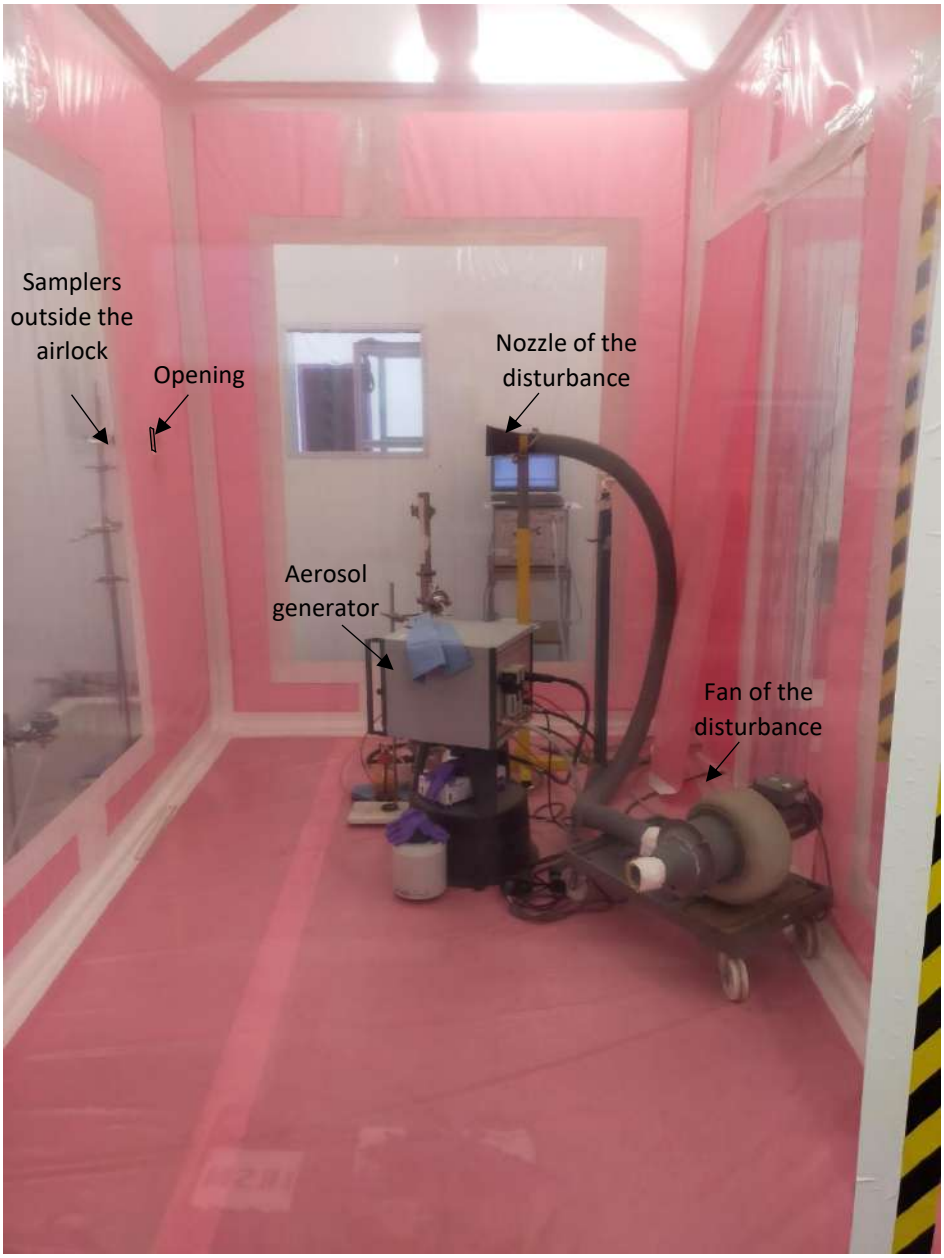

Figure 5-4 Experimental device inside the airlock in the case of a counter-current disturbing jet

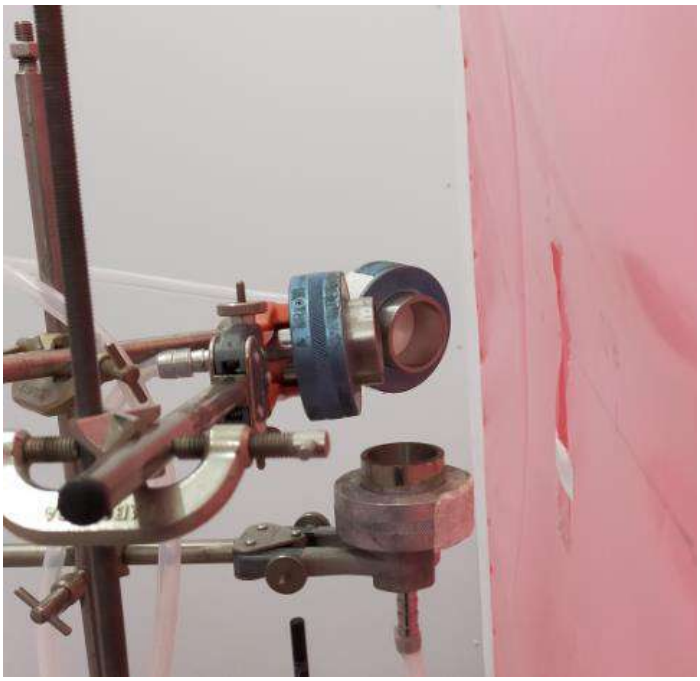

Figure 5-5 Three samplers added near the opening of the airlock

5.1.2 Backflow coefficients results for the full-size airlock

Figure 5-6 shows the evolution of the gaseous and particulate backflow coefficients *K* (%) versus V_{dist}/U_{ope} near the opening in the case of the counter-current internal disturbing jet.

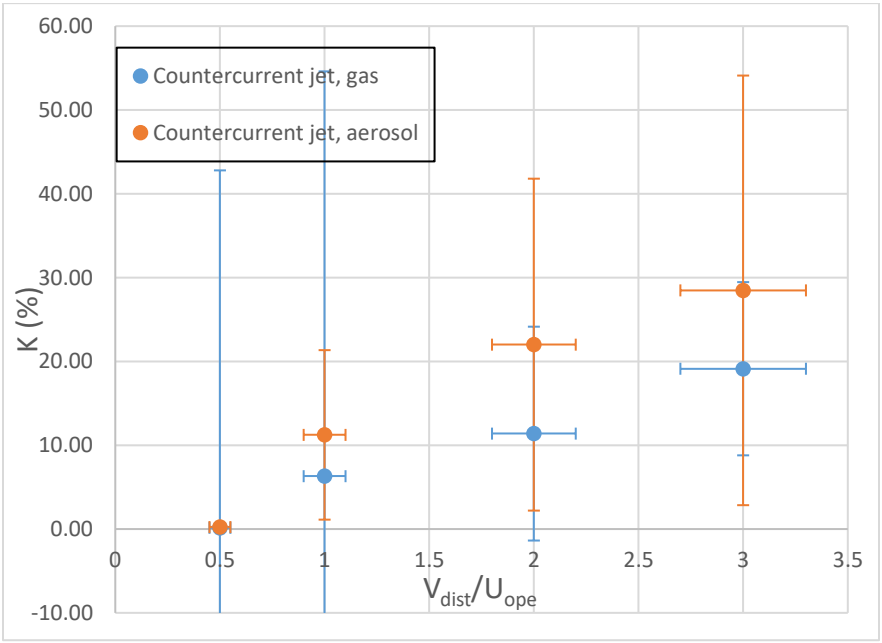

Figure 5-6 Evolution of the gaseous and particulate backflow coefficients K (%) versus V_{dist}/U_{ope} near the opening in the case of the counter-current internal disturbing jet

As we see in Figure 5-6, the gaseous and particulate backflow coefficients *K* (%) have an increasing trend when the perturbation velocity increases. For the first configuration V_{dist}/U_{ope}=0.5, the concentrations near the opening were very close to the ambient value, then we cannot really claim backflow is occuring for this disturbance value. The large error bars for the particulate backflow coefficients are due to the strong variations between the concentrations of the 3 samplers located near the opening. For the gaseous pollutant, the uncertainty bars are also high for lowest disturbance values (up to V_{dist}/U_{ope} = 1) due to strong fluctuations in concentrations around the mean value during the sampling period. They are more stable at higher concentration values, hence for higher value of V_{dist}/U_{ope}. However, the particulate and gaseous backflow coefficients seems to be of the same order of magnitude within uncertainties. Overall behavior is very similar from gas to particles dispersion in this disturbance configuration.

Figure 5-7 shows the evolution of the gaseous and particulate backflow coefficients *K* (%) versus V_{dist}/U_{ope} near the opening in the case of the parietal internal disturbing jet.

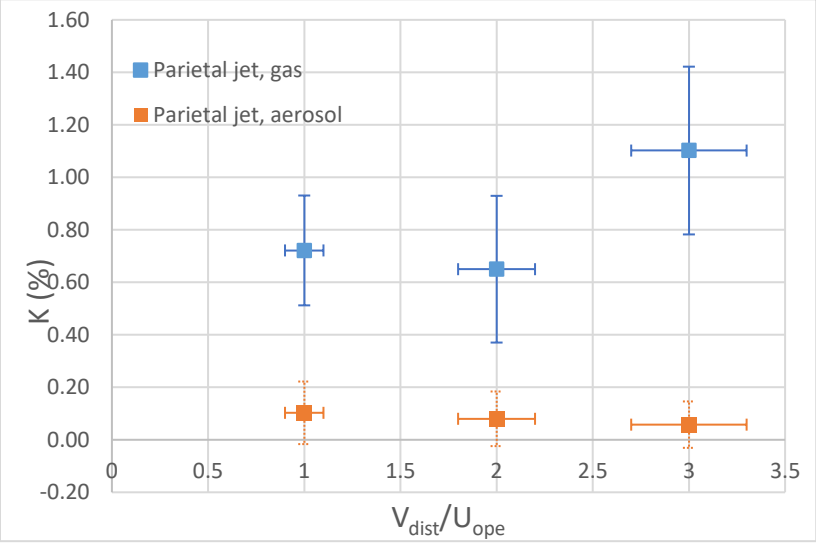

Figure 5-7 Evolution of the gaseous and particulate backflow coefficients K (%) in function of V_{dist}/U_{ope} near the opening in the case of the parietal internal disturbing jet

As we see in Figure 5-7, the gaseous and particulate backflow coefficients are very low (below 1.1%). Indeed, we have to perform additional experiments with higher disturbing jet velocities to understand the curves trend and the relative behavior between gas and 5 µm aerosol.

Comparing the values of the counter-current and parietal internal backflow coefficients for the gaseous and particulate pollutants, we can clearly claim that the backflow phenomenon corresponding to the counter-current internal disturbance is much higher than for the parietal internal jet.

5.2 Numerical simulations

We performed numerical simulations using the SST-DES hybrid model in order to validate its performance on a full-size airlock. However, the boundaries corresponding to the numerical airlock are assumed to be rigid unlike the experimental apparatus which may have small deformations due to airflow.

5.2.1 Numerical procedure

5.2.1.1 Description of the geometry and characteristics of the mesh

The simulation domain, as shown in Figure 5-8, has the following geometric characteristics:

- an internal domain of dimensions (3 × 2.5 × 2) m^3 corresponding to the experimental airlock described above. An extraction unit of circular shape with diameter 15 cm is added on the right-side wall of the airlock. A rectangular surface is present on the rear wall of dimensions (1 × 2) m^2 that corresponds to the additional airlock that we used to control the airlock flow rate. The counter-current disturbance has a circular shape at the inlet (diameter 4 cm) and a rectangular shape at the outlet of dimensions (0.1 × 0.01) m^2 and is located at 50 cm facing the opening;

- an external domain around the opening of dimensions (0.93 × 0.6 × 0.7) m^3 in order to detect the flow inversions near the opening;

- an opening of dimensions (0.1 × 0.03) m^2 connecting the internal and the external domains.

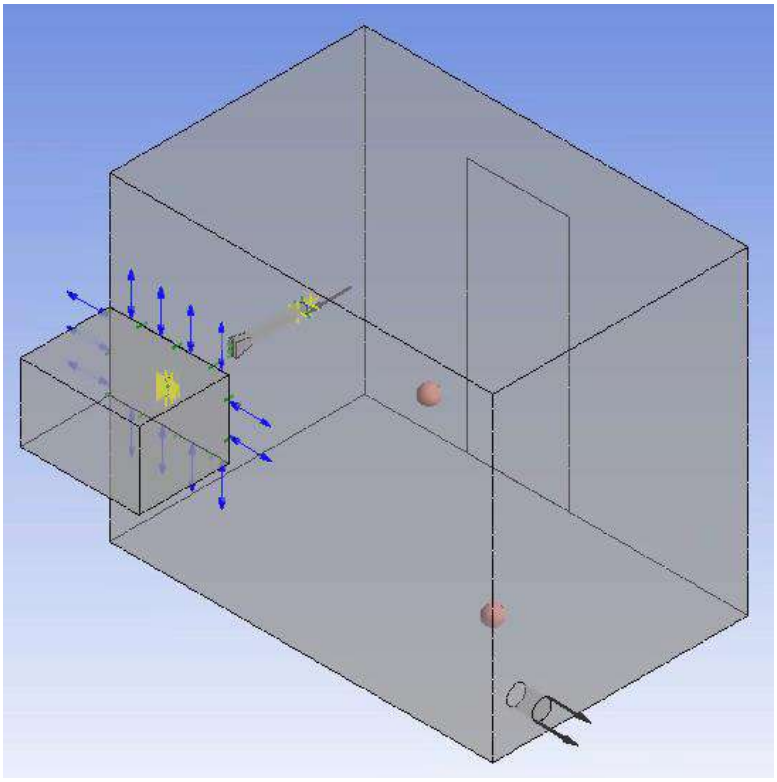

Figure 5-8 Numerical domain for the full-size airlock

The mesh of the airlock is composed of 630977 nodes and 3651129 tetrahedral elements. It is refined near the opening of the airlock, near the extraction unit and along the flow path of the disturbing jet. Figure 5-9 and Figure 5-10 show external and internal 3D views of mesh of the airlock.

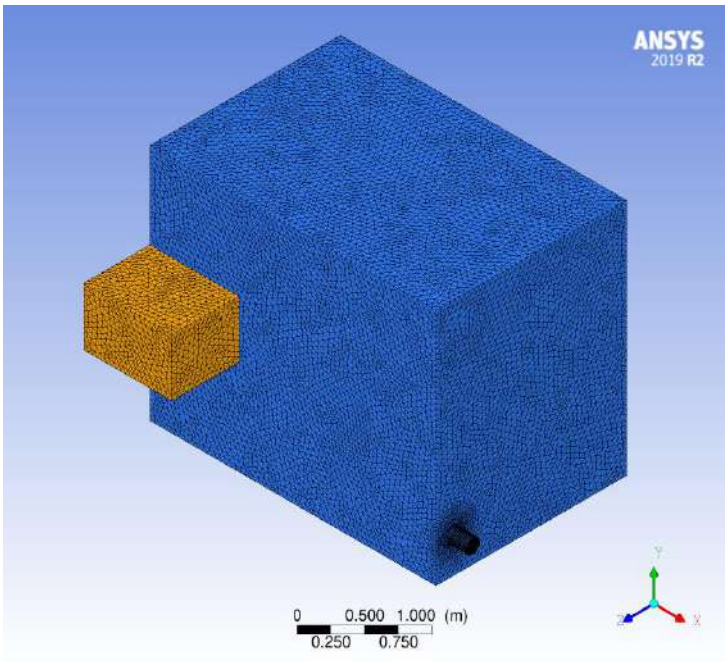

Figure 5-9 External 3D view of the mesh for the airlock

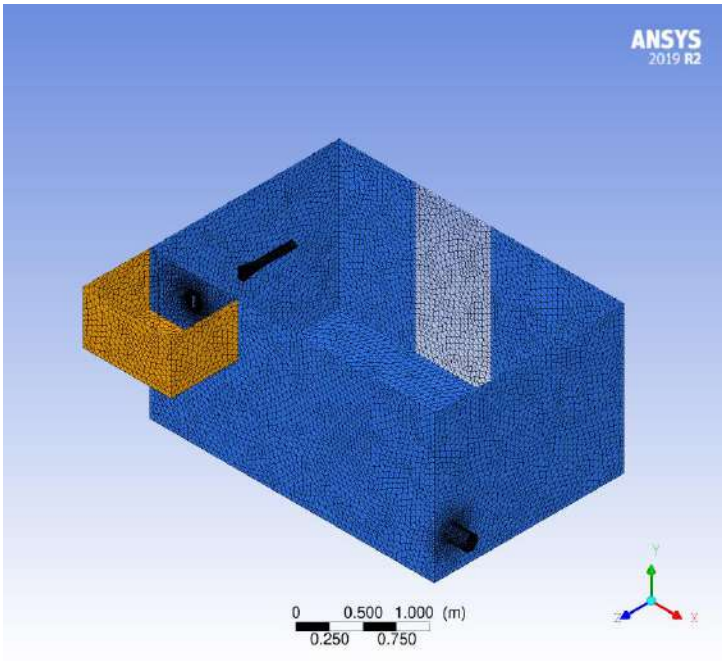

Figure 5-10 Internal 3D view of the mesh inside the airlock

5.2.1.2 Boundary conditions

The boundary conditions for our numerical simulations are the following:

- an 'outlet' condition with an imposed velocity U_{ext} = 2.8 m/s is applied on the extraction unit corresponding to a volume flowrate of about $Q_{airlock}$ = 180 m^3/h within the airlock. It is the sum between the desired inflow at the opening $Q_{opening}$ and the flowrate that we impose in the additional airlock $Q_{additional}$.

- a 'wall' condition with no-slip boundaries is applied on the domain corresponding to the additional airlock. A continuous source of fluid with mass flowrate $q_{additional}$ = 0.054 kg/s is applied. It corresponds to a volume flowrate $Q_{additional}$ that is the difference between the extraction volume flowrate $Q_{airlock}$ (180 m^3/h) and the desired inflow at the opening $Q_{opening}$ (5.4 m^3/h).

- an 'opening' condition with static reference pressure is applied on the external domain. This condition allows the motion of the fluid in the external domain.

- an 'inlet' condition with a mass flowrate corresponding to the mass flowrate extracted at the disturbance sink point is applied on the inlet of the counter-current disturbance device. In simulations, the disturbance nozzle has a circular inlet and a rectangular outlet as in our experiments.

- a 'wall' condition with no-slip boundaries is applied on the physical walls of the airlock internal domain, as well as on the boundaries of the disturbance.

- a 'source point' condition at the center of the enclosure corresponding to the injection of the pollutants (helium and 5 µm diameter particles). The mass flowrates of helium and aerosol are respectively q_{He} = 21.5 g/h and $q_{aerosol}$ = 0.093 g/h.

- a 'sink point' condition at the right side of the enclosure corresponding to the aspiration of a volumetric flowrate Q_{inlet} of the mixture (air/ helium/ 5 µm particles). This flowrate corresponds to the desired velocity at the disturbance nozzle V_0.

Boundary conditions are summarized in Table 5-2.

Table 5-2 Boundary conditions for the SST-DES model

Boundary conditions	Type and value
Disturbance injection	Inlet, q_{inlet} (that corresponds to V_0) $k = \frac{3}{2}(I\,U)^2, \varepsilon = C_\mu \rho \frac{k^2}{\mu_t}, \omega = \frac{\varepsilon}{k}$ $\mu_t = 1000 I\mu\ (I = 3{,}7\%)$
Airlock extraction	Outlet, U_{ext} = 2.8 m/s
Helium and aerosol injection	Source point, q_{He}, $q_{aerosol}$
Disturbance sink	Source point, -q_{inlet}
External domain	Opening, P_{rel} = 0 Pa, Φ_{He} = 0, $\Phi_{aerosol}$ = 0
Additional airlock	Wall, no slip wall, boundary source: $q_{additional}$
Airlock walls and disturbance boundaries	Wall, no slip wall

5.2.1.3 Simulation characteristics of the unsteady regime model

The turbulence model we selected is SST-DES. The fluid is a mixture at STP (standard temperature and pressure) of air at 25 °C (constraint component), He (transport equation) and 5 microns diameter particles (algebraic equation given by the simplified Eulerian transport model (Nerisson et al, 2011)) as shown in chapter 4. An advection 'central difference' scheme for the hybrid calculation and a 'second order backward Euler' transient scheme are used to solve equations of the model. The time step is adaptive and varies between 10^{-4} s and 10^{-3} s. The simulation time is 100 s. The simulation characteristics are summarized in Table 4-5.

Table 5-3 The simulation characteristics used for the DES simulations

Model	DES-SST
Fluids	Air at 25 °C (constraint)
	He at STP (transport equation)
	Particles (algebraic equation)
Advection scheme	Central difference
Transient scheme	Second order backward Euler
Time step	Adaptive, between 0.0001 s and 0.001 s
Simulation time	100 s

5.2.1.4 Steady state for the initial conditions

The initial conditions consist in the situation where there is no disturbance applied inside the airlock. Helium and 5 µm diameter aerosol were injected simultaneously inside the airlock in order to fill out the entire domain. The extraction unit is of type 'outlet' with U_{ext} = 2.8 m/s and the continuous boundary source of $q_{additional}$= 0.054 kg/s is maintained on the rectangular wall. The injection unit of the disturbance is considered as a wall. Boundary conditions are presented in Table 4-6. The fluids injected are air, helium and particles with 5 µm diameter at 25°C. The RANS turbulent model SST k-ω with high resolution and auto time step was used to reach steady state. Boundary conditions and simulation characteristics for the steady state conditions are shown in Table 5-4 and Table 5-5.

Table 5-4 Boundary conditions for the steady state conditions

Boundary conditions	Type and value
Airlock extraction	Outlet, U_{ext} = 2.8 m/s
Helium and aerosol injection	Source point, q_{He}, $q_{aerosol}$
External domain	Opening, P_{rel} = 0 Pa, Φ_{He} = 0, $\Phi_{aerosol}$ = 0
Additional airlock	Wall, no slip wall, boundary source: $q_{additional}$
Airlock walls, disturbance injection and disturbance boundaries	Wall, no slip wall

Table 5-5 Simulation characteristics for the steady state conditions

	RANS
Model	SST k-ω
Fluids	Air at 25°C, He at STP, Particles of 5 µm
Advection scheme	High resolution
Time step	Auto timescale
Maximum number of iterations	8000

5.2.2 Numerical results on the backflow

5.2.2.1 Visualization

Figure 5-11 shows helium molar fraction fields in the vertical median plane of the opening at different time steps for an inflow velocity of U_{ope} = 0.5 m/s and for the case of a counter-current disturbing jet with V_0 = 6.58 m/s corresponding to a velocity at 3 cm from the opening V_{dist} = 1.5 m/s.

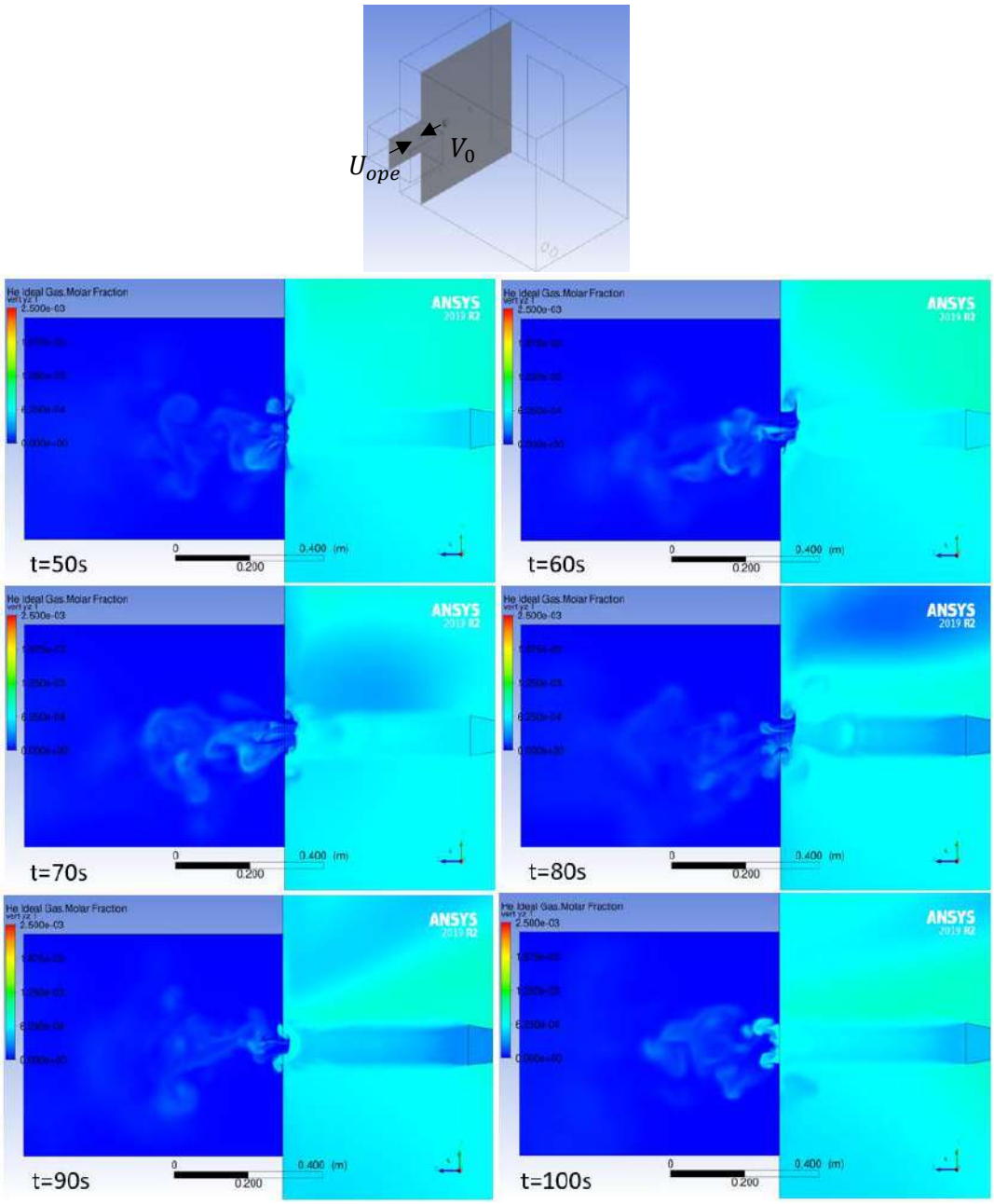

Figure 5-11 Helium molar fraction fields in the vertical median plane of the opening at different time steps for V_{dist}/U_{ope} = 3

As we see in Figure 5-11, the vertical helium fields show that the leakage occurs towards the external domain near the opening under the effect of the containment flow and the countercurrent disturbing jet. Flow inversions are detected inside and outside the airlock near the opening.

Figure 5-12 shows helium molar fraction (left) and particles mass concentration (right) fields in the vertical median plane of the opening of the airlock for t=30 s for an inflow velocity of U_{ope}=0.5 m/s and for the case of a counter-current disturbing jet for V_{dist}/U_{ope} = 3.

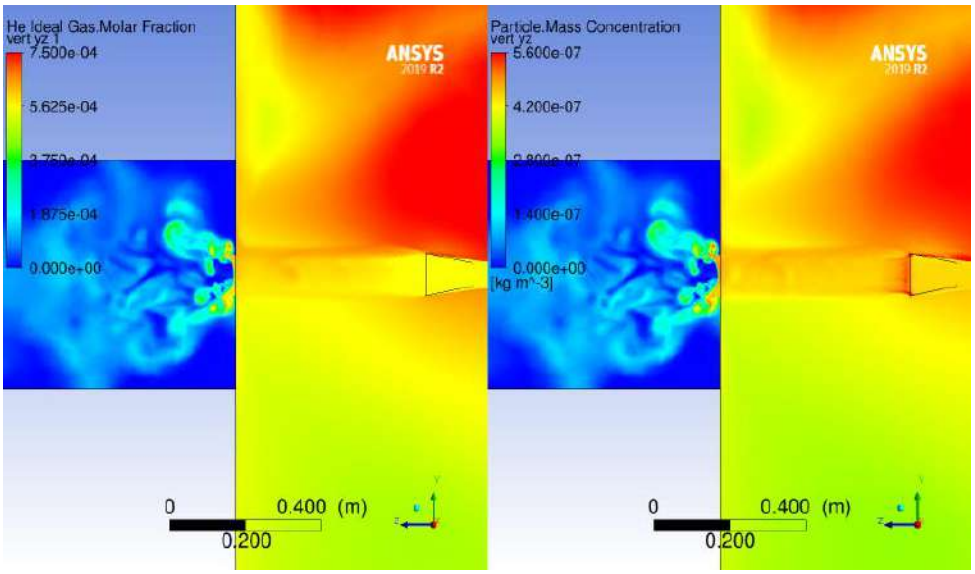

Figure 5-12 Helium molar fraction (left) and particles mass concentration (right) fields in the vertical median plane of the opening of the airlock for t = 47 s for an inflow velocity of U_{ope} = 0.5 m/s and for the case of a counter-current disturbing jet

As we see in Figure 5-12, the backflow phenomenon seems to be similar near the opening for the gaseous and particulate tracers. This may reveal a similar behavior between the gas and the 5 µm diameter aerosol as found previously in our study.

5.2.2.2 Quantitative results

We performed numerical simulations corresponding to V_{dist}/U_{ope} = 1, 2 and 3 respectively. Figure 5-13 shows the evolution of the backflow coefficient *K* (%) in function of V_{dist}/U_{ope} for helium and 5 µm diameter aerosol in the case of an inflow of U_{ope} = 0.5 m/s and a counter-current internal jet.

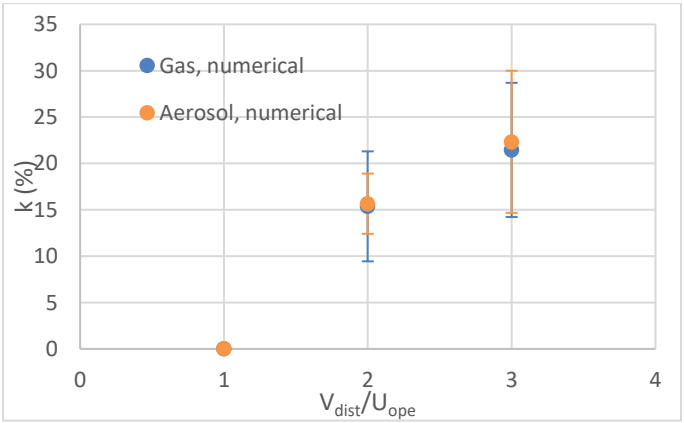

Figure 5-13 Evolution of the numerical backflow coefficient K (%) versus V_{dist}/U_{ope} for helium and 5 µm diameter aerosol in the case of an inflow of U_{ope} = 0.5 m/s and a counter-current internal jet

As we see in Figure 5-13, the gaseous and particulate backflow coefficients show an increasing trend with disturbing jet intensity. Simultaneously, the gaseous and particulate backflow coefficients are of the same order of magnitude, showing a similar behavior between the gas and the aerosol with 5 µm diameter. For V_{dist}/U_{ope} = 1, the backflow coefficients were extremely low (below 0.03%).

5.2.3 Comparison between the experimental and numerical backflow coefficients

Figure 5-14 shows the evolution of the experimental and numerical backflow coefficients *K* (%) in function of V_{dist}/U_{ope} for helium and 5 µm aerosol in the case of an inflow of U_{ope} = 0.5 m/s and a counter-current internal disturbing jet.

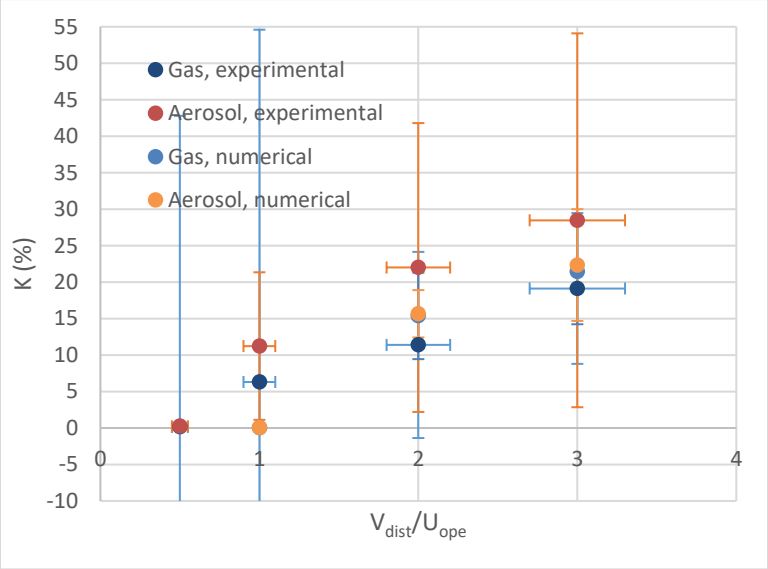

Figure 5-14 Experimental and numerical backflow coefficients K (%) in function of V_{dist}/U_{ope} for helium and 5 µm aerosol in the case of an inflow of U_{ope}=0.5 m/s and a counter-current internal disturbing jet

As we see in Figure 5-14, the numerical and experimental backflow coefficients have both an increasing trend. For V_{dist}/U_{ope}=1, the numerical backflow coefficient is lower than for experiments but remains within uncertainties. The four curves corresponding to the numerical and experimental backflow coefficients for the gas and the aerosol of 5 µm have a consistent trend with similar order of magnitude. One more time we can say that the behavior of the gas and particles is similar in a full-size airlock. Simultaneously we can claim that the SST-DES model succeeded to quantify the backflow phenomenon near the opening for a full-size airlock for counter-current disturbing jet.

Conclusion

Experiments performed on a full-size airlock confirm that the backflow phenomenon occurs under the presence of a counter-current or parietal internal disturbing jets. These could be related to blowing phenomenon inside the airlock as mentioned in chapter 1. The backflow coefficients of the counter-current disturbing jet are higher than those of the parietal disturbing jet, as we noticed for the small-size enclosure in chapter 3. The behavior between the gas and the 5 µm diameter aerosol seems to be similar

also near the opening. Additionally, we showed that the SST-DES model successively succeeded to capture the unsteady nature of backflow near the opening and to quantify the leakage. The comparison between the experimental and numerical results validates the reliability of SST-DES turbulence model for the case of a counter-current disturbing jet. We did not have enough time to perform numerical simulations for parietal disturbing jet.

Conclusions & Perspectives

The backflow phenomenon can occur in ventilated airlocks that are set under negative pressure drop around contaminated areas during nuclear maintenance and dismantling operations. Some operating activities are among the main causes leading to the transfer of gaseous and particulate pollutants to outside the airlock through nominal or accidental openings due in particular to the presence of unwanted disturbing flows such as air jets from the process or the ventilation. ISO standards such as (ISO-17873, 2004) and (ISO-16647, 2018) recommend to maintain a minimum value of negative pressure drop or inflow velocity through any airlock opening in order to guaranty an efficient dynamic containment. However, they recommend also to evaluate each configuration specifically. Because very few investigations were carried out on characterizing flow inversion phenomena at openings in depressurized enclosures, the approach we adopted was to reproduce the phenomenon under different controlled configurations and to measure the leakage intensity of gas and particulate pollutants that results from the backflow.

Our study is following the PhD of S. Kaissoun that studied experimentally and numerically the gaseous pollutant backflow on a small-scale enclosure. S. Kaissoun's works showed that an additional flow in form of disturbing jet inside or outside the enclosure, along with the existing containment inflow leads to the backflow of pollutants to outside the enclosure. She highlighted a new aeraulic criterion that compares the velocity V of the disturbing jet with respect to the containment inflow U_{ope} which must be kept under a threshold value in order to guaranty an efficient dynamic containment and then to prevent the backflow phenomenon. Additionally, she showed that the LES turbulence numeric model has the ability to reproduce qualitatively the backflow phenomenon of pollutants near the opening.

Our additional contribution to S. Kaissoun works includes two main parts:

- For the experimental part, 5 µm particulate pollutant was studied in addition to the gaseous pollutant. We designed and used of an external envelope around the small-size enclosure in order to collect the global amount of gaseous and particulate pollutants due to the backflow through the opening. Two types of internal disturbing jets were investigated, the counter-current and parietal internal disturbing jets with two types of frontal wall: the rigid and flexible frontal walls.
- For the numerical part, a quantitative validation of CFD simulations with a hybrid turbulence model was established for different experimental scales and different pollutant materials.

Additionally, two procedures for the experimental and numerical quantification of the backflow were performed: the local backflow detection near the opening and the global backflow characterization using the envelope placed around the enclosure.

In chapter 1, we presented the recommendations applied to containment systems during maintenance and dismantling operations on site to guaranty an efficient dynamic containment. However, we showed that there was not a standard criterion that prevents the backflow of pollutants to outside the enclosure, except for S. Kaissoun criterion. Regarding backflow description, we presented various studies of pollutants backflow through ventilated enclosure with moderate and large-scale openings but we showed that this phenomenon through small openings was not well investigated in the literature. After that, and since our works cover the particulate pollutants, we described particle-laden flows and presented

interactions that may exist between gas and particles. Indeed, we explained how particles aerodynamic diameter and velocity intensity affect the particles behavior in response to gas flow in particle-laden flows. Finally, we presented many turbulence models that can be used for the backflow study, and in particular the hybrid model SST-DES that was chosen for our study based on its reliability in this context. Additionally, we presented various particle-laden approaches such as Eulerian and Lagrangian approaches that are used for modelling the particulate phase. The aerosol model chosen for our study is a simplified Eulerian approach (Nerisson, 2011).

In chapter 2, we proposed the article "Experimental study of backflow air leakage through an opening from a depressurized enclosure" accepted for publication in Journal of Nuclear Science and Technology (JNST). This article deals with the experimental study of gaseous pollutant backflow through small opening in small-size enclosure and with the presence of internal and external disturbing jets (S. Kaissoun, 2018). Laser visualization technique offered the opportunity to detect leakage of gas tracer to outside the enclosure and flow inversions near the opening. The PIV technique provided information on local flow structures and the velocity magnitude of the turbulent flow near the opening. Gas tracing technique was applied to quantify the backflow phenomenon near the opening for different disturbing jet types. These results correspond to the evolution of backflow coefficients K (%) as a function of the dimensionless aeraulic parameter V/U_{ope} for different dynamic containment flowrates through the opening U_{ope}. We showed that this dimensionless aeraulic parameter V/U_{ope} was relevant to characterize the aeraulic conditions effects on the onset of backflow.

The chapter 3 was dedicated to the experimental analysis of backflow for gaseous and 5 µm particulate pollutants through the opening of a small-size ventilated enclosure. Visualization techniques allowed to detect the backflow and flow inversions near the opening for different disturbing jet configurations and frontal wall types. They showed that the counter-current disturbing jet resulted in higher quantity of backflow near the opening than that of parietal jet for the same disturbing jet velocity. Simultaneously they showed that for the counter-current disturbing jet, there was no influence of the type of the frontal wall (rigid or flexible) on the backflowed pollutant intensity near the opening. For the parietal disturbing jet, and due to very weak backflow detected near the opening, we cannot claim if there was really a significant difference between the two types of frontal walls. However, we detected that there was a preferential side for the backflow near the opening for the parietal disturbing jet configuration: to the opposite side of the disturbing jet, and to the bottom side of the opening for the case of the flexible wall type.

Quantitative results that showed the evolution of the backflow coefficient K (%) in function of the aerodynamic parameter V_{dist}/U_{ope} performed locally near the opening and globally inside the envelope, gave access to the threshold of the backflow release for each disturbance configuration. We found also that these evolutions had a unique trend regardless of the inflow velocity U_{ope} for the gaseous and particulate pollutants. The local backflow coefficients related to the concentration near the opening have an increasing trend and reached a plateau value near the opening above $V_{dist}/U_{ope} = 2$. This may be explained by the behavior of the jet near the opening, in form of puffs for low V_{dist}/U_{ope} values or continuous backflow above $V_{dist}/U_{ope} = 2$. The global backflow coefficients related to the concentration within the envelope extraction duct had a continuous increasing trend with V_{dist}/U_{ope} and were directly related to the mass flowrate of the backflowed pollutants outside the enclosure. Indeed, the tracer concentrations sampled within the envelope extraction duct, and hence the global backflow coefficients depended on the extraction flowrate of the envelope. However, these concentrations gave access to the

total mass flowrate of backflowed pollutants transmitted to outside the enclosure that were of primary interest.

Additionally, we found that the gas and 5 µm aerosol have a similar behavior in our aeraulic and geometric conditions: referring to Stokes number, we observed they were in equilibrium regime, and hence the particles followed completely the gas streamlines.

Furthermore, we checked the influence of the disturbing jet and frontal wall types on the backflow. Indeed, the orientation of the disturbing jet did affect the quantity of the backflow near the opening: the configuration of the counter-current disturbing jet reduced more the dynamic containment and generated more backflow quantity than the parietal jet configuration. However, the influence of the frontal wall on the backflow is depending on the disturbance configuration. In the case of the counter-current disturbing jet, we found that the backflow coefficient did not depend on the nature of the frontal wall. In this case, the velocity value of the counter-current disturbing jet was strong enough to induce the backflow phenomenon. Finally, this meant that there was no need to simulate numerically the flexible frontal wall for this type of disturbing jet and for our geometric conditions. However, for the parietal disturbing jet, we found that the flexible frontal wall generated more backflow than the rigid frontal wall: the vibrations of the flexible wall or the deformation of the opening shape could be the reasons behind this result. Therefore, in order to obtain valid numerical results for the parietal internal jet, the flexibility of the frontal wall should be taken into account numerically. However, due to its complexity in numerical simulations, it was not taken into account in the context of our works.

The chapter 4 referred to the numerical validation of the gaseous and particulate backflow phenomenon, locally near the opening of the enclosure and globally in the external envelope. Visualization fields and quantitative backflow evolutions demonstrated that the hybrid turbulence model SST-DES was an appropriate numerical approach to predict the backflow phenomenon near the opening. Comparison between experimental and numerical backflow coefficients near the opening under the effect of a counter-current or parietal internal turbulent jet showed a good agreement between them. Additionally, we found that the behavior between the gas and the 5 µm particles was similar, referring to an equilibrium regime. We noted that increasing the particles diameter to 20 microns and more, particles started to deviate from gas streamlines and adopted preferential concentration regime.

In order to calculate numerically the global backflow coefficients, we found that due to the low renewal rate inside the envelope, numerical simulations required between 2 or 3 months to reach an equilibrium concentration at the envelope extraction duct. However, by following the mass flowrate sampling in the enclosure extraction duct we were able to have access to the backflow mass flowrate and then to deduce the concentration in the envelope extraction duct. This eliminated the necessity to simulate numerically the flow dynamics in the entire envelope and then reduced the simulation time down to about 5 days.

Furthermore, we showed that local backflow coefficient K (%) gave access to the concentrations of the backflowed pollutants near the opening. Its precise value depends on the locations of samplers near the opening. The main advantage of the envelope was to collect and to quantify the total amount of gaseous and particulate pollutants that escaped from the enclosure and then did not depend on these local collectors. We showed that it was better to represent the global backflow coefficients in terms of mass (K_m) than in terms of concentration (K_{env}) in order to eliminate the dependency of this coefficient with the renewal rate of the envelope.

We define a mass backflow coefficient K_m (%) that represents the ratio of the mass flowrate of the backflow $q_{out\_backflow}$ that escapes from the enclosure over the mass flowrate in the extraction of the enclosure $q_{in\_enclosure}$ in order to neglect the amount of particle deposit in the case of particulate pollutant inside the enclosure.

$$K_m\,(\%) = \frac{q_{out\_backflow}}{q_{in\_enclosure}} \times 100$$

Figure 0-1 shows a synthetic figure for the evolution of the experimental and numerical mass backflow coefficient K_m (%) for gas and 5 µm aerosol versus V_{dist}/U_{ope} for the counter-current disturbing jet. Figure 0-2 illustrates the parity curve between our experimental and numerical local and global backflow coefficients for gas and 5 µm aerosol and for the counter-current and parietal disturbing jets. In Figure 0-2, the uncertainties related to experimental results were between 20% and 30% and those related to numerical results were between 15% and 25%. We added 2 lines corresponding to confidence intervals of 25% from the parity curve.

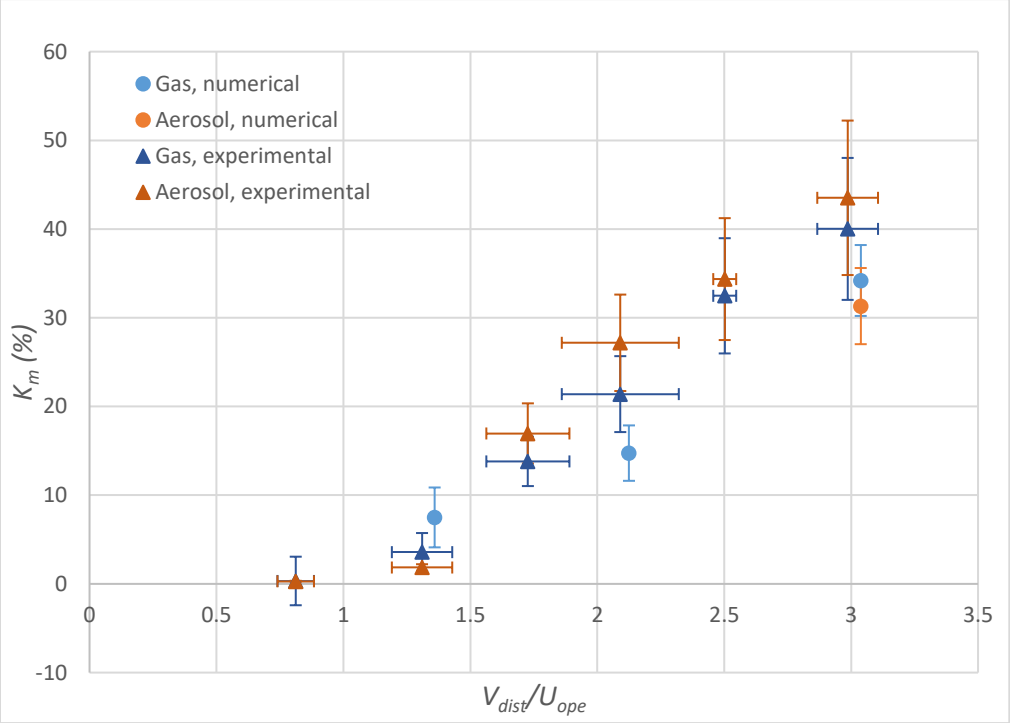

Figure 0-1 Synthetic figure for experimental and numerical mass backflow coefficients K_m (%) for gas and 5 µm aerosol in function of V_{dist}/U_{ope} in the case of counter-current disturbing jet

As we see in Figure 0-1, the numerical and experimental mass backflow coefficients K_m (%) are in good agreement for the gaseous and 5 µm particulate pollutants. This means that the SST-DES model is able to predict the pollutants backflow intensity expresses with the K_m ratios. Simultaneously, these results confirm the similar behavior between the gas and 5 µm particles in terms of mass flowrates.

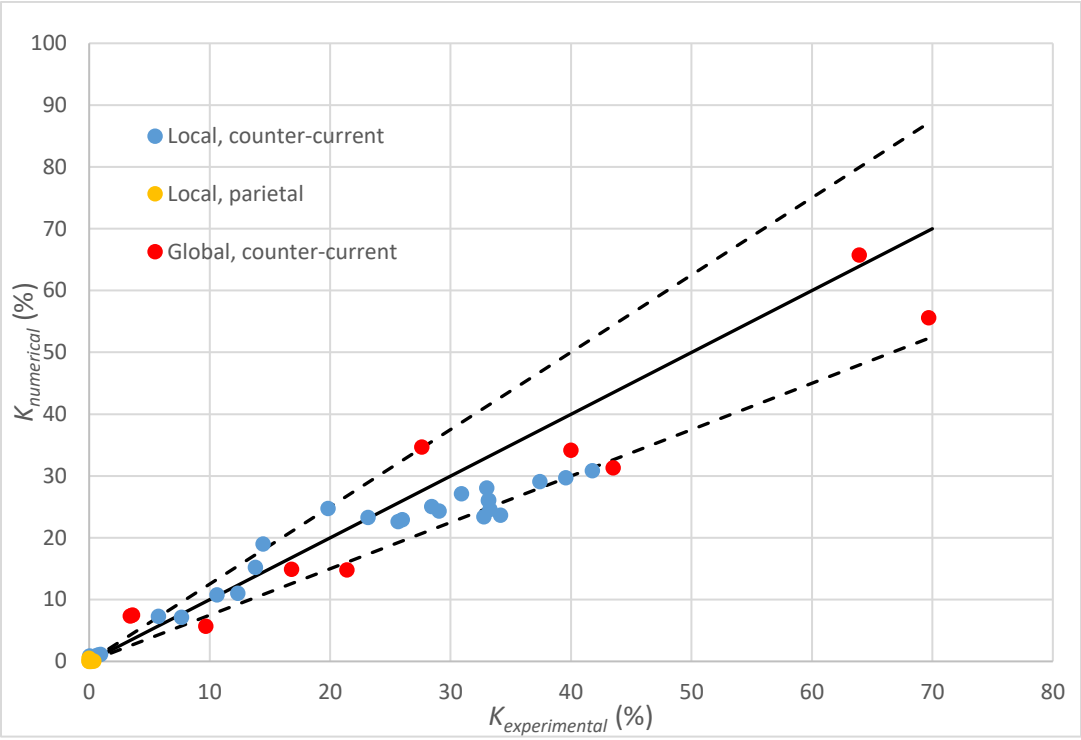

Figure 0-2 Parity curve (± 25 %) between the experimental and numerical backflow coefficients

As we see in Figure 0-2, the numerical results are in good agreement with the experimental results, within the uncertainties, for the local and global quantification and for the two types of disturbing jets (note that for the parietal jet, it is hard to distinguish the results since backflow is very weak). This figure validates the reliability of the hybrid turbulence model SST-DES to predict the backflow phenomenon.

The last chapter was dedicated to a discussion of experimental and numerical studies on a full-size airlock built with flexible walls, subject to the presence of a counter-current or a parietal internal disturbing jet. These jets can be caused by the disconnection of a pressurized gas line or by a cutting process or by a blower, for example. We concluded that for our aeraulic and geometric conditions, the behaviors of the gas and 5 µm aerosol were similar experimentally and numerically.

Then, comparison between experimental and numerical backflow coefficients validates the reliability of SST-DES turbulence model for the case of a counter-current disturbing jet. Unfortunately, we could not test numerically the case of parietal disturbing jet for lack of time.

The perspectives of our works are related to perform numerical parametric study using the hybrid SST-DES turbulence model while varying some aeraulic and geometric conditions. For example, we may modify the type of aeraulic disturbing jets such as varying the angle between the jet and the opening axis, varying the position or the number of disturbing jets. Additionally, we may change the geometric configurations of the enclosure such as other shapes, dimensions and number of the openings that could be presented on the enclosure. It is a matter of anticipating these pollutant transfer phenomena in the case of various accidental scenarios. Additionally, numerical simulations taking into account the flexibility and the vibrations of the frontal wall are also interesting, especially for the case of the parietal disturbing jet since we detected experimental differences between the results corresponding to the rigid and flexible frontal walls.

Appendix 1. Laser visualizations

Laser visualizations fields in the median horizontal and vertical planes in the opening of the enclosure with its rigid and flexible fontal wall for the counter-current and parietal internal disturbing jets are presented in the following.

A- Visualizations fields in the median horizontal plane in the opening of the enclosure with its rigid frontal wall and with a counter-current internal disturbing jet are shown in Figure 0-3.

a) $U_{ope} = 1$ m/s, $V = 0$ m/s

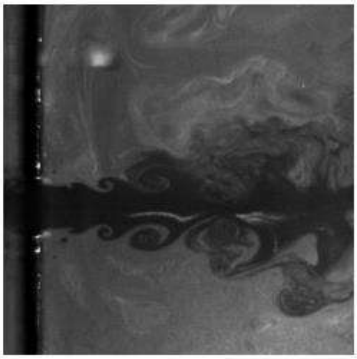

b) $U_{ope} = 1$ m/s, $V = 3.2$ m/s

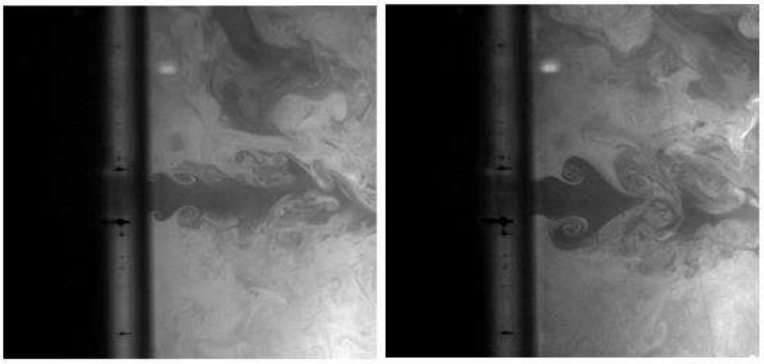

c) $U_{ope} = 1$ m/s, $V = 5$ m/s

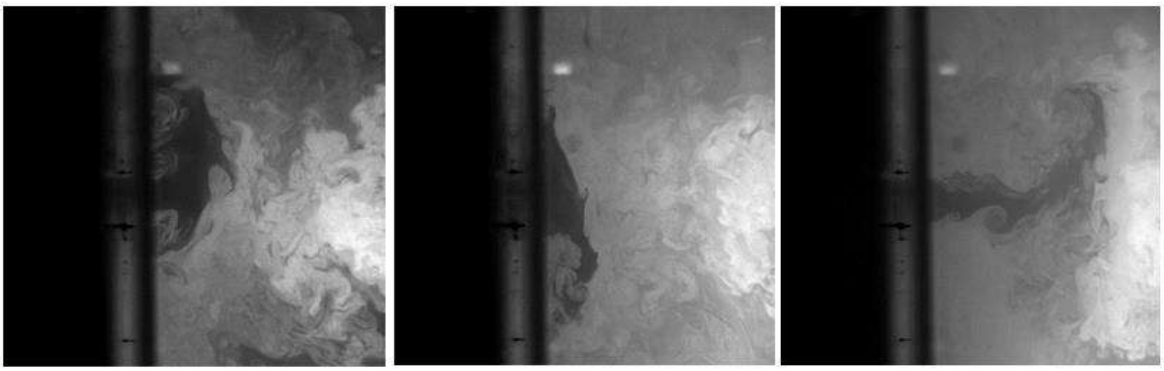

d) U_{ope} = 1 m/s, V = 6 m/s

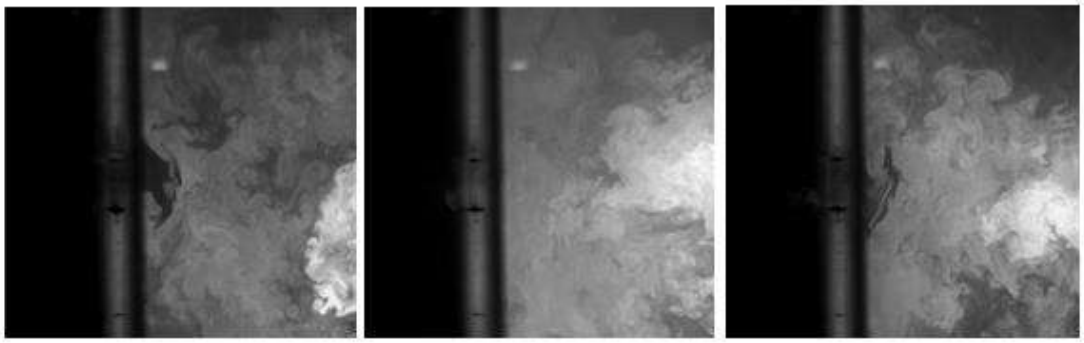

e) U_{ope} = 1 m/s, V = 8.4 m/s

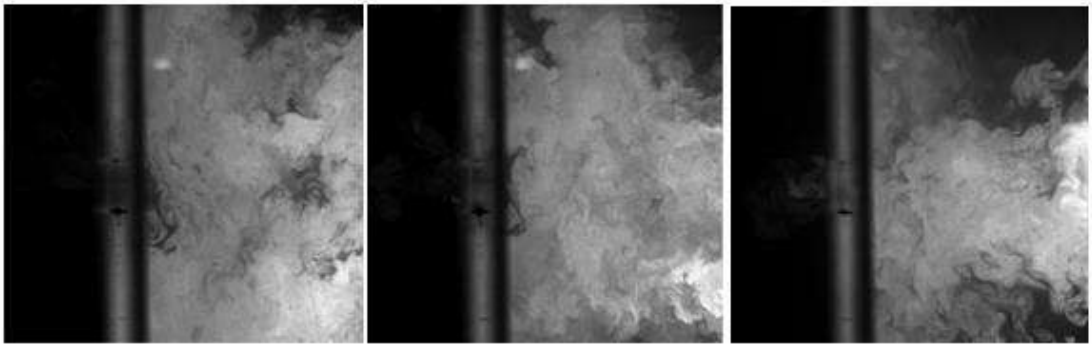

f) U_{ope} = 1 m/s, V = 11.7 m/s

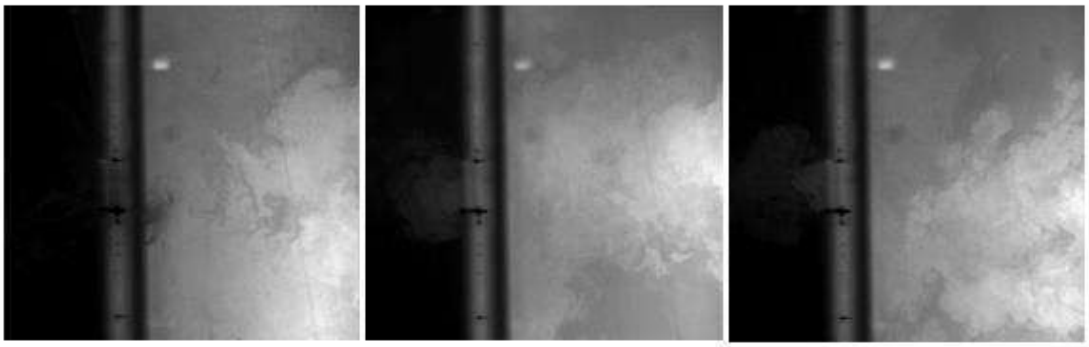

g) U_{ope} = 1 m/s, V = 14 m/s

Figure 0-3 Visualizations fields in the median horizontal plane of the opening of the enclosure with its rigid frontal wall and with a counter-current internal disturbing jet

B- Visualizations fields in the median vertical plane in the opening of the enclosure with its rigid frontal wall and with a counter-current internal disturbing jet are presented in Figure 0-4.

a) $U_{ope} = 1$ m/s, $V = 0$ m/s

b) $U_{ope} = 1$ m/s, $V = 3.2$ m/s

c) $U_{ope} = 1$ m/s, $V = 5$ m/s

d) U_{ope} = 1 m/s, V = 6 m/s

e) U_{ope} = 1 m/s, V = 8.4 m/s

f) U_{ope} = 1 m/s, V = 11.7 m/s

g) U_{ope} = 1 m/s, V = 14 m/s

Figure 0-4 Visualizations fields in the median vertical plane in the opening of the enclosure with its rigid frontal wall and with a counter-current internal disturbing jet

C- Visualizations fields in the median horizontal plane in the opening of the enclosure with its flexible frontal wall and with a counter-current internal disturbing jet, outside the enclosure are shown in Figure 0-5.

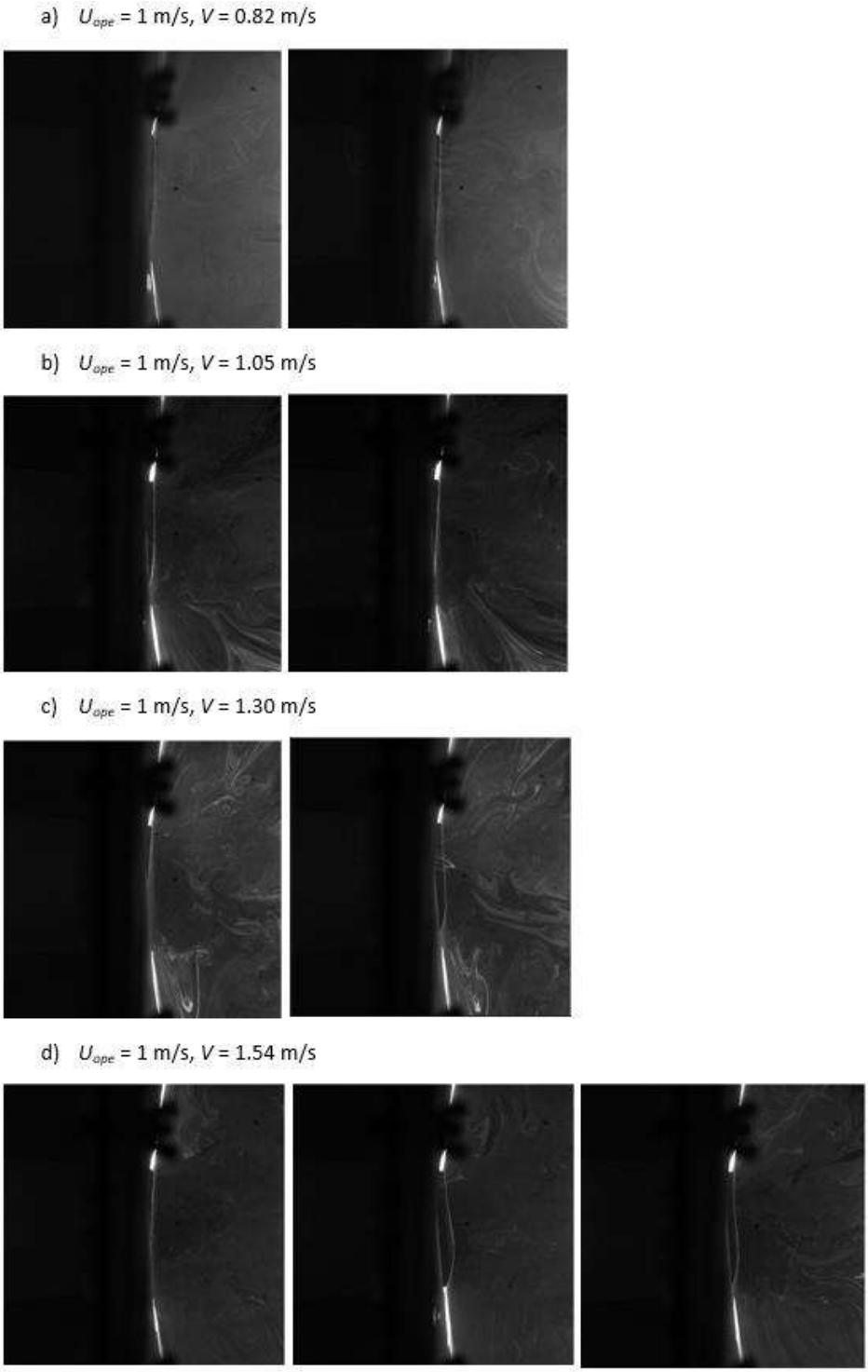

Figure 0-5 Visualizations fields in the median horizontal plane in the opening of the enclosure with its flexible frontal wall and with a countercurrent internal disturbing jet, outside the enclosure

D- Visualizations fields in the median horizontal plane in the opening of the enclosure with its flexible frontal wall and with a countercurrent internal disturbing jet, inside the enclosure (without smoke particles) are showed in Figure 0-6.

a) U_{ope} = 0.5 m/s, V = 0.60 m/s

b) U_{ope} = 0.5 m/s, V = 1.56 m/s

c) U_{ope} = 0.5 m/s, V = 1.54 m/s

Figure 0-6 Visualizations fields in the median horizontal plane in the opening of the enclosure with its flexible frontal wall and with a counter-current internal disturbing jet, inside the enclosure

E- Visualizations fields in the median horizontal plane in the opening of the enclosure with its flexible frontal wall and with a counter-current internal disturbing jet, inside the enclosure are presented in Figure 0-7.

a) U_{ope} = 0.5 m/s, V = 0.65 m/s

b) U_{ope} = 0.5 m/s, V = 1.09 m/s

c) U_{ope} = 0.5 m/s, V = 1.56 m/s

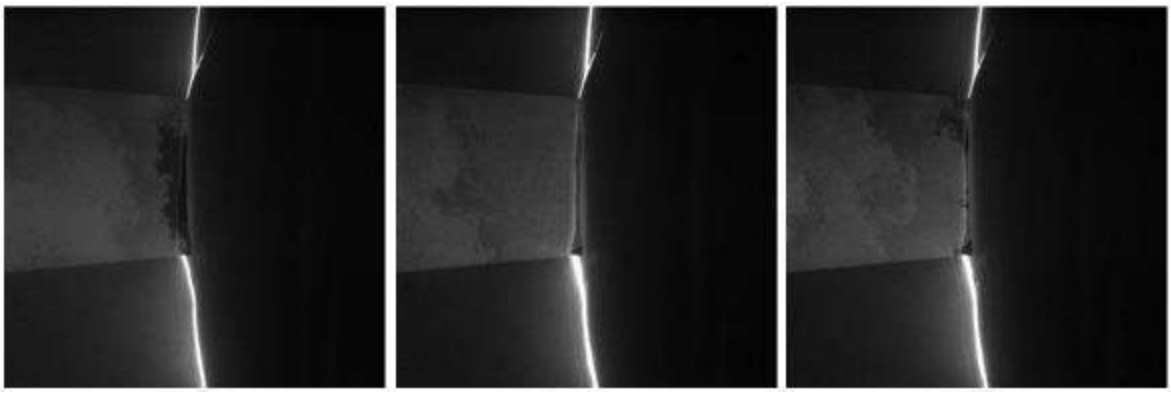

Figure 0-7 Visualizations fields in the median horizontal plane in the opening of the enclosure with its flexible frontal wall and with a counter-current internal disturbing jet, inside the enclosure

F- Visualizations fields in the median horizontal plane in the opening of the enclosure with its flexible frontal wall and with a parietal internal disturbing jet, outside the enclosure are presented in Figure 0-8.

a) U_{ope} = 0.5 m/s, V = 0.78 m/s

b) U_{ope} = 0.5 m/s, V = 1.42 m/s

c) U_{ope} = 0.5 m/s, V = 2.03 m/s

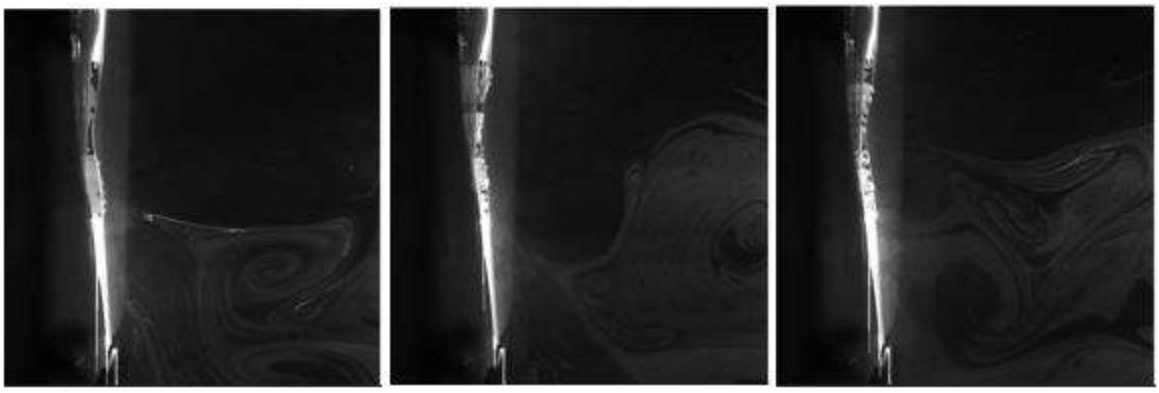

Figure 0-8 Visualizations fields in the median horizontal plane in the opening of the enclosure with its flexible frontal wall and with a parietal internal disturbing jet, outside the enclosure

G- Visualizations fields in the median horizontal plane in the opening of the enclosure with its flexible frontal wall and with a parietal internal disturbing jet, inside the enclosure are shown in Figure 0-9.

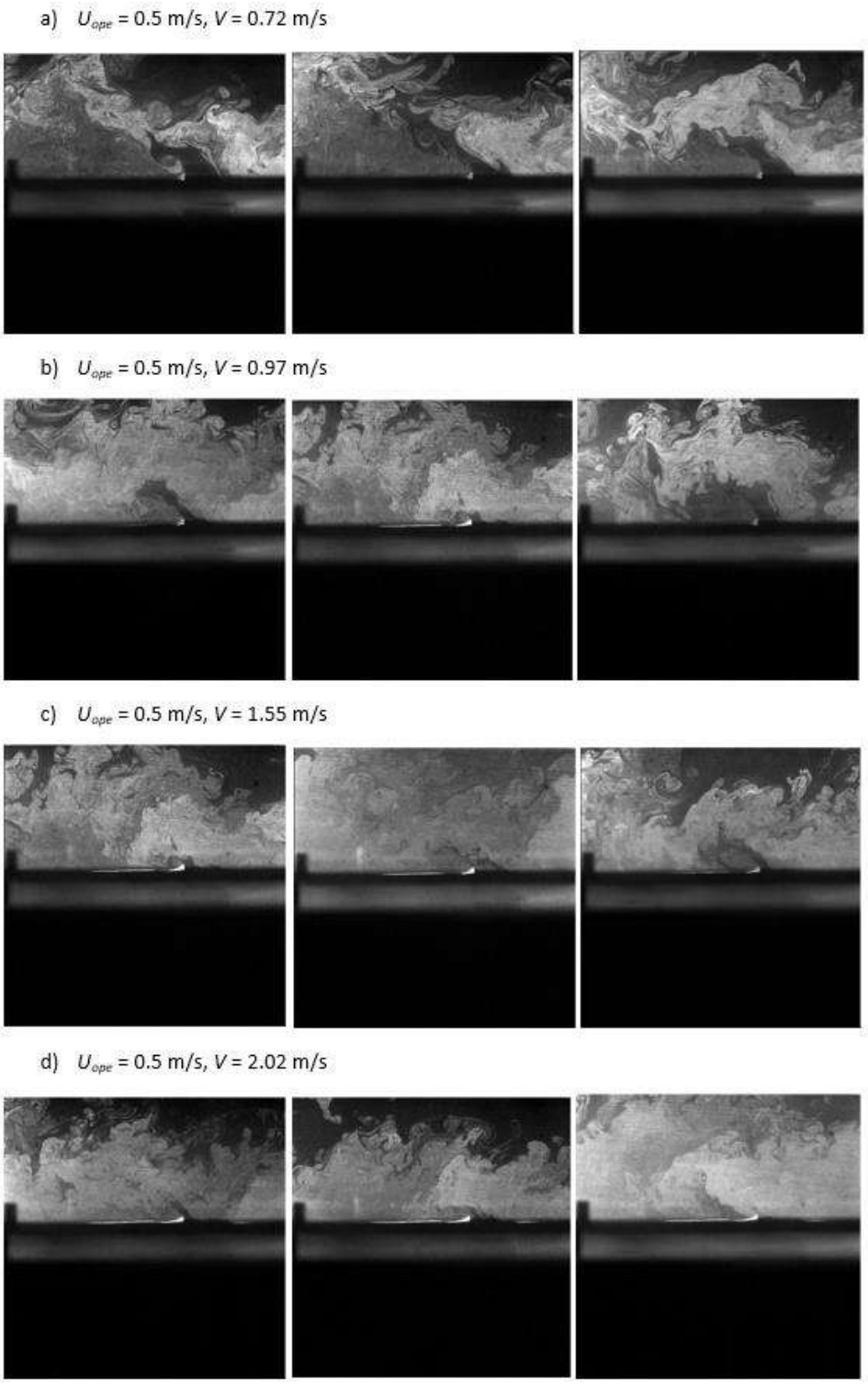

Figure 0-9 Visualizations fields in the median horizontal plane in the opening of the enclosure with its flexible frontal wall and with a parietal internal disturbing jet, inside the enclosure

Appendix 2. Determination of the uncertainties

2.1. Determination of uncertainties on measurement of the backflow coefficient K, related to gas and particulate tracing technique

The uncertainty considered $U_{r(K)}$ is an expanded relative uncertainty, expressed as a percentage, with a widening coefficient K_e = 2 corresponding to a 95 % confidence interval. It is calculated with the method of propagation of uncertainties by considering the different uncertainties perfectly independent of each other.

Eq. 1 gives the expanded relative uncertainty $U_{r(K)}$ on the backflow coefficient K.

$$U_{r(K)} = \pm 2 \sqrt{\left(\frac{U_{r\,(\Delta C_{in_{eq}})}}{2}\right)^2 + \left(\frac{U_{r\,(\Delta C_{out_{eq}})}}{2}\right)^2} \quad \text{(Eq. 1)}$$

Where $\Delta C_{in_{eq}}$ and $\Delta C_{out_{eq}}$ are given by Eq. 2 and Eq. 3 respectively.

$$\Delta C_{int_{eq}} = \overline{C_{in_{eq}}} - C_{ambient} \quad \text{(Eq. 2)}$$

$$\Delta C_{out_{eq}} = \overline{C_{out_{eq}}} - C_{ambient} \quad \text{(Eq. 3)}$$

The expanded relative uncertainty $U_{r(\Delta C_{int})}$, with a widening coefficient K_e = 2, related to the measurement of $\Delta C_{int_{eq}}$, is given by Eq. 4:

$$U_{r\left(\Delta C_{int_{eq}}\right)} = \pm 2 \sqrt{\frac{U_{\,(\Delta C_{in_{eq}})}}{\left(\Delta C_{in_{eq}}\right)^2}} \quad \text{(Eq. 4)}$$

The main sources of uncertainties to be considered when measuring a helium concentration of an air / helium gas mixture are generally due to the measurement instrumentation, the ambient environment and the sample to be analyzed. The uncertainty $U_{\left(\Delta C_{int_{eq}}\right),gas}$ related to gas is as follows (Eq. 5):

$$U_{\left(\Delta C_{int_{eq}}\right),gas} = \left(\frac{E_{A\,(\overline{C_{in_{eq}}})}}{2}\right)^2 + \left(\frac{U_{INS\,(\overline{C_{in_{eq}}})}}{2}\right)^2 + 2\left(\frac{U_{SM\,(\overline{C_{in_{eq}}})}}{2}\right)^2 + \left(\frac{E_{A\,(C_{ambient})}}{2}\right)^2 + \left(\frac{U_{INS\,(C_{ambient})}}{2}\right)^2 + 2\left(\frac{U_{SM\,(C_{ambient})}}{2}\right)^2 + (\sigma)^2 \quad \text{(Eq. 5)}$$

Where $E_{A\,(C)}$ represents the drift of accuracy of the mass spectrometer between two calibrations, with respect for each measured concentration value.

$U_{INS\,(C)}$ is the uncertainty associated with the instrumentation used for measuring *C*, ie that of the spectrometer-acquisition-software unit; it is fixed at 4%.

$U_{SM\ (C)}$ is the uncertainty associated with standard mixtures used in the measurement of concentration *C*; it is fixed at 2% by the supplier.

σ is the dispersion of the concentration from the mean value.

The main sources of uncertainties to be considered when measuring aerosol concentration of an air / particles mixture are generally due to the measurement instrumentation (fluorimeter and sampling pump), the ambient environment and the volume of sample to be analyzed. The uncertainty $U_{\left(\Delta C_{int_{eq}}\right),aerosol}$ related to aerosol is as follows (Eq. 6):

$$U_{\left(\Delta C_{int_{eq}}\right),aerosol} = \left(\frac{U_{fluorimeter(\overline{C_{int_{eq}}})}}{2}\right)^2 + \left(\frac{U_{dilution\ volume(\overline{C_{int_{eq}}})}}{2}\right)^2 + \left(\frac{U_{sampling\ pump\ volume(\overline{C_{int_{eq}}})}}{2}\right)^2 + \left(\frac{U_{fluorimeter(C_{ambient})}}{2}\right)^2 + \left(\frac{U_{dilution\ volume(C_{ambient})}}{2}\right)^2 + \left(\frac{U_{sampling\ pump\ volume(C_{ambient})}}{2}\right)^2 + (\sigma)^2 \quad \text{(Eq. 6)}$$

$U_{fluorimeter(\overline{C_{int_{eq}}})}$ is related to the uncertainty given by the fluorimeter for each sampler.

$U_{dilution\ volume(\overline{C_{int_{eq}}})}$ is the uncertainty related to the dilution of sampled mass in a volume of ammonia water.

$U_{sampling\ pump\ volume(\overline{C_{int_{eq}}})}$ is the uncertainty that refers to the piston pump used in our experiments to sample the mixture (air/particles).

σ corresponds to the dispersion of the value on each filter sampler from the mean value

The same terms are used to determine the larger relative uncertainty related to the measurement of the helium concentration at the opening $\Delta C_{out_{eq}}$ for gas and aerosol.

2.2. Determination of the uncertainties related to the ratio V_{dist}/U_{ope}

Likewise, the expanded relative uncertainty related to the determination of the ratio V_{dist}/U_{ope}, expressed with a widening coefficient K_e = 2, is as follows (Eq. 7):

$$U_{r(Vdist/U_{ope})} = \pm 2\sqrt{\left(\frac{U_{r\,(U_{ope})}}{2}\right)^2 + \left(\frac{U_{r\,(Vdist)}}{2}\right)^2} \quad \text{(Eq. 7)}$$

U_{ope} is determined from the extraction rate of the enclosure $Q_{extraction}$ by means of the gas tracing technique.

The expanded relative uncertainty $U_{r(U_{ope})}$ is therefore equal to the relative larger uncertainty of the extraction rate that depends of q_0 and $\Delta C_{in_{eq}}$.

$U_{r(U_{ope})}$ is given by Eq. 8. The relative uncertainty of the helium injection flow meter used $U_{r(q_0)}$ is 0.53%.

$$U_{r(U_{ope})} = \pm 2\sqrt{\left(\frac{U_{r\,(q_0)}}{2}\right)^2 + \left(\frac{U_{r\,(\Delta C_{in_{eq}},gas)}}{2}\right)^2} \quad \text{(Eq. 8)}$$

The absolute uncertainty $U_{a\,(Vdist)}$ on the measured velocity V_{dist} by the hot-wire anemometer is provided by the manufacturer by Eq. 9:

$$U_{a\,(Vdist)} = 0.0087\ V_{dist} + 0.051 \quad \text{(Eq. 9)}$$

The relative uncertainty $U_{r\,(Vdist)}$ can be deduced by Eq. 10.

$$U_{r\,(Vdist)} = \frac{U_{a\,(Vdist)}}{Vdist} \quad \text{(Eq. 10)}$$

For our studied disturbing velocities V_{dist}, $U_{r\,(V)}$ varies between 1.5% and 5%.

Appendix 3. Simulation sensitivity of the backflow coefficient K (%)

We aimed to check the sensitivity of the local backflow coefficient K (%) with the samplers positions and numbers near the opening. For this, we performed the following tests.

3.1. Sensitivity of the backflow coefficient with the samplers positions

In our experiments, many filters of DN40 are placed around the opening to sample the particles coming from the backflow outside the enclosure. Simultaneously the gas were sampled near the pumps connected to these filters. In order to take that into consideration in our simulations, we added five discs samplers of a diameter of 40 mm around the opening and we varied their locations:

Position 1: we added 4 discs in the up, down, right and left sides at 0,5 cm from the opening and 1 disc at 4.5 cm facing the opening. This position corresponds to our experimental conditions and is very close to the punctual samplers.

Position 2: we added 4 discs in the up, down, right and left sides at 1 cm from the opening and 1 disc at 5,5 cm facing the opening.

Position 3: we added 4 discs in the up, down, right and left sides at 4 cm from the opening and 1 disc at 8 cm facing the opening.

Position 4: we added 4 discs in the up, down, right and left sides at 6 cm from the opening and 1 disc at 10 cm facing the opening.

Figure 0-10 shows the locations in side view of these samplers around the opening in positions 1 and 4 that are used in our simulations. Figure 0-11 shows the particles mass concentration at the five discs samplers near the opening for the position 1, hence as in our experimental conditions.

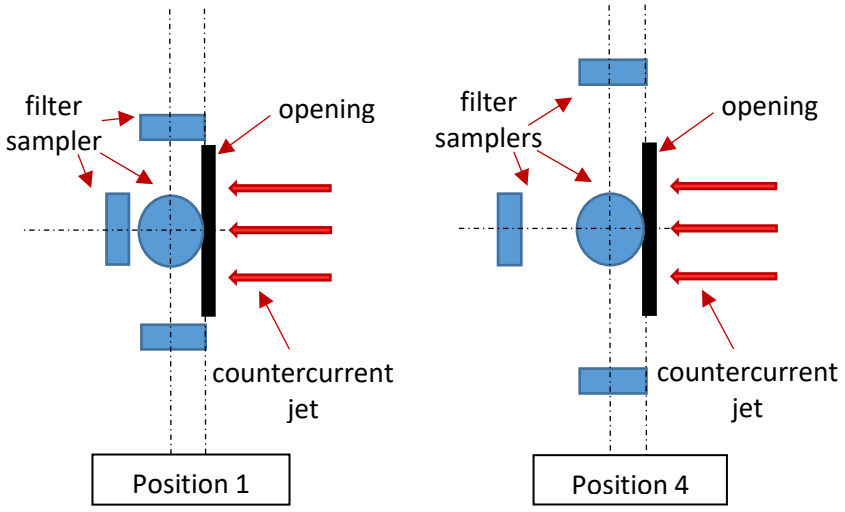

Figure 0-10 Schemes of the filter samplers near the opening used for our simulations in positions 1 and 4 (side views)

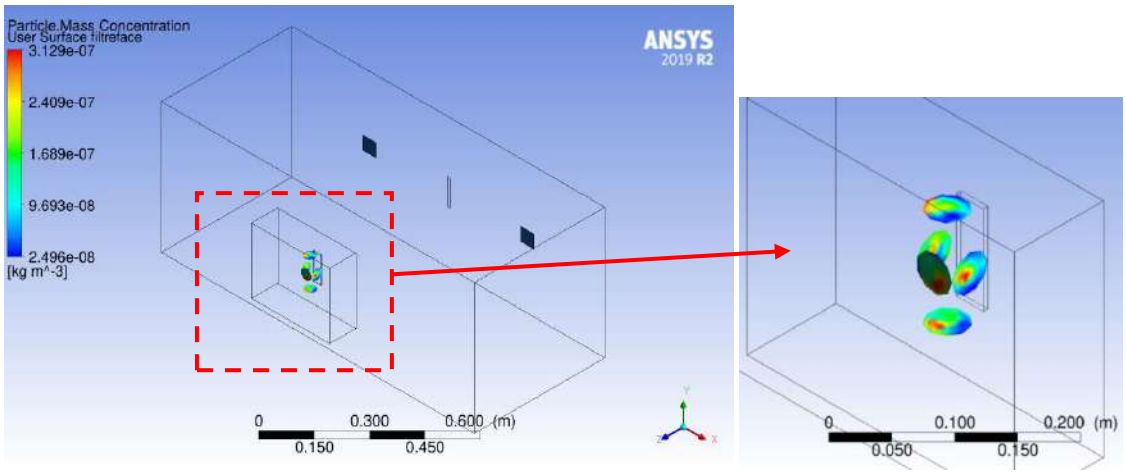

Figure 0-11 Particles mass concentration at the five discs samplers near the opening

Based on our SST-DES numerical simulations, we calculate the mean value of the particles concentrations on these discs that corresponds to $C_{out-aerosol}$ for each position. Then, we can deduce their corresponding particulate backflow coefficients *K* (%). Figure 0-12 shows the curves of the particulate backflow coefficient *K* (%) versus V_0/U_{ope} calculated through the punctual samplers near the opening, then with the 5 discs samplers located at positions 1, 2, 3 and 4.

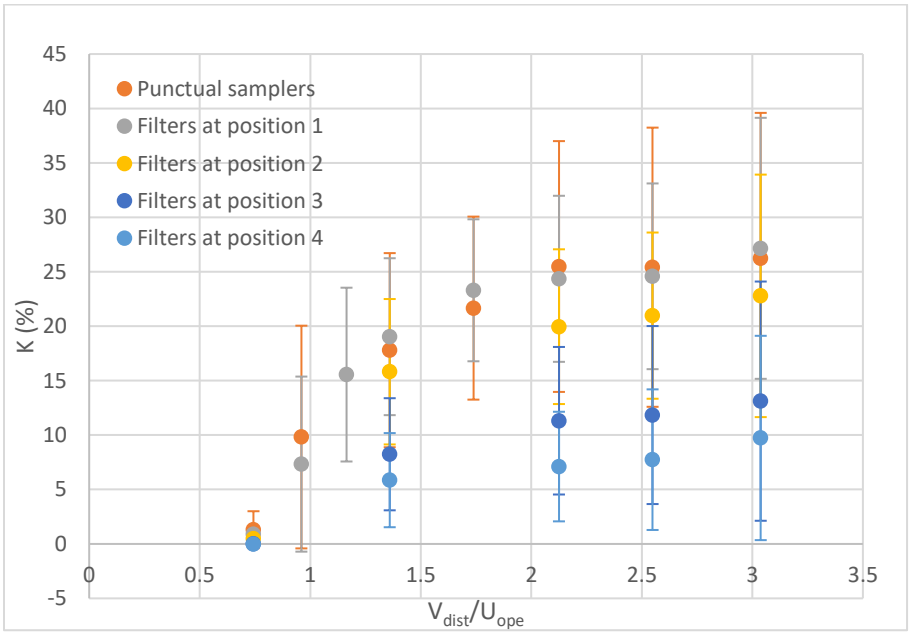

Figure 0-12 Evolution of the particulate backflow coefficient K(%) as a function of V_{dist}/U_{ope} calculated through the punctual samplers then at the 5 discs at 4 positions near the opening

As we can see in Figure 0-12, all curves have a global increasing trend and reach a constant value for V_{dist}/U_{ope}=2. By comparing the curves between them, we observe that the curves corresponding to the punctual samplers and filters in position 1 are at the same order of magnitude. This is normal since filters in position 1 were added close to the punctual samplers. However, once we move away from the punctual samplers in position 2, the backflow coefficients are lower than those corresponding to the punctual

samplers. Moving farther in positions 3 and 4, the backflow coefficient decrease significantly. For the case of position 4, the backflow coefficient is about three times lower than those of position 1.

Then, the distance of the samplers to the opening does influence the particulate backflow coefficient. Indeed since the backflow coefficient depends on the concentration measured at the filters, once they move away from the opening this concentration decreases due to dilution and then the backflow coefficient decreases. Simultaneously the variations of the backflow coefficient are important when varying the samplers positions of only few centimeters due to the small dimensions of the opening of $(0.1 \times 0.01)\ m^2$.

We should mention that in our preliminary experiments, the filters were positioned far from the punctual samplers near the opening (position 3). Then we relocated them near the punctual samplers (position 1) in order to be coherent between the gaseous and the particulate pollutants. After that we performed the sampling of gas at the pump connected to the particulate samplers in order to compare the gas and particulate results adequately.

3.2. Sensitivity of the backflow coefficient with the sampler numbers:

We aim to check the sensitivity of the backflow coefficient in response to the number of samplers placed near the opening. In our experimental works, we start by adding 5 filters near the opening. After that and in order to simplify our experiments, we just leave 3 filters near the opening in the following locations according to the opening: left side, down side and facing side. These locations were chosen based on the maximum concentrations detected on these filters in comparison with the other two locations (top and right sides).

First of all, we checked numerically the aerosol mean concentration on each sampler location normalized by the concentration of the sampler facing the opening for an inflow velocity U_{ope} = 0.5 m/s and a countercurrent disturbing jet corresponding to V_0 = 10 m/s in Figure 0-13.

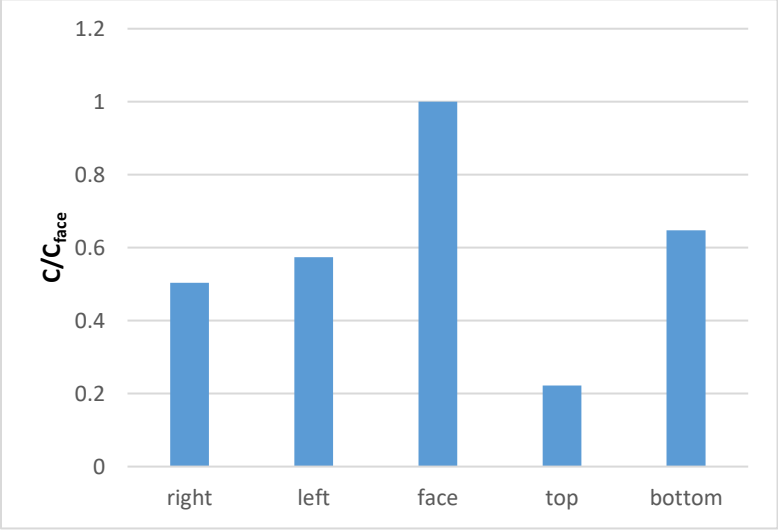

Figure 0-13 Sampler mean concentration over the concentration of the sampler facing the opening for each sampler location for U_{ope} = 0.5 m/s and V_0 = 10 m/s

As we see in Figure 0-13, the sampler facing the opening has the maximum mean concentration. Then the samplers at the bottom, left and right locations have comparable values. The sampler at the top of the opening has a minimum mean concentration value. It is normal that the sampler facing the opening has the maximum mean concentration since the type of the disturbing jet is countercurrent facing the opening. The mean concentration on each location also depends on the velocity of the countercurrent disturbing jet, but the sampler facing the opening has the maximum mean concentration for all calculated disturbing jet velocities. We should also mention that the gas behavior on these locations was similar to the aerosol behavior.

We decide to calculate the particulate backflow coefficient *K* (%) in three cases as shown in Figure 0-14:

Case 1: using the mean concentration detected on the sampler facing the opening since it was the sampler that corresponds to the maximum mean concentration.

Case 2: using the mean concentration detected on three locations based on our experimental locations: left, bottom and facing sides.

Case 3: using the mean concentration detected on five filters locations: left, right, top, bottom and facing sides.

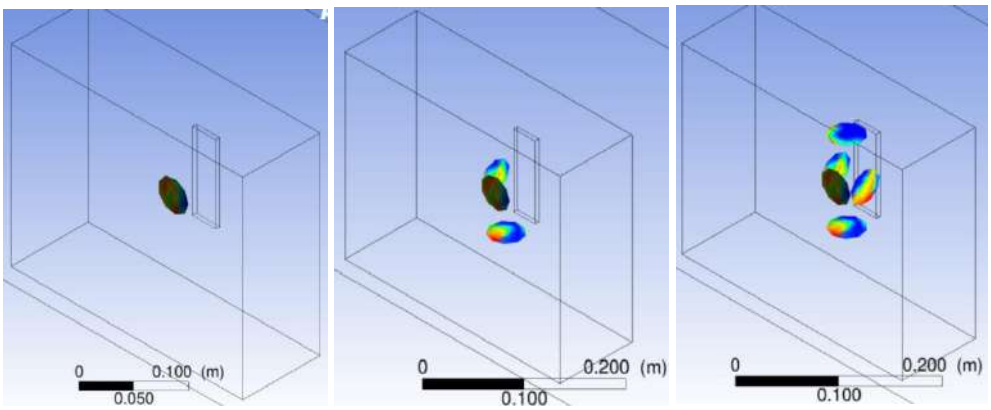

Figure 0-14 Circular samplers added near the opening for each case. Rrom left to right: 1 sampler, 3 samplers and 5 samplers

Figure 0-15 shows the evolution of the particulate backflow coefficient *K* (%) as a function of V_{dist}/U_{ope} calculated in each case: through 1 filter, 3 filters and 5 filters placed near the opening.

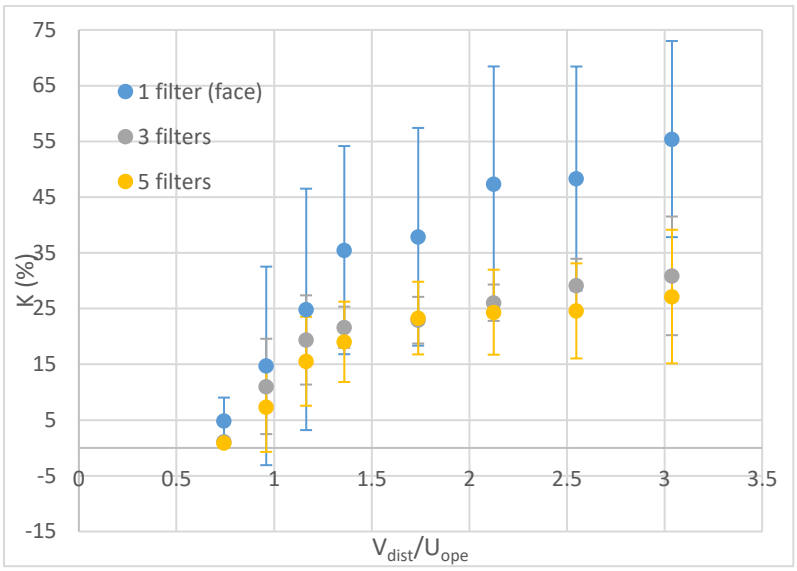

Figure 0-15 Evolution of the particulate backflow coefficient K (%) as a function of V_{dist}/U_{ope} calculated through 1 filter, 3 filters and 5 filters placed near the opening

As we see in Figure 0-15, the backflow coefficient calculated on one filter facing the opening has the maximum values. The backflow coefficient calculated through the three filters is a little bit higher than that calculated through the five filter. However the values of the backflow coefficient calculated on one filter facing the opening are about the double of those calculated using three or five filters. For the case where there is three or five filter, the concentrations of aerosol measured away from the front of the opening dilute the total mean concentration and then the backflow coefficients on three or five samplers have a values lower than that on one filter facing the opening.

Appendix 4. Feasibility study of the Background Oriented Schlieren (BOS) technique

In this appendix, we introduce the state of art of an optical technique to visualize density gradient of a gaseous tracer: the Background Oriented Schlieren (BOS). We detail first the procedure and different equipment needed to perform the experiment. Then we show tests done on a circular helium jet to check the feasibility of BOS, with its post-processing. Finally, we describe some results obtained on our experimental enclosure.

4.1. State of the art

The necessity to study the dynamics of gaseous systems by non-intrusive techniques requires the development of new concentration measurements techniques. Conventional techniques such as sampling probes or mass-spectrometer are considered as intrusive method since they need to be present inside the flow, which will affect the flow characteristics. In contrast, the optical methods are preferred since they do not perturb the flow. Optical visualization techniques have been developed over the last decades, such as Schlieren, shadowgraphy, interferometry and others. These techniques detect the deflection of the light rays while passing through regions with refractive index inhomogeneities (SETTLES, 2001), (TANDA & DEVIA, 1998). These differences in the fluid refractive index will allow the measurements of density variations and give qualitative information of the density distribution (SETTLES , 2001). Note that Schlieren technique provides information about the first derivative of density, while the shadowgraph provides information about the second derivative. Due to extreme requirements of their optical components, these techniques are usually used for studying small-or medium-sized fields of view and are less feasible for large- or full-scale application (RICHARD & RAFFEL, 2001). There is a need to find a method that provides quantitative information on the density distribution, without sophisticated optical equipment, and that can be applied on large scale applications.

The progress in digital image processing allows the creation of synthetic Schlieren method such as Background Oriented Schlieren (BOS). BOS is a visualization technique that provides qualitative and quantitative information on the density gradients, within a simple system, and is adaptive for large scale domains. It permits to obtain the spatial distribution of the density of a fluid that is related to variations of the refractive index. This technique is well described by Raffel and Richard (RICHARD & RAFFEL, 2001), (RAFFEL, 2015) and is sensitive to pressure, temperature and density gradients.

4.1.1. Theory

As we mentioned before, the simple implementation and procedure characterize this method: it requires the presence of a light source, a reference image, the density gradient fluid and the acquisition system (CCD camera and computer) as shown in Figure 0-16.

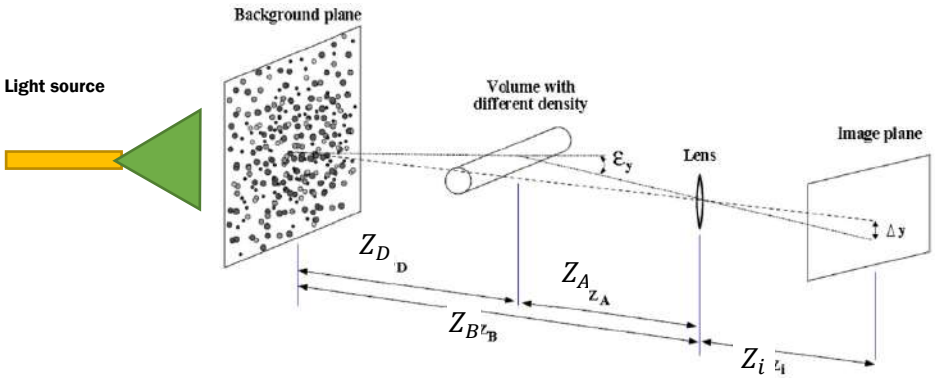

Figure 0-16 Scheme of the optical setup for BOS technique (RICHARD & RAFFEL, 2001)

The theory of this technique depends on variation of the refraction index due to presence of a variable density fluid domain. Then the light beam trajectory coming from the light source will be deflected while passing through the variable density fluid domain, and this deflection is related to spatial gradient of the refractive index along the line of sight. Assuming paraxial recording and small deflection angles ($\varepsilon_y \approx \tan \varepsilon_y$), we can write a formula for the image displacement *Δy* (DALZIEL, HUGHES, & SUTHERLAND, 2000):

$$\Delta y = Z_D \, M \, \varepsilon_y \tag{4.1}$$

with $M = Z_i/Z_B$ is a magnification factor of the background, Z_i tis he distance between lens and the image plane, Z_B is the distance between the background plane and lens, Z_D is the distance between the dot pattern and the density gradient, and ε_y is the deflection angle defined by:

$$\varepsilon_y = \frac{1}{n_0} \int \frac{\partial n}{\partial_y} \mathrm{d}z \tag{4.2}$$

The image displacement *Δy* can thus be rewritten as:

$$\Delta y = f\left(\frac{Z_D}{Z_D + Z_A - f}\right)\varepsilon_y \tag{4.3}$$

with Z_A the distance from the lens to the object and f the focal length of the lens.

The refractive index, *n*, is related to the density variations of the fluid by the Gladstone-Dale relation for gaseous media:

$n = G.\rho + 1$ (RICHARD & RAFFEL, 2001), (RAFFEL, 2015) (4.4)

where *G* is the Gladstone-Dale constant.

BOS technique is applied on axisymmetric fluid geometries as well as on non-axisymmetric geometries.

For general fluid geometry, density is related to the displacement by Poisson equation (TIPNIS, 2013):

$$\frac{\partial^2}{\partial x^2}\rho(x,y) + \frac{\partial^2}{\partial y^2}\rho(x,y) = S(x,y) \tag{4.5}$$

where S(x,y) is the source term of the observed displacements.

The final expression of density field can be written in the form (ZNAMENSKAYA, 2012):

$$\frac{\partial^2 \rho}{\partial a^2} + \frac{\partial^2 \rho}{\partial b^2} = -\frac{2R_b R_o}{Gh(2L_b + h)}\left(\frac{\partial p_x}{\partial a} + \frac{\partial p_y}{\partial b}\right) \tag{4.6}$$

where R_b and $R_o$correspond to one pixel size in the background plane and in the phase object plane, $a=x/R_o$ and $b=y/R_o$ are coordinates in image measured in pixels, p_x and p_y are displacement components, also measured in pixels, h is the thickness of the density gradient domain, L_b is the distance from the density gradient domain to the background plate.

We need to solve the equation (4.6) above to obtain the quantitative density field of the flow. Boundary conditions (Dirichlet or Neumann) should be imposed to solve the second order partial differential equation (PDE). This is considered as limitions of this technique, since boundary conditions of the domain under-investigation are not all well known. However, a calibration that relates the displacement vectors to fluid density could be applied to recalculate the density field in a general geometry fluid.

For axisymmetric fluid geometry as jets, density field can be calculated using geometric fluid conditions. The refractive index can be calculated by the following relation (DUBOIS, 2008):

$$n(r) = n_a\left(1 - \frac{1}{\pi}\int_r^{d/2} \frac{\varepsilon_y}{\sqrt{y^2 - r^2}} dy\right) \tag{4.7}$$

Then, density gradient can be deduced using the Gladstone-Dale equation.

A suitable post-processing that relates the obtained density to concentration, temperature or pressure could be then applied to obtain these parameters.

4.1.2. Setup

As shown in figure 4-1, this method requires presence of a light source (halogen lamp), a reference image (random dot pattern with high spatial frequency), a fluid (with density gradient) and an acquisition system (CCD camera and computer).

In literature, the light source used is usually a halogen lamp that does not generate a temperature gradient, since this method is sensitive to temperature gradient. Reference image corresponds usually to an A4 black paper, on which fine and randomly white dots patterns are printed. This paper is then attached to a transparent Plexiglas to eliminate the paper vibrations. The fluid thickness should be very small compared to distance between the background and the fluid, and that between the fluid and the camera. A camera with a CCD sensor is recommended for a better image resolution (HAIN, KAHLER, & TROPEA, 2007). A computer is required to acquire and post process the images. An image correlation procedure is performed using standard computerized algorithms (usually PIV algorithms).

A source light is applied behind the background pattern. The imaging system should be focused on the background for better contrast. Recording is performed as follows: first, a reference image of randomly dot pattern is recorded through air (without injected gas). Then, during injection of the gas, another image is taken. The presence of density gradients represented by the fluid between the camera and the

background area deviates light beams from their initial trajectory. This will displace patterns positions recorded by the CCD sensor and will create a shift between the reference image and those recorded with the fluid. To obtain these virtual local displacements, both images are correlated via a standard image correlation algorithm (computerized PIV algorithms). The calculated displacements fields are proportional to integral density gradient in the observed area.

Distance between background and fluid is smaller than that between fluid and camera but in the same order of magnitude. The typical size of an individual dot pattern in the background image is in the order of 3-5 pixels. Best resolution for an individual dot pattern size is of 2-3 pixels (KLINGE, 2001). Conventional cameras can be used, and a PIV algorithm can be used for the correlation. BOS image displacements are usually smaller than that of PIV, which leads to higher accuracy, but to measurements errors larger than that obtained from PIV (2-3% for BOS and 1% for PIV) (ELSINGA, OUDHEUSDEN, SCARANO, & WATT, 2004), (VINNICHENKO, 2012).

4.1.3. BOS applications in literature

BOS is being used in a variety of flow applications, due to its simple setup and its accurate results. It leads to a quantitative results for axisymmetric geometry: determination of density fields of helium circular axisymmetric jets (DUBOIS, 2008) as shown in Figure 0-17(left), supersonic rectangular axisymmetric free jets (TIPNIS, 2013) as shown in Figure 0-17(right) and supersonic cone-cylinder model (VENKATAKRISHNAN, 2004) as well as concentration measurements of hydrogen round jets (KOTCHOURKO, 2013), (KESSLER). Figure 0-17 (right) shows displacement vectors for development of a vertical axisymmetric helium jet and normalized density contours for a horizontal axisymmetric rectangular jet obtained by the BOS technique.

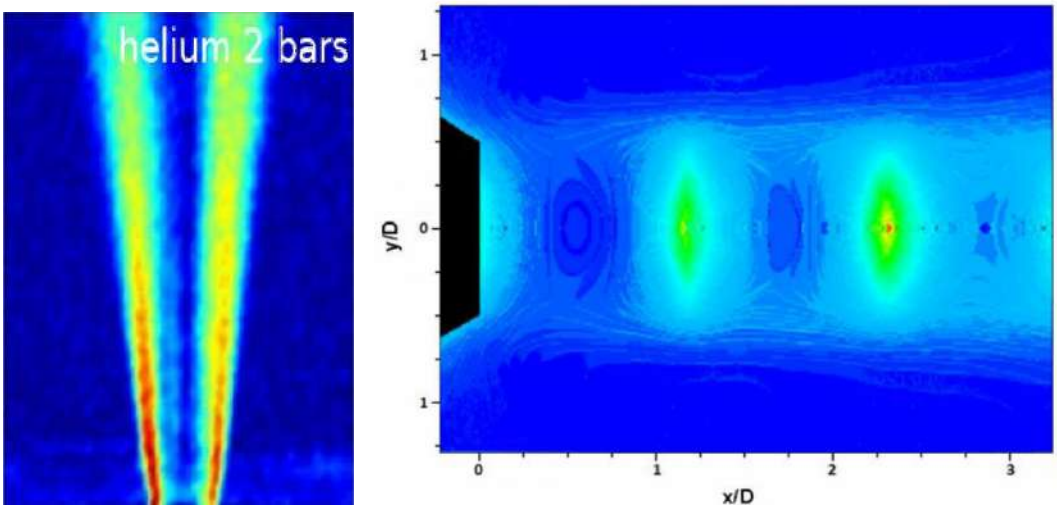

Figure 0-17 (left): Displacement vector module maps for development of a helium jet for a pressure of 2 bars (DUBOIS, 2008) – (right): Normalized density contours for the rectangular axisymmetric nozzle jet obtained by BOS measurements (TIPNIS, 2013)

Figure 0-18 shows displacement vector map of development of an axisymmetric hydrogen jet obtained by BOS technique and corresponding displacement values.

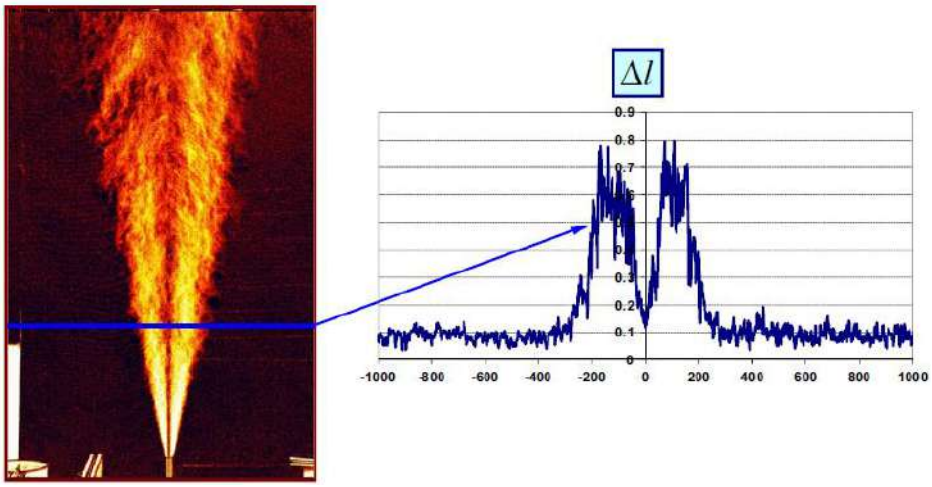

Figure 0-18 Typical BOS image (left) and the displacement data (right) for a one z-elevation for the development of an axisymmetric hydrogen jet (KOTCHOURKO, 2013)

BOS is also useful to study convective heat transfer of flow (RAJSHEKHAR, 2018) such as in a cryogenic wind tunnel environment (STADLER, 2016). It has been used also for gas leakage detection (TING, 2013). Due to its large scale application, it is used in aeronautic industry to perform full scale flow visualization (SETTLES, 1995), aeronautics NASA's tests for jet-surface interactions (CLEM, 2013) and a full-scale helicopter vortex flow characterization (DALZIEL, HUGHES, & SUTHERLAND, 2000), (RAFFEL, TUNG, RICHARD, YU, & MEIER, 2000). Figure 0-19 shows a typical BOS application on the aerodynamic industry tested by NASA on a helicopter during its flight. Obtained displacement fields indicate different density lines due to movement of the helicopter, hence on large scale measurements.

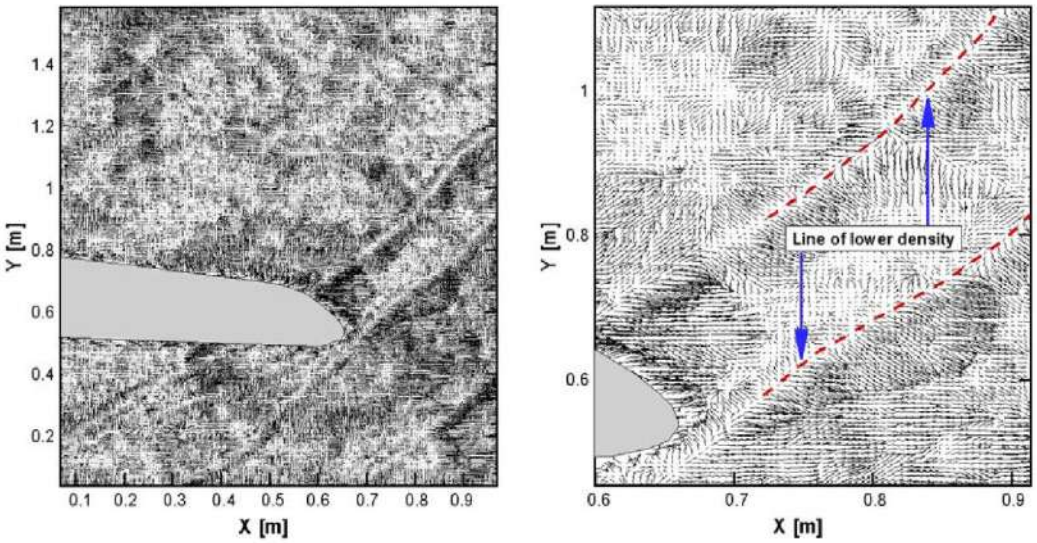

Figure 0-19 Displacement field proportional to density gradients tested by NASA on a helicopter during a flight (RICHARD & RAFFEL, 2001)

In addition, this technique was applied to visualize supersonic flows (COSI, 2015), to measure density gradient in shock waves (HAYASAKA, 2016), (ZNAMENSKAYA, 2012) and to obtain a full-field density measurement of transparent liquids in a stratified fluid (VERSO, 2015). BOS could also be used to characterize 3D density fields (SRIVASTAVA, 2013), (GOLDHEN, 2007).

4.2. Our preliminary tests on a circular helium jet

4.2.1. Setup

To test the feasibility of background Schlieren technique (BOS) on our experimental conditions, we performed some preliminary tests to visualize fluid density gradient of an helium jet. Figure 0-20 shows preliminary experimental setup. It consists of a light source (torch then halogen lamp), a background (target), a camera and a density gradient (helium jet) of a 1 cm circular diameter.

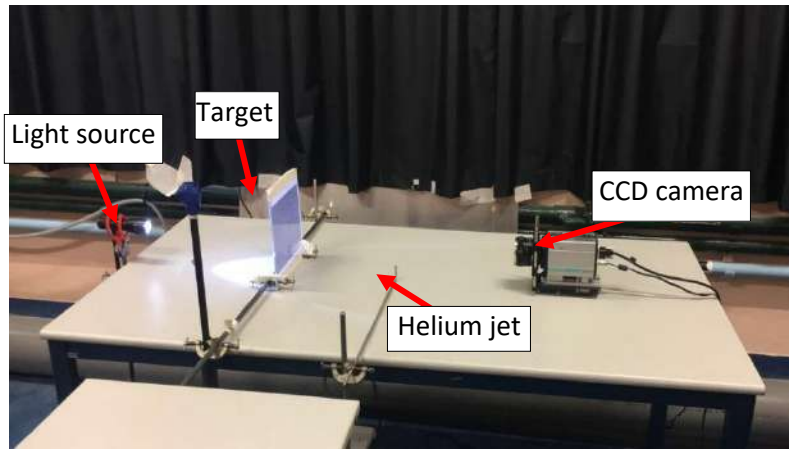

Figure 0-20 Preliminary tests apparatus on a jet of helium

A halogen lamp is used: Knightsbridge LED projector 60 LED, with a power of 30 W and dimensions of (154 x 181 x 112) mm^3. The background is an A4 white paper, on which a randomly black dots are printed using a Matlab program. This paper is fixed on a Plexiglas® plane screen. The fluid is helium that is injected through a metallic cylinder of 8 mm diameter. The camera is CCD Zyla with an objective of 200 mm. The field of view of camera is approximately (5 x 4.5) cm^2. A post processing is performed on Dynamic Studio software provided by Dantec Company for PIV correlation or via MatLab. Distance between the light source and the background is 60 cm, between the background and the jet is 50 cm and that between the jet and the lens is 50 cm. Helium is injected vertically or horizontally by switching the jet position.

4.2.2. Some results

The images acquisition and post processing procedure are shown in Figure 0-21. First, we take an image of the background without injection of helium jet; then we inject helium and we take a second image with helium jet (image (a)). A correlation of both images using Dantec software gives us displacement field which is proportional to the index gradient (image (b)). An adequate post processing using MatLab to solve the second order Poisson equation and the Gladstone-Dale equation gives us the density field, and then the concentration field (image (c)). However, boundary conditions (Dirichlet or Neumann type) are mandatory and should be imposed to solve the second order PDE, and they are not all known in our case. In Figure 0-21, arbitrary boundary conditions (for air) are imposed to calculate the concentration field.

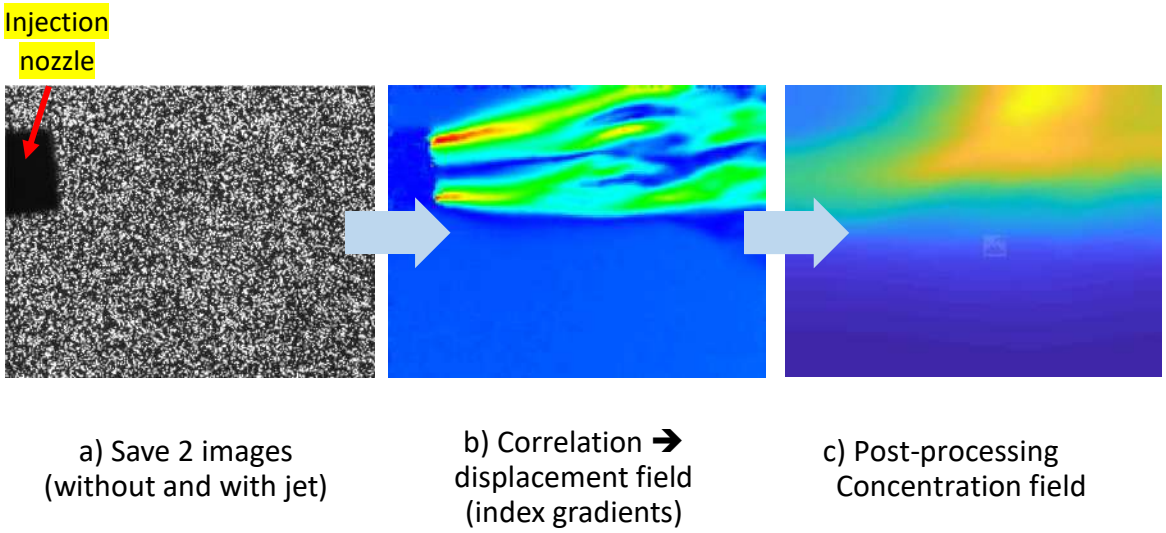

Figure 0-21 Procedure of images acquisition and post processing for a pure helium circular jet of 1 cm diameter

4.2.3. Results

Preliminary tests are performed respectively on circular and rectangular helium jets of 1 cm hydraulic diameter. For each case, density gradient was calculated by the software. As seen in Figure 0-21, this method allows detection and the reconstruction of the helium jet.

We tested successively many helium concentrations: 100%, 10%, 5%, 0.1 % (1000 ppm.v) and 0.01% (100 ppm.v). After applying the correlation on images ((a), (b) and (c) procedure), we detected low concentrations of helium around 100 ppm.

Then, we tried to solve the second order equation presented above to calculate density field. However, the necessity of imposing boundary conditions constitutes the limitations of this technique, since we do not have the value of density presented in boundaries of the domain. However, after imposing same arbitrary boundary conditions (air density) for different helium injected concentrations, we can see that calculated density field is proportional to the injected helium concentration as shown in Figure 0-22.

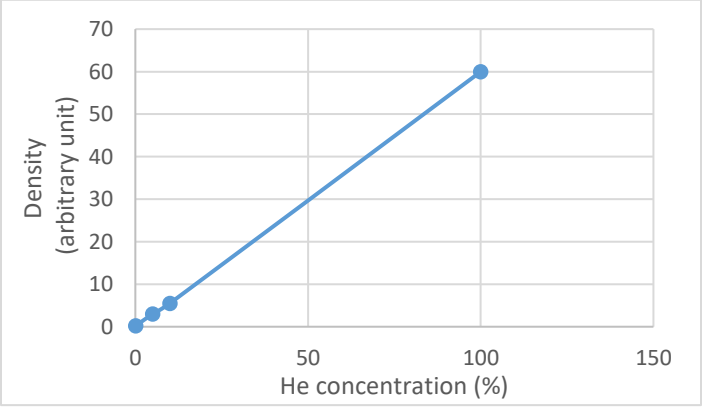

Figure 0-22 Evolution of calculated density as a function of helium concentration

Figure 0-23 shows results obtained in a transparent cell we have dimensioned. A transparent Plexiglas® cell was built in which helium was injected during acquisition. Inside the cell, helium concentration is homogeneous; then as we see in figure there is no density gradient variation inside the cell. However, the cell was not completely sealed. So as we see in this figure, some amount of helium escaped from cell and is presented by density gradients variations detected around cell. Therefore, we observe in this experiment that the amount of backflowed helium is well visualized by this technique.

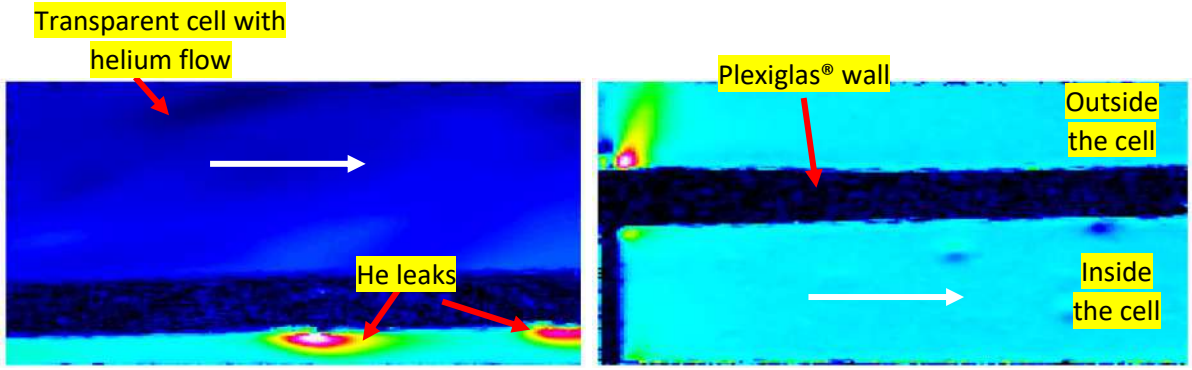

Figure 0-23 Visualization of backflow of helium from a rectangular cell

4.3. Preliminary experiments on the experimental enclosure

4.3.1. Description of the experiment

We performed some tests on the real enclosure to check the feasibility of BOS technique, applied to gas backflow visualization.

As seen in Figure 0-24, a camera, a background screen and a light source (halogen lamp) are easily implemented on the system to follow the backflowed helium which it is likely to be present at the opening in the case where a countercurrent internal jet of helium is imposed in the enclosure. Therefore, vertical plan normal to the opening represents the location of fluid density gradient. The camera has an objective of 50 mm. The camera field of view was (11 x 10) cm^2. The opening was located at 50 cm from the background and 50 cm from the camera.

We performed acquisition during various aeraulic flowrates disturbances, to visualize the gaseous backflow from the opening and then to evaluate the response.

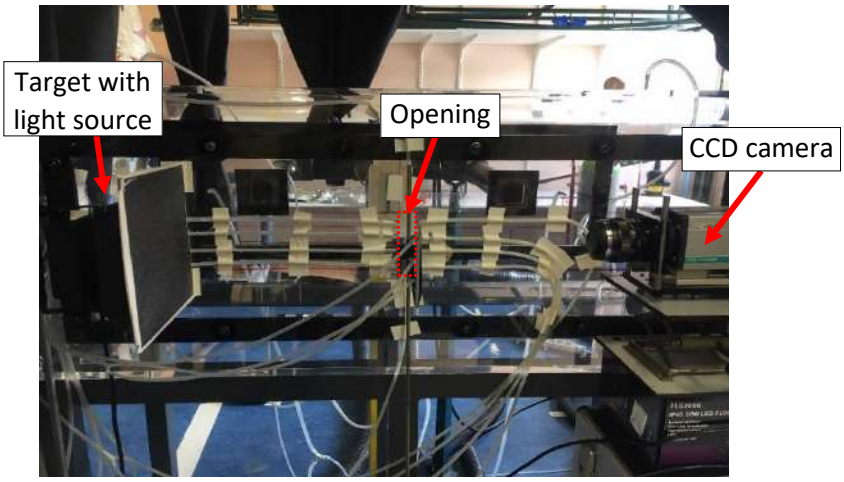

Figure 0-24 Implementation of BOS equipment near the opening of the enclosure

4.3.2. The post-processing

A post-processing of images acquired near the enclosure opening gives density gradient fields presented in Figure 0-25. Colors of the density gradients in the figure vary from blue for low density gradients to red for higher density gradients. The non-uniformities of density gradients in results indicate a presence of helium near the opening, hence a presence of the backflow. The form and intensity of density gradient varies according to the rate of the disturbance imposed.

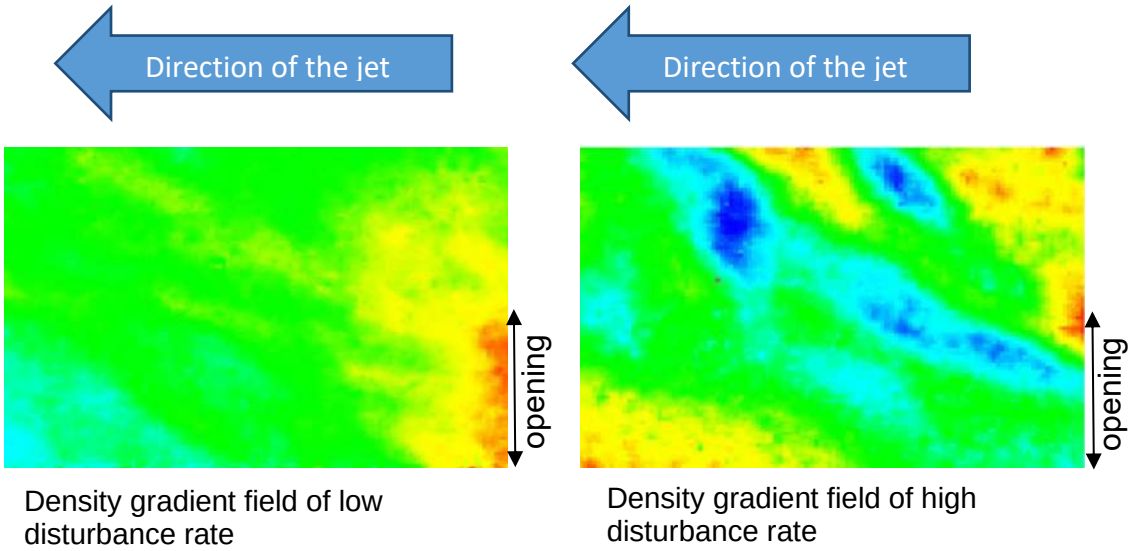

Figure 0-25 Visualization of the density gradients resulting near the opening in the case of an internal counter-current disturbance

In conclusion, we showed qualitatively the feasibility of BOS application in our study to detect and then examine the helium concentration profile near the opening based on density gradient variations. In order to quantify helium concentration, we did not have access on the values of boundary conditions near the opening, which are considered as limitation of this technique. However, additional works should be done

further using this technique in order to find a way to quantify the gas concentrations. We should also mention that in order to improve the resolution of this technique, we ordered a target consisting of black background made of glass with white dots containing a light source in place of the A4 paper. However due to covid-restrictions, the order arrived very late and we did not have enough time to perform BOS tests using this new target.

References

Clem. (2013). Background Oriented Schlieren Implementation in a Jet-Surface Interaction Test.

Cosi. (2015). Development of a background-oriented schlieren technique with telecentric lenses for supersonic flow.

Dalziel, S., Hughes, G., & Sutherland, B. (2000). Whole-field density measurements by 'synthetic schlieren' . *Exp. Fluids*, 28 322-35.

Dubois. (2008). Étude de jets sous-détendus axisymétriques d'air et d'hélium par la méthode BOS.

Hayasaka. (2016). Optical-flow-based background-oriented schlieren technique for measuring a laser-induced underwater shock wave.

Elsinga, G., Oudheusden, B. V., Scarano, F., & Watt, D. (2004). Assessment and application of quantitative schlieren methods: calibrated color schlieren and background oriented schlieren. *Exp. Fluids*, 36(2):309-325.

Goldhen. (2007). The background oriented schlieren technique: sensitivity, accuracy, resolution and application to a three-dimensional density field.

Hain, R., Kahler, C., & Tropea, C. (2007). Comparison of ccd, cmos and intensified cameras. . *Exp. in Fluids*, 403-411. 71.

Kessler. (s.d.). Hydrogen detection: visualisation of hydrogen using non invasive optical schlieren technique BOS.

Klinge, F. (2001). Investigation of Background Oriented Schlieren (BOS) towards a quantitative Density Measurement System. Brusseles: Project report VKI.

Kotchourko. (2013). Concentration measurements in a round hydrogen jet using Background Oriented Schlieren (BOS) technique.

Raffel, M. (2015). Background-oriented schlieren (BOS) techniques. *Exp. Fluids*, 56:60.

Rajshekhar. (2018). Multi-scale approach for analyzing convective heat transfer flow in background-oriented Schlieren technique.

Richard, H., & Raffel, M. (2001). Principal and applications of the background oriented schlieren method. . *Meas. Sci. Technol.*, 12:1576-1585.

Settles. (1995). Full-Scale Schlieren Flow Visualization.

Settles, G. (2001). Schlieren and shadowgraph techniques : visualizing phenomena in transparent media. *Springer*.

Srivastava. (2013). Development and application of color schlieren technique for investigation of three-dimensional concentration field.

Stadler. (2016). On the influence of wind on cavity receivers for solar power towers: Flow visualisation by means of background oriented schlieren imaging.

Tanda, G., & Devia, F. (1998). Application of a schlieren technique to heat transfer measurements in free-convection. *Exp. Fluids*, 24:285-290.

Ting, C.-C. (2013). Detection of gas leakage using microcolor schlieren technique.

Tipnis. (2013). Density Measurements for Rectangular Free Jets using Background-Oriented Schlieren

Venkatakrishnan. (2004). Density measurements using the Background Oriented Schlieren technique.

Verso. (2015). Background Oriented Schlieren in a Density StratifiedFluid.

Vinnichenko. (2012). Accuracy of background oriented schlieren for different background patterns and means of refraction index reconstruction.

Znamenskaya. (2012). Quantitative measurements of the density gradient on the flat shock wave by means of background oriented schlieren.

References

Ameur, A. (1983). *La vantilation d'un local nucléaire : modélisation, validation expérimentale, conséquences.* Saclay: Thèse de l'Institut National des Sciences et Techniques Nucléaires.

ANSYS, I. (2020). Dans *ANSYS CFX-Solver Theory Guide.*

AREVA. (2012). *Principes de conception des sas de confinement pour les opérations de démantèlement.* Note technique d'AREVA.

Areva. (2012). *Principes de conception des sas de confinement pour les opérations de démantèlement. Note technique d'AREVA.*

Bai, Y., & Jin, W.-L. (2016). Chapter 49 - Explosion and Fire Response Analysis for FPSO. Dans *Marine Structural Design (Second Edition)* (pp. Pages 907-938).

Balachandar, S., & Eaton, K. (2010). Turbulent Dispersed Multiphase Flow. *Annu. Rev. Fluid Mech.* , 111–33.

Berne, P. (1997). *Quelques réflexions sur les phénomènes de rétrodiffusion dans les systèmes de confinement dynamique.* Grenoble: Note technique, CEA.

Boussinesq, J. (1877). Théorie de l'écoulement tourbillant - Mem. Présentés par Divers Savants. *Acad. Sci. Inst. Fr*, 23(46-50), 6-5.

Burton, T., & Eaton, J. (2005). Fully resolved simulations of particle-turbulence interaction. *J. Fluid Mech.*, 545:67–111.

Carrier, G. (1958). Shock waves in a dusty gas. *J. Fluid Mech.*, 4:376–82.

CEA. (2011). *Critères de réception du confinement dynamique des sas d'intervention en vinyle pour les opérations d'assainissement et de démantèlement.* Note technique CEA.

Charuau, J. (1982). *Etude du dépôt des particules dans les conduits. Optimisation des tubes de prélèvement des aérosols radioactifs.* Rapport CEA-R-5158.

Chen, C., Zhao, B., Yang, X., & Li, Y. (2011). Role of two-way airflow owing to temperature difference in severe acute respiratory syndrome transmission: revisiting the largest nosocomial severe acute respiratory syndrome outbreak in Hong Kong. *The Royal Society*, 699–710.

Chern, M.-J., & Cheng, W.-Y. (2007). Numerical investigation of turbulent diffusion push-pull and exhaust fume cupboards. *Annals of Occupational Hygiene, 51.6*, 517-531.

Chung, J. N., & Troutt, T. R. (1988). Simulation of particle dispersion in an axisymmetric jet. *J. Fluid Mech. 186*, 199-222.

Colgate, S., & RH., W. (1966). The hydrodynamic behavior of supernova explosions. *Astrophys. J.*, 143:626–81.

Colin, R., & Prevost, C. (2006). *Etudde de l'efficacité de confinement des boîtes à gants en situations normales et accidentelles.* IRSN.

Comte-Bellot, G., & Corrsin, S. (1971). Simple Eulerian time correlation of full- and narrow-band velocity signals in grid generated isotropic turbulence. *Journal of Fluid Mechanics*, 48(2) :273–337.

Crowe, C. T., Chung, J. N., & Troutt, T. R. (1988). Particle mixing in free shear flows. *Prog. Energy Combust. Sci.*, 171-194.

Crowe, C. T., Gore, R., & Troutt, T. R. (1985). Particle dispersion by coherent structures in free shear flows. *Particulate Sci. Tech. 3*, 149-158.

Cruz, A. S., Coste, N., Makhloufi, R., Guillou, S., & Delboulbé, E. (2011). Airflow inside an open ventilated system: Influence of operator's arms or moving conveyor. *Journal of Food Engineering 105*, 197–209.

Da Silva, C. B., Lopes, D., & Raman, V. (2015). The effect of subgrid-scale models on the entrainment of a passive scalar in a turbulent planar jet Carlos. *Journal of Turbulence, Vol. 16, No. 4*, 342–366.

Dimotakis, P. (2000). The mixing transition in turbulent flow. *J. Fluid Mech.*, 409:69–98.

Dimotakis, P. E. (2000). The mixing transition in turbulent flow. *J. Fluid Mech.*, 409:69–98.

Dimotakis, P. E. (2005). Turbulent mixing. *Annu. Rev. Fluid Mech.*, 37:329–56.

Druzhinin, O., & Elghobashi, S. (1998). Direct numerical simulations of bubble-laden turbulent flows using the two-fluid formulation. *Phys. Fluids* , 10:685–97.

Ducos, J. (2016). *Confinement dynamique des enceintes de ventilation - Présentation de l'outil SMART-DOG.* ATSR – 5ème Forum Européen De Radioprotection.

Dupoux, N., Laborde, J., & Prevost, C. (1997). *Etude des criteres de confinement dynamique au niveau des ouvertures d'une enceinte.* Rapport d'étude IRSN.

Durst, F., & PEREIRA, J. C. (1991). Experimental and Numerical Investigations of the Performance of Fume Cupboards. *Building and Environment*, Vol. 26, No. 2, pp. 153-164.

Durst, F., & Pereira, J. C. (1991). Experimental and numerical investigations of the performance of fume cupboards. *Building and Environment, 26.2*, 153-164.

Eames, I., Shoaib, D., Klettner, C. A., & Taban, V. (2009). Movement of airborne contaminants in a hospital isolation room. *The Royal Society*, vol. 6, S757–S766.

Eaton, J. K., & Fessler, J. R. (1994). Preferential concentration of particles by turbulence. *Int. J. Multiphase Flow*, 169-209.

Elghobashi. (1994). On predicting particle-laden turbulent flows. *Appl. Sci. Res.*, 309-329.

Elghobashi, S. (1991). Particle-Laden turbulent flows: Direct simulation and closure models. *Appl. Sci. Res. 48*, 301.

Elghobashi, S., & Abou Arab, T. (1983). A two-equation turbulence model for two-phase flows. *Phys. Fluids*, 931-938.

Ferry, J., & Balachandar, S. (2001). A fast Eulerian method for two-phase flow. *Int. J. Multiphase Flow*, 27:1199–226.

Ferry, J., Rani, S., & Balachandar, S. (2003). A locally implicit improvement of the equilibrium Eulerian method. *Int. J. Multiphase Flow* , 29:869–91.

Fevrier, P., Simonin, O., & Squires, K. (2005). Partitioning of particle velocities in gas-solid turbulent flows into a continuous field and a spatially uncorrelated random distribution: theoretical formalism and numerical study. *J. Fluid Mech.*, 533:1–46.

Frohlich. (2008). Hybrid LES/RANS methods for the simulation of turbulent flows. *Progress in Aerospace Sciences*.

Geurts, B. J., Clercx, H., & Uijttewaal, W. (2007). *Particle-Laden Flow: From Geophysical to Kolmogorov Scales.* ERCOFTAK series.

Glawe, D. D., & Samimy, M. (1993). Dispersion of solid particles in compressible mixing layers. *J. Propulsion Power 9*, 83-89.

Goldberg, U. (2017). A Realizable Version of the k-w Turbulence Model. . *Studies in Engineering and Technology.* .

Gore, R. A., & Crowe, C. T. (1989). Effect of particle size on modulating turbulent intensity. *Int. J. Multiphase Flow Vol. 15, No. 2*, pp. 279-285.

Gore, R. A., & Crowe, C. T. (1989). Effect of particle size on modulating turbulent intensity. *Int. J. Multiphase Flow 15*, 279-285.

Gosman, A., & Ioanides, E. (1981). Aspects of computer simulation of liquid-fuelled combustors. *AIAA 19th Aerospace Sciences Meeting*, (pp. 81-0323). St. Louis.

Gulayev, A., Kozlov, V. Y., & Secundov, A. (1993). A universal one-equation model for turbulent viscosity. *Fluid Dynamics*, 28(4) :485–494.

Hang, J., Li, Y., Ching, W., Wei, J., Jin, R., Liu, L., & Xie, X. (2015). Potential airborne transmission between two isolation cubicles through a shared anteroom. *Building and Environment 89*, 264-278.

Hinds, W. (1999). *Aerosol Technology.* A Wiley-Interscience Publication. Second edition.

Hirche, D., Birkholz, F., & Hinrichsen, O. (2019). A hybrid Eulerian-Eulerian-Lagrangian model for gas-solid simulations. *Chemical Engineering Journal 377*.

Ishima, T., Hishida, K., & Maeda, M. (1993b). Particle dispersion in a flow field with vortex shedding behind a pair of vortices. *In ASME FED-Vol 166, Gas-Solid Flows*, 215-220.

ISO-16647. (2018). *Nuclear facilities — Criteria for design and operation of confinement systems for nuclear worksite and for nuclear installations under decommissioning.*

ISO-17873. (2004). *Norme internationale, installations nucléaires - critères pour la conception et l'exploitation des systèmes de ventilation des installations nucléaires autres que les réacteurs nucléaires.*

Jebakumar. (2015). Comparison of the structure of computed and measured particle-laden jets for a wide range of Stokes numbers.

Johnson, A. E., & Fletcher, B. (1996). The effect of operating conditions on fume cupboard containment. *Safety Science, Vol. 24, No. 1*, 51-60.

Johnson, A. E., & Fletcher, B. (1996). The effect of operating conditions on fume cupboard containment. *Safety Science*, Vol. 24, No. 1, pp. 51-60.

Jones, W., & Launder, B. (1974). The prediction of laminarization with two equation model of turbulence. *International journal of heat and mass transfer*, 15, 301-314.

Kaissoun, S. (2018). *Mécanismes de transfert aéraulique au travers d'ouvertures : application à l'efficacité du confinement dynamique d'enceintes de chantier.*

Kalliomaki, P., Saarinen, P., Tang, J. W., & Kosk, H. (2016). Airflow patterns through single hinged and sliding doors in hospital isolation rooms e Effect of ventilation, flow differential and passage. *Building and Environment 107*, 154-168.

Karaismail, E., & Celik, I. (2010). On the inconsistencies related to prediction of flow into an enclosing hood obstructed by a worker. *Journal of occupational and environmental hygiene, 7.6*, 315-325.

Karaismail, E., & Celik, I. (2010). On the Inconsistencies Related to Prediction of Flow into an Enclosing Hood Obstructed by a Worker. *Journal of Occupational and Environmental Hygiene*, 7: 315–325.

Kim, I., Elghobashi, S., & Sirignano, W. (1993). Three dimensional flow interactions between a cylindrical vortex tube and a spherical particle. *J. Fluid Mech.*

Kolmogorov, A. N. (1940). Local structure of turbulence in an incompressible viscous fluid at very high Reynolds numbers. *Dokl. Akad. Nauk SSSR*, 30(299).

Lafanechère, L. (2009). *Guide méthodologique de conception et exigences d'exploitation des sas de confinement des chantiers.* Note technique EDF.

Lazaro, B. J., & Lasheras, J. C. (1989). Particle dispersion in a turbulent plane, free shear layer. *Phys. Fluids A 1*, 1035-1044.

Longmire, E. K., & Eaton, J. K. (1992). Structure of a particle-laden round jet. *J. Fluid Mech.*, 217-257.

Mannan, S. (Volume 2, 2005). 29 - Computer Aids. Dans *Lees' Loss Prevention in the Process Industries (Third Edition)* (pp. Pages 29/1-29/5).

Marble, F. (1970). Dynamics of dusty gases. . *Annu. Rev. Fluid Mech.* , 2:397–446.

Martin, H. (1977). Heat and mass transfer between impinging gas jets and solid surfaces. *Advances in Heat Transfer, Academic Press New York 13*, 1-6.

Maxey, M. R., & Corrsin, S. (1986). Gravitational settling of aerosol particles in randomly orientated circular flow fields. J. Atmospherical Sci, Vol 43. 1112-1134.

Menter, F. (1994). Two-equation eddy-viscosity turbulence models for engineering applications. *AIAA Journal, 32(8)*, 1598-1605.

Menter, F., Langtry, R., Kuntz, M., & al., e. (2003). Ten years of industrial experience with the SST turbulence model. *Turbul. Heat Mass Transf.*, 4, 625–632.

Merle, A., Legendre, D., & Magnaudet, J. (2005). Forces on a high-Reynolds-number spherical bubble in a turbulent flow. *J. Fluid Mech.*, 532:53–62.

Mocho, V. M. (2008). *Mesure du taux de renouvellement d'un local par tracage gazeux.* IRSN.

Nerisson, P., Olivier, S., Ricciardi, L., Douce, A., & Fazileabasse, J. (2011). Improved CFD transport and boundary conditions models for low-inertia particles. *Computers & Fluids*, 79–91.

Nicholson, G., Clark, R., & CalcinaGoff, M. (2000). Computational fluid dynamics as a method for assessing fume cupboard performance. *Annals of Occupational Hygiene, 44(3)*, 203-217.

Phares, D. J. (2000). The wall shear stress produced by the normal impingement of a jet on a flat surface. *J. Fluid Mech., vol. 418*, 351-375.

Prevost, C. (2020). *Programme d'étude du phénomène de rétrodiffusion à échelle réelle dans le dispositif MASSALE.* Rapport n°IRSN/2020-00721.

Prevost, C., & Lacan, J. (2003). *Etude de l'efficacité de confinement d'une boîte à gants en situations accidentelles de fonctionnement.* Paris: CFA Conference.

Prevost, C., Bouilloux, L., & Lacan, J. (2005). *Etude de l'efficacité de confinement assuré par une boîte à gants en situations accidentelles de fonctionnement.* Nantes: SFRP Conference.

Prévost, C., Dupoux, N., & Laborde, J. (2000). Applications of laser velocimetry techniques for air flow analysis in pollutant transfer studies. *7 th International Conference on Air Distribution in Rooms*.

Rayleigh. (1883). Investigation of the character of the equilibrium of an incompressible heavy fluid of variable density. *Proc. London Math. Soc.*, 14:170–77.

Reeks, M. W. (1991). On a kinetic equation for the transport of particles in turbulent flows. *Phys. Fluids* , 446-456.

Renoux, A., & Boulaud, D. (2003). *Physique des aérosols.*

Richardson, L. (1922). Weather prediction by numerical process. Cambridge University Press.

RIDA, Z. (2020). *Rapport de 1ère année de thèse, Aeraulic transfer mechanisms through maintenance and dismantling sites openings: Evaluation of aerosol aerodynamic behavior contribution to backscatter phenomenon.* IRSN/2019-871.

RIDA, Z. (2021). *Aeraulic transfer mechanisms through openings on enclosures in maintenance and dismantling sites: evaluation of aerosol aerodynamic behavior contribution to backflow phenomenon.* Rapport n°2021-00087.

Shih, Y.-C., Chiu, C.-C., & Wang, O. (2007). Dynamic airflow simulation within an isolation room. *Building and Environment 42*, 3194–3209.

Shur, M., Spalart, P., Strelets, M., & Travin, A. (1999). Detached-eddy simulation of an airfoil at high angle of attack. *4th Engineering Turbulence Modelling and Experiments*, 669–678.

Shur, M., Travin, A., Spalart, P. R., & Strelets, M. (2016). The Delay of RANS-to-LES Transition in Hybrid RANS-LES Approaches and Some Recently Proposed Remedies. *Notes on Numerical Fluid Mechanics and Multidisciplinary Design*.

Spalart, P. (2001). Young-person's guide to Detached-Eddy Simulation grids. *National Aeronautics and Space Administration, Virginia 23681-2199.*

Spalart, P., & Allmaras, S. (1992). A one-equation turbulence transport model for aerodynamic flows. *30th Aerospace Sciences Meeting & Exhibit*.

Spalart, P., & Allmaras, S. (1994). A one-equation eddy-viscosity model for aerodynamic flows. *La Recherche Aérospatiale*, 1 :5–21.

Spalart, P., Jou, W.-H., Strelets, M., & Allmaras, S. (1997). Comments on the feasibility of LES for wings and on hybrid RANS/LES approach. *1st AFOSR International Conference on DNS/LES, Advances in DNS/LES. Louisiana Tech University*.

Squires, K., Forsythe, J., Morton, S., & al., e. (2002). Progress on detached-eddy simulation of massively separated flows. *Aerospace sciences meeting*.

Stoyanov, V. (2019). Numerical study of heat transfer between impinging gas jets and solid surfaces. *IOP Conference Series: Materials Science and Engineering 618.*

Strelets, M. (2001). Detached eddy simulation of massively separated flows. *39th Aerospace sciences meeting and exhibit, USA* .

Strelets, M., Shur, M., Travin, A., & Spalart, P. R. (2016). The delay of RANS-to-LES transition in hybrid RANS-LES approaches and some recently proposed. *Notes on Numerical Fluid Mechanics and Multidisciplinary Design*.

Tanga, J., Eamesb, I., Lic, Y., Tahad, Y., Wilsone, P., Bellinganf, G., . . . Breuerd, J. (2005). Door-opening motion can potentially lead to a transient breakdown in negative-pressure isolation conditions: the importance of vorticity and buoyancy airflows. *Journal of Hospital Infection* , vol. 61, 283–286.

Taylor, G. (1950). The instability of liquid surfaces when accelerated in a direction perpendicular to their planes. *Proc. R. Soc. London Ser.*, A 201:192–96.

Temmerman, L., & Hirsch, C. (2008). Towards a successful implementation of DES strategies in industrial RANS solvers. *Advances in Hybrid RANS-LES Modelling*, 232– 241.

Travin, A., Shur, M., Strelets, M., & al., e. (2000). Detached-eddy simulations past a circular cylinder. *Flow. Turbul. Combust.*, 63, 293–313.

Travin, A., Shur, M., Strelets, M., & Spalart, P. (2000). Physical and Numerical Upgrades in the Detached Eddy Simulation of Complex Turbulent Flows. *412 EUROMECH Colloquium on LES of Complex Transitional and Turbulent Flows*.

Tsuji, Y., Morikawa, Y., & Shiomi, H. (1984). LDV measurements of an air-solid two-phase flow in a vertical pipe. *J. Fluid Mech. 139*, 417-434.

Tung, ,. Y.-C., Shih, Y.-C., & Hu, S.-C. (2009). Numerical study on the dispersion of airborne contaminants from an isolation room in the case of door opening. *Applied Thermal Engineering 29*, 1544–1551.

Uhlmann, M. (2008). Interface-resolved direct numerical simulation of vertical particulate channel flow in the turbulent regime. *Phys. Fluids* , 20:053305.

Varaksin. (2007). Turbulent particle-laden gas flow. Dans Varaksin.

Varaksin, A., & Zaichik, L. (1998). The effect of a fine divided impurity on the turbulence intensity of a carrier flow in a pipe. *High Temp. (Engl. transl.)*, 983.

Wang, L., & Maxey, M. (1993). Settling velocity and concentration distribution of heavy particles in homogeneous isotropic turbulence. *Journal of Fluid Mechanics, 256*, 21-68.

Wen, F., Kamalu, N., Chung, J. N., Crowe, C. T., & Troutt, T. R. (1992). Particle dispersion by vortex structures in plane mixing layers. *J. Fluids Engng 114*, 657-666.

Wicker, R. B., & Eaton, J. K. (2000). structure of a swirling recirculating coaxial free jet and its effect on particle motion. *International Journal of multiphase flow 27*, 949-970.

Wilcox, D. C. (1998). *Turbulence modeling for CFD, 2nd ed.* ISBN 0-9636051-5-1.

Xie, X., Li, Y., Chwang, A., Ho, P., & Seto, W. (2007). How far droplets can move in indoor environments e revisiting the wells evaporation-falling curve. *Indoor Air 17*, 211-225.

Yuu, S., Yasukouchi, N., & Hirosawa, Y. a. (1978). Particle turbulent diffusion in a dust-laden round jet. *J. AIChE*, 509-519.

Zaichik, L., Pershukov, V., Kozelev, M., & Vinberg, A. (1997). Modeling of dynamics, heat transfer and combustion in two-phase turbulent flows: 1. Isothermal flows. *Exp Therm Fluid Sci*, 15:291–310.

Zaichik, L., Simonin, O., & Alipchenkov, V. (2003). Two statistical models for predicting collision rates of inertial particles in homogeneous isotropic turbulence. *Phys Fluids*, 15(10):2995–3005.

Zaichik, L., Soloviev, S., Skibin, A., & Alipchenkov, V. (2004). A diffusion–inertia model for predicting dispersion of low-inertia particles in turbulent flow. *5th International conference on multiphase flow, Japan*.

Zheng, W., Yan, C., Liu, H., & Luo, D. (2016). Comparative assessment of SAS and DES turbulence modeling for massively separated flows. *Acta Mech. Sin.* , 32(1):12–21.